The Dissertation Committee for Michael Vincent Pachuilo
certifies that this is the approved version of the following dissertation:

Study of Non-Equilibrium Plasma Streamer Discharges in High Pressure Molecular Gases

Committee:

Laxminarayan L. Raja, Supervisor

Philip L. Varghese, Co-Supervisor

Noel T. Clemens

Gary A Hallock

Dmytro Levko

Study of Non-Equilibrium Plasma Streamer Discharges in High Pressure Molecular Gases

by

Michael Vincent Pachuilo

DISSERTATION

Presented to the Faculty of the Graduate School of

The University of Texas at Austin

in Partial Fulfillment

of the Requirements

for the Degree of

DOCTOR OF PHILOSOPHY

THE UNIVERSITY OF TEXAS AT AUSTIN

December 2017

Dedicated to my parents, Keith and Tammy Pachuilo, and Sarah Kendzior.

Acknowledgments

There are many people who played a vital role in the completion of this dissertation. I wish to thank my parents Keith and Tammy Pachuilo, and my girlfriend Sarah Kendzior for all their support and encouragement throughout my dissertation. I thank my advisor, Dr. Laxminarayan L. Raja for his support throughout my studies. I appreciate the freedom I was afforded to explore research topics which interested me. I thank my co-advisor Prof. Philip Varghese for his guidance and suggestions. I also thank Dr. Dmytro Levko for his help in development of the plasma chemical model, and for our numerous discussions. I thank Dr. Noel Clemens and Dr. Gary Hallock for being on my doctoral committee. I thank Dr. Roger Bengtson for his guidance in plasma spectroscopy. I also thank Joesph Pokluda for all his help in the machine shop and encouragement, as well as Geetha Rajagopal, Stephen Sanders, and Scott Messec who all made this journey possible. I thank Francis Stefani and Louis Rosocha for all their help, guidance, and support throughout my studies. Finally, I thank all my friends and colleagues - Doug, Hari, Alex, Eliseo, Vivek, Ashish, Miles, Kostas, Dylan, Yunho, Anand, Christopher, and Young-Joon, for their support.

Study of Non-Equilibrium Plasma Streamer Discharges in High Pressure Molecular Gases

Publication No. _____

Michael Vincent Pachuilo, Ph.D.
The University of Texas at Austin, 2017

Supervisor: Laxminarayan L. Raja
Co-Supervisor: Philip L. Varghese

A study of streamer discharge properties in the context of their applications in: large-gap arc breakdown, and plasma reforming of carbon-dioxide is presented. The first part of this work focused on the characterization and optimization of volume streamers for reforming applications in carbon dioxide. In the second part of this work the dynamics of surface streamer discharges were investigated, and their application as a non-intrusive fuse wire to breakdown a large-gap which ultimately results in an arc discharge. Both the non-equilibrium surface streamer discharge and the subsequent arc discharge were characterized by instantaneous broadband imaging, wide-band optical emission spectroscopy (OES), and voltage-current (VI) characteristics. In addition to the diagnostics described above, instantaneous narrowband imaging and a two-dimensional plasma fluid model were used to characterize the volume streamer discharges in carbon dioxide.

Instantaneous broadband imaging of the volume streamers in CO_2 showed that the spatial distribution of excited species in the streamer discharge was dependent upon the voltage polarity. The streamer velocity ($\sim$700-1000 km/s) and diameter ($\sim$ 100 μm) were also estimated from the broadband imaging. Spectral bandpass filters were then coupled with a low-resolution survey spectrum (OES) to identify the spatial distribution and temporal evolution of excited species. These narrowband instantaneous images that electronically excited CO($B^1\Sigma^+ \rightarrow A^1\Pi$) and O(^{5}P) were produced in different polarity streamers. The excited CO production was favored in diffuse negative streamers, while excited O was produced in constricted positive streamers.

Plasma spectroscopy showed significant thermal non-equilibrium in the discharge with a spatial average electron temperature of 0.6 eV, CO_2 vibrational temperature of $\sim$ 3000 K, and a gas temperature of 670 K. Additionally, the electron density was determined to be 10^{21} m^{-3}, and the CO concentration found to be 10^{23} m^{-3} which corresponds to a conversion efficiency of $\sim$ 1-2%. The experimental results were compared with a 2D axisymmetric plasma fluid model with a finite rate chemistry including vibrational kinetics. The fluid model and experiments showed good correlation between the streamer and plasma properties. Modeling showed that conversion efficiency was dependent on the pulsing frequency. The increase in CO conversion with pulsing is attributed to the vibrational ladder climbing mechanism. Additionally, simulations of multi-streamer arrays showed there is a characteristic packing factor above which multiple streamer interactions can be neglected.

In the surface streamer investigations, broadband imaging showed that the surface streamer bridged a gap of a few cm in a few 100 ns. These streamers (in argon) were characterized by an average electron temperature of 1.25 eV, and electron density of $10^{19} - 10^{20}$ m^{-3} from a CR model and OES. The CR model incorporated 42 energy levels of Ar and accounted for the dominant population and depopulation mechanisms of the $2P_i$ (Paschen notation for Ar I $4P_i$) states. Additionally, OES of the discharge indicated gas heating (815 K), and partial local thermodynamic equilibrium, PLTE, of the Ar II 4P ions with an excitation temperature 0.7 eV. This method reliably produced high-purity thermal arcs in argon at voltages ∼100 times lower than the Paschen breakdown threshold, but with minor concentrations of methane, the surface discharges were quenched preventing arc formation. The quenching of the discharge was caused by electron energy losses to the low energy vibrational levels in methane.

The thermal plasma was characterized by an electron temperature and density of ∼1 eV (estimated from the Boltzmann plot technique), and $\sim 10^{23}$ m^{-3} (from Stark broadening of hydrogen lines), respectively. SEM images showed that after several hundred firings, plasma damage of the quartz chamber was confined to a depth of 3.3 μm, while minimal damage was observed on a single-crystal sapphire test specimen. Energy dispersive x-ray spectroscopy, EDXS, of the test specimen, showed deposition of a thin layer of carbon and silicon. Molecular dynamics (MD) simulations confirmed experimental observations. MD showed that argon atoms with a temperature of ∼1-3 eV pro-

duced no surface ablation; it was only high energy atoms (>3 eV) which lead to an ablation event. This was a result of the redistribution of the incident atoms energy to multiple surface atoms.

Table of Contents

List of Tables

List of Figures

Chapter 1

Introduction

Non-equilibrium (cold) plasmas are increasingly used in the chemical processing of gases for: fuel synthesis, exhaust treatment, plasma assisted combustion, bio-fuels, plasma medicine, sterilization, plasma deposition, and etching. Typically, these discharges are operated at low pressure ($\sim$100's mTorr) constituting a uniform diffuse glow discharge. In recent years interest has increased in understanding and developing of cold high pressure (atmospheric) discharges.

These cold atmospheric pressure plasma discharges are characterized by thermal non-equilibrium, where the electron, vibrational, rotational, and translational temperatures can differ, some by orders of magnitude. The nature of the non-equilibrium in these plasmas arises from preferential heating of electrons. These mobile electrons gain high energies in the presence of an electric field. Then through electron impact collisions the energy is efficiently distributed into other degrees of freedom (vibration, excitation, and ionization), while the bulk gas remains cold. If the electron energy distribution is properly tailored, specific reaction pathways can be selected. To maintain a non-equilibrium discharge, one must prevent plasma thermalization. This is

achieved through rapid pulsing (of the order 10-100's nanoseconds), high series resistance, barrier discharges, or corona discharges.

There are several advantages of non-equilibrium discharges operating at elevated pressures. For instance, a complex vacuum system is no longer needed which makes the design of a gas reactor much simpler. Additionally, the density of active species ($\sim 10^{22}$ m^{-3}) is orders of magnitudes higher than conventional glow discharges ($\sim 10^{18}$ m^{-3}), and energy can be directly coupled into specific channels rather than gas heating. At these pressures the plasma length scales are reduced and usually smaller than the chamber dimensions. This causes the plasma to form complex structures rather than a uniform discharge.

For example, at high pressures and reduced electric fields constricted plasma filaments are formed. These filaments are termed, streamers. Streamers are a part of the thermal breakdown process which precede an arc or spark as reviewed by [14]. It has been shown that streamers follow similarity laws. At a given voltage and for decreasing pressures, the same structure and growth will be observed for streamers, but the length and time scales of these filaments will vary. This is evident from the variation of the streamer diameter with pressure for atmospheric sprites [5]. When the pressure is 10 mTorr the diameter is $\sim$10 m, while at atmospheric pressures the diameters are $\sim$100 μm [15].

In the work presented herein, we focus on high pressure non-equilibrium streamer discharges to ignite large volume arc discharges (Chapter 8) and

carbon dioxide splitting (Chapter 2-7). In the first part of this thesis the optimization of nanosecond pulsed streamer discharges in carbon dioxide with applications in reforming are presented. The second part of this work examines the ability of surface tracking streamer discharges for igniting high purity large gap arc discharges at atmospheric pressure. As part of this work, the high-density arc discharges were also analyzed as well as thermal plasma material interactions (Appendix A).

An outline for the thesis is as follows: an overview of plasmas and streamer theory will be presented here, followed by Chapter 2-7 which discusses volume streamer discharges in carbon dioxide for reforming applications, Chapter 8 discusses surface streamer discharges as an electron seed source for thermal plasma ignition. The thermal plasma material interactions are described in Appendix A. The concluding statements and future recommendations will be presented in Chapter 9.

1.1 The Plasma State

Over 99% of the observable universe exists in the plasma state, often referred to as the fourth state of matter. It was Irving Langmuir who first used the term plasma. He defined it as a region of quasi-neutral ionized gas which consists of a soup of charged species: electrons and ions in equal proportions, as well as neutrals, radicals, and excited species. It is these electrically charged and chemically active species that make the plasma state a valuable resource for industrial and laboratory applications. Plasmas can be broadly classified

into two regimes: thermal, and non-thermal or non-equilibrium plasmas.

1.1.1 Equilibrium Plasmas

Thermal plasmas occur at high pressures. Figure 1.1 shows the variation of the bulk gas temperature and electron temperature as a function of the pressure. At pressures above ∼10 kPa, collisional energy transfer dominates over radiative transfer and the system is said to be in local thermodynamic equilibrium (LTE) [3, 16]. For a system in LTE, all species are defined by a single temperature, the electron temperature [17]. These thermal plasmas are characterized by temperatures of ∼1-3 eV and plasma electron densities in excess of 10^{21} m^{-3} [3]. The extremely high energy densities and high pressures are key to activating important thermo-chemical processes within the plasma discharge. For example, a thermal arc can nearly completely decompose the gas medium into its atomic state with a high degree of ionization [4]. Thermal plasmas have been implemented in a variety of applications such as: reforming and conversion [4, 18], space propulsion [19, 20], plasma torches [21], electrothermal launchers [22], plasma pyrolysis [23],spark-plugs for combustion ignition [24], and material processing [11, 24, 25]. They can also be inadvertent byproducts of operation of devices such as electrical circuit breakers and faults in switch-gears [26, 27].

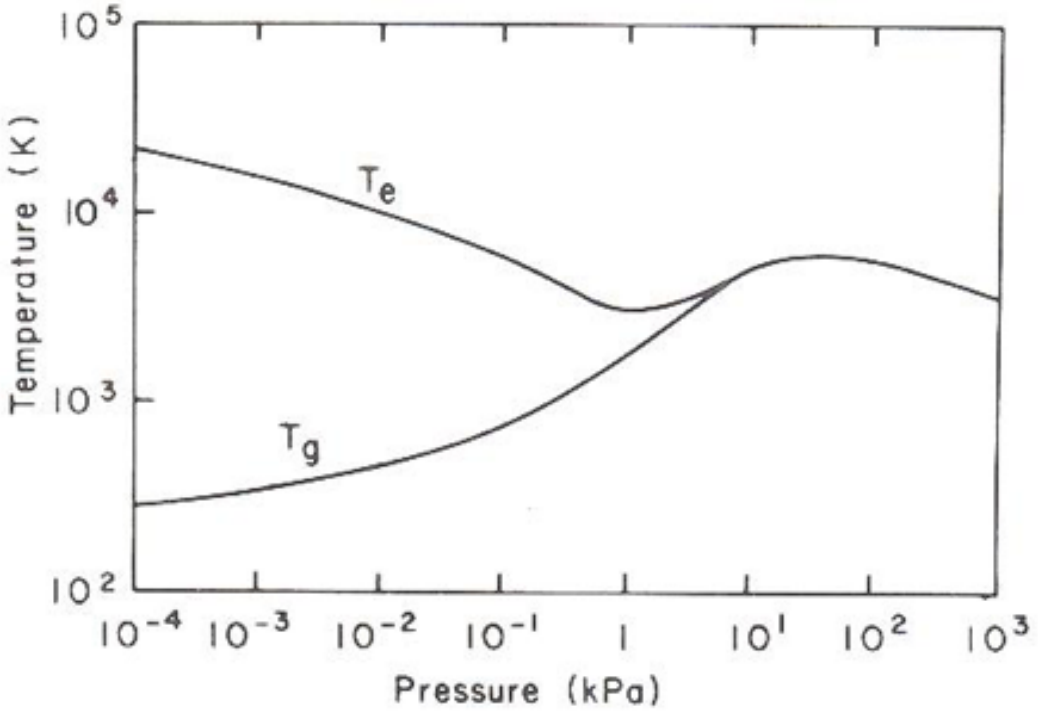

Figure 1.1: The variation of gas and electron temperatures in plasma as a function of pressure [3]

1.1.2 Non-Equilibrium Plasma

In contrast to thermal plasmas, non-equilibrium discharges are characterized by two temperatures: the electron temperature, and the bulk gas temperature, as indicated by Fig. 1.1 . These discharges easily occur at low pressures where electrons gain significant energy from the applied field prior to colliding with bulk background species [3, 28]. These low pressure or glow discharges are commonly observed in neon lights, and are used extensively in the microelectronics industry for etching and deposition processes [28]. Non-equilibrium discharges can also be generated at atmospheric pressure by minimizing Joule heating and preventing thermalization.

There are several different types of atmospheric non-equilibrium discharges including: corona [29], dielectric barrier discharge (DBD) [30], streamers [31], and plasma jets [32]. These non-equilibrium discharges are weakly ionized, with an ionization coefficient, α, less than $\sim$1%. The electron number densities range from $10^{15} - 10^{19}$ m^{-3} for coronal discharges [29] and $10^{19} - 10^{22}$ m^{-3} for streamers occurring in dielectric barrier discharges, DBDs, and plasma jets [33–37]. Additionally, the average electron temperatures are generally $\sim$1-2 eV, while the bulk gas temperature is significantly lower, typically 300-2000 K. These non-equilibrium discharges have found recent applications across many fields such as biomedical germicidal treatments [37–39], flow actuation [40, 41], removal of volatile organic compounds (VOCs) [42], plasma assisted combustion (PAC) [43], plasma reforming [44–47], and polymer surface treatments [48] where high bulk gas temperatures are not desirable.

1.2 Theory of Breakdown in Gaseous Insulators: The Requirement for Fast Ionization Waves at High Pressures

Under normal conditions gases are good insulators with a conductivity of $\sim \sigma_C = 10^{-14}$ Ω^{-1}m^{-1}, compared to metal conductors with $\sim \sigma_M = 10^7$ Ω^{-1}m^{-1} [49]. The non-zero conductivity arises due to permanent ionization events such as the solar wind, natural radioactivity, and cosmic background radiation. When an electric field is applied across two electrodes of certain strength, which is dependent upon the gas composition and electrode geometry, a transition occurs and the gas becomes a moderately good conductor. The transition from an insulator to a conductor is termed electrical breakdown, and the voltage that this occurs at, the breakdown potential.

In the early work of Paschen (1889) and Muller (1880) a simple experiment was conceived to investigate the dependence of pressure and gap distance on the breakdown voltage. Parallel plate electrodes were used providing a uniform electric field within the gap. The cathode surface was uniformly illuminated with UV radiation to generate a local source of electrons. The breakdown potential was found experimentally to vary with the similarity parameter, Pd, where P is the pressure of the discharge, and d is the gap distance. This relation between the pressure-distance product and breakdown voltage is known as Paschen's law, and it is given by Eqn. 1.1 [50]:

$$V_B = \frac{BPd}{\ln APd - ln[ln(\frac{1}{\gamma} + 1)]} \tag{1.1}$$

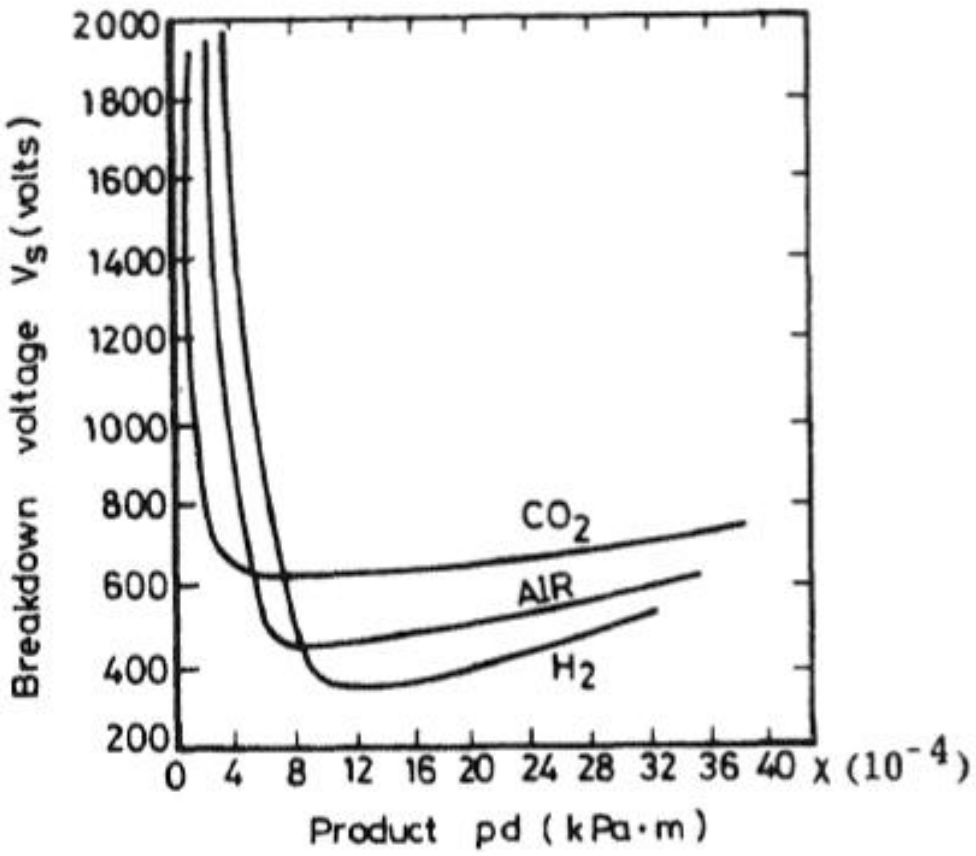

Figure 1.2: Paschen curve for carbon dioxide, air, and hydrogen: breakdown voltage as a function of pressure-distance [4].

Here, V_B is the breakdown voltage, B is related to the excitation and ionization energy, A is the saturation ionization at a particular reduced electric field E/N, and γ is the secondary emission coefficient for the electrode surface. A and B are determined experimentally for a finite range of E/N. Figure 1.2 shows the breakdown voltage as a function of the pressure-distance for carbon dioxide, hydrogen, and air, or the Paschen curve [4].

The shape of the Paschen curve (Fig. 1.2) can be explained as follows. At low pressure-distance products and consequently large mean free paths (high Knudsen number $Kn = \lambda/L$), a high voltage is necessary to increase the chance of collisional-ionization processes (α) and maintain the breakdown condition. For higher pressure-distances the mean free path is small, and higher electric fields are necessary to overcome collisional losses. Due to these two competing processes a local minimum breakdown voltage exists.

In similar parallel plate experiments, Townsend investigated the breakdown processes which led to the derivation of Eqn. 1.1. These experiments were conducted at low pressures ($\lesssim$ 100 Torr) and voltages ($\lesssim$ 2000 V) [50]. Townsend proposed that electrons in the presence of an electric field that gained energy above the ionization potential of the atoms or molecules, would lead to an exponential growth in the current, or an avalanche process. This critical energy, is a function of the reduced electric field E/N, as it depends on collisional losses as well. Maintaining a constant E/N (to maintain constant mean energy of electrons to investigate the spatial growth of current or the ionization processes), as the distance and voltage were increased, the current grew at a rate faster then exponential. The increase in current growth is attributed to secondary ionization processes such as secondary electron emission, photoionization, Penning ionization, or photoelectric effect as described by Eqn. 1.2:

$$I = \frac{I_o e^{(\alpha d)}}{1 - \frac{\omega}{\alpha}[e^{(\alpha d)} - 1]} \quad and \quad \frac{\omega}{\alpha} = \frac{\beta}{\alpha} + \frac{\delta}{\alpha} + \gamma + \frac{\epsilon}{\alpha} + \frac{\eta}{\alpha} \tag{1.2}$$

Where I_o is the initial background electron current, α is the Townsend first ionization coefficient, and ω is the generalized Townsend secondary ionization coefficient which accounts for all secondary ionization processes [50]: electrons produced by positive ion drift in the field (β), secondary electron emission from ion impacts on the cathode (γ), number of photoelectrons emitted from the surface due to photons (δ), cathode emission due to diffusion of excited species (ϵ_{ex}, ϵ_m), and photoionization of the gas from energetic particles η. Typically, the secondary electron emission from the cathode surface is the dominant secondary ionization process for the "low" pressure-distance products considered.

The breakdown potential described by Eqn. 1.1 is derived by setting the denominator of Eqn. 1.2 to zero. This corresponds to infinite growth in the discharge current and correspondingly a breakdown event: $\frac{1}{\gamma} + 1 = e^{\alpha d}$. The passage of a large current though would induce a space-charge which invalidates Eqn. 1.2. Therefore, the above condition for breakdown should be considered as a condition that, if met, leads to a self-sustained discharge in which I_o also tends to zero leading to a finite current. The breakdown voltage should also be independent of the current so long as the current is limited such that the space charge induced field is smaller than the applied field. This self-sustained discharge is known as a Townsend (dark) discharge because the currents are low and there is not significant radiation. Further increase in current leads to a transition from a dark discharge to the well known glow discharge, and an associated drop in the applied voltage.

In the range of $Pd \lesssim 200$ Torr·cm the Townsend avalanche mechanism can be quantitatively described by the observed characteristics of the breakdown processes in gases; but at higher pressures and Pd the mechanism is no longer able to predict the experimental observations. These experimental deviations from the proposed Townsend mechanism can be summarized as follows [50–53]:

1. The time required for the voltage to collapse (or the breakdown mechanism to manifest) in a uniform electric field with a 1 cm gap at atmospheric pressure in air was found to be $\sim 10^{-7}s$. These time scales are far faster than the microsecond time scales necessary for ion movement and secondary processes (γ) predicted by the Townsend mechanism. Additionally, when the cathode was illuminated with various intensities of radiation (photoelectric effect) the increased background electron current should lead to a decrease in the time lag, but at these Pd products no change was observed.

2. The sparking potential for $Pd > 200$ Torr ·cm was found to be insensitive to the cathode material which indicates that secondary electron emission (SEE) processes are insignificant in the breakdown process. Though the Townsend mechanism shows reduced sensitivity to γ processes at higher pressures, the breakdown potential still depended upon the value of SEE (O(10%)). Additionally, experiments conducted at these pressure-distances did not detect a measurable γ coefficient, and

in lightning and positive corona discharges there is clearly no influence of the cathode material on the discharge. All these observations indicate that the theories based on SEE processes are not applicable at high Pd.

3. The Townsend mechanism predicts a diffuse discharge, but observations of sparks at high pressures showed thin filamentary discharges. This observation can not be explained by the cumulative action of primary and secondary ionization processes. Furthermore, discharges were observed to be initiated mid gap between the two electrodes, rather than from the anode or cathode.

These observations made it clear that a new breakdown theory for $Pd \gtrsim 200$ Torr$\cdot$ cm was needed. This new ionization process only required a single avalanche process, which resulted in a fast ionization wave initiated by the high electron density at the head of the avalanche. Furthermore, the process must be independent of the cathode surface. Loeb and Meek [51] proposed a new theory for the breakdown process at high pressure-distances, termed streamer theory. Raether and Kohrmann [52] also proposed a similar mechanism to streamer theory at the same time as Meek and Loeb, it was termed kanal theory.

1.3 The Streamer Discharge

Non-equilibrium discharges in high-pressure gases are characterized by highly constricted fast moving streamer channels that bridge the inter-electrode

gap. These streamers are a source of charged species and active radicals at low (nearly room) sensible temperatures, and are an enabling feature in many engineering applications of these discharges. The electrons in these discharges have very high temperatures ($\sim$10 eV) at the leading edge of the streamer front and lower ($\sim$1 eV) temperatures in the main body of the streamer which results in a unique environment for the processing of molecular gases.

The streamer theory was developed by Reather [36, 52], Meek [53], and Loeb [51, 54, 55] in the early to mid 1900's. Additionally, Raizer [14] presents a good review of the subject. Early experiments at high pressures, $Pd \gtrsim$ 200 Torr$\cdot$ cm, indicated that Eqn. 1.2 did not correctly predict the observed current characteristics. This indicated that the Townsend breakdown theory which relied on secondary process was invalid for these conditions, and a new breakdown mechanism was needed. The theory must show that the breakdown can proceed from a single avalanche process as shown in current waveforms from experiments. Loeb and Meek [54, 56], and simultaneously Raether and Kohrmann [52], proposed the following breakdown mechanism:

1. There are no effects of secondary electron emission from the cathode surface on the breakdown voltage as is necessary in the Townsend mechanism. Any secondary emissions would lead to a similar avalanche and the same mechanism. The pre-breakdown currents on a semi-log plot, where $I = I_o exp(\alpha d)$, are straight lines with respect to gap distance. This is contrary to Eqn. 1.2 which leads to asymptotic growth near the

breakdown voltage. Furthermore, this conforms to experimental observations and Paschen's law (experimental) for high Pd.

2. The current growth $I = I_o exp(\alpha d)$, corresponds to an electron avalanche. This avalanche continues to grow until a critical value is reached, typically $N \sim exp(\alpha d) = O(\sim 10^9)\ m^{-3}$. At this critical density the space charge is distorted significantly, and breakdown occurs. Meek's criterion for streamer formation states that a streamer will form when the radial field about the positive space charge formed in the electron avalanche attains a value of the order of the external applied field [53].

3. A high space charge is produced from electron impact ionization and gives rise to a local electric field distortion. In the wake of the electron avalanche, the relatively immobile ions remain stationary. Around these positive ions, a high localized field is produced. This high field region is necessary to accelerate electrons forming secondary avalanches. A plasma (quasi-neutral region) can then form from the secondary electrons.

4. The generation of secondary electrons occurs through photoionization. Therefore, generation of high-energy photons is necessary in the avalanche for streamer propagation.

The proposed streamer mechanism accounts for the short breakdown times at high Pd and thin filamentary channels. Additionally, streamers can

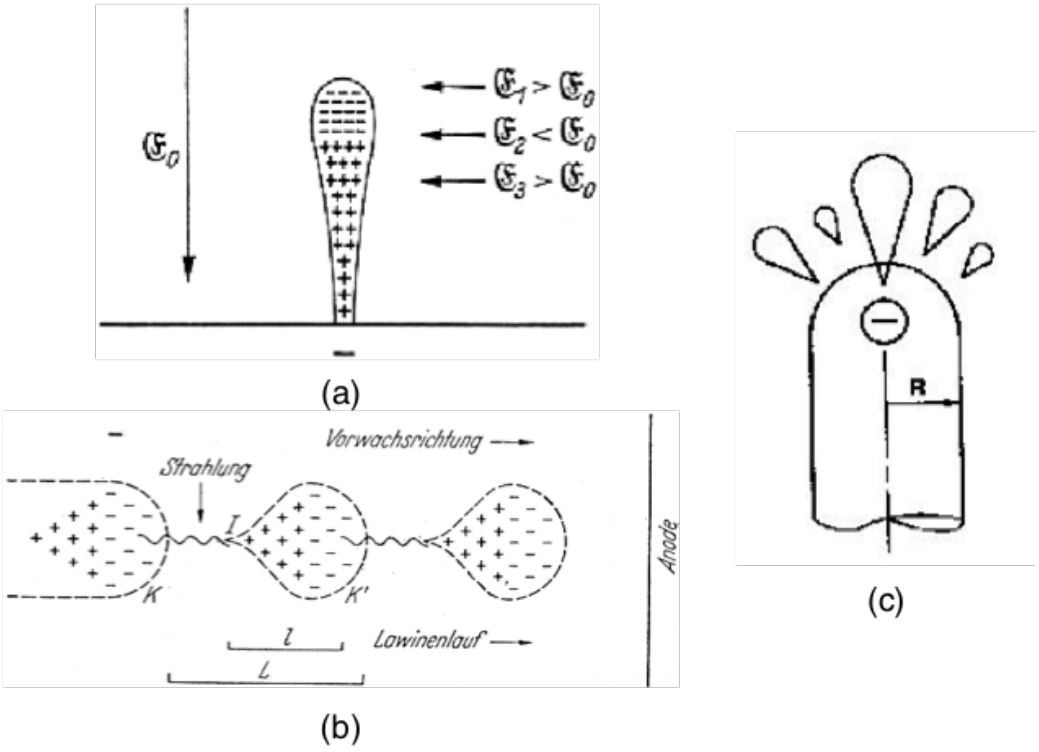

Figure 1.3: Anode directed streamer propagation showing (a) the electron avalanche process, and the propagation of the streamer by photoionization and secondary avalanches (b) and (c) [5]

account for the observations of luminous tracks forming midway between electrodes as well as anode and cathode directed streamers.

In general, a streamer is a filamentary plasma ionization wave which forms at moderate to high pressures. A streamer consists of two main parts: an energetic head with electron temperature of O(10 eV), and streamer column or tail with electron temperatures of O(1 eV). Two types of streamers form depending on the propagation direction of the streamer head: a positive

cathode directed or a negative anode directed streamer. The primary mechanism for propagation of a positive streamer is through photoionization. The photoionization process occurs as electrons are accelerated into the streamer head where they ionize and excite species. These excited species release energetic photons which then further ionize the gas ahead of the streamer head forming secondary avalanches. In cathode directed streamers, these secondary electron avalanches are accelerated towards the positive streamer head and generate new energetic photons. Though photoionization is required for cathodic streamers, it is proposed that anode directed streamers do not require photoionization to propagate. This is because the electron drift is in the direction of the streamer propagation. Therefore, the electrons can be accelerated by the large negative electric field at the anodic streamer head and ionize the medium ahead of the streamer forming additional secondary electrons.

Figure 1.3 shows an illustration of the propagation and evolution of an anodic streamer discharge. The electron avalanche and space charge formation is shown in Fig. 1.3 (a). When the average energy gained by the electron in the external field is greater than the ionization threshold an avalanche is formed. The more mobile electrons move in the external applied field while the ions remain in the wake. Once the radial field due to space charge accumulation is of order the applied field (Meek's Criterion) a self-sustained streamer discharge is formed, Fig. 1.3 (b) and (c). The streamer propagates by energetic photons that ionize the gas upstream of the streamer head, and forms secondary avalanches. For a anodic directed streamer the electrons drift in the

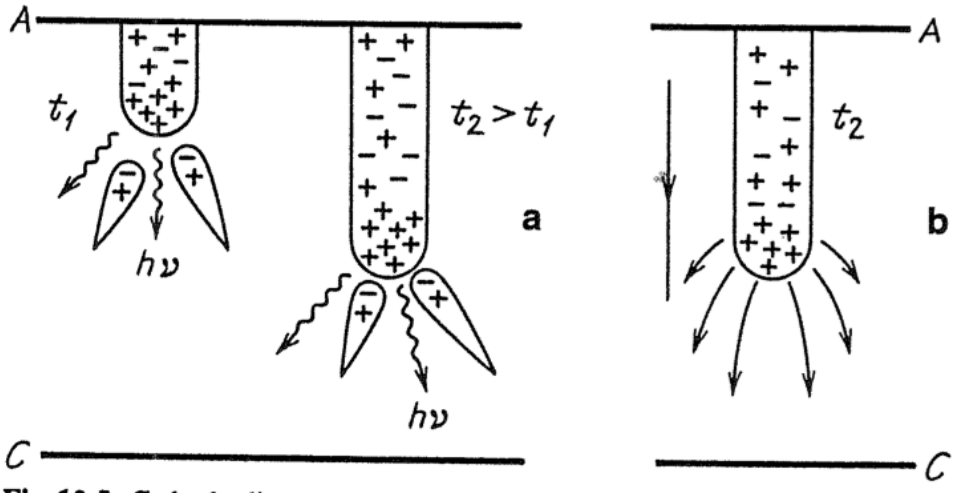

Figure 1.4: Cathode directed streamer at two different times with secondary avalanches (a) and the (b) the electric field lines near the streamer head [6].

direction of the field. Therefore, the ion trail from secondary avalanche processes merges with the primary electrons forming a quasi-neutral plasma. The secondary electrons are accelerated by the field, and now form the streamer head.

In a cathode directed streamer, the streamer begins from the anode and has a positive space charge at the streamer head, Fig. 1.4. Photoionization forms secondary electron avalanches. The secondary electrons drift towards the positive space charge in the streamer head forming a quasi-neutral plasma region. The immobile secondary ions form the new streamer head. Both streamer mechanisms rely on photoionization from excited species generated in the primary electron avalanche, but for cathodic streamers a second mechanism is possible since the electrons drift with the field.

1.4 Objectives

In the thesis presented we are specifically interested in non-equilibrium high pressure streamer discharges for CO_2 reforming, and as a seed electron source for thermal plasma reactors. In non-equilibrium atmospheric plasma reforming applications a dielectric barrier discharge (DBD) reactor is commonly used. During a single pulse cycle in a DBD reactor, a large multitude of streamer discharges occur and are responsible for the discharge's luminous glow. In Chapters 2-7, we analyze a single pulsed streamer discharge in CO_2, investigating both negative and positive polarity pulses. In this work we seek to understand how to optimize the streamer discharge for applications in DBD reactors. In Chapter 8 we have analyzed streamer discharges and the effects of additive molecular gas species for igniting a thermal plasma for material surface interactions (Appendix A). The main objectives from these works are summarized below:

1. **Volume streamers for carbon dioxide reforming:**

   To understand plasma chemical kinetic processes in streamer discharges, and how to optimize these discharges for efficient splitting of carbon dioxide. To this end a single streamer discharge was investigated through experiments, and supported by high fidelity computational plasma fluid modeling. Other works in carbon dioxide reforming reported in the literature have focused on macroscopic system efficiencies and processes, such as zero-dimensional reaction kinetics model for DBD's.

Here we seek to understand how to optimize a single element of the DBD reactor for the population of low lying vibrational states. If there is sufficient density of these low lying vibrational states, the vibrational ladder climbing mechanism becomes efficient. This is important because the ladder climbing dissociation mechanism is the most efficient dissociation mechanism in carbon dioxide. Developing an understanding of how streamers operate in carbon dioxide can be extrapolated to the design and optimization of atmospheric pressure reactors in other molecular gases and mixtures.

2. **Surface streamer discharges as a seed electron source for thermal plasma generation:**

   The main objective of this work was to understand the dynamics of surface tracking streamer discharges with specific applications in designing a high purity pulsed thermal plasma source. Previous thermal sources produced significant contamination of the thermal plasma plume due to ablation of plasma facing components. The use of surface streamers would prevent the need for ablative liners and fuse ignition wires. In addition to understanding the surface streamer breakdown mechanism, the effects of pulsed high density thermal plasmas on plasma facing components was investigated. These high density thermal plasmas are used in a variety of applications ranging from space propulsion to plasma reforming. Any thermal plasma system has plasma facing components. Over time these components degrade and erode which ultimately results

in the system failure. Understanding these plasma material interactions is paramount to design of thermal plasma systems and predicting the lifetime of such devices.

1.5 Contributions

Streamer discharges in molecular gases have been investigated for two applications: (1) CO_2 reforming, and (2) ignition of thermal discharge. It was found that the streamers low energy tail primarily excite vibrational modes of molecular gases, while the streamer head is responsible for ionization and dissociation reactions.

In (1) the excitation of the vibrational modes resulted in a secondary dissociation mechanism which was utilized to increase the conversion of CO_2. In this work (1), pulsing of the streamer discharges populated the low lying vibrational levels which led to vibrational exchange, and excitation of high vibrational levels. These high vibrational levels then dissociate increasing the conversion of CO_2.

In (2) excitation of the vibrational levels prevented the surface streamer discharge from bridging the inter-electrode gap. The decrease in conductivity due to vibrational losses prevented the ignition of thermal discharges in argon-methane mixtures.

1.5.1 Principal Findings:

Volume Streamers for Carbon Dioxide Reforming:

1. A nanosecond high-voltage pulsed-power system was designed for generation of non-equilibrium streamer discharges for CO_2 reforming applications. The system was capable of generating 40 kV pulses, with ∼200 ns FWHM.

2. Narrow band (10 nm) instantaneous imaging of the volume streamers in CO_2 showed that the spatial distribution of excited species in the streamer discharge was dependent upon the voltage polarity. The streamer velocity (∼700-1000 km/s) and diameter (∼ 100 μm) were also estimated from the broadband imaging. Spectral bandpass filters were then coupled with a low-resolution survey spectrum (OES) to identify the spatial distribution and temporal evolution of excited species. These instantaneous narrowband images showed that electronically excited CO($B^1\Sigma^+ \rightarrow A^1\Pi$) and O(^{5}P) were produced in different polarity streamers. The excited CO production was favored in diffuse negative streamers, while excited O was produced in constricted positive streamers.

3. Plasma spectroscopy showed significant thermal non-equilibrium in the discharge with an average electron temperature of 0.6 eV, CO_2 vibrational temperature of ∼ 3000 K, and a gas temperature of 670 K. Additionally, the electron density was determined to be 10^{21} m^{-3}, and the CO concentration found to be 10^{23} m^{-3} which corresponds to a conversion ratio of ∼ 1-2%.

4. A reduced chemical mechanism for streamers in CO_2 which included vibrational kinetics was developed. It was determined that in a single streamer pulse only the low lying vibrational levels were populated. The CO conversion in a single streamer was limited to less than 0.01 %, but with proper voltage pulsing the conversion was increased to a few percent. The experimental results were compared with the 2D axisymmetric plasma fluid model and showed good correlation between the streamer and plasma properties. Modeling showed that conversion efficiency was dependent on the pulsing frequency with a characteristics threshold frequency. Additionally, there was a characteristic packing factor above which multiple streamer interactions can be neglected.

Surface Streamers for Generation of a Thermal Plasma Source:

1. A novel pulsed, high density, large volume, thermal plasma system was designed which limited impurities, and increased firing rate for plasma material surface interactions. The plasma source relied upon a surface tracking streamer breakdown mechanism. The surface streamers proved to be able to ignite argon thermal discharges at voltages an order of magnitude below the Paschen breakdown potential. It was shown that the addition of small concentrations of molecular gases suppressed the streamer discharge.

2. Plasma facing components in the pulsed thermal plasmas were investigated with scanning electron microscopy and molecular dynamic simu-

lations. Both modeling and experiments showed minimal effects due to thermal sputtering in argon plasmas.

1.6 Thesis Outline:

1. Chapter 1 provides a background of plasma discharges and theory of breakdown at high pressures, after which a review of streamer discharge applications is presented.

2. Chapters 2-7 start with a motivation for CO_2 reforming and a literature review of carbon dioxide reforming. The experimental and computational methods are then discussed followed by their respective results. The section is then closed with a discussion of the parametric investigations and optimization strategies for CO_2 reforming with streamer discharges.

3. Chapter 8 discusses the use of surface streamers for thermal ignition. An overview of the experimental setup is presented followed by the results which cover the streamer dynamics in argon, plasma spectroscopy, and the effects of molecular additive gases.

4. Chapter 9 presents the major findings of these two works and recommendations for future work.

5. Appendix A discusses the thermal plasma source, and thermal plasma material interactions.

Chapter 2

Volume streamer discharges for carbon dioxide reforming

2.1 Motivation

In recent decades, the reduction of greenhouse gases has become a growing international concern as their anthropogenic production has led to global climate change.[1] The United Nations Convention on Climate Change and the Intergovernmental Panel on Climate Change have made their principal objective to limit greenhouse gas production, and prevent global temperatures from rising above 2 °C. However, many models predict that with the current rate of greenhouse gas production (1.5 ppm/year) the global warming limit will be exceeded in the next 100 years. As CO_2 accounts for 80% of all greenhouse gases (produced primarily from fossil fuels), it is paramount to find an efficient and economical technology that reduces the production of CO_2.

Contemporary industrial applications for CO_2 utilization have been limited. This is ultimately because the splitting of carbon dioxide is a highly

[1]Some of the following work has already been published in: Pachuilo MV, Levko D, Raja LL, Varghese PL. Experimental and Numerical Investigations of a Pulsed Nanosecond Streamer Discharge in CO2. In 55th AIAA Aerospace Sciences Meeting 2017 (p. 1968). The author was the main contributer to this work. Dr. Raja and Dr. Varghese advised this work and Dr. Levko helped in development of the chemical mechanism.

endothermic reaction (5.5 eV/mol) normally requiring reactive catalysis and high temperature processes. Fortunately, non-thermal plasmas of electrical discharges present a viable alternative to conventional reforming technologies. In these non-equilibrium discharges, electrical energy mainly heats the mobile electrons to a few eV while the heavy ions and neutrals remain cold. Therefore, little energy is wasted in gas heating, and the reaction kinetics is initiated by electron impact processes such as dissociation, ionization and excitation of electronic and vibrational states of primary species.

It was shown in the 1970s and 80s that the disparity between the electron and gas temperatures is ideal for dissociation kinetics in CO_2 [57, 58]. In these works, and as summarized by Fridman, the most efficient mechanism for dissociation is through cumulative vibration-vibrational (VV) excitation while minimizing the primary loss mechanism, vibration-translational (VT) relaxation. Since non-equilibrium discharges have low gas temperatures, VT-relaxation is minimized. Furthermore, the vibrational excitation cross-sections for electron impact reactions are largest for low energy electrons ($\sim$1 eV) which are characteristic of moderate to high pressure non-thermal discharges.

The conditions described above were realized in microwave discharges [4]. However, in recent years the interest of researchers has shifted to dielectric barrier discharges (DBD). A DBD consists of a multitude of streamers which together constitute the observed luminescent glow. DBDs have been extensively investigated for high-pressure plasma processes [35, 42, 59, 60] but currently show low CO_2 energy conversion efficiency when compared to alter-

native non-thermal discharges such as microwave discharges. Though DBDs have shown low conversion efficiency, they have several advantages compared to other non-thermal discharges.

First, DBDs can be operated at atmospheric or higher pressures making them valuable for industrial applications, whereas microwave discharges require reduced pressures to be efficient. Additionally, at elevated pressures the conversion rate increases for streamers due to the decrease of the reduced electric field [61]. Finally, DBD reactors are simple to design and manufacture, and have already shown industrial scalability in such areas as wastewater treatment and ozone generation [35, 62]. Furthermore, it was shown in [47, 63] that the efficiency increases with addition of a catalyst and a packed-bed DBD reactor. These studies indicate the potential for efficient CO_2 conversion utilizing streamer processes, but have focused on macroscopic investigations.

Comprehensive numerical modeling of complex plasma processes is indispensable. Modeling increases the understanding of plasma processes illuminated by experiments, and provides a description of quantities that cannot be directly measured. Furthermore, it supplies information of the dominant reaction kinetics and the underlying fundamental mechanisms. Though modeling is a powerful tool, special care must be taken when formulating the chemical mechanism, as there is a trade off between completeness and computational feasibility. Much of the modeling work for CO_2 splitting with DBD discharges has been done by the PLASMANT research group which has relied upon a zero-dimensional reaction kinetics models. [64–66] These models incorporate a

comprehensive plasma chemistry of CO_2 reforming which includes the detailed vibrational kinetics of CO_2. The use of 0D model is justified by the long residence time of the mixture in DBD reactors and because it is computationally infeasible to model the complete physics and chemistry for a DBD reactor.

In our work, studies focus on single high-pressure nanosecond (ns) pulsed streamer discharges. In the present work, streamer discharges in CO_2 have been investigated both experimentally and computationally. The experimental techniques and numerical fluid model will be discussed, followed by the numerical model results which are compared with the experimental findings.

2.2 Literature Review of Carbon Dioxide

Current industrial uses of carbon dioxide are limited, with urea being the primary industrial product. This is mainly due to to the following factors: (1) CO_2 is highly oxidized and thermodynamically stable, and requires highly reactive catalysis or physical energy input for reactions to proceed (i.e. the cost to split carbon dioxide), and (2) the cost of CO_2 separation, purification, and transportation. With the current rate of increase of 1.5 ppm/year of atmospheric CO_2, the overall carbon dioxide levels cannot be reduced with current industrial uses. [67, 68] Recent technologies, such as plasma reforming, have been developed to deal with the growing need for CO_2 utilization and reduction. Additionally, CO_2 has gained recent interest for circuit breaker arc-quenching as a replacement gas to SF_6 which has ~ 20 times the global warming impact as carbon dioxide. [69, 70] It is therefore necessary to have

a detailed understanding of the plasma state of carbon dioxide for reforming technologies, high-voltage circuits, and other potential industrial uses of CO_2.

2.2.1 Why Non-Equilibrium Plasmas for CO_2 Reforming?

Non-thermal and thermal plasmas each have their own advantages and disadvantages. Thermal plasmas have high energy density and high gas temperatures. Though these high gas temperatures are beneficial for some applications, thermal discharges have limited selectivity and are primary used when complete pyrolysis of all species is desired or simply for thermal heat sources. Contrary to thermal plasmas, non-equilibrium plasmas have high selectivity and low gas temperatures. They preferentially couple the electrical energy into electrons rather than into gas heating. These energetic electrons then transfer their energy to bulk species through electron impact reactions. By selectively energizing the electrons, energy can be preferentially pumped into to the desired reaction pathways.

Both thermal and non-thermal discharges have been reported for carbon dioxide splitting. Thermal plasmas have a reported energy efficiency of 15% with a theoretical maximum of 43-48% [4, 71, 72]. The energy efficiency is defined as $\eta = \delta H / E_{CO}$ where δH is the enthalpy for dissociation for CO_2 (2.9 eV/mol), and E_{CO} is the actual energy cost. These thermal sources act primarily as a heater, maintaining the thermal equilibrium necessary for carbon dioxide dissociation. There are two dominant issues which prevent efficient reformation of carbon dioxide in thermal plasmas: requirement for rapid quench-

ing of the product stream, and equilibrium of states. Once carbon dioxide has been split, rapid quenching of the products outside of the hot plasma zone is necessary. If the quenching process occurs too slowly, then the reverse recombination reaction takes place resulting in reformation of carbon dioxide. Even in the case of absolute quenching of the products, thermal plasmas are limited due to the law of equipartition of energy for a system in thermal equilibrium. The law of equipartition of energy is defined as a state in thermal equilibrium where energy is shared equally between all degrees of freedom. Hence, only a portion of the energy of the system is used in dissociation and the rest is distributed into other states which do not contribute to the dissociation reaction (gas heating).

To solve the above-mentioned issues, a non-equilibrium plasma is necessary. Non-equilibrium discharges render quenching unnecessary as reverse reaction rates (VT relaxation processes) are low at low gas temperatures. Additionally, the selective nature of non-equilibrium discharges allows a way to preferentially populate the relevant reaction pathways for dissociation.

In non-equilibrium discharges the temperatures of the system can be characterized as follows: $T_g \leq T_R \leq T_V \leq T_{EXT} \leq T_e$. The translational temperature (T_g) and rotational temperature (T_R) are typically assumed in thermodynamic equilibrium for moderate to high pressure discharges. This is because the effective lifetime of the excited state is much longer than the time for thermalization of the rotational manifold [73].

Furthermore, the vibrational (T_V) , excitation (T_{EXT}), and electron

temperatures (T_e) are much greater than the gas temperature, $T_V \approx T_{EXT} \approx T_e >> T_g$ for electron temperatures larger than 12,000 K [74]. It is the non-equilibrium of the molecular degrees of freedom, specifically the translational and vibrational modes, that leads to an energy efficiency increase of up to 60% when quasi-equilibrium is assumed for forward and reverse reactions [4]. This efficiency increase occurs because direct endothermic reactions (CO_2 splitting) are primarily excited by molecular vibrations while reverse exothermic reactions (recombination of CO_2) are mainly activated by translational temperature which leads to a net production of CO [4].

2.2.2 Non-Equilibrium Plasma Reforming Technologies

As mentioned above, non-equilibrium discharges are preferable to thermal plasmas for energy efficient conversion of CO_2. One would speculate that low pressure glow discharges would be more efficient at splitting than atmospheric discharges because they are easier to maintain a stable thermal non-equilibrium, and electronic impact reactions dominate. But it has been shown that this direct electronic excitation has proven to be an inefficient means for CO_2 dissociation, as evidenced by the low conversion efficiencies of only 8% for glow discharges [4]. A more efficient mechanism for CO_2 splitting is through vibrational-vibrational energy exchange. It is therefore desirable to have a sustained discharge at moderate to high pressures such as: non-equilibrium microwave discharges, DBDs, and other non-thermal discharges.

Microwave discharges have shown the most promise for an energy effi-

cient means of CO_2 conversion. The highest recorded efficiencies were reported in the late 1970s and early 80s by Legasov and Asivov [4]. These discharges were operated at moderate pressures ranging from 50-200 Torr, and at subsonic or supersonic flow conditions. Under supersonic flow conditions Asivov reported a 90% energy efficiency, while Legasov showed 80% efficiency for subsonic conditions. These high efficiencies have yet to been reproduced, with efficiencies of 55% reported in 2013 for similar conditions as Asivov [75]. For industrial applications it is desirable to have a system which is simple and can operate at atmospheric conditions, but when the pressure is increased to atmospheric conditions the microwave discharge efficiency drops to 40% [4]. Furthermore, implementation of a microwave plasma system is more complex than other non-thermal devices such as DBD reactors.

DBD reactors are easily designed and operate at atmospheric pressures. These discharges have already shown industrial scalability in ozone production for water purification plants, but have low energy and conversion efficiencies for CO_2 reforming process [76]. DBDs have reported efficiencies of only 2-10% [63], but with the use of packed bed DBD reactors and catalysis the efficiency can be improved as observed in the work of H. L. Chen et al [77]. In 2015 Bogaert's group showed that with a packed bed DBD reactor the CO_2 conversion efficiency reached 38% with an energy efficiency of 6.4% [78].

Mei et al. in 2014 studied the effects of packing materials on CO_2 conversion efficiency [79]. They found that a packed bed DBD with photocatalysis led to an increase in the conversion and energy efficiency. Bogaert's

et al. and Mei et al., believe that the main mechanism for conversion efficiency enhancement from packed bed reactors is through an increase in the mean electron energy [78, 79]. Additionally, Mei et al. suggested that the photocatalysis may have been activated by the increased electron energy leading to additional electron hole pairs on the dielectric surface which would lead to an increased efficiency [79].

In the works reported on DBD reactors, there is limited information about the details of the streamer process. These authors ([64, 78, 79]) have focused on plasma reactor designs rather than the underlying streamer mechanism. The purpose of our work is to develop a detailed understanding of the dynamics and chemical kinetics of a streamer discharge, a single element of the DBD reactors, in CO_2. A combined experimental and modeling approach is implemented to understand the primary processes in the dissociation of CO_2 by a streamer discharge.

2.2.3 CO_2 Plasma Chemistry

Carbon dioxide is one of the simplest polyatomic molecules. In its ground state CO_2 is a linear triatomic molecule ($D_{\infty,h}$ point group with electric quadrupole, because of electric dipole cancellation), with an ionization energy of 13.777 eV, and a dissociation energy of 5.451 eV [10]. The decomposition of CO_2 is a highly endothermic reaction limited by the dissociation reaction:

$$CO_2 \rightarrow CO + O \quad \Delta H = 5.451 \frac{eV}{mol} \tag{2.1}$$

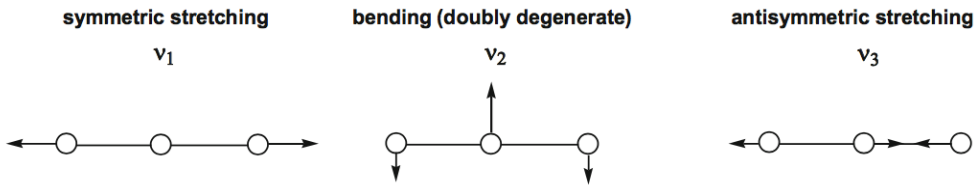

Figure 2.1: Vibrational modes of carbon dioxide [7].

The complete decomposition of CO_2 occurs with the conversion of O into O_2 by recombination or reaction with another CO_2 molecule.

The rotational and vibrational spectra of CO_2 have been widely investigated, and incorporated into the HITRAN database. The rotational and vibrational energy levels are mostly observed in the IR spectral region and are expressed as:

$$E(v, J) = G_v + B_v J(J+1) - D_v[J(J+1)]^2 \tag{2.2}$$

CO_2 has four normal modes of vibration ($3N - 5$, with N = number of atoms), with the bending mode being doubly degenerate. Figure 2.1 shows the three modes: symmetric stretching (v_1), bending (v_2), and antisymmetric stretching (v_3). The vibrational state is defined as $v = (v_1, v_2, v_3)$, and J is the rotational quantum number. G_v, B_v, and D_v are spectroscopic constants which are given by Table 2.1. There are two additional features associated with the CO_2 spectra: (1) Fermi resonance and (2) a vibrational angular momentum quantum number.

Fermi resonance occurs when two vibrational modes with nearly the

$v = (v_1, v_2, v_3)$	G_v (cm^{-1})	B_v (cm^{-1})	D_v $(10^{-7}$ $cm^{-1})$
000	0	0.3902	1.333
010 $(l_2 = 1)$	667.4	0.3906	1.353
020$((l_2 = 1)$	1285	0.3905	1.571
100	1388	0.3902	1.149
001	2349	0.3871	1.330

Table 2.1: Spectroscopic constants for carbon dioxide

same energy mix. The mixing causes an increase in the splitting of the energy levels, and as a consequence of it the splitting of spectral lines and equalization of the intensities of the two original lines. Fermi resonance usually occurs between the fundamental vibration and an overtone or combination. In CO_2 the vibrational energy of the fundamental symmetric-stretching mode (v_1) is merely twice that of the v_2-bending mode, so levels (v_1, v_2, v_3) and $(v_1 - 1, v_2 + 2, v_3$ are very close together, resulting in Fermi resonance. The double degeneracy of the bending mode leads to angular momentum about the inter-nuclear axis, with angular momentum quantum number $l_2 = v_2, v_2 - 2, ..., 1 \quad or \quad 0$.

CO_2 has two IR active modes: the v_3-antisymmetric stretching mode and the v_2-bending mode , but is transparent in the visible and mid to near ultraviolet regions. Carbon dioxide does exhibit photon absorption in the vacuum ultraviolet (VUV) region, and radiation in the VUV can lead to photo-ionization or photo-dissociation.

2.2.4 Dissociation Kinetics of Carbon Dioxide in Non-Equilibrium Discharges:

As stated previously, thermal plasmas simply act as heaters, which shift the dissociation reaction to favor the production of CO. These thermal discharges have several limitations as discussed, and low efficiencies. Hence, non-thermal discharges are desired for energy efficient dissociation of CO_2. The advantage of non-equilibrium discharges lies in the ability to selectively input energy into the most efficient reaction pathway for dissociation. It has been shown that vibrational excitation by electron impact of ground state molecules is the most efficient means of dissociation of CO_2 [4, 57, 80].

1.	Attachment	E + CO2 CO + O-	(E = 0 eV)	DISSOCIATIVE ATTACHMENT
2.	Effective	E + CO2 E + CO2	(m/M = 0.0000124)	EFFECTIVE CROSS-SECTION
3.	Excitation	E + CO2 E + CO2(0.083eV)	(E = 0.083 eV)	ASYMMETRIC VIBRATIONAL
4.	Excitation	E + CO2 E + CO2(0.167eV)	(E = 0.167 eV)	VIBRATIONAL EXCITATION
5.	Excitation	E + CO2 E + CO2(0.252eV)	(E = 0.252 eV)	VIBRATIONAL EXCITATION
6.	Excitation	E + CO2 E + CO2(0.291eV)	(E = 0.291 eV)	VIBRATIONAL EXCITATION
7.	Excitation	E + CO2 E + CO2(0.339eV)	(E = 0.339 eV)	VIBRATIONAL EXCITATION
8.	Excitation	E + CO2 E + CO2(0.422eV)	(E = 0.422 eV)	VIBRATIONAL EXCITATION
9.	Excitation	E + CO2 E + CO2(0.505eV)	(E = 0.505 eV)	EXCITATION
10.	Excitation	E + CO2 E + CO2*(10.5eV)	(E = 10.5 eV)	ELECTRONIC EXCITATION
11.	Excitation	E + CO2 E + CO2(2.5eV)	(E = 2.5 eV)	VIBRATIONAL EXCITATION
12.	Excitation	E + CO2 E + CO2*(7.0eV)	(E = 7 eV)	ELECTRONIC EXCITATION
13.	Ionization	E + CO2 E + E + CO2+	(E = 13.3 eV)	TOTAL IONIZATION

Table 2.2: Cross-Sectional Data for CO_2: Vibrational and electronic excitation, dissociative attachment, and ionization. [1, 2]

Figure 2.2 shows the vibrational and electronic excitation, attachment, and ionization cross-sections for electron impact processes in CO_2 as a function of electron energy (taken from Phelps and BOLSIG+). Table 2.2 provides an overview of the reactions listed. At low electron energies, below $\sim$7 eV the

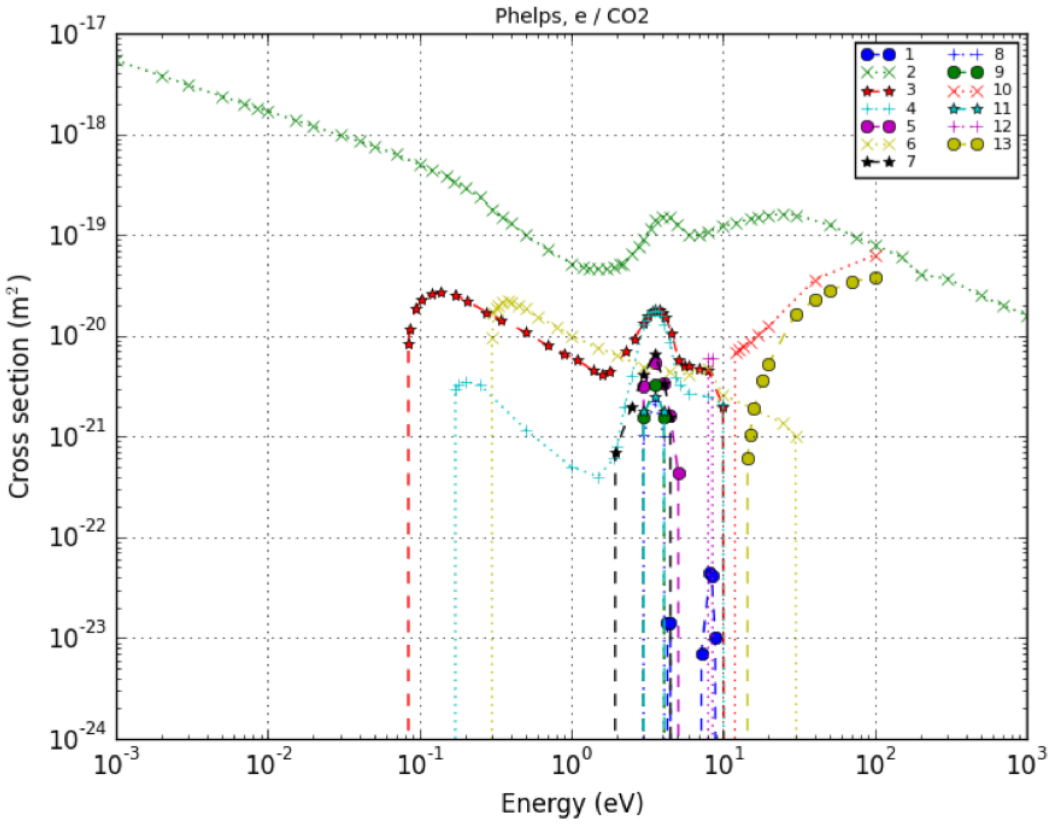

Figure 2.2: Cross-sectional data CO_2 [1, 2]

vibrational cross-sections are significant, while ionization and electronic excitation thresholds are: 13.3 eV and 7 eV, respectively. Therefore, for DBDs (in the streamer tail), and other non-equilibrium discharges with average electron temperatures of 1-3 eV, a majority of the electron energy will be deposited into low lying vibrational levels.

In endothermic reactions like the dissociation of CO_2, the vibrational energy exchange of the reactants (CO_2) is the most efficient means of dissociation. This is because when the highly excited vibrational states reach the bond energy for dissociation, 5.5 eV for CO_2, a vibrational-vibrational non-adiabatic transition occurs. Through the VV quantum exchange only the energy necessary to form CO and O in their respective ground states is required, whereas adiabatic vibrational excitation would require more than 7 eV to dissociate. For the adiabatic electronic vibrational dissociation mechanism (spin conservation), CO is formed in the ground state while O is in an electronically excited state. Therefore, adiabatic dissociation requires more energy than the VV exchange process. In the case of direct electron impact excitation for dissociation, an energy of more than 8 eV is required due to the Frank-Condon (vertical transition) principle.

At high electron energies, the primary dissociation mechanism is through direct electron impact leading to low lying electronic levels of CO_2. If the electron energies are high enough a significant portion of the energy will go into forming electronically excited CO. These conditions are usually met for low pressure discharges with high reduced electric fields, and in the head of a

streamer discharge which has electron temperature of O(10 eV). The energy threshold for dissociation can be reduced by vibrational excitation, since the energy threshold for dissociation is reduced.

The dominant loss mechanism for vibrational excited states is through vibrational translational relaxation. For non-equilibrium plasmas, which are operated at low temperatures, usually 300-1000 K, the VT relaxation process is slow and mostly related to the symmetric vibrational mode. Therefore, for a sufficiently ionized plasma a non-equilibrium vibrational distribution will be established with high population of high lying vibrational states (For example Treandor distribution).

Streamer discharges present a complicated scenario for CO_2 dissociation because they have two characteristic electron temperatures, 10 eV in the head and 1-2 eV in the tail. Additionally these discharges are a transient unsteady process. Therefore, the dissociation mechanism for streamers can potentially progress through two methods: VV vibrational exchange, and direct electron impacts. It will be shown that both processes are important for streamer discharges with direct electron impact dissociation dominant for single streamer discharges, and VV exchange arising in pulsed discharges due to the population of low lying vibrational levels in the streamer tail.

To optimize these streamer discharges the EEDF should have an average electron temperature of around 1 eV. By setting the E/N such that an electron temperature of $\sim$ 1 eV is obtained, population of the asymmetric stretch mode (v_3) of CO_2 is possible. The asymmetric mode has lower VT

(vibration-translational) loses compared to the symmetric mode, the largest cross-section for e-V (electron impact vibrational excitation) processes, and higher VV transfer cross-sections.

Chapter 3

Experimental Setup

3.1 Experimental Methods

A synopsis of the experimental setup and methods are presented in this section.[1] An overview of the experimental setup is shown in Fig. 3.1, (A), and an image of the reaction chamber in (B). The remainder of this section will discuss the gas regulation system (1) and reaction chamber (3), the pulse power system (2) and electrical diagnostics (5), and the imaging and spectroscopic diagnostic techniques (4).

3.2 Reaction Chamber

The experimental framework consists of a high-voltage (HV) ns pulsed-power circuit, and the reaction chamber. The reaction chamber is capable of reaching temperatures of ∼800 K with pressures ranging from ∼5-500 kPa. In the test presented the temperature was held fixed at 300 K and two pressures were investigated: 115 and 200 kPa.

[1]Some of the following work has already been published in: Pachuilo MV, Levko D, Raja LL, Varghese PL. Experimental and Numerical Investigations of a Pulsed Nanosecond Streamer Discharge in CO2. In 55th AIAA Aerospace Sciences Meeting 2017 (p. 1968). The author was the main contributer to this work. Dr. Raja and Dr. Varghese advised this work.

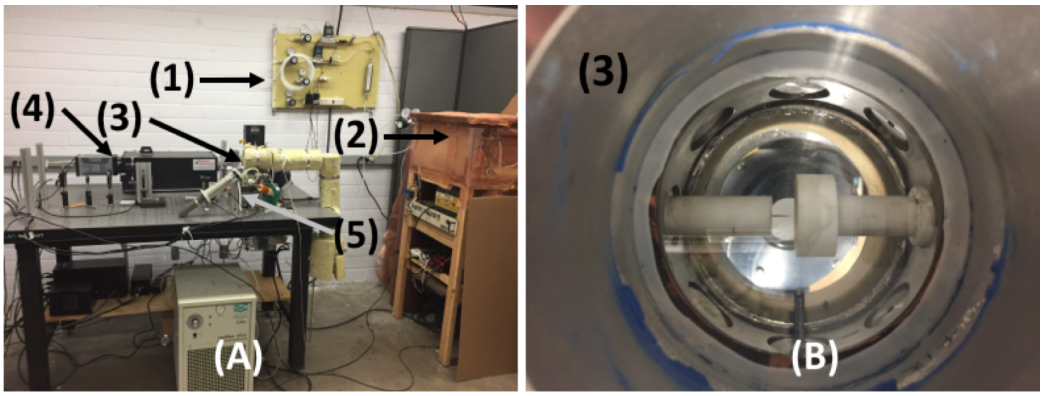

Figure 3.1: An overview of the experimental setup is shown in (A). The pressure vessel with the electrodes is shown in (B). (1) indicates the gas regulation systems, (2) the high-voltage pulsed power system, (3) pressure vessel, (4) PIMAX 4 and SP2500 spectrometer, and (5) electrical diagnostics including the high-voltage Tektronix P6015A and Pearson 6585 current monitor.

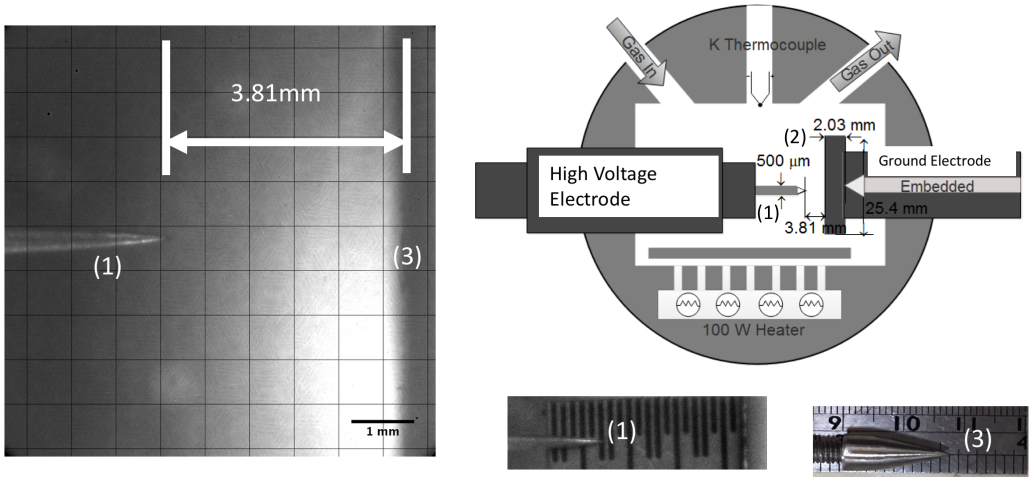

Figure 3.2: A schematic of the reaction chamber (B) and the electrode configuration (A). The high-voltage electrode (1) is 3.81 mm from the macor dielectric surface (3), and the ground electrode (2) is embedded behind 2 mm of macor dielectric. The entire electrode configuration is sealed inside a stainless-steel pressure vessel or reaction chamber. The reaction chamber is fitted with process gas inlet and exit. Additionally, the chamber is monitored with a thermocouple and pressure gauge. denotes the increments for each ruler in (B) 1 and 2.

Figure 3.2 shows the reaction chamber (B) and the electrode configuration (A). The reaction chamber is a cylindrical domain with a diameter of 76 mm and a depth of 30 mm. The chamber consists of a stainless-steel pressure vessel with two quartz viewing windows, and eight 25.4 mm ports spaced 45 degrees around the perimeter. Five ports are used in the experiments: one for the HV electrode (1 in Fig. 3.2), the ground electrode (2 in Fig. 3.2), the gas inlet and exit, and a thermocouple, while the other three ports are plugged and sealed.

A 2 mm thick and 25.4 mm diameter macor dielectric covers the ground electrode (2 in Fig. 3.2). This prevents thermalization and spark-over of the streamer discharge formed in the inter-electrode gap during a ns pulse. The ground electrode is a sharpened stainless-steel rod with a 20 degree taper that is held fixed within the chamber. A pin-vise secures the HV electrode (1 in Fig. 3.2) which allows the inter-electrode distance to be adjusted. The HV electrode is composed of stainless-steel with a diameter of 550 μm and a tip radius of 0.6 μm. The HV electrode is insulated with a macor sleeve to prevent breakdown to the pressure vessel.

High-purity gas cylinders provide the feed stock gas CO_2, and additive probing gases (argon, nitrogen, and hydrogen) used for plasma spectroscopy diagnostics. The gases are regulated, metered and mixed prior to entering the reaction chamber. If the discharge is to be heated the gas stream is passed through a 3 kW air process heater. The temperature and pressure inside the chamber are monitored, and a PID controller is used to maintain the desired

experimental conditions.

After the gas has been processed by the plasma, it is passed through a set of cooling coils (if the gas is heated) prior to being exhausted to the atmosphere. If sub-atmospheric pressures are desired, the cooled exhaust stream is then connected to a vacuum pump.

To ensure that each discharge pulse is independent of the previous, a constant flow rate ($\dot{V}$) is maintained throughout the chamber such that the pulse period (freq. $\sim 4 - 7$ Hz) is greater than the flow residence time (τ) given by Eq. 3.1.

$$\frac{1}{\tau} = \frac{\dot{V}}{V} \tag{3.1}$$

3.3 Pulsed Power Supply

The pulsed power system is presented in Fig. 3.3. A Spellman SL600 HV power supply charges the 2100 pF discharge capacitor to a positive HV (12.5-40 kV). The minimum charge voltage (∼12.5 kV) is determined by the spark-gaps [(1) in Fig. 3.3] minimum ignition threshold, while the maximum voltage is set by the capacitor, HV supply, and insulation.

The trigger electrode of the spark-gap is maintained at half the charge voltage of the capacitor. This is accomplished with a simple voltage divider [(1) in Fig. 3.3]. A 500 pF decoupling capacitor isolates the spark-gap trigger electrode from the HV spark-gap trigger generator.

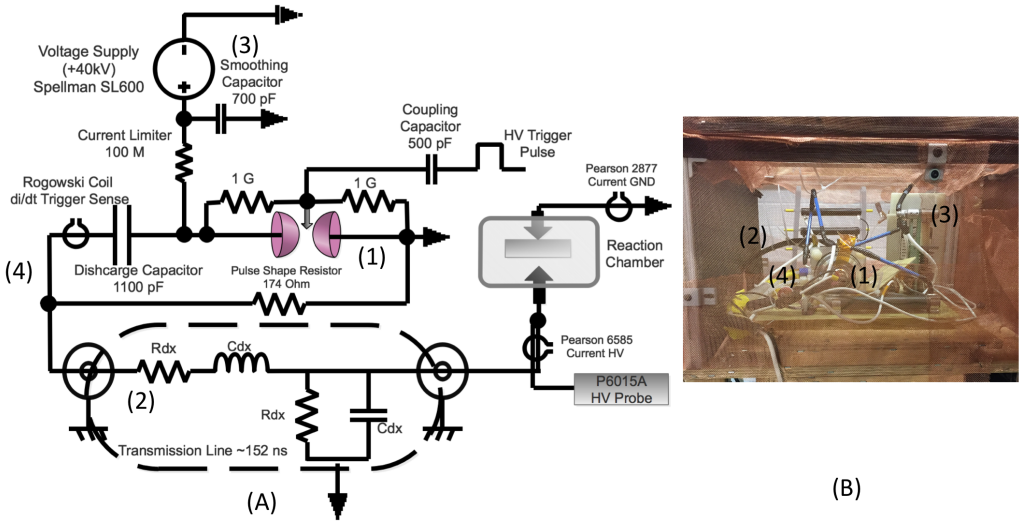

Figure 3.3: A schematic (A) and photograph (B) of the pulsed power system used for generating nanosecond high-voltage pulses. Here, a reverse dump pulsed power design is implemented. A high-voltage power supply (3) charges the discharge capacitor. A spark-gap (1) is then triggered which results in a fast negative-polarity high-voltage pulse. A pulse shape resistor (4) is used to tailor the primary pulse width and decay time. The pulse then transits through a transmission delay line (2) prior to reaching the discharge chamber. The pulse power system is kept in a Faraday cage and isolation transformers are used to reduce the transmitted and conducted electromagnetic interference.

The spark-gap is triggered with an automotive ignition module and a step-up transformer. Once the spark-gap breaks down, the discharge capacitors positive HV terminal is shorted to ground. This causes the grounded terminal of the discharge capacitor to drop rapidly to a negative voltage approximately equivalent to the charge voltage.

The primary negative HV pulse shape is determined by the RC time constant [(4) in Fig. 3.3] of the discharge capacitor (2100 pF) and pulse shape resistor (174 Ω). From these quantities, the RC time constant is 190 ns. Because of the short duration of the pulse as well as the jitter (typically of order 100 μs) associated with triggering the spark-gap, the diagnostics could not be sequenced using the BNC 555 delay generator.

To trigger the diagnostics, specifically the PI-MAX 4, which requires a minimum of 29 ns before the intensifier can be gated on, a 30 m transmission delay line is used. The delay line produces 152 ns of delay between the initial pulse formation at the discharge capacitor and its arrival at the discharge chamber.

A Rogowski coil is placed at the capacitor terminal upstream of the discharge chamber to determine when the voltage pulse is initiated. A Rogowski coil measures the rate of change of current ($\frac{dI}{dt}$) induced in a loop of wire from an external magnetic field. Rogowski coils provide a fast response to changes in current making them ideal for sensing pulsed systems. This triggering scheme allowed the entire voltage pulse to be analyzed.

3.4 Discharge Diagnostics

The discharge diagnostics include: current-voltage diagnostics and instantaneous broadband imaging, instantaneous narrowband imaging, and spectroscopy. The electrical pulse characteristics are determined on the HV electrode from a Tektronix P6015A HV probe and a Pearson 6585 current monitor (Fig. 3.1). A second current monitor (Pearson 2877) is placed on the ground electrode to monitor the transmitted current.

A PI-MAX 4 ICCD (intensified charge coupled device) camera is used to image the discharge throughout the voltage pulse. A set of bandpass filters is used to isolate radiation from specific excited states to determine the spatial distribution of these excited species. The PI-MAX was also coupled with 500 mm triple grating spectrometer to determine plasma properties such as: electron temperature and density, vibrational and gas temperature, and conversion efficiency.

As discussed previously, the pulse power system operates in the high frequency radio (RF) range at high powers ($\sim$500 kW). In this operational regime electromagnetic inference (EMI) becomes an issue with the diagnostics, and both radiated and conducted EMI was considered.

To reduce the radiated EMI, the pulsed power system is placed in a Faraday cage [Fig. 3.3] and a coaxial HV transmission line is used to transmit the wave to the discharge chamber. To reject common mode noise on the AC lines, voltage isolation transformers are used for both the pulsed power

system and the diagnostic power supplies. Though EMI mitigation strategies have been implemented, when the system is operated at high powers radiated transmission can be problematic and noise is coupled to instrumentation.

3.5 Instantaneous Broadband Imaging Diagnostics

A PI-MAX 4 1024i Intensified Charge Coupled Device (ICCD) (Fig. 3.1) is used to acquire time resolved images of the streamer discharges. An intensified-CCD is required to temporally resolve streamer discharges which have typical velocities of mm/ns at atmospheric pressure. In addition CO_2 has little emission in the visible range of the detector [81].

Figure 3.4 shows the quantum efficiency curves for Generation II intensifiers. The PI-MAX 4 used in this work is equipped with the SR GEN II intensifier which corresponds to a usable wavelength range of 200-900 nm. The CCD is a Kodak KAI-1003 interlaced with square pixels measuring $12.8\mu m$. The CCD is composed of a square pixel array, 1024x1024, pixels equipped with the SR GEN II 18 mm intensifier tube. The PIMAX 4 is capable of gate times down to 2.81 ns and a sustained repetition rate of 8 kHz with MCP gating.

3.6 Imaging Calibrations

Detector calibration is necessary to eliminate non-data elements from the detector array such as the bias offset, bias pixel structure, dark noise, uneven field illumination, and even dust. To calibrate the detector a set of 3

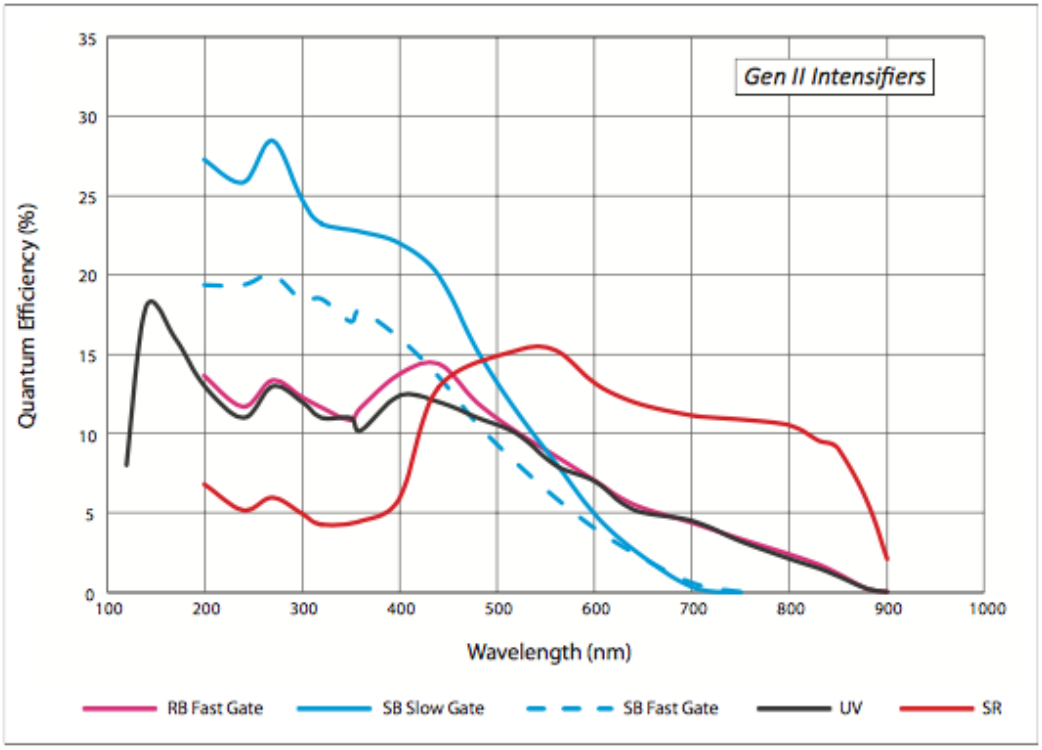

Figure 3.4: Quantum Efficiency curves for the PIMAX 4 Generation II intensifiers. The PIMAX 4 1024i used in this work is equipped with SR GEN II Intensifier which corresponds to a wavelength coverage of 200-900 nm. [8]

calibration images must be taken for each experimental setup: a bias, dark or thermal, and flat-field frame. From these calibration frames a set of master frames can be made which are then used to calibrate the science data frames.

The bias frame is used to remove the inherent detector bias level applied to each pixel element. All detectors have a set bias voltage to prevent the detector from registering negative readout signals. To form the master bias frame a set of 10 bias images is taken with the ICCD covered. The intensifier gain is set to that of the test conditions ($G = 90$) and the integration time is set to the cameras minimum gate width, 2.81 ns. These frames are then median averaged to form a master bias frame.

The second calibration frame required is a dark or thermal frame. The dark frame is used to measure the thermal noise accumulated during the exposure and is a linear function of the integration time. A set of 10 dark frames is taken with the ICCD covered at the experimental gain setting (90) and for the integration time of the test (e.g. 10, 30, or 350 ns). A master dark frame is computed by taking each of the ten dark frames for a given integration time and subtracting the master bias. The dark frames are then divided by the integration time and median averaged forming the master dark frame.

A dark frame can then be generated for any integration time by taking the master dark frame and multiplying by the integration time. Alternatively, a dark frame can be generated for each integration time by covering the ICCD and exposing the ICCD to the same integration time as the test condition. This method directly captures both the bias and dark current for each experimental

condition. To reduce the thermal noise of the detector the ICCD is cooled to -23°C, resulting in $< 2e^{-}/p/sec$.

The last calibration frame is a flat-field image. A flat-field calibration was done with a DH-2000 calibration source and an integrating sphere which produced a Lambertian surface. The flat-field image is used to calibrate varying sensitivity of the detector, and any imperfections in the optical setup such as dust particles which lead to uneven field illumination of the detector. The flat-field images were taken at the experimental gain setting and with a uniform field illumination from a tungsten lamp source. The flat-field should be exposed long enough to collect $35 - 50\%$ of the full saturation level. A master flat-field is constructed by subtraction of the master bias and a scaled master dark frame.

A calibrated science image (C) is produced by subtracting the master bias frame (B), and the scaled master dark frame (D) from the raw data image stack (R). The raw image stack is then divided by the master flat-field image (F). The resulting stack is then median averaged and multiplied by the image average value of the flat-field (m), producing the final calibrated science image. Equation 3.2 shows how a calibrated science frame is formed.

$$C = \frac{R - (D + B) * m}{F - (D + B)} \tag{3.2}$$

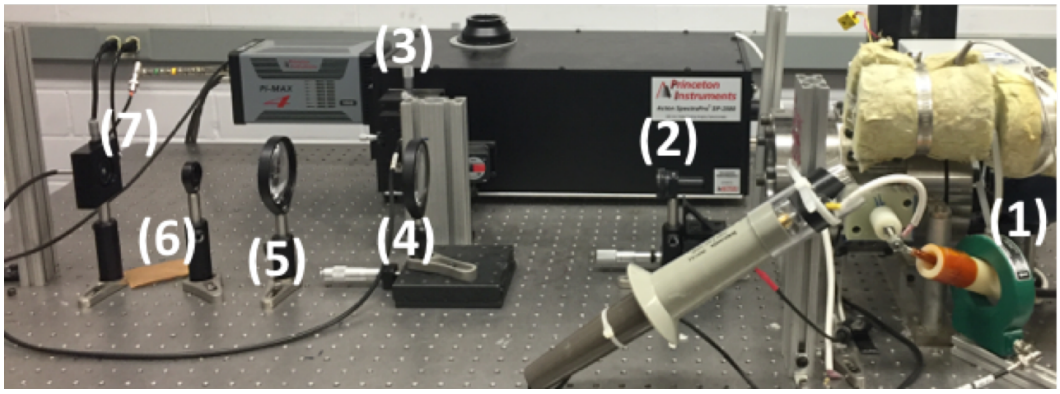

Figure 3.5: An image of the spectroscopy setup is shown with a modular 3.3 inch 3 port integrating sphere (1), iris (2), plano-convex focusing lens (4 and 5), the SP2500 500 mm spectrometer coupled with the PIMAX 4 ICCD (3), order sorting filter (6), and fiber bundle (7).

3.7 Spectroscopic Diagnostics

An overview of the spectroscopic diagnostics will be described in this section including: the optical system, the spectrum splicing and wavelength calibration procedure, and absolute spectral radiance calibration.

3.8 Observation System

The spectroscopy optical setup is shown in Fig. 3.5. The setup consists of a 3.3 inch 3 port integrating sphere from Newport, (1). The integrating sphere is coated with a highly reflective Polytetrafluoroethylene (PTFE) which covers a wavelength range of 250-2500 nm with $\sim$ 98% reflectivity. The integrating sphere is used for absolute spectral radiance calibrations discussed later.

An iris (2) is used to determine the F-number of the optical system

and the etendue for absolute spectral calibrations. A 500 mm SP2500 Princeton Instruments triple grating spectrometer (3) equipped with 300, 1200, and 1800 g/mm gratings blazed at 500 nm is used to acquire the spectrum of the streamer discharge. The spectrograph is also equipped with a variable entrance slit which can be varied from $10\mu m$ to $3mm$, depending on the spectral resolution needs. The SP2500 spectrometer has two exit planes, one is coupled with the PIMAX 4 shown in Fig. 3.5, and the second port has a variable exit slit where a PMT may be mounted. The second port is used here to back illuminate the optical pathway to determine the effective F-number of the system as well as for optical alignment and focusing. The SP2500 has an $F/\# = 6.5$.

Two 75 mm diameter (ϕ) uncoated ultra-violet grade fused silica plano-convex lenses (4 and 5) are used to acquire the emission from the plasma discharge. These lenses have over 90% transmission over the 200-1200 nm wavelength range. The first lens in the optical path (4), will be defined as the objective lens. It has a focal length (f_o) of 500 mm, and an $F/\# = \frac{f}{\phi} = 6.67$. The second lens element in the optical path (5) will be defined as the imaging lens. The imaging lens has a focal length (f_i) of 200 mm, and an $F/\# = 2.67$. The two lens optical system is setup such that the plasma discharge is at the focal length of the objective lens and hence the fiber bundle is at the focal length of the imaging lens. The two lens system then magnifies the fiber bundle (7) by a factor $M = f_o/f_i = 2.5$.

The fiber bundle (7) consist of 19, $200\mu m$ diameter fibers each with a $22.5\mu m$ thick cladding. The fiber bundle is arranged in a circular fashion on

the imaging end, while the fibers are arranged in a single column to match the SP2500 vertical entrance slit. These fibers are composed of fused silica with a wavelength range of 190-1100 nm. At wavelengths $>$ 550 nm order sorting bandpass filters (6) are necessary. The bandpass filters serve to block the second and third order spectrum of lines originating at lower wavelengths (200-500 nm).

Equation 3.3 gives the location of the diffraction grating maximum, where m is the order, λ is the wavelength, d is the inverse of the grating spacing (mm/groove), and θ is the diffraction angle.

$$m\lambda = d\sin(\theta) \tag{3.3}$$

It is evident from Eq. 3.3 that first order emission lines from 300-400 nm (typical of nitrogen second positive system, and CO Angstrom bands) will appear in the emission spectrum taken at 600-800 nm. Therefore bandpass filters have been used to filter out any higher order lines from the spectrum for wavelengths greater than 550 nm.

The instrumental profile profile of the spectral system is determined from two methods: (1) the response to a monochromatic HeNe laser source, and (2) line radiation from low pressure gas discharge tubes. In the spectroscopy results presented the slit width is held fixed at $100\mu m$, and two gratings are used: 300 g/mm and 1800 g/mm.

The 300 g/mm grating is used to obtain a broadband spectrum cov-

ering the entire range of the spectral observation system (250-900 nm). The instrumental profile is estimated as a Gaussian profile with a full-width-half-maximum (FWHM) of 0.8 nm for a 300 g/mm grating, $100\mu m$ slit, and 500 mm spectrometer. The 1800 g/mm grating is used for determining the rotational temperature and for electron density broadening measurements. The FWHM with the 1800 g/mm grating is 0.106 nm.

3.9 Splicing Procedure and Wavelength Calibration

The plasma radiation was collected over a range of 250-900 nm. To acquire a spectrum covering such a wide spectral band with a ICCD array detector several individual spectra must be taken at various grating angular positions. These individual spectra are then spliced together to form a single extended spectrum. This splicing procedure is necessary due to the limited spatial dimensions of the array detector systems.

For example, a typical spectral coverage in these experiments taken with a 500 mm spectrometer and using a 300 g/mm grating is ~ 80 nm, see Fig. 3.7. It is therefore necessary to collect ~ 12 individual spectra at different center wavelengths, ensuring to leave an overlap region so that adjacent spectra can be fitted together. Prior to the 1D spectra being spliced together, the raw (2D) ICCD images must be processed, wavelength calibrated, and binned to form a 1D spectrum.

The raw ICCD spectral images are calibrated in much the same manner as the instantaneous broadband images were, but with the addition of two

images to account for the wavelength calibration and spectral sensitivity of the detector. To calibrate the raw ICCD images a set of four images are taken: the bias, dark, spectral intensity calibration, and wavelength calibration frames. The spectral intensity calibration frame accounts for the spectral sensitivity of the detector. This process will be described in the following section. It is noted that the spectral intensity calibration frame is the spectral equivalent to flat-fielding frame.

The bias and dark frames are the same as those described in the imaging calibration section. The master bias and dark frames are computed for the experimental conditions and subtracted from the set of raw ICCD spectral images. For each experimental condition several frames are collected. Once the frames are dark and bias subtracted the resulting images are then median averaged to increase the signal-to-noise ratio. Instead of dividing by a flat-field image in the 2D image, a 1D spectrum was first composed. Before the 1D image was formed an initial wavelength calibration was needed.

An initial wavelength calibration was done using a mercury-argon (Hg-Ar) lamp, in LightField. LightField is a software package that accompanies the PIMAX 4 and SP2500 spectrometer. The software interfaces with the both PIMAX 4 and SP2500 spectrometer. To conduct the initial wavelength calibration the Hg-Ar lamp source is imaged with the spectroscopic optical system described above. The wavelengths of the strong emission lines are loaded into the LightField software, and a function is generated which relates the grating angular position and ICCD pixels to a known wavelength. The

software automatically sweeps through various grating rotations to calibrate the system. The calibration process than provides an estimate of the pixel to wavelength conversion. To verify the wavelength calibration holds throughout the splicing procedure raw ICCD images of the Hg-Ar Lamp are acquired.

To form a 1D spectrum the 2D ICCD image must be binned. For the spectrometer system used here, the x pixel axis is the dispersion axis (wavelength) while the y pixel axis corresponds to the spatial position along the entrance slit. Therefore, to generate a 1D spectrum for the 2D ICCD image a binning region must defined in the y-axis. Figure 3.6 shows a calibrated ICCD image of the Hg-Ar lamp at a center wavelength of 700 nm. In Fig. 3.6 the 19 fibers composing the fiber bundle are visible. Each of these fibers corresponds to a spatial location in the plasma domain. The highlighted rectangle region corresponds to a circular region with a diameter of $\sim 500\mu m$ located at the electrode tip. This region was binned to form the 1D spectrum, Fig. 3.7. The same binning region is used for all images and calibration frames.

Figure 3.7 shows the result of binning the 2D spectrum. The total spectral coverage for a single frame taken with a 500 mm spectrometer and 300 g/mm grating is $\sim 80nm$. To cover the entire spectral range of the detector (200-900 nm), 2D images are taken at center wavelengths from 250 to 850 nm in steps of 50 nm. This ensures sufficient spectral overlap for splicing each spectrum together. At each of these center wavelengths three images are taken: raw science frame, Hg-Ar lamp, and DH2000 spectral radiance source. For each 2D image a 1D spectrum is generated. Next these 1D spectra must

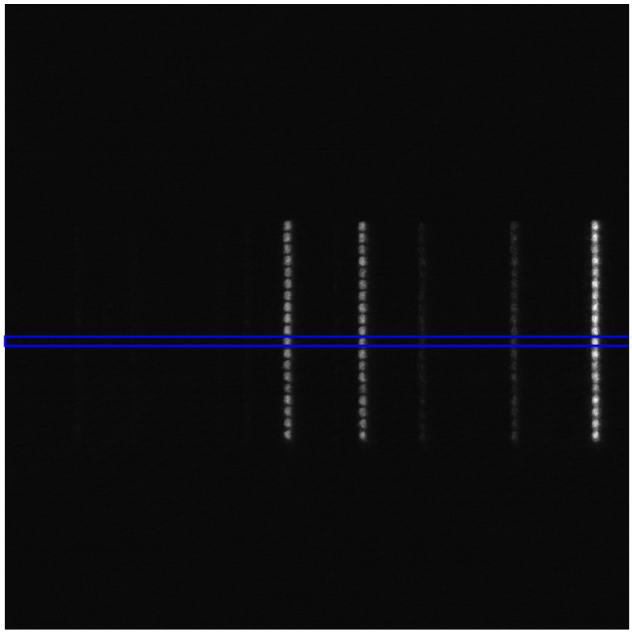

Figure 3.6: A 2D ICCD image taken at a center wavelength of 700 nm of Hg-Ar lamp with 300 g/mm grating and 500 mm spectrometer. The image is the result of (dark+bias) subtraction and median averaging. The rectangle box indicates the binning region.

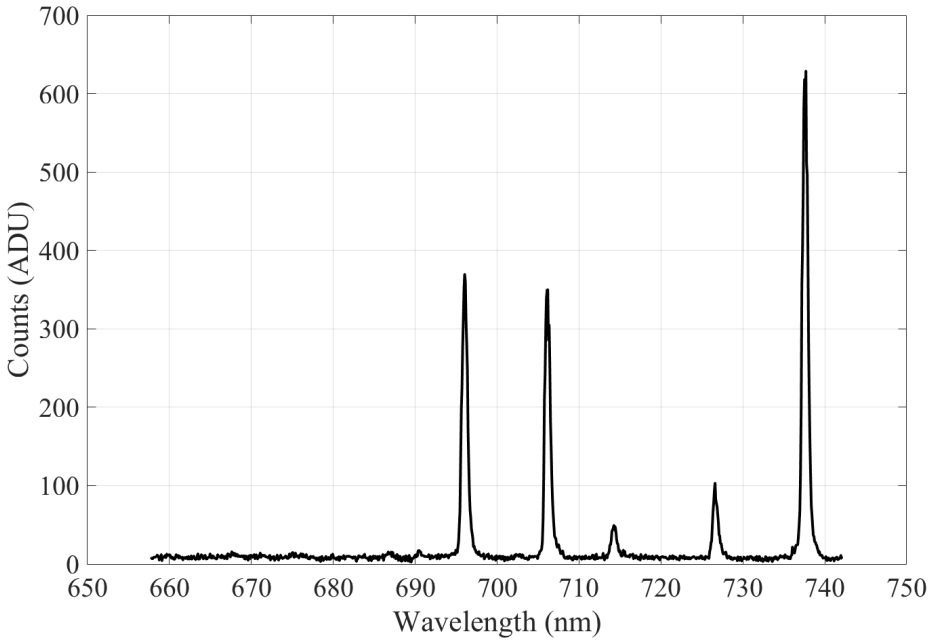

Figure 3.7: A 1D spectrum generated from binning Fig. 3.6. The center wavelength is 700 nm with a spread of ~ 80 *nm. A 500 mm spectrometer with 300 g/mm grating were used to generate the spectrum.*

be spliced together.

The splicing procedure takes several partial spectra and merges them together to form a single spectrum. To splice the spectra together, one of the spectra must be pinned with respect to wavelength. All other spectra are then spliced together around the pinned spectrum. In this work, the UV spectrum (or lowest wavelength) was pinned and the other spectra were aligned in reference to this spectrum.

To align each spectrum in wavelength, the cross-correlation between two adjacent spectra is determined. The maximum value of the cross-correlation

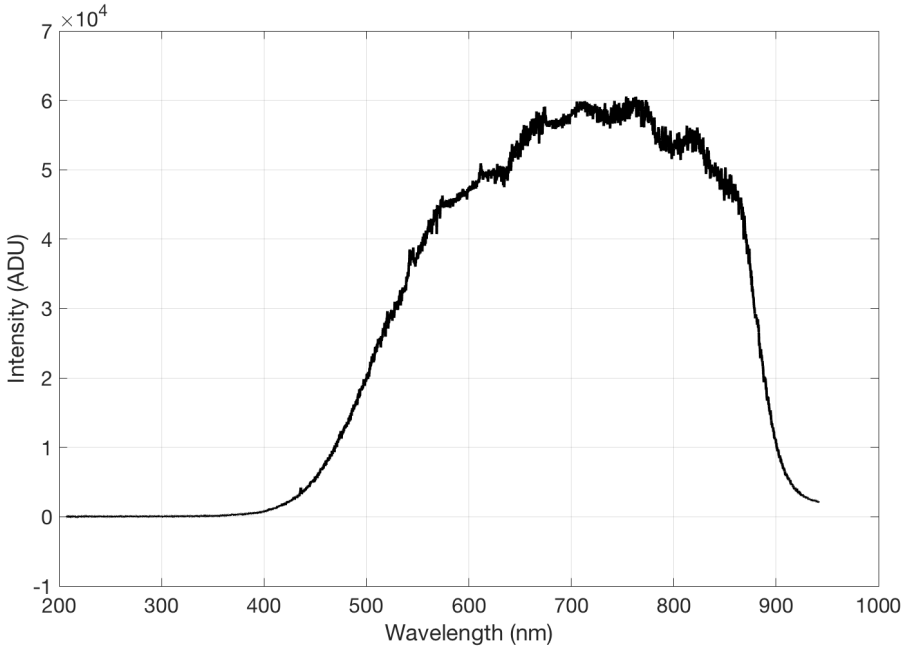

Figure 3.8: A spliced spectrum of the detector response to the DH2000 Halogen spectral radiance calibration source.

determines the amount needed to shift the adjacent signal to align it with the pinned spectrum. Once all the spectra have been wavelength aligned with respect to the pinned spectrum the spectra are spliced together according to [82]. To summarize, each partial spectrum is joined at the midpoint of the wavelength overlap region. The intensity of the spectra are then shifted such that continuity is maintained at the midpoint. Figure 3.8 shows a spliced spectrum of the detector response to the DH2000 Halogen lamp output.

The last step in the splicing procedure is to determine the wavelength calibration function between the measured spectra after the splicing procedure and the known lines of the Hg-Ar calibration lamp. Figure 3.9 shows a plot of

the measured wavelength to the known wavelength. The black circles indicate the data points while the dotted black line is a linear least squares fit to the data. The residuals (R) are calculated as $R = fit - known$.

The largest wavelength deviations of the splicing procedure occur below 650 nm, with a maximum deviation of 0.8 nm. In the NIR region there are more lines present from the Hg-Ar source, and the splicing procedure performs better with a maximum deviation of 0.25 nm. Therefore the wavelength calibration will give wavelengths accurate to ± 0.25 nm above 650 nm and ± 0.8 nm from 300-650 nm. In addition the residuals show no systematic shift associated with the splicing procedure. Therefore, a wavelength calibration is necessary correctly identify the plasma line positions.

3.10 Absolute Spectral Radiance Calibration

The signal registered by the detector is given in arbitrary units [counts]. To determine the relative emission line intensities and estimate the population densities of the upper excited states, the sensitivity of the detector as a function of wavelength and the optical path must be accounted for. The absolute calibration then converts the ADU [counts] to spectral radiance (L_λ) in [$Wm^{-2}sr^{-1}nm^{-1}$].

Figure 3.10 shows a schematic of the spectroscopy setup. The absolute calibration system consist of a calibration source (DH-2000-BAL) and integrating sphere. An aperture is used to determine the collection numerical aperture, and the order sorting filters prevent higher order lines. The inte-

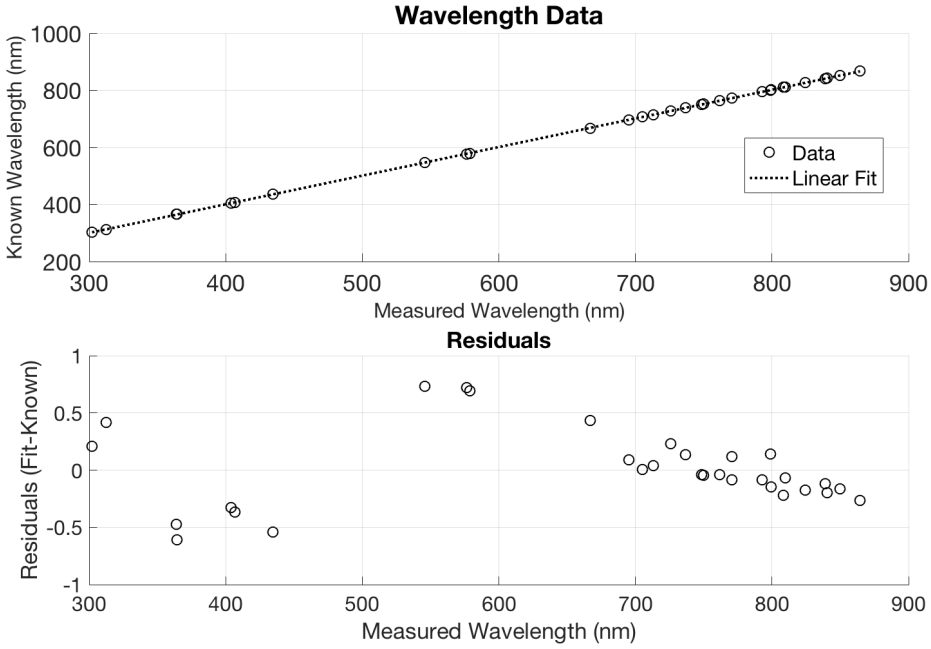

Figure 3.9: Wavelength calibration of a spliced spectrum of the detector response to the Hg-Ar calibration source. (A) compares the measured wavelength after splicing to the known wavelength. A linear trend is observed. (B) shows a plot of the residuals (nm), indicating a maximum wavelength deviation of 0.8 *nm.*

grating sphere is placed in the optical path of the spectroscopic observation system such that the collection optics are completely filled by the calibration source.

As discussed previously, the fiber bundle consists of 19 fibers in a circular array. Due to the stochastic nature of the streamer discharges not all fibers are always illuminated during a discharge. Therefore, the fiber corresponding to the electrode tip is chosen, because all streamers originate from this location. This ensures that the collection optics are completely filled by the plasma. Therefore, all plasma properties are estimated from the plasma discharge localized at the electrode tip, as shown in Fig. 3.10.

Designing the spectroscopic system such that both the calibration and plasma sources fill the entire collection optics provides a direct calibration for absolute spectral radiance. If the plasma does not completely fill the collection optics (or the source), then the solid angle of the plasma (source) must be determined to calculate the absolute spectral radiance.

The plasma collection volume is determined from the collection optics shown in Fig. 3.10. Each fiber is projected into the plasma domain by the plano-convex lenses with the ratio of the focal lengths determining the magnification factor ($m = f_2/f_1 = 2.5$). Using this magnification and the fiber diameter (200μm) the plasma collection region corresponds to a circular cross-section with a diameter of 500 μm. The plasma collection region is smaller than the diameter of the electrode (550 μm), which ensures that the collection optics are always filled by the plasma. This has been verified with instanta-

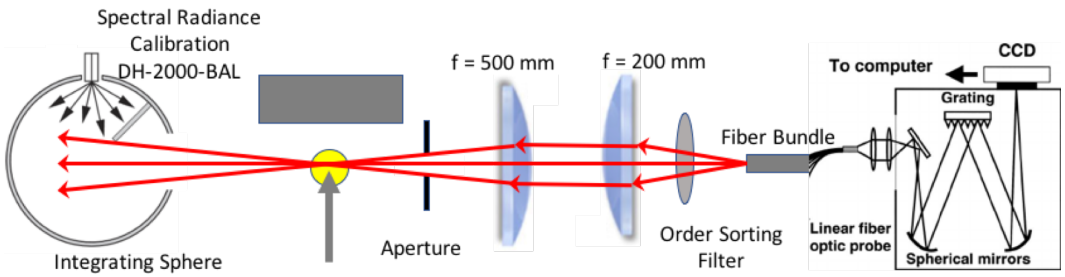

Figure 3.10: A schematic overview of the absolute calibrated spectroscopy setup.

neous broadband imaging. The length of the plasma column is also determined from the broadband images, and has a typical value of few hundred microns.

An Ocean Optics DH-2000-BAL NIST traceable spectral irradiance, E_λ [$\mathrm{Wm^{-2}nm^{-1}}$], calibration source was used to determine the spectral sensitivity of the detector. The calibration source consist of two independent light sources, a deuterium lamp and tungsten-halogen lamp. These two source have a combined spectral coverage of 200-1000 nm. The DH-2000-BAL is coupled with a modular integrating sphere with a highly reflective PTFE coating. The integrating sphere provides a Lambert surface for absolute spectral radiance measurements. The spectral radiance,L_λ, is given by Eq. 3.4. Where ρ is the spectral reflectance of the integrating sphere surface, and f is the ratio of open ports to total sphere area ($f = \sum(A_i)/A_s$).

$$L_\lambda = \frac{E_\lambda}{\pi} \frac{\rho(\lambda)}{1 - \rho(\lambda)(1 - f)} \tag{3.4}$$

Figure 3.11 shows the spectral reflectivity of three common integrating sphere surfaces. The integrating sphere used in this work is equipped with

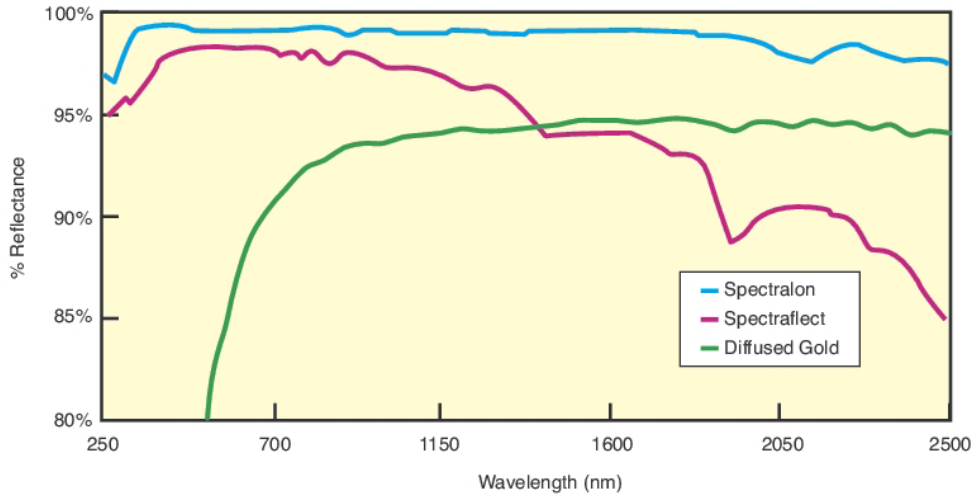

Figure 3.11: Spectral reflectance of three materials used in integrating spheres. A Spectralon, or PTFE, 3.3 inch integrating sphere is used in this work. It is evident that the spectral reflectance ($\rho(\lambda)$) is approximately constant for the PTFE with a value of 0.98. *[9]*

PTFE, or Spectralon. The PTFE coated sphere produces a relatively uniform response (ρ) over the range of wavelengths considered in this work (300-900 nm). To estimate the spectral radiance a constant value of $\rho = 0.98$ was used. The area ratio is determined from the number of open ports (two), to the total sphere area. The integrating sphere has an internal diameter of 8.4 cm, and each port is 2.54 cm in diameter. From Eq. 3.4 it is observed that the spectral radiance is related to the spectral irradiance by a constant factor.

Figure 3.12 shows the spectral radiance calibration as a function of wavelength for the DH-2000-BAL. The deuterium lamp covers the ultraviolet (UV) to near ultraviolet (NUV) spectral regions, while the tungsten-halogen lamp covers from the upper region of the NUV band to the NIR. To determine

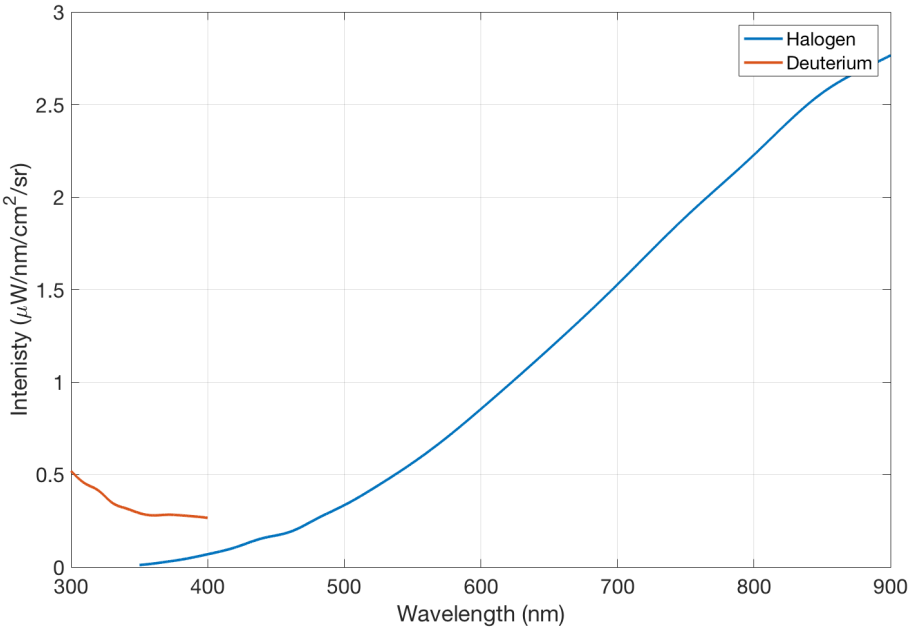

Figure 3.12: Spectral radiance calibration curves of the DH-2000-BAL tungsten-halogen and deuterium Lamps

the spectral sensitivity of the detector several partial spectra were acquired and spliced together using the procedure described previously (see for example Fig. 3.8).

Spectra of the calibration system were taken for different integration times to determine the spectral sensitivity and linearity of the detector and compute the scale factor. The total integration time is defined by the gate time multiplied by the number of on ICCD accumulations.

The gate time for all frames was held fixed at 5000 ms, and the number of on ICCD accumulations was varied. Figure 3.13 shows the spectral sensitiv-

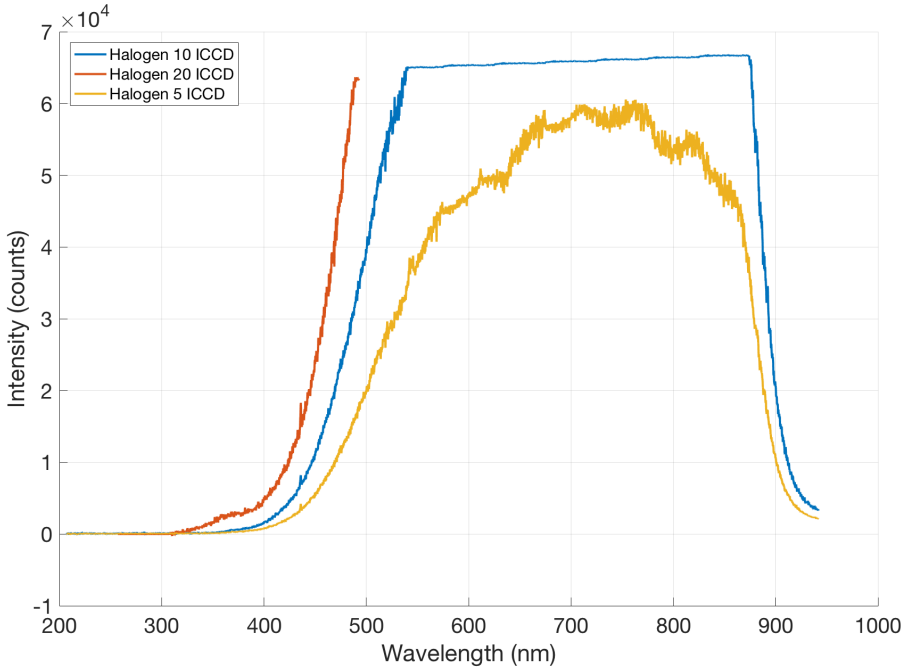

Figure 3.13: Spectral sensitivity of the detector in counts as a function of wavelength for the DH-2000-BAL tungsten-halogen lamp at various integration times

ity of the detector as a function of wavelength for the DH-2000-BAL halogen lamp for various integration times. At wavelengths below 400 nm the halogen source has a low intensity. Therefore, to resolve these lower wavelengths longer integration times are needed. In the region below 350 nm no emission is observed for the tungsten-halogen light source. Therefore to resolve the entire spectral domain the deuterium lamp source was used.

Figure 3.14 shows both the tungsten-halogen and deuterium light sources sensitivity normalized by the integration time as a function of wavelength. The sensitivity curves align when they are normalized by the integration time. This

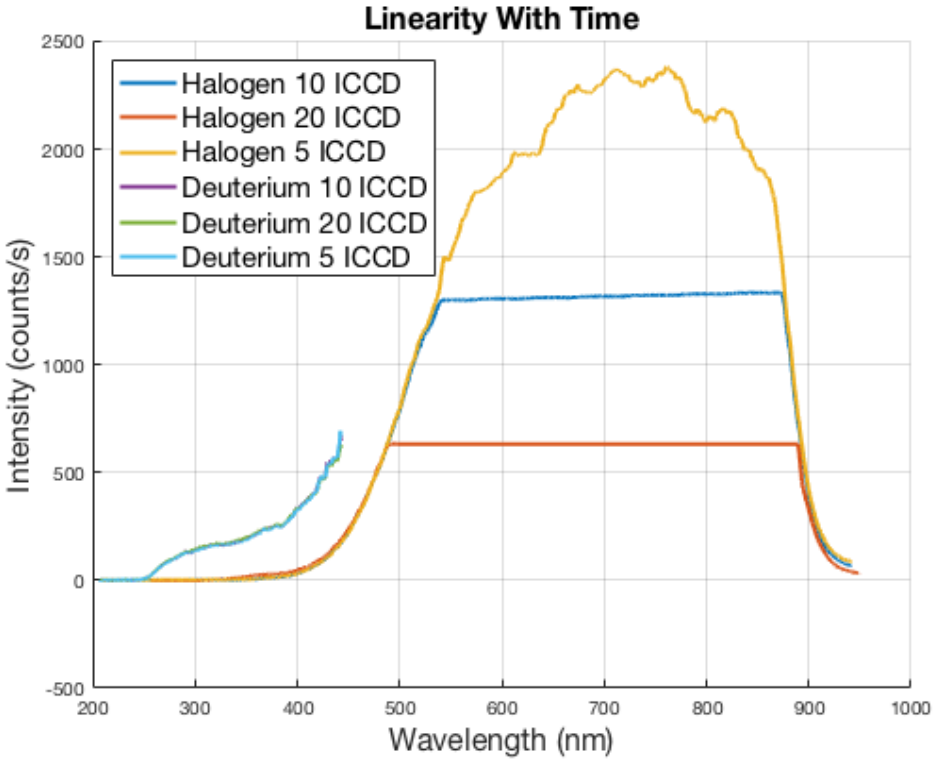

Figure 3.14: Spectral sensitivity of the detector in counts/s as a function of wavelength for the DH-2000-BAL tungsten-halogen and deuterium lamps. When normalized by the integration time the curves overlap for both lamps showing the linearity of the detector.

indicates the linearity of the detector over time.

A unique sensitivity curve for the spectrum was composed by splicing the response to the halogen and deuterium curves together and requiring continuity at the midpoint of the overlap region. The scale factor is given by the DH-2000-BAL spectral radiance calibration curve (Fig. 3.12) divided by the spectral sensitivity of the detector (Fig. 3.14). Multiplication of the scale factor with the observed plasma emission spectrum results in the absolute cali-

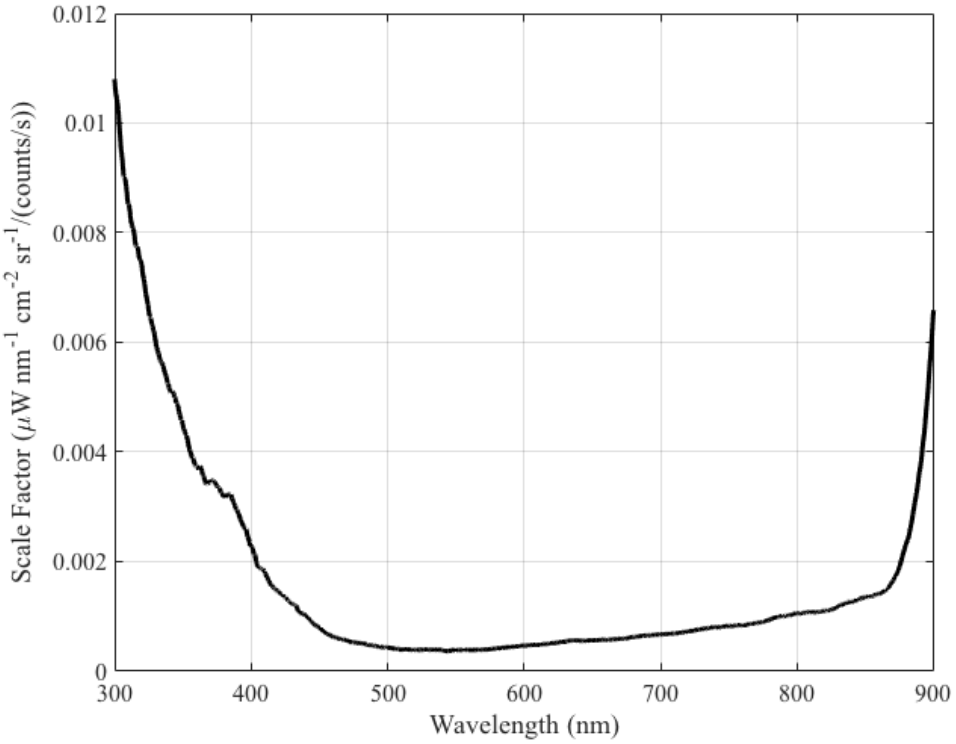

Figure 3.15: Calibration factor as a function of wavelength for 500 mm spectrometer with a 300 g/mm grating. The multiplication of the scale factor with the observed emission spectra in (counts/s) converts to $\mu W cm^{-2} nm^{-1} sr^{-1}$.

brated spectrum. Integrating each spectral line with a Gaussian profile results in the absolute radiance from which the emission coefficient and population densities can be determined. In the Boltzmann plotting technique only the relative intensities are needed, and hence absolute calibration is not necessary.

Chapter 4

Computational Plasma Fluid Model

A two-temperature, self-consistent, plasma fluid model with finite rate chemistry is used to simulate a non-equilibrium streamer discharge in CO_2. An axisymmetric simulation domain congruent with the experimental configuration described in previous section is used. For full details of the model see [39, 83, 84]. [1] In this domain, the governing equations for charged and neutral species production/destruction and transport are solved, as well as the self-consistent electrostatic field, and electron energy conservation equation. A chemical mechanism consisting of 59 species and 363 reactions between them is adapted from Ref. [85]. The plasma governing equations, boundary conditions, chemical mechanism, and geometric simulation configuration are discussed in this section.

[1] Some of the following work has already been published in: Pachuilo MV, Levko D, Raja LL, Varghese PL. Experimental and Numerical Investigations of a Pulsed Nanosecond Streamer Discharge in CO2. In 55th AIAA Aerospace Sciences Meeting 2017 (p. 1968). The author was the main contributer to this work. Dr. Raja and Dr. Varghese advised this work and Dr. Levko helped in development of the chemical mechanism.

4.1 Plasma Governing Equations

The individual species densities are determined from the continuity equations:

$$\frac{\partial n_k}{\partial t} + \vec{\nabla}.\vec{\Gamma}_k = \dot{G}_k \quad (k = 1, .., K_g, k \neq k_b) \tag{4.1}$$

Here, the species densities (n_k) are solved for every species k, except for a single dominant background species CO_2. In Eqn. 4.1, Γ_k is the species flux, and $\dot{G}_k$ is the source term for the net rate of production/destruction of species k due to plasma chemical reactions. The gas chemistry source term is determined from a mass-action kinetics formulation for the reaction rate.

The dominant background species density is calculated from the ideal gas law:

$$p = \sum_{k}^{K_g} n_k k_B T_k \tag{4.2}$$

Here, k_B is the Boltzmann constant and T_k is the species temperature which is assumed the same for all heavy species ($T_k = T_g$). The total gas pressure is assumed to be constant for the transience of the plasma. The partial species pressures (P_k) are known for every species except the dominant background species. Therefore the background species density can be calculated.

The species number flux (Γ_k) is obtained using the drift-diffusion approximation:

$$\vec{\Gamma}_k = n_k \vec{u}_k = -\mu_k n_k \vec{\nabla}\phi - D_k \vec{\nabla} n_k \tag{4.3}$$

Here, $\vec{u}_k$ is the species velocity, μ_k is the species mobility, D_k is the species diffusion coefficient, and ϕ is the electrostatic potential. The latter is obtained from the Poisson equation:

$$\nabla^2 \phi = -\frac{q_e}{\epsilon_0 \epsilon_r} \sum_k Z_k n_k \tag{4.4}$$

Here, q_e is the elementary charge, ϵ_0 is the permittivity of free space, ϵ_r is the relative permittivity, and Z_k is the charge number.

The electron energy is calculated from the electron energy conservation equation:

$$\begin{aligned} \frac{\partial e_e}{\partial t} + \vec{\nabla}.\left[(e_e + P_e)\vec{u}_e - \kappa_e \vec{\nabla} T_e\right] = &+ q_e \Gamma_e.\vec{\nabla}\phi - q_e \sum_i \left[\Delta E_i^e r_i\right] \\ &- \frac{3}{2} k_B n_e \frac{2m_e}{m_{k_b}} \left(T_e - T_g\right) \bar{\nu}_{e,k_b} \end{aligned} \tag{4.5}$$

The total electron energy e_e is assumed to be equal to the mean electron energy $e_e \approx 3/2 k_B T_e$, and the electron pressure P_e is determined from the ideal gas law. Then, the electron energy conservation equation is solved for the electron temperature.

The four terms on the left-hand side of Eqn. 4.5 are as follows from left to right: unsteady, convective, pressure work, and heat conduction flux terms.

On the right-hand side of Eqn. 4.5, the three source terms are: Joule heating, inelastic collision loss term, and elastic collision loss term. The term ΔE_i^e is the energy lost for an inelastic collision with reaction i, at a rate of progress of r_i. The remaining terms are the thermal conductivity of electrons κ_e, and the electron-neutrals momentum transfer collision frequency $\bar{\upsilon}_{e,k_b}$.

For the time scales associated with the streamer dynamics ($\sim$1-10 ns), the gas dynamic response is assumed negligible. Consequently, the gas temperature and the total gas pressure are assumed to be constant during the simulation and set according to the corresponding experimental conditions. For all test cases presented unless otherwise noted (parametric and optimization investigations), the gas temperature was held fixed at 300 K while the pressure was set to either 1 or 2 atmospheres.

To simulate the afterglow, and effects of voltage pulsing a zero-dimensional model is used. A zero-dimensional model is necessary to simulate longer time-scales of the order microseconds. The 0D model neglects the spatial derivatives found in the above equations. This is discussed in a section afterglow 5.4 and in chapter 7 which discusses optimization.

4.2 Transport Properties

The transport properties must be specified for the governing equations. The total collision frequencies $\bar{\upsilon}_{e,k_b}$ between species k and the background are used to compute the species diffusion coefficients (D_k) and mobility (μ_k) from an effective momentum transfer collision cross-section ($\bar{\sigma}_k$), for all heavy

species given as:

$$\bar{\upsilon}_{e,k_b} = n_b \bar{g}_k \bar{\sigma}_k \tag{4.6}$$

Here, $\bar{g}_k$ is the relative velocity between species k and CO_2. The diffusion and mobility coefficients are calculated from the effective collision frequency as:

$$D_k = \frac{k_B T_k}{m_k \bar{\upsilon}_k} \tag{4.7}$$

and mobility:

$$\mu_k = \frac{Z_k q_e}{m_k \bar{\upsilon}_k} \tag{4.8}$$

The transport properties for ions and electrons are related to one another through the Einsteins relation:

$$\frac{D_k}{\mu_k} = \frac{k_B T_k}{Z_k q_e} \tag{4.9}$$

Therefore, knowing the mobility as a function of E/N allows the diffusion coefficient to be determined directly. The electron thermal conductivity is defined as:

$$\kappa_e = \frac{5}{2} \frac{k_B D_e}{n_e} \tag{4.10}$$

The electron mobility is computed from the 0D Boltzmann equation solver BOLSIG+ [1].

4.3 Boundary Conditions

Here, the boundary conditions for the equations are provided. The species flux boundary conditions are specified for all plasma equations. For solid surfaces, the flux of electrons towards the wall with unit outward normal ($\hat{n}_s$) is specified as:

$$\vec{\Gamma}_e.\hat{n}_s = \frac{1}{4} n_e \left(\frac{8 k_B T_e}{\pi m_e} \right)^{1/2} - \sum_k \gamma_k \Gamma_k^{s+} \tag{4.11}$$

Here, it is assumed that the electrons near the wall are in thermal equilibrium with temperature, T_e. With this assumption, the thermal flux to the surface is computed [first term on the right hand side of Eqn. 4.11]. The second term on the right hand side of Eqn. 4.11 is the outward flux of secondary emitted electrons emitted from the surface into the plasma domain due to heavy species impacting the wall. The secondary electron emission is computed from the secondary electron emission coefficient (γ=0.01) and the wall flux (Γ_k^{s+}) of ion species k.

The ion and neutral wall flux boundary conditions are, respectively:

$$\vec{\Gamma}_i.\hat{n}_s = \frac{1}{4} n_i \left(\frac{8 k_B T_g}{\pi m_i} \right)^{1/2} - n_i.max\left(0, -\mu_i \hat{n}_s.\vec{\nabla}\phi\right) \tag{4.12}$$

and

$$\vec{\Gamma}_n.\hat{n}_s = \Gamma_n^{s+} = \frac{1}{4} n_n \left(\frac{8 k_B T_g}{\pi m_n} \right)^{1/2} \tag{4.13}$$

The second term in Eqn. 4.12 accounts for the mobility-limited flux for ions, or drift flux due to the sheath potential. For a positive sheath (decreasing poten-

tial towards the wall) and positive ions, the second term in is non-zero while for negative ions it evaluates to zero. The model also includes surface chemistry so the sign of the net flux is dependent on these surface reactions. Additionally, Dirichlet boundary conditions can be imposed for fixed flux quantities, and for symmetry boundary conditions, the fluxes normal to the boundary are set to zero, i.e. RHS of equations are set to zero.

The electrostatic potential boundary conditions at solid electrode surfaces are specified by a Dirichlet boundary condition. For symmetry boundary conditions, the normal potential gradient is set to zero. At dielectric surfaces, charge trapping occurs which leads to a local surface charge induced electric field. The surface charge density (ρ_s) is determined from:

$$\frac{\partial \rho_s}{\partial t} = q_e \sum_k Z_k \Gamma_k . \hat{n}_s \tag{4.14}$$

The flux of electron energy ($\vec{Q}_e$) to a solid surface is calculated as follows:

$$\vec{Q}_e . \hat{n}_s = e_{se} \left(\frac{1}{4} n_e \left(\frac{8 k_B T_e}{\pi m_e} \right)^{1/2} \right) - q_e \Delta E^e_{se} \sum_k \gamma_k \Gamma^{s+}_k \tag{4.15}$$

Every electron which impacts the wall is assumed to carry with it $e_{se} = 5/2 k_B T_e$ units of energy, with a thermal flux $\left(\frac{1}{4} n_e \left(\frac{8 k_B T_e}{\pi m_e} \right)^{1/2} \right)$. In Eq. 4.15, ΔE^e_{se} is the energy of the secondary electron which enters the plasma domain which is dependent upon the work function of the material and the energy of the incident species.

4.4 Simulation Configuration

Figure 4.1 shows the mesh geometry and boundary conditions used in our studies. The axisymmetric domain is used with an inter-electrode spacing of 3.81 mm. The geometry is taken to be similar to that in the experimental investigations. Near the HV electrode the mesh is refined to better resolve large gradients present in the sheath regions. In Fig. 4.1, a magnified insert is presented which shows the resolution of the mesh domain. In the dielectric subdomain, a coarser mesh is used, as only the electrostatic potential equation is solved in this subdomain. The mesh consists of ∼160,000 cells in the plasma subdomain, and 6,000 cells in the dielectric subdomain.

The dielectric constant (ϵ_r) is assumed to be a constant of 5. This value is estimated from the experimental dielectric constant of Macor (5.64) measured at a frequency of 8.5 GHz, which is similar to the operational pulse frequency observed in experiments. Electrode (D) in Fig. 4.1 is held at a fixed ground potential. The HV electrode (C) has a diameter of 550 μm with a radius of curvature of ∼250 μm. A DC HV is applied to electrode (C). This is done to reduce the computational time, as each experimental voltage pulse last ∼100s ns. To find the breakdown threshold for both positive and negative polarities, a parametric study was conducted using DC voltages. Once, the breakdown voltage is found the simulations are run until the streamer bridges the inter-electrode gap.

The boundary conditions for each equation are described in Fig. 4.1. In the plasma subdomain all equations are solved while in the dielectric sub-

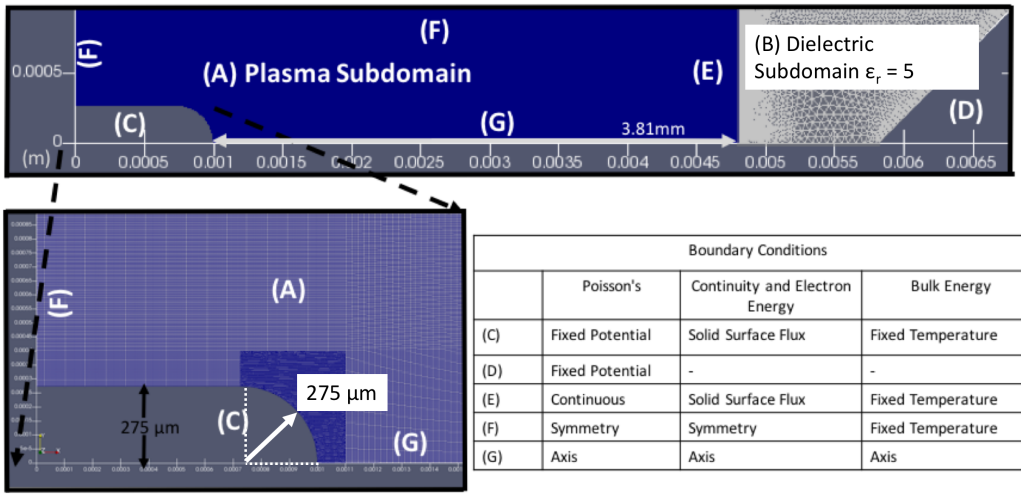

Boundary Conditions			
	Poisson's	Continuity and Electron Energy	Bulk Energy
(C)	Fixed Potential	Solid Surface Flux	Fixed Temperature
(D)	Fixed Potential	-	-
(E)	Continuous	Solid Surface Flux	Fixed Temperature
(F)	Symmetry	Symmetry	Fixed Temperature
(G)	Axis	Axis	Axis

Figure 4.1: Pin-to-pin electrode discharge mesh geometry and boundary conditions. The discharge gap is 3.81 mm and the high-voltage electrode (C) has a radius of 275 µm. A DC voltage is applied to (C), while (D), the ground electrode, is held fixed at 0 volts. The simulation is axis-symmetric about (G) axis. The species continuity equation, Poisson equation, and the electron and bulk energy equations are solved in the plasma subdomain (A), while only Poisson equation is solved in the dielectric subdomain (B).

domain only the Poisson equation is solved. Symmetry boundary conditions are used along the axis (G) for all equations. At the HV electrode surface (C), fixed potential and solid surface fluxes are used. A constant secondary electron emission coefficient of 0.01 is assumed at the electrode for all heavy species. Furthermore, all surfaces [Fig 4.1. electrode (C) and dielectric (E)] are modeled as quench surfaces where excited species and ions return to stable ground state species, while electrons are absorbed.

4.5 CO_2 Plasma Chemistry

The chemistry mechanism is an extension of the mechanisms found in Ref. [47, 64, 85]. The primary aspects of the mechanism [47, 85] will be summarized here.[2] Table 4.1 provides a summary of all the species considered in the model. The full mechanism consist of 82 species and 1725 reactions between them.

The author's main addition to the mechanism is the inclusion of electronic states for oxygen, and carbon monoxide. The mechanisms considers a complex set of CO_2 vibrational levels from the ground state all the way to the dissociation energy of 5.5 eV. CO vibrational levels are also consider up to the tenth level.

[2]Some of the following work has already been published in: Pachuilo MV, Levko D, Raja LL, Varghese PL. Experimental and Numerical Investigations of a Pulsed Nanosecond Streamer Discharge in CO2. In 55th AIAA Aerospace Sciences Meeting 2017 (p. 1968). The author was the main contributer to this work. Dr. Raja and Dr. Varghese advised this work and Dr. Levko helped in development of the chemical mechanism.

The notation of the electronically excited states are as follows: CO_{2e1} ($^1\pi_g$), CO_{2e2} ($^1\Delta_u$); CO_{e1} ($A^3\Pi$), CO_{e2} ($A'^3\Sigma^+$), CO_{e3} ($A^1\Pi$), CO_{e4} ($B^3\Sigma^+$), CO_{e5} ($B^1\Sigma^+$), CO_{e6} ($C^1\Sigma^+$), CO_{e7} ($E^1\Pi$); O_{2e1} (sum $a^1\Delta$ and $b^1\Sigma$), O_{2e2} (sum of $A^3\Sigma$, $A'^3\Delta$, and $c^1\Sigma$), O_{2e3} (sum of $B^3\Sigma$ and higher triplet states); O_{e1} (1D), O_{e2} (1S), O_{e3} ($3S$), O_{e4} ($4S$), O_{e5} ($3D$), and O_{e6} ($8D$). All data for the electron impact reactions is taken from the LxCat database [1, 10].

Carbon dioxide has three vibrational modes: symmetric (v_1) and asymmetric stretching (v_3), and bending (v_2), where v_i are the vibrational quantum numbers. Since CO_2 is a linear molecule the bending mode is doubly degenerate, and a fourth quantum number $l_2 = v_2, v_2-2, v_2-4, ...$ is used to determine the angular momentum about the principal axis.

The energy levels of CO_2 are approximated by the anharmonic oscillator Eq. 4.16 [85]. Where x_{ij}, $x_{l_2l_2}$, and ω_i are spectroscopic constants, and $d_i = (1, 2, 1)$ is the degeneracy of each vibrational mode.

$$\frac{E_{CO_2}}{hc} = \sum_i \omega_i(v_i + d_i/2) + \sum_{j\geq i} x_{ij}(v_i + d_i/2)(v_j + d_j/2) + x_{l_2l_2}l_2^2 \qquad (4.16)$$

To minimize the complexity of the reaction mechanism only the important vibrational modes of CO_2 are considered as outlined in Chapter 5 of [4]. The asymmetric mode is primarily responsible for efficient dissociation of carbon dioxide. This is because the asymmetric stretch mode has lower vibration translational (VT) relaxation loses compared to the other two modes, it is ex-

Neutrals and Radicals	Ions	Excited States
CO_2, CO, C_2O, C, C_2	CO_2^+, CO_4^+, CO^+, $C_2O_2^+$, $C_2O_3^+$, $C_2O_4^+$, C^+, C_2^+, CO_3^-, CO_4^-	CO_{2e1}, CO_{2e2}, CO_{2va}, CO_{2vb}, CO_{2vc}, CO_{2vd}, CO_{2v1}... CO_{2v21}, CO_{e1}...CO_{e7}, CO_{v1}... CO_{v10}
O_2, O_3, O	O^-, O_2^-, O_3^-, O_4^-	O_{2e1}, O_{2e1}... O_{2e3}, O_{2v1}... O_{2v3}, O_{e1}... O_{e7}

Table 4.1: Summary of all species included in the model.

cited by low energy electrons (1-3 eV), and vibrational energy exchange (VV relaxation) is faster than that of the symmetric or bending modes.

The fast VV relaxation can lead to efficient population of highly excited states which results in an efficient dissociation mechanism. Therefore the model considers all asymmetric levels up to the dissociation energy, while only the first four lower levels of the symmetric mode are considered. The symmetric levels are denoted as $CO_{2va}, CO_{2vb}, CO_{2vc}$, and CO_{2vd} while asymmetric levels are numbered from 1 to 21.

The CO vibrational energy levels are calculated by Eq. 4.17. Again, ω_e, and x_e are spectroscopic constants, and v is the vibrational quantum number. Only the first 10 vibrational excitations of CO are considered which corresponds to a vibrational energy of 2.51 eV.

$$\frac{E_{CO}}{hc} = \omega_e(v + \frac{1}{2}) - \omega_e x_e(v + \frac{1}{2})^2 \tag{4.17}$$

The dominant population mechanism in plasma streamer discharges is through electron impact reactions. The electron impact reaction rates are determined from cross section data and an off-line Boltzmann Solver BOLSIG+ [1]. The reaction set for electrons, ions, neutrals, and electronically excited species are taken from [47, 85] and the references therein.

The excited states share the same chemistry as their corresponding ground state. Vibrationally excited states may experience a stimulated dissociation (lowers the activation energy for dissociation), and electronically excited states have reduced activation energy for ionization. It is assumed that the activation energy for dissociation is reduced by the same amount as the vibrational excitation energy, similarly for electronically excited species and the ionization threshold. In charge exchange reactions the rate constant (K) of electronically excited species is scaled as $K = K_o \left(\frac{E_i}{E_e}\right)^2$. K_o is the ground state rate coefficient for the charge exchange, E_e is the excitation energy, and E_i is the ionization energy.

Vibrationally excited species can react in three ways: vibrational translation relaxation (VT), vibrational vibrational (VV) relaxation between two molecules in the same vibrational mode or VV' relaxation between two different modes of vibration, and chemical reactions. The vibrational energy exchange in molecular collisions (VT, VV, VV') are taken from [85] and the references therein.

For electron impact excitation of vibrational levels, only the low lying levels have tabulated data. To determine the excitation of higher vibrational

states the Fridman approximation is used to scale the cross sections [4, 85]. The Fridman approximation (Eq. 4.18) gives the scaled cross section σ_{nm} for the electronic excitation of a vibrational state CO_{2n} to CO_{2m}. The cross section is shifted in energy to account for the lowering of threshold energy. The magnitude of the cross section is scaled by two parameters α and β, which are 0.5 and 0 for CO_2 [4]. Lastly, the Fridman-Macheret α model is used to estimate the rate coefficients for chemical reactions involving vibrationally excited species and neutrals that results in the splitting of the vibrating molecule.

$$\sigma_{nm}(\epsilon) = exp\left(\frac{-\alpha(m-n-1)}{1+\beta n}\right)\sigma_{01}(\epsilon + E_{01} - E_{nm}) \tag{4.18}$$

4.5.1 Model Validation and Reduction

The above mechanism was developed for 0D reaction kinetics modeling, and is not suited for 2D plasma fluid modeling for two reasons: (1) the computational simulation time is not tractable, and (2) during the streamer phase only the excitation reactions (electron impact) are dominant. Therefore, a reduced subset of the chemical reactions described was used in the plasma fluid modeling. These included electron impact reactions, neutral-ion reactions, neutral-neutral reactions, and vibrational excitation for CO_2 and CO. The reduced mechanism consists of 59 species and 363 reactions between them.

The reduced model contains all the same reactions for neutrals, ions, electronic excitation, and vibrational energy exchange for CO_2 and CO. To re-

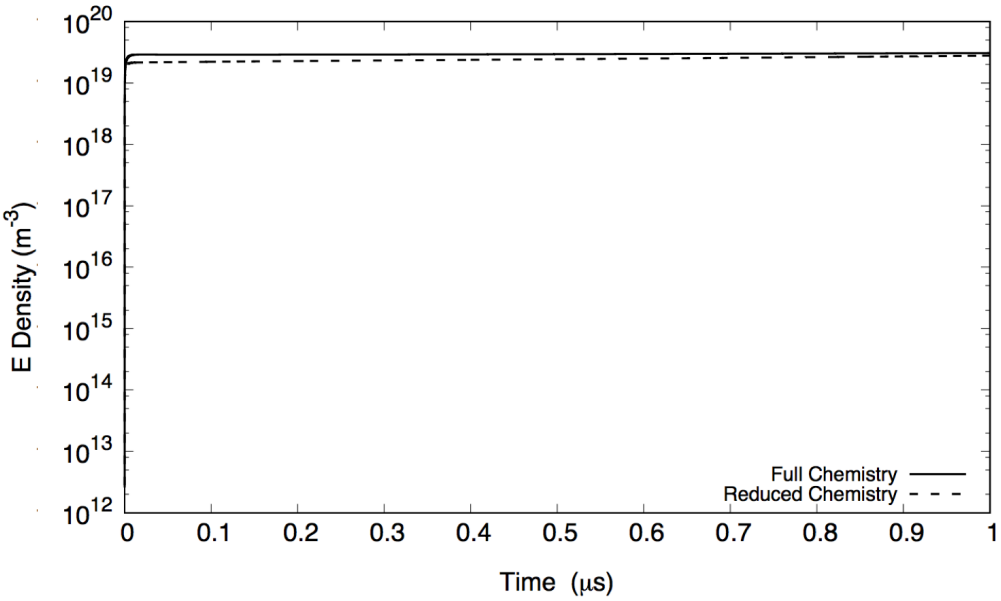

Figure 4.2: A Comparison between the full and reduced chemical mechanism, showing the temporal evolution of the electron density.

duce the computational time electronic species have been grouped into lumped parameters. This decreases the number of reactions while still modeling the electron energy losses.

The reduced model does not account for vibrational and electronic reactions of O, O_2, nor multi-quantum vibrational exchange of CO_2, and CO. Additionally, the reduced model also does not consider vibrational and electronic scaling effects on the reduction of chemical reaction energy thresholds for ionization and dissociation. Due to the fast streamer time scales, a few ns, chemical reactions are not expected to play a significant role in the plasma chemical kinetics. Therefore, the dominant reaction pathways through electron collisions are maintained in the model as well as vibrational relaxation pathways, specifically vibrational ladder climbing.

A 0D model with a constant power was used to compare the accuracy of the reduced model kinetics to the full chemical mechanism adapted from [85]. Figures 4.2-4.4 show the temporal evolution of the electron density (Fig. 4.2), density of the first asymmetric vibrational level of carbon dioxide (Fig. 4.3), and the density first symmetric vibrational level of carbon dioxide (Fig. 4.3).

Figure 4.2 shows the evolution of the electron density. Both the full and reduced mechanisms tend to steady state within one microsecond. The electron densities between the two mechanisms are nominally the same, with the full model predicting the electron density to within a factor of 1.2.

The electron density production is determined by ionizing reactions

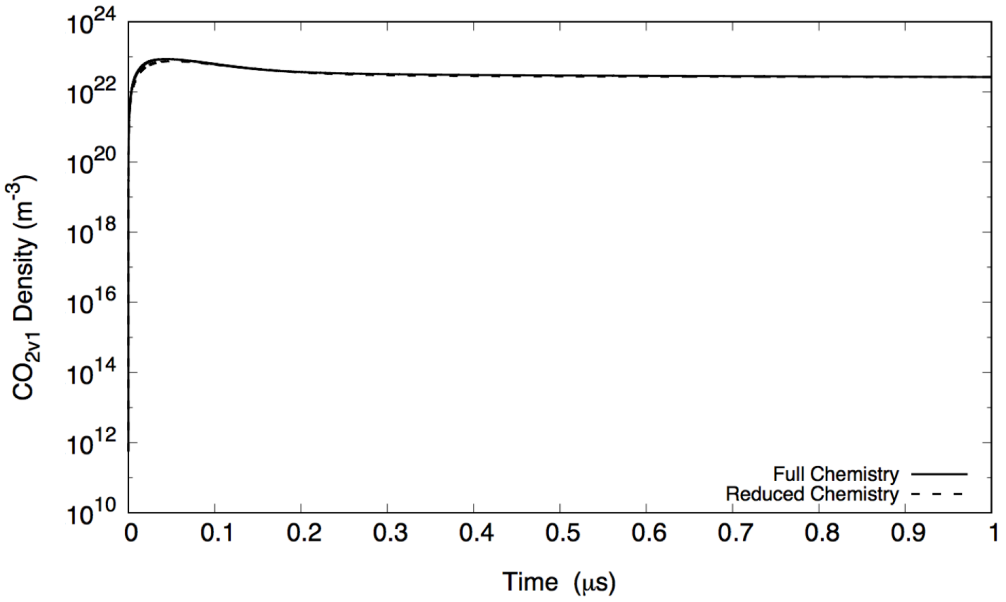

Figure 4.3: A comparison between the full and reduced chemical mechanism, showing the temporal evolution of the first asymmetric vibrational excitation level of carbon dioxide.

through electron impacts while the dominant electron quenching mechanisms are through electron-ion recombination. Both the reduced and full chemical mechanism maintain the same ionizing and recombination reactions. Therefore, the electron kinetics are reproduced by the reduced mechanism.

The vibrational densities of CO_2 for the first symmetric and asymmetric states are given in Fig. 4.4 and 4.3, respectively. Both the reduced and full mechanisms show similar transients with both tending to steady state at 1 μs. The full mechanism considers multi-quantum vibrational exchange, vibrational reactions which share the same kinetics as the CO_2 ground state, and stimulated dissociation. The reduced mechanism only considers vibrational

Neutrals and Radicals	Ions	Excited States
CO_2, CO, C_2O, C, C_2	CO_2^+, CO_4^+, CO^+, $C_2O_2^+$, $C_2O_3^+$, $C_2O_4^+$, C^+, C_2^+, CO_3^-, CO_4^-	CO_{2e1}, CO_{2e2}, CO_{2va}, CO_{2vb}, CO_{2vc}, CO_{2vd}, CO_{2v1}... CO_{2v21}, CO_{v1}... CO_{v10}
O_2, O_3, O	O^-, O_2^-, O_3^-, O_4^-	

Table 4.2: Summary of all species included in the reduced model.

quenching reactions with the dominant background species and electronic excitation of the low lying vibrational levels.

It is evident that multi-quantum vibrational exchange, and stimulated dissociation do not play significant roles in replicating the vibrational excitation kinetics for the timescales considered. In addition, the reactions of vibrationally active states with other excited and non-background neutral species do not contribute significantly to the population of the vibrational states. This is mainly attributed to their low densities at these time scales. For longer time scales such as simulation of reactors with millisecond residence times the full mechanism is needed. At these times the the excited states will become sufficiently dense that their rate coefficients are no longer negligible [63, 85].

The reduced mechanism discussed above will be used in determining the reaction kinetics for the streamer discharge in CO_2, and pulsed discharges up to 1 μs. Table 4.2 outlines the species used in the reduced model. The reduced model considers vibrational energy relaxation (VV', VV, VT) for CO_2 and CO.

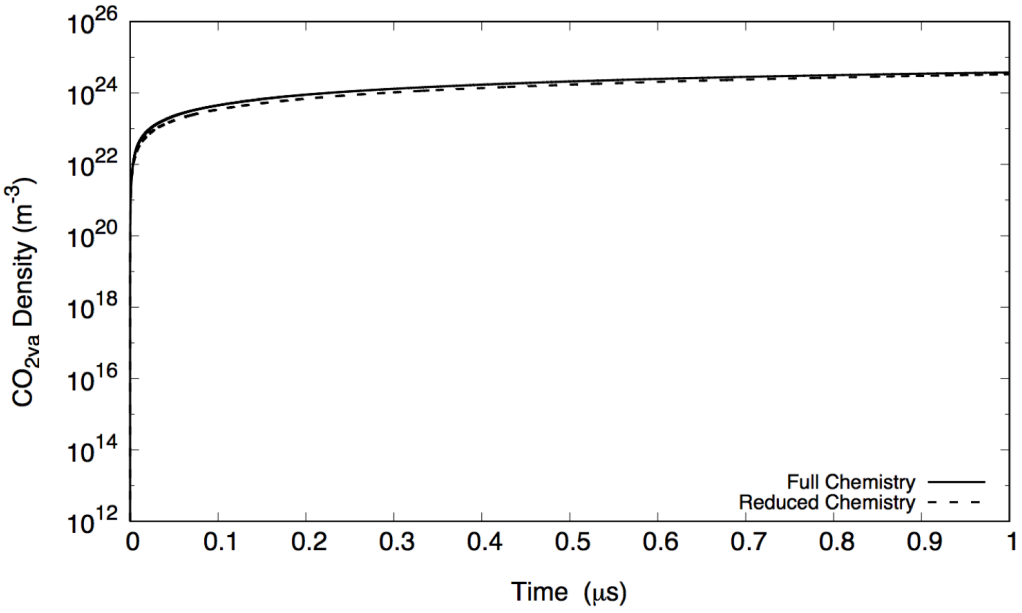

Figure 4.4: A Comparison between the full and reduced chemical mechanism, showing the temporal evolution of the first symmetric vibrational excitation level of carbon dioxide.

Chapter 5

Computational Results

The computational results are discussed here. The modeling consisted of two main objectives: (1) comparison and validation with experimental results, and (2) parametric and optimization investigations. The first part of the modeling section (Chapter 5) covers comparison and validation with the experiments. This is then followed by the experimental results Chapter 6. Chapter 7 then covers the parametric investigations in pressure and temperature, and optimization strategies including pulsing and multi-streamer interactions[1].

5.1 Effects of Gas Pressure

Simulations for the gas pressure of 101.3 kPa and 202.6 kPa were performed which is determined by the experimental conditions (see Chapter 6). The voltage is held fixed at 20 kV for both pressures. Figures 5.1-5.3 show the results of simulations obtained for both pressures.

It is known that the propagation of both cathode- and anode-directed

[1]Some of the following work has already been published in: Pachuilo MV, Levko D, Raja LL, Varghese PL. Experimental and Numerical Investigations of a Pulsed Nanosecond Streamer Discharge in CO2. In 55th AIAA Aerospace Sciences Meeting 2017 (p. 1968). The author was the main contributer to this work. Dr. Raja and Dr. Varghese advised this work and Dr. Levko helped in development of the chemical mechanism.

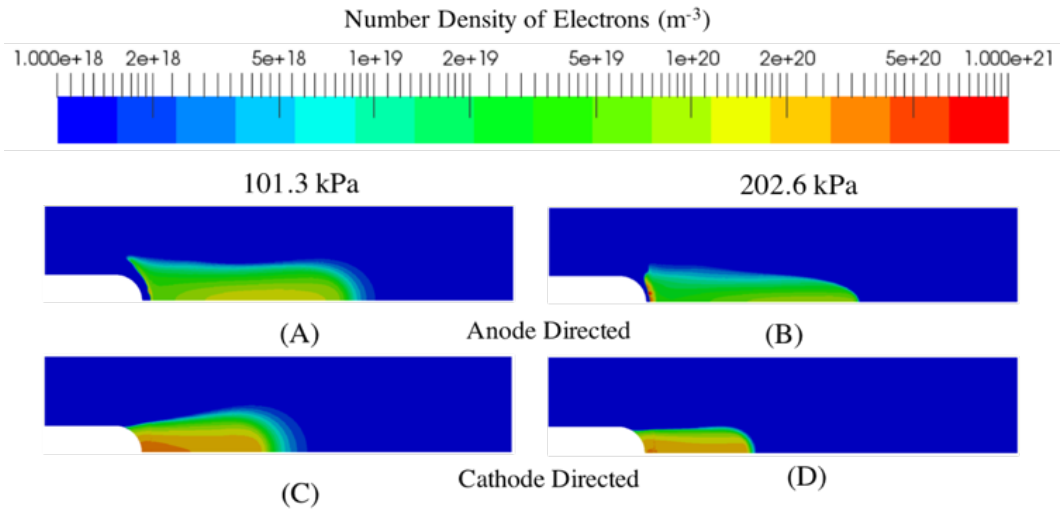

Figure 5.1: Contour plots of the electron number density (in m^{-3}) as the function of gas pressure and voltage polarity: (a,c) 1 atm. at 0.6 ns, and (b,d) 2 atm. at 0.6 ns.

streamers is supported by the multiplication of electrons seeded in the cathode-anode gap. Since the electrical conductivity of the streamer body is high, the electric field in this part of the streamer is small (Fig. 5.2). Therefore, the electric field is mainly concentrated at the streamer head (Fig. 5.2) and is responsible for the self-consistent streamer propagation. For the cathode-directed streamer electrons seeded in front of the streamer head are accelerated toward the streamer head, while for the anode-directed streamer these electrons are accelerated from the streamer head toward the anode.

Figure 5.1 shows the contour plots of the electron density as a function of pressure and voltage polarity. An increase in the gas pressure results in the decrease in the streamer diameter at 0.6 ns for 1 atm. and 0.6 ns for 2

atm.. This is explained by the requirement of higher breakdown electric field at higher gas pressure. For the conditions of our studies, the gap voltage is the same for both pressures. Therefore, in order to obtain higher electric field strength at the streamer head at higher pressure, the streamer diameter must decrease.

The streamer diameter is estimated from the full width at half maximum (FWHM) of the electron density profile at a distance of 400 μm from the streamer head. Here, the streamer head is determined from the spatial distribution of the electron temperature, T_e. At the streamer head, the electron temperature is $\sim$10 eV, while in the tail T_e $\sim$1 eV (Fig. 5.3). Based on the definition of the streamer diameter, the anode-directed streamer diameter is 400 μm at 101.3 kPa [Fig. 5.1 (a)], and 200 μm at 202.6 kPa [Fig. 5.1 (b)]. The diameter of the cathode-directed streamer is 622 μm at 101.3 kPa [Fig. 5.1 (c)], and 510 μm at 202.6 kPa [Fig. 5.1 (d)].

The average electron density is determined for both pressures and polarities. It is estimated from the FWHM value of the electron density profile taken at 400 μm from the streamer head. The anode-directed streamers have an electron density which is an 1 order of magnitude lower than the cathode-directed streamers for both pressures. This difference is explained by different mechanisms of streamer propagation and cannot be explained by the electron temperature in the streamer tail (Fig. 5.3).

Indeed, Fig. 5.3 shows that at 101.3 kPa, T_e is higher for the cathode-directed streamer, while at 202.6 kPa it is higher for the anode-directed streamer.

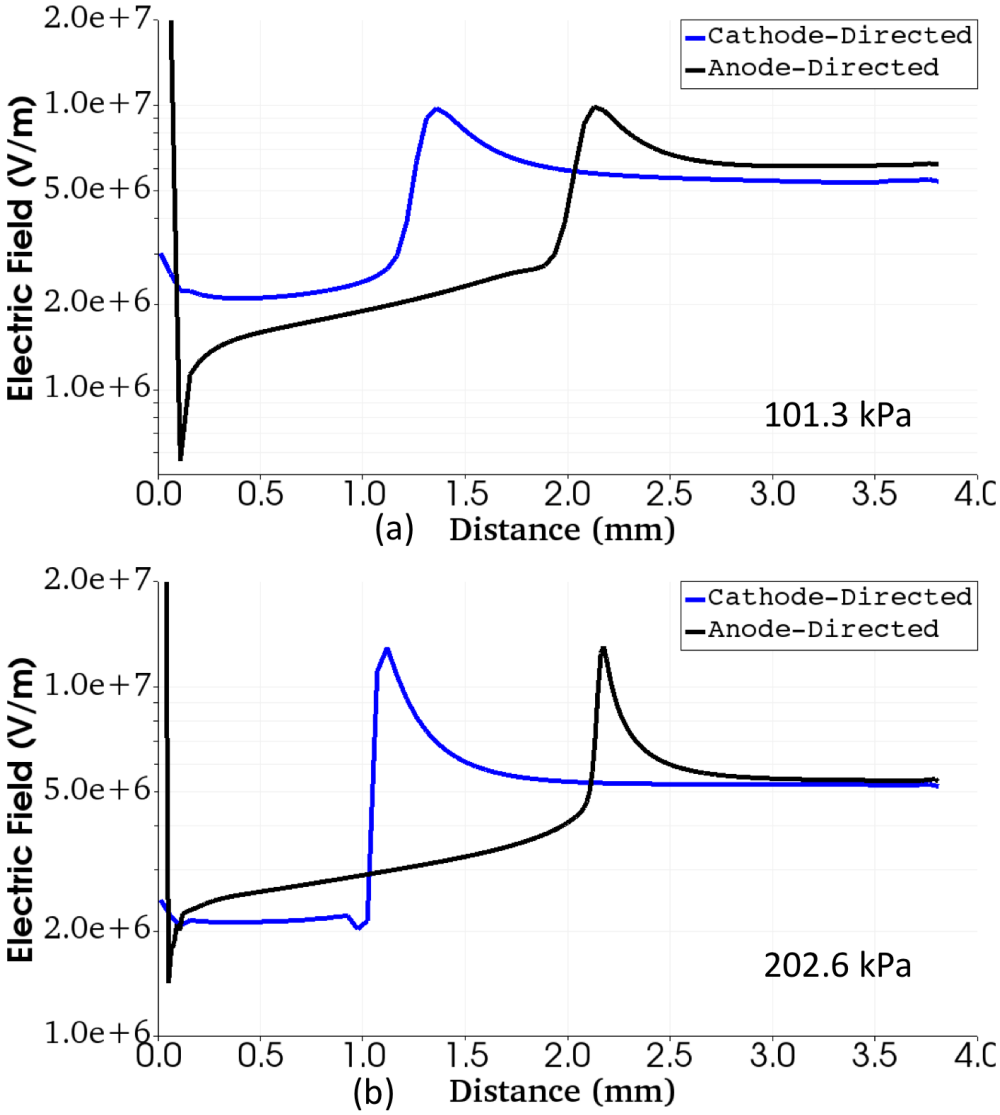

Figure 5.2: Electric field (in V/m) at the axis as the function of gas pressure and voltage polarity: (a) 101. 3 kPa (0.6 ns), and (b) 202.6 kPa (0.6 ns). The blue lines correspond to a cathode directed streamer, and black lines correspond to a anode directed streamers. The cathode sheath region is also observed by the sharp rise of the electric field at the electrode tip (0 mm) for the cathode-directed streamer discharges.

Figures 5.2 and 5.3 show comparable electric fields and electron temperatures at the heads of both streamers. Therefore, it is concluded that the ionization rates at the heads of both streamers are comparable. However, the cathode-directed streamer consumes electrons being accelerated and generated at the streamer head while the anode-directed streamer pushes them from the streamer. This explains higher electron density in the tail of the cathode-directed streamer. Additionally, this indicates that at the considered conditions electron density in the streamer tail is defined by the electrons being generated at the streamer head rather than the local tail parameters at any given time.

Figure 5.1 shows the electron density contours as a function of pressure and polarity. It is observed that the electron density increases as pressure decreases for both voltage polarities. This is explained by the fact that the increase in the gas pressure results in the increase in the electron energy losses in inelastic collisions such as excitation of vibrational and electronic levels of CO_2. These processes have high rate coefficients at low electron temperature and limit the electron energy gain which decreases the number of ionizing reactions and hence electron density.

The streamer velocity is estimated for both pressures and polarities. It is calculated using the position of the streamer head for a given integration time. The position of the streamer head is determined from the electron temperature profile. Figure 5.3 shows the highest electron temperature at the streamer head. Then, taking the position of the head and the known

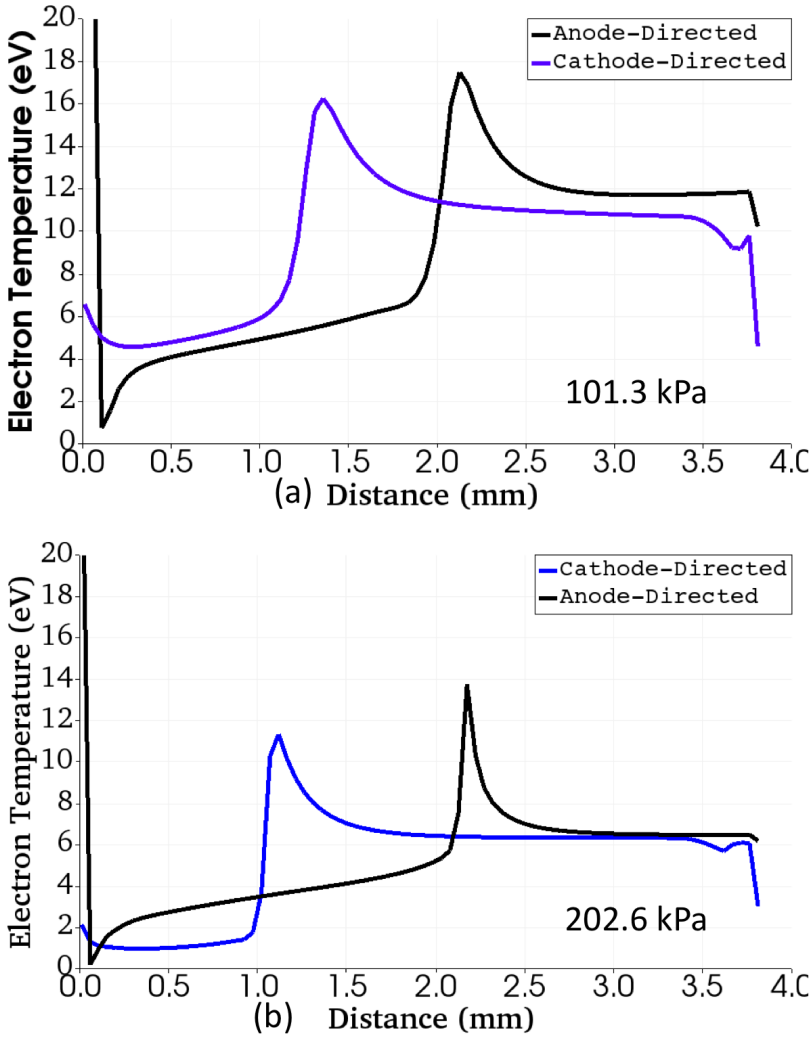

Figure 5.3: Electron temperature (in eV) at the axis as the function of gas pressure and voltage polarity: (a) 101. 3 kPa (0.6 ns), and (b) 202.6 kPa (0.6 ns). The blue lines correspond to a cathode directed streamer, and black lines correspond to a anode directed streamers.

integration time the streamer velocity is calculated. The cathode-directed streamer velocity is 3.5 and 12.8 mm/ns for 202.6 and 101.3 kPa, respectively. Comparable velocities are obtained for the anodic streamers, namely, 5.3 and 17.0 mm/ns for 202.6 and 101.3 kPa, respectively. Both streamers propagate faster for lower pressures, and anodic streamers are always faster than cathodic ones.

5.2 Effects of Voltage and Polarity

In order to study the effects of voltage and polarity, the gas pressure was held constant at 202.6 kPa. Voltages of $\pm 10, \pm 12.5, \pm 15$, and $\pm 20 kV$ were applied to the left electrode.

Figure 5.4 and 5.5 shows the electron density contours for the cathode- and anode-directed streamers as the function of the DC voltage. It is concluded from Fig. 5.4(a) that for ± 10 kV a corona discharge is obtained. A corona discharge is a low density plasma region which remains localized at the electrode tip, this means that an initial avalanche never transits to the streamer. This is explained by insufficient plasma density of a corona in order to screen the applied voltage ($n_e \sim 10^{15}$ m^{-3}, $T_e \sim 1$ eV). This condition allowed the breakdown voltage to be defined as the voltage at which the corona-to-streamer transition occurs.

Figure 5.4(b) shows that for -12.5 kV, the corona is still observed. We see that the electron density increases to the value $\sim 10^{17}$ m^{-3} which is still not enough to screen the applied voltage. At the same time, Fig. 5.5(b) shows

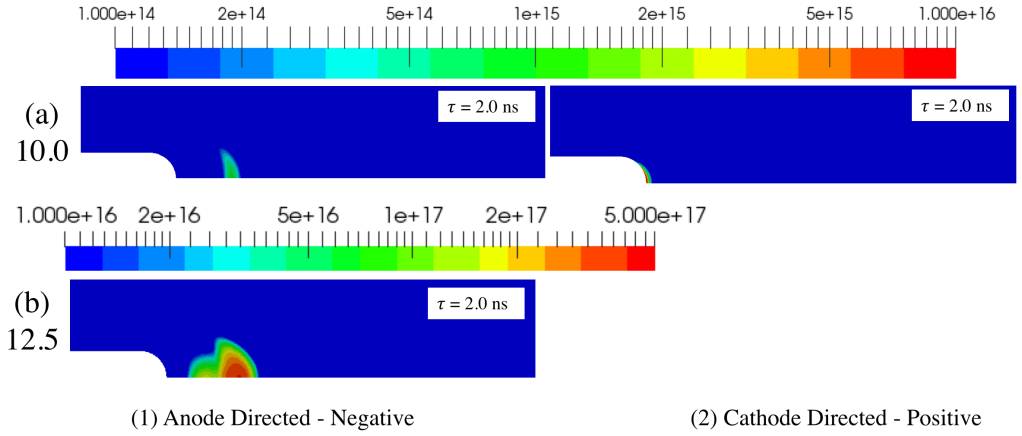

Figure 5.4: Electron density (in m^{-3}) contours for anode and cathode directed streamers as a function of the DC voltage. A corona discharge is observed at voltages below 15 kV for negative polarities, and voltages below 12.5 kV for positive polarities. Coronas are characterized by a low electron density. The time (τ) in the top corner corresponds to the integration time for the electron density snap-shot presented.

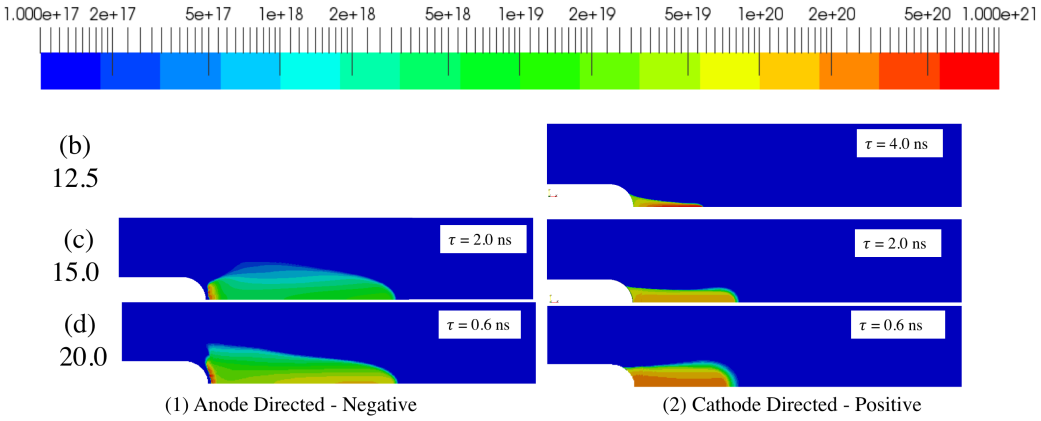

Figure 5.5: Electron density (in m^{-3}) contours for anode and cathode directed streamers as a function of the DC voltage. Corona discharge are observed at voltages below 15 kV for negative polarities, and voltages below 12.5 kV for positive polarities. Coronas are characterized by a low electron density. The time (τ) in the top corner corresponds to the integration time for the electron density snap-shot presented.

the streamer propagating from the anode to the cathode for 12.5 kV. Thus, this voltage can be defined as the breakdown voltage for the cathode-directed streamer. The cathode-directed streamer has the peak of electron density $\sim 10^{20}$ m^{-3} in the streamer body, which is $\sim$4 orders of magnitude greater than that for corona. Figure 5.5(c) shows that at 15 kV a streamer is obtained for both polarities. This voltage is used to define the anode-directed streamer breakdown voltage.

The electron density and temperature for each voltage and polarity are summarized in Table 5.1 and Figures 5.4, 5.5, 5.6, and 5.7. The electron density is measured in the tail of the streamer. If a corona is present, the spatially averaged density is used. When a streamer is present the peak electron temperature along the axis of symmetry in the head and the average electron temperature along the axis of symmetry in the tail are quoted. If a corona is observed the electron temperature is defined at the peak electron density. It is concluded that in the cathode-directed corona, the temperature varies in the range $\sim$1-10 eV. Comparing Fig. 5.6 and 5.7 with Fig. 5.4(a) that the peak of T_e for cathode-directed streamers corresponds to the peak of the electron density. It is also observed that the peak electron temperature occurs at the electrode tip regardless of voltage polarities (Fig. 5.6 and 5.7), but the location of peak electron density depends upon the polarity.

An anode-directed corona tends to be more diffuse and offset from the electrode. Again, peak electron temperature ($\sim$4 eV) is observed at the cathode tip (Fig. 5.4 and 5.7), but it does not correspond to the peak electron

Voltage (kV)	n_e (m^{-3})	T_e(eV) Head	T_e(eV) Tail
	Anode-Directed		
10	1.5×10^{15}	4 (Corona)	
12.5	3.8×10^{17}	3-4 (Corona)	
15	6.8×10^{18}	7.7	3.0
20	9.2×10^{19}	12.95	3.5
	Cathode-Directed		
10	2.5×10^{15}	7.6 (Corona)	
12.5	6.3×10^{20}	9.5	0.34
15	1.6×10^{20}	10.9	0.35
20	2.1×10^{21}	11.45	0.98

Table 5.1: Electron temperature and density as a function of voltage and polarity. All tests correspond to a pressure of 202.6 kPa.

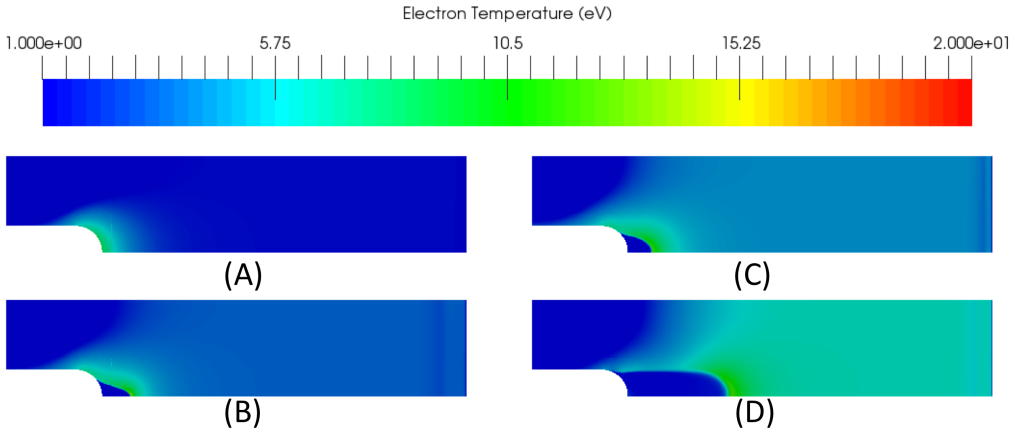

Figure 5.6: Electron temperature (in eV) contours for cathode-directed streamers as a function of the DC voltage. Corona discharge are observed at voltages of 10 kV (A). Streamers are observed for 12.5 kV (B), 15 kV (C) and 20 kV (D).

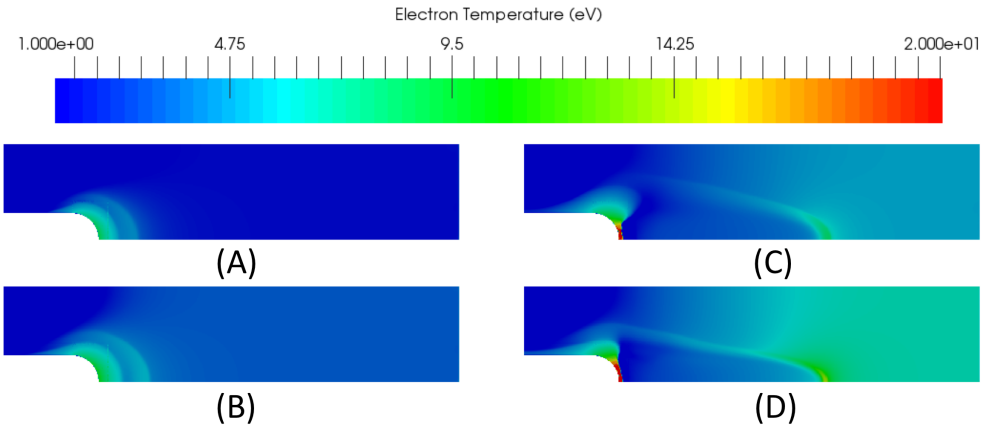

Figure 5.7: Electron temperature (in eV) contours for anode-directed streamers as a function of the DC voltage. Corona discharge are observed at voltages of 10 kV (A) and 12.5 kV (B). Streamers are observed for 15 kV (C) and 20 kV (D).

density. The peak electron density is observed to be offset from the electrode [Figs. 5.4(a) and (b)].

The simulations have shown that the electron temperature in the streamer head and tail vary significantly depending on the magnitude and polarity of the voltage, as shown in Fig. 5.1 and 5.12 and Table 5.1. The electron temperature in the cathodic streamer heads is ∼9-12 eV, with a much lower value ∼0.3-1.0 eV in tail. Anodic streamers also show a wide variability in the streamer temperature at the head (∼7-13 eV). Additionally, the anodic streamer tail is considerably hotter (∼3-4 eV) compared to the cathodic streamer. The increase of T_e for increasing gap voltage is explained by the increasing electric field in front of the streamer and in the streamer tail.

Figure 5.8 shows the streamer velocity (a) and diameter (b) as the func-

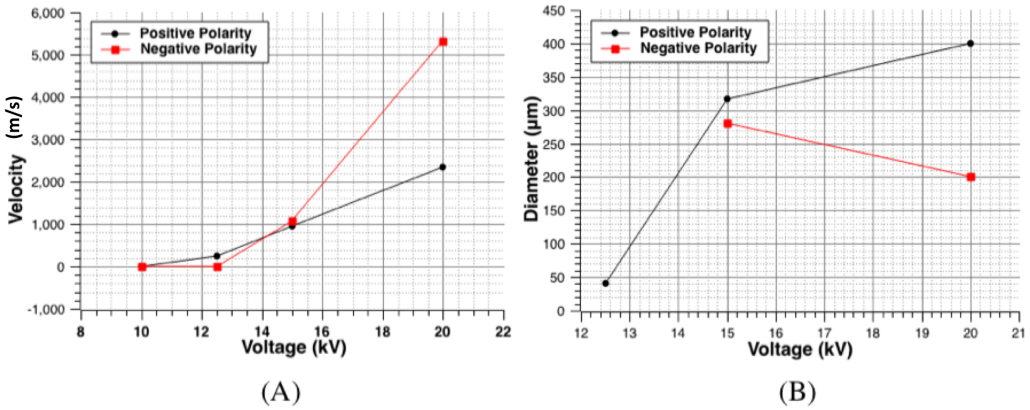

Figure 5.8: The streamer velocity (A) and diameter (B) as a function of voltage and polarity.

tion of the voltage magnitude and polarity. For the cathode-directed streamers the velocity increases with voltage with values ranging from 200 km/s to 2200 km/s. Once the anodic streamer is formed the velocity is greater than that of the cathodic one for the same voltage. Figure 5.4 and 5.5 shows that an increase in the gap voltage leads to a decrease of the diameter of the anodic streamer. As a consequence, the electric field at the head of the anode-directed streamer increases. The opposite effect is obtained for the cathode-directed streamer (Fig. 5.4 and 5.5). The increase of the diameter and decrease in the electric field leads to a slower increase in the velocity as a function of voltage.

As follows from the previous discussion, the electron temperature is high at the streamer head and is small in the streamer tail (Fig. 5.6 and 5.7). At the same time, the electron density is higher in the streamer body than at the head (Fig. 5.4 and 5.5). Thus, it is concluded that the propagation of the streamer head through the cathode-anode gap is accompanied by the electron

impact ionization and dissociation of CO_2. The primary reaction leading to the plasma generation at the streamer head is (Fig. 5.10):

$$CO_2 + e \rightarrow CO_2^+ + 2e \tag{5.1}$$

while the primary dissociation reaction is (Fig. 5.10):

$$CO_2 + e \rightarrow CO + O + e \tag{5.2}$$

Both reactions have high energy thresholds (13.3 eV and 10.0 eV, respectively) and are very efficient at the streamer head. This is due to the high electron temperatures at the streamer head (O(10 eV)) (Fig. 5.6 and 5.7). The electrons generated in the streamer head are sustained by electrons with $T_e \sim$1 eV in the streamer tail. The comparison between the calculated rate coefficients of reactions 5.1 and 5.2 show that the former is the dominant reaction for $T_e >$4 eV, i.e. at the streamer head.

It is seen in Fig. 5.9 that in the streamer tail the dominant positive ion species are $C_2O_4^+$. They are generated from CO_2^+ in the three-body reaction 5.3 where CO_2^+ is primarily produced in the streamer head as seen in Fig. 5.9 and 5.10:

$$CO_2^+ + CO_2 + CO_2 \rightarrow C_2O_4^+ + CO_2 \tag{5.3}$$

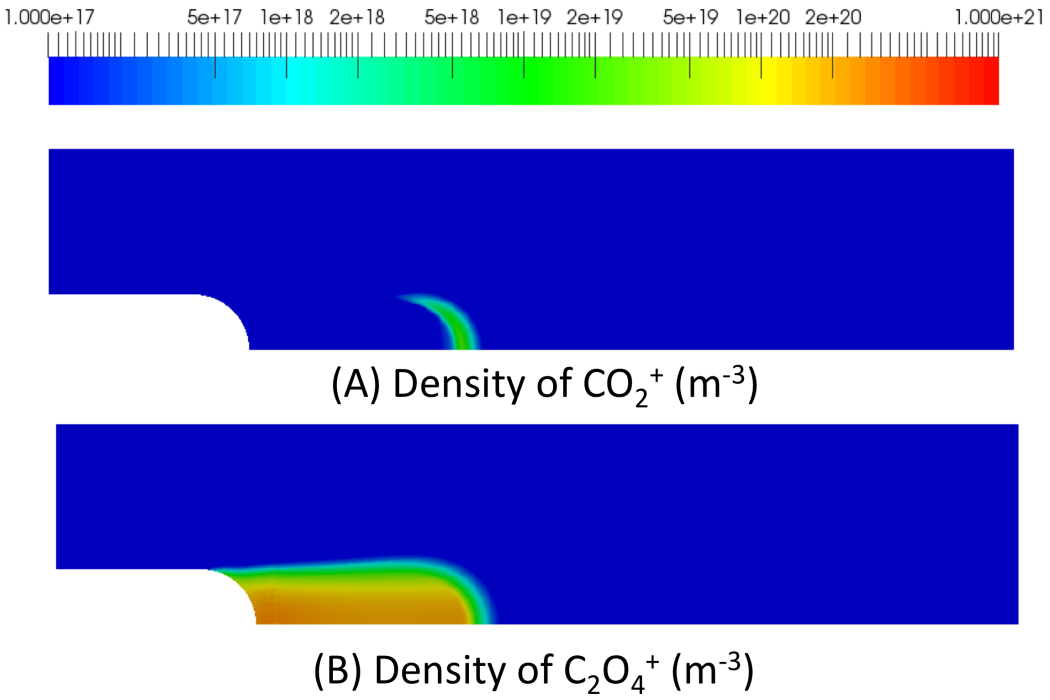

Figure 5.9: Contour plots of the density of positive ions CO_2^+ (A) and $C_2O_4^+$ (B) for a cathode-directed streamer discharge at 2 atm.

The density of $C_2O_4^+$ is ~2 orders of magnitude higher than the density of CO_2^+. Additionally, the generation of negative ions CO_3^- and O^- is observed in Fig. 5.11. Ions O^- are mainly generated in the streamer tail in the electron attachment reaction:

$$CO_2 + e \rightarrow CO + O^- \tag{5.4}$$

The rate coefficient of this reaction exceeds the rate coefficient of reaction 5.1 for T_e <4 eV, i.e. it is very efficient in the streamer tail. Ions CO_3^- are generated from O^- in reaction:

$$O^- + CO_2 + CO_2 \rightarrow CO_3^- + CO_2 \tag{5.5}$$

This reaction leads to two orders of magnitude larger density of CO_3^- than the density of O^-. However, it is important to note that regardless of the streamer polarity the density of negative ions is much smaller (1-2 orders of magnitude) than the density of positive ions. Additionally, in both cathode and anode directed streamers the dominant negative ion density (CO_3^-) is comparable (10^{18} m^{-3}) (compare Fig. 5.11 and 5.12), whereas the dominant positive ion density ($C_2O_4^+$) varies by an order of magnitude depending upon the polarity: cathode-directed 10^{20} m^{-3}, and anode-directed 10^{19} m^{-3} (compare Fig. 5.9 and 5.12).

It is concluded that the streamer head is an ionizing plasma region while the streamer tail is a recombining plasma region. The higher positive

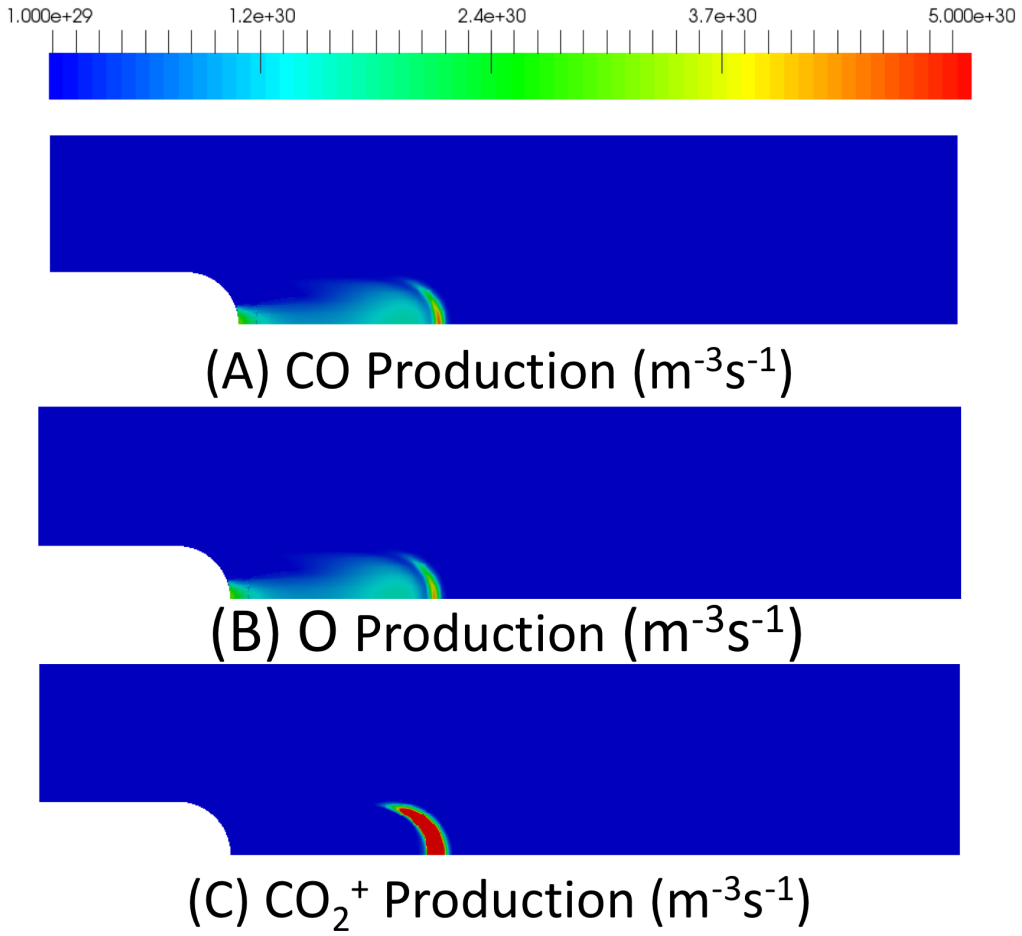

Figure 5.10: Contour plots of the production rate of CO (A), O (B), CO_2^+ (C) for a cathode-directed streamer discharge at 2 atm.

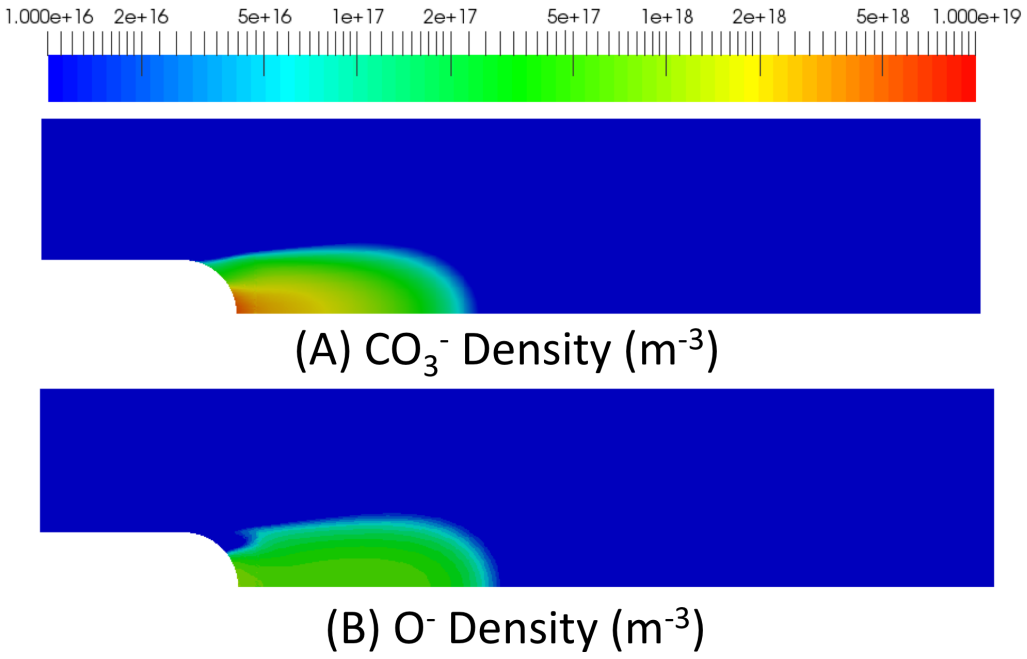

Figure 5.11: Contour plots of the density of CO_3^- (A), and O^- (B) for a cathode-directed streamer discharge at 2 atm.

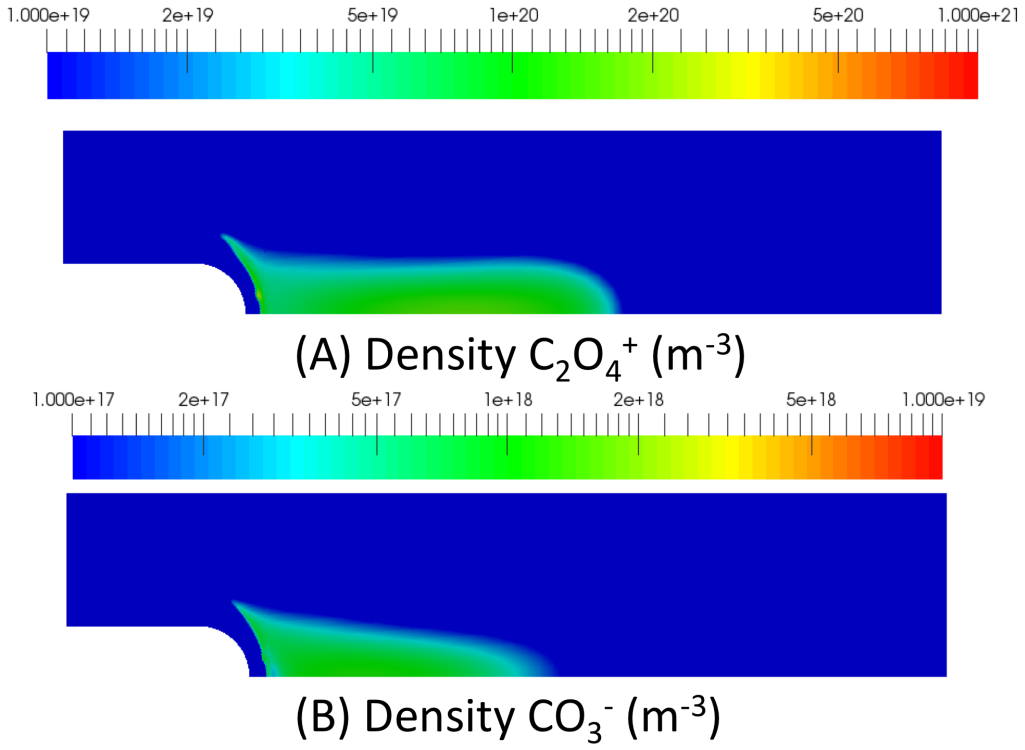

Figure 5.12: Contour plots of the density of CO_3^- (A), and O^- (B) for a anode-directed streamer discharge at 2 atm.

ion densities in the cathode-directed streamer are directly related to higher electron densities which are attributed to the polarity of the streamer head. Therefore, it is desirable to have a cathode-directed (positive) streamer for the production of excited species (specifically vibrationally excited states) in the streamer tail since these states are populated by direct electron impact reactions by low energy electrons.

The simulation results have shown that on the nanosecond time scale the density of vibrationally excited CO_2 reaches $\sim 10^{22} - 10^{23}$ m^{-3} (see Fig.

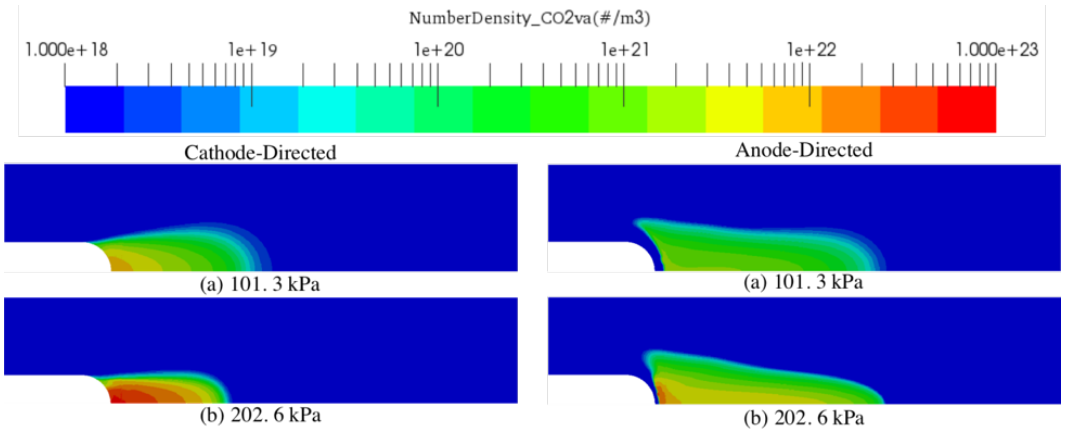

Figure 5.13: Contour plots of the density of the first symmetric vibrationally excited CO_2 (in m^{-3}) level for both streamers at the pressure of 101.3 kPa and 202.6 Pa.

5.13). The density of these excited species is two orders of magnitude larger than the density of other excited species (e.g., O). This is explained by the high values of the rate coefficients of vibrational excitation reactions in the temperature range 1-3 eV. It is determined from Fig. 5.13 that the cathode-directed streamer is more efficient for the generation of vibrationally excited CO_2. This is explained by more favorable electron temperature in the streamer tail for this streamer, and the higher electron density (see Table 5.1 and Fig. 5.3, 5.4, and 5.5).

5.3 Vibrational Population Distribution and Conversion Efficiency

Figure 5.14 shows several contour plots of the low lying vibrational levels for a positive (cathode-directed) streamer discharge at standard temperature and pressure. The first four degenerate symmetric stretch levels which

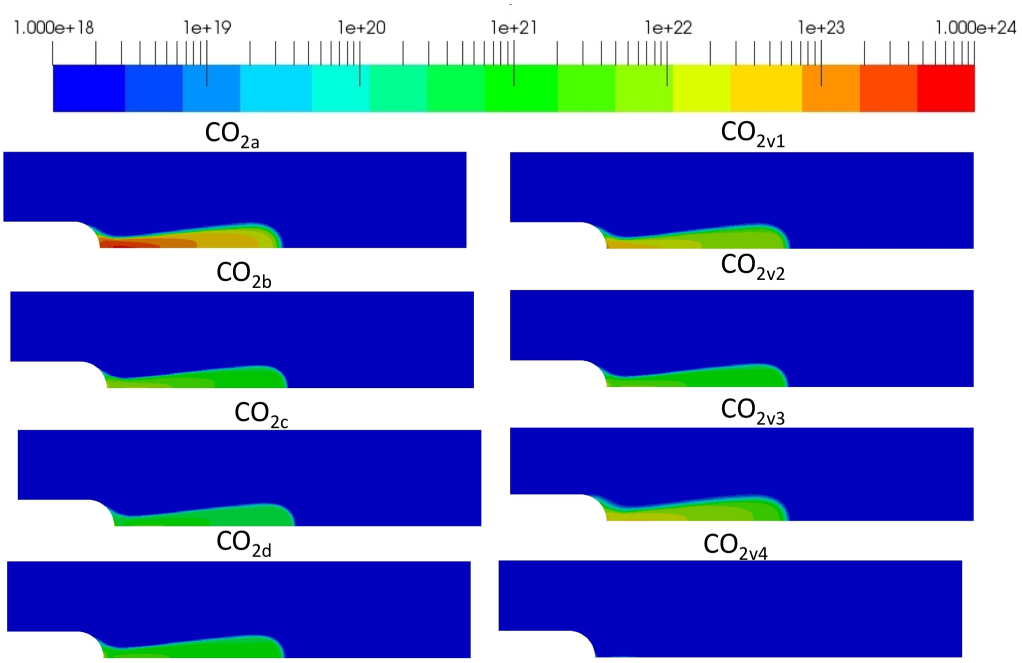

Figure 5.14: Contour plots of the low lying vibrationally excited CO_2 levels (in m^{-3}) in a cathode-directed streamer.

include the resonant bending levels are denoted as CO_{2a-d} where CO_{2va} is the (0, 1, 0) level, CO_{2vb} is the sum of the (0, 2, 0) + (1, 0, 0) states, CO_{2vc} is the sum of the (0, 3, 0) + (1, 1, 0) states, and CO_{2vd} is the sum of the (0, 4, 0) + (1, 2, 0) + (2, 0 ,0) states. The first four asymmetric stretch levels indicated by numbers (1-4) are also plotted in Fig. 5.14. The first four symmetric levels (a-d) have vibrational excitation energies of 0.08, 0.17, 0.25, and 0.33 eV, and the first four asymmetric levels have vibrational energies 0.29, 0.58, 0.86, and 1.14 eV.

During a single streamer discharge, the symmetric mode is preferentially populated with the highest density occurring in the first symmetric vi-

brational level. In addition, only the first three excited states of the asymmetric stretch vibrational mode are populated by the streamer discharge. The peak densities for all vibrational levels in both modes are observed near the electrode tip which is characterized by high electron densities, and low (1-3 eV) plasma temperatures.

In the streamer head, where electron temperatures are high ($\sim$ 10 eV), the vibrational populations are at a minimum. Therefore, the streamer tail is the most efficient region for populating the low lying vibrational levels. However, due to the transient nature of the streamer discharge and low density of vibrational states, a multitude of streamers is necessary to have successful vibrational pumping of the low lying vibrational states.

The asymmetric stretch vibrational temperature is estimated from the population of the low lying vibrational levels. Assuming a Boltzmann distribution of the excited states, the vibrational temperature (T_v) is determined from the density ratio of the first two asymmetric vibrational levels, given by Eq. 5.6 where N_1 $(0, 0^0, 1)$ and N_2 $(0, 0^0, 2)$.

$$T_v = -\frac{E_v}{k_B \ln(\frac{N_2}{N_1})} \tag{5.6}$$

where the density of the vibrational states are given by N_i, and E_v is the vibrational energy of the asymmetric stretch mode. The vibrational temperature is estimated to be $\sim$ 4900 K.

Figure 5.15 shows the CO, O, and O_2 densities. The CO and O densities

are two orders of magnitude lower than those of the vibrationally excited states of CO_2, while molecular oxygen is three orders of magnitude lower. Additionally, the O_2 distribution is localized with peak densities in the region furthest from the streamer head. This indicates that the region near the electrode is a recombination zone, while the streamer head is responsible for ionizing and dissociation reactions.

Therefore, the primary mechanism for CO and O formation in the streamer is due to direct electron impact dissociation in the head (refer to Fig. 5.10), $e + CO_2 \rightarrow CO + O + e$. This results in a low overall conversion of CO_2, $\frac{N_{CO}}{N_{CO_2}} = 0.01$ %. To increase the conversion rate for streamer discharges, the population of the low lying vibrational levels must be increased so that vibrational ladder climbing is possible, $CO_{2v1} + CO_{2v1} \rightarrow CO_{2v2} + CO_2$. Vibrational ladder climbing is not possible for single streamer discharges, as indicated by Fig. 5.14, but the presence of several streamers in a DBD reactor will be able to populate the low lying vibrational levels and increase the total conversion.

5.4 Afterglow

A streamer discharge is a fast transient ionization wave lasting approximately 1-3 ns. At these time scales only electrons are capable of responding, therefore the primary reaction kinetics in a streamer are attributed to electron impact excitations. The relaxation processes in a streamer occur in the afterglow at timescales of the order microseconds. To simulate at these timescales

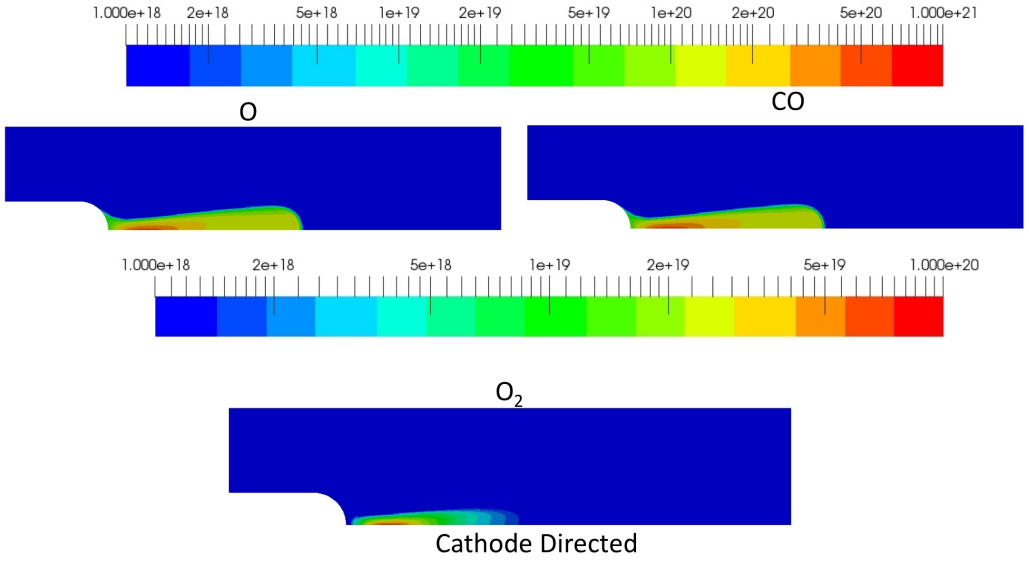

Figure 5.15: Contour plots of the CO, O and O_2 densities (in m^{-3}) for cathode-directed streamer.

using a plasma fluid model is not feasible, so a 0D model was formulated by neglecting the spatial terms in the plasma fluid model equations. The 0D model is used to investigate the afterglow of the streamer discharge, and the relaxation of the vibrational population distribution, Fig. 5.14.

To simulate the afterglow in the 0D model an external power source is needed which replicates the energy deposited by a streamer discharge. The external power term for the zero dimensional model is determined from the 2D plasma fluid model by measuring the temporal evolution of the electron Joule heating at a fixed spatial location. The resulting pulse profile is fitted and used as the input power for the 0D model. The 0D models is run for 1 atm. and 300 K.

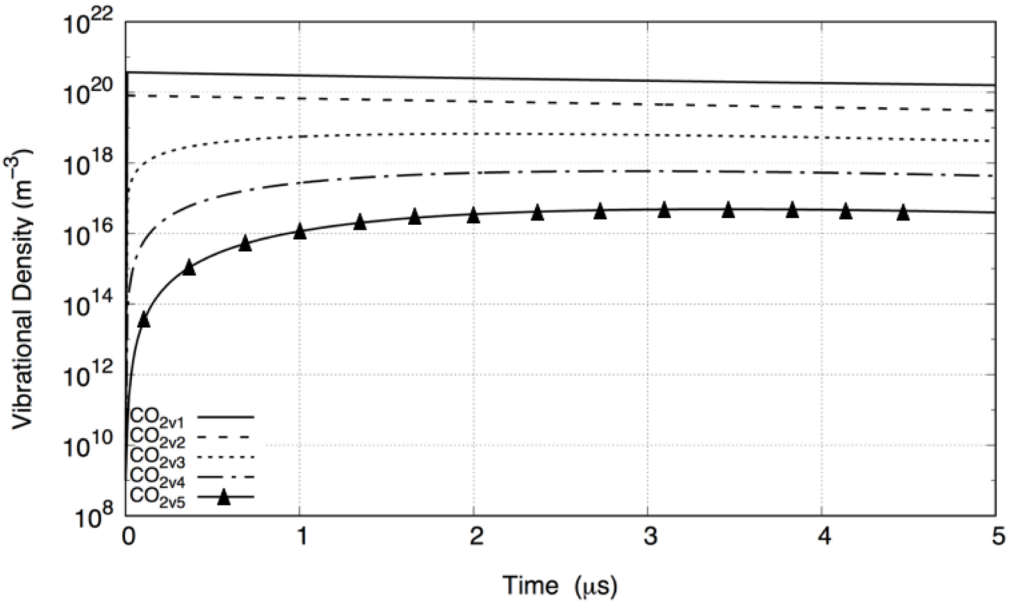

Figure 5.16: A 0D simulation of the afterglow of a streamer discharge showing the population of the first five asymmetric vibrational levels of CO_2 (in m^{-3}). The top solid line corresponds to the first asymmetric vibrational level, and bottom solid line corresponds to the fifth vibrational level.

The resulting power pulse is a Gaussian profile with a FWHM of 0.1 ns and a peak power density of $5x10^{12}$ Jm^{-3}. In the first few nanoseconds after the applied power pulse the electron temperature relaxes to the background gas temperature, while the electron density decreases by an order of magnitude in the first microsecond. Therefore, the afterglow is governed by the chemical kinetics of the bulk excited species, and electron impact reactions which were dominant in the streamer excitation phase play a minimal role.

Figure 5.16 shows the vibrational relaxation of the first five asymmetric stretch levels of CO_2. The first two vibrational levels are populated within

the first 3 ns due to electron impact collisions during the streamer discharge phase, after which they exhibit monotonic decay. The higher vibrational levels ($CO_{2v3\text{-}5}$) reach their peak density in the first 3 microseconds of the afterglow. Furthermore, as the vibrational quantum number increases the density of the state decreases, and the peak density is shifted further in time.

The monotonic decay (refer to Fig. 5.17) of the first two vibrational levels and shift of the peak density of higher vibrational levels in time is explained by the vibrational ladder climbing mechanism, given by Eq. 5.7

$$\begin{aligned} CO_{2v1} + CO_{2v1} &\rightarrow CO_{2v2} + CO_2 \\ CO_{2v2} + CO_{2v2} &\rightarrow CO_{2v3} + CO_{2v1} \\ CO_{2v3} + CO_{2v3} &\rightarrow CO_{2v4} + CO_{2v2} \\ &\dots \end{aligned} \tag{5.7}$$

for single quantum vibrational exchange. The first two vibrational levels CO_{2v1} and CO_{2v2} are populated directly by the streamer discharge, while the population of subsequent vibrational levels (v_j) depends upon the density of the adjacent lower vibrational level (v_{j-1}) and the collision frequency. Hence, as seen in Fig 5.17, as the first two vibrational populations are depopulated their energy is transfered to higher vibrational levels resulting in an increase of the adjacent upper vibrational level.

Though a single streamer does populate the low lying vibrational levels, there isn't sufficient density of the first level for the high lying vibrational states to be populated through VV relaxation. Additionally, there is no re-

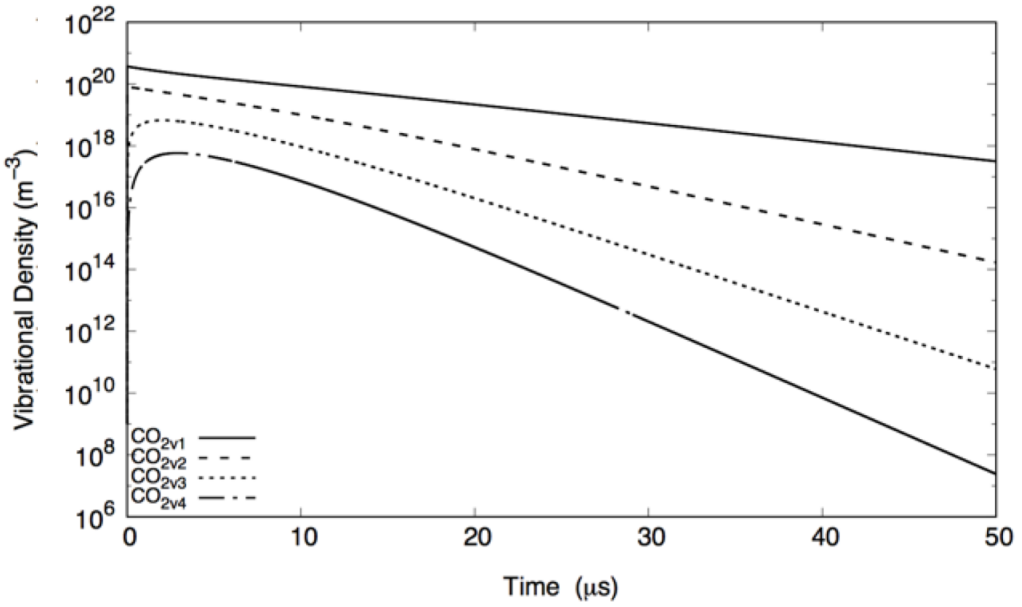

Figure 5.17: A 0D simulation of the afterglow of a streamer discharge showing the population of the first four asymmetric vibrational levels of CO_2 (in m^{-3}), showing the monotonic decay of the vibrationally excited states.

population of the low lying levels from electron impact reactions. Therefore, multiple streamers are necessary to pump higher vibrational states.

Chapter 6

Experimental Results

In this section, the experimental results are presented and analyzed using the fluid model results presented in the previous section.[1] The discharge electrical properties were diagnosed with time resolved voltage and current (V-I) measurements. These V-I measurements were correlated with instantaneous broadband images, and instantaneous narrowband images. The image sequences showed the dynamical behavior and distribution of excited species as a function of the electrical pulse characteristics. Optical emission spectroscopy was conducted and the plasma properties determined: electron temperature and density, vibrational temperature, rotational temperature, and conversion percentage.

6.1 Electrical Discharge Characteristics

In the reverse dump configuration described earlier, a negative HV pulse is generated once the spark-gap is triggered and breakdown occurs. This

[1]Some of the following work has already been published in: Pachuilo MV, Levko D, Raja LL, Varghese PL. Experimental and Numerical Investigations of a Pulsed Nanosecond Streamer Discharge in CO2. In 55th AIAA Aerospace Sciences Meeting 2017 (p. 1968). The author was the main contributer to this work. Dr. Raja and Dr. Varghese advised this work and Dr. Levko helped in development of the chemical mechanism.

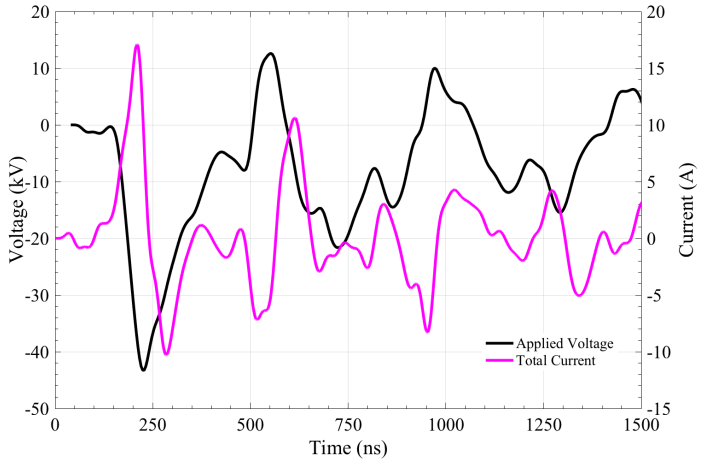

Figure 6.1: The voltage and current measured for the discharge voltage 38 kV. The solid black line indicates the voltage measured across the discharge gap, and the solid magenta line shows the total current measured on the ground electrode. Reflected pulses are observed every ∼300 ns.

negative HV pulse then travels down a ∼30 m transmission delay line. The delay line imparts ∼150 ns worth of delay and expands the initial pulse shape in time due to the line inductance (∼60 μH). Figure 6.1 shows the V-I characteristics as a function of time for a discharge voltage of 38 kV. The voltage is measured across the chamber electrodes while the current is measured at the ground electrode.

The initial voltage pulse can be estimated from discharge resistor (174 Ω) and capacitor (2100 pF) and given by the time constant $\tau = RC$, which gives a decay time of ∼365 ns. The rise time is determined from the inductance of the reverse dump system once the spark-gap is triggered [see Fig. 3.3(a)]. These parameters determine the pulse V-I characteristics if there was no delay line. In Fig. 6.1, several voltage pulse oscillations are observed. This

circuit ringing occurs due to the transmission line inductance, as well as the impedance mismatch once the voltage pulse reaches the discharge chamber.

The discharge chamber impedance prior to the plasma formation is an open circuit with a characteristic capacitance, while the impedance of the transmissions line is $\sim$50 Ω. When the HV pulse reaches the discharge chamber, a portion of the RF wave is reflected down the transmission line leading to the under-damped system response observed in Fig. 6.1. Furthermore, the chamber effective capacitor begins charging until the breakdown voltage is reached and initially insulating gas begins to conduct.

At the breakdown voltage, a plasma is formed within the chamber gap which alters the circuit impedance. The total current measured in Fig. 6.1 accounts for both the discharge current and the displacement current. To define the discharge current, the system electrical parameters must be determined without a discharge. From the differences in the circuit impedance when there is no discharge and when plasma is formed, the discharge current can be estimated.

The voltage was measured across the electrode gap and the current was measured on the grounded electrode [see Fig. 3.3(a)]. The current measured at the grounded electrode accounts for the total discharge current (i_{tot}) which is a combination of the displacement current (i_{Disp}) and the discharge current (i_{Dis}) as given by:

$$i_{tot} = i_{Disp} + i_{Dis} \tag{6.1}$$

The displacement current arises due to the electrical impedance of the system, namely, the stray capacitance. It does not indicate the current carried by the streamer formed during the breakdown. In order to calculate the discharge current, the displacement current is estimated as:

$$i_{Disp}(t) = \frac{\int_0^t C(\tau)\frac{dV}{dt}(t-\tau)d\tau}{\int_0^t d\tau} \tag{6.2}$$

Here, C is the effective capacitance of the system, and $\frac{dV}{dt}$ is the time rate of the voltage change. Equation 6.2 is a convolution integral.

The electrical properties of the system used in Eq. 6.2 can be determined when the discharge current in Eq. 6.1 is set to zero. The measured current is then equal to the displacement current and Eq. 6.2 can be evaluated by performing a Fourier transform of Eq. 6.2. The transfer function $C(\omega)$ is given as:

$$C(\omega) = \frac{F[i_{Disp}(t) = i_{Tot}]}{F[\frac{dV}{dt}(t)]}\Delta t \tag{6.3}$$

where ω is the frequency, Δt is the integration time, and F indicates the Fourier transform operator.

The transfer function was determined from a test case which minimized the observed discharge. Figure 6.4 shows a set of instantaneous broadband

images taken at various voltage and pressure conditions (see discussion below). When the chamber is pressurized to two atmospheres and charged to the minimum voltage for the spark-gap to breakdown (12.5 kV) a low luminosity localized corona is observed at the HV electrode [see Figs. 6.4(c) and (d)]. These conditions are used as the no discharge case to characterize the electrical transfer function of the system.

Figure 6.1 shows the V-I waveforms for a single pulse. The pulse is divided into two phases based on the type of streamer discharge, namely, anode- or cathode-directed one. Anode- and cathode-directed streamers have different dynamics and properties (see previous section). Since the streamer always originates at the exposed electrode for all voltages above the breakdown threshold (Fig. 5.1), the anode- and cathode-directed phases are defined based upon the voltage of the exposed electrode.

Figure 6.2 shows the average voltage and current waveforms from 30 independent test cases for both negative [Figs. 6.2(a) and (b)] and positive [Figs. 6.2(c) and (d)] polarities. The pressure is 101.3 kPa. In Fig. 6.2, two discharge voltages are shown: 12.5 kV [(a) and (c)] and 38 kV [(b) and (d)]. The solid black lines are the applied voltage, the solid blue line shows the total discharge current, the dot-dashed red line indicates the displacement current, and the dotted green line indicates the discharge current calculated from the above relations. A positive current corresponds to positive electron flow towards the ground electrode.

For the voltage of 12.5 kV [Figs. 6.2(a) and (c)], the total measured

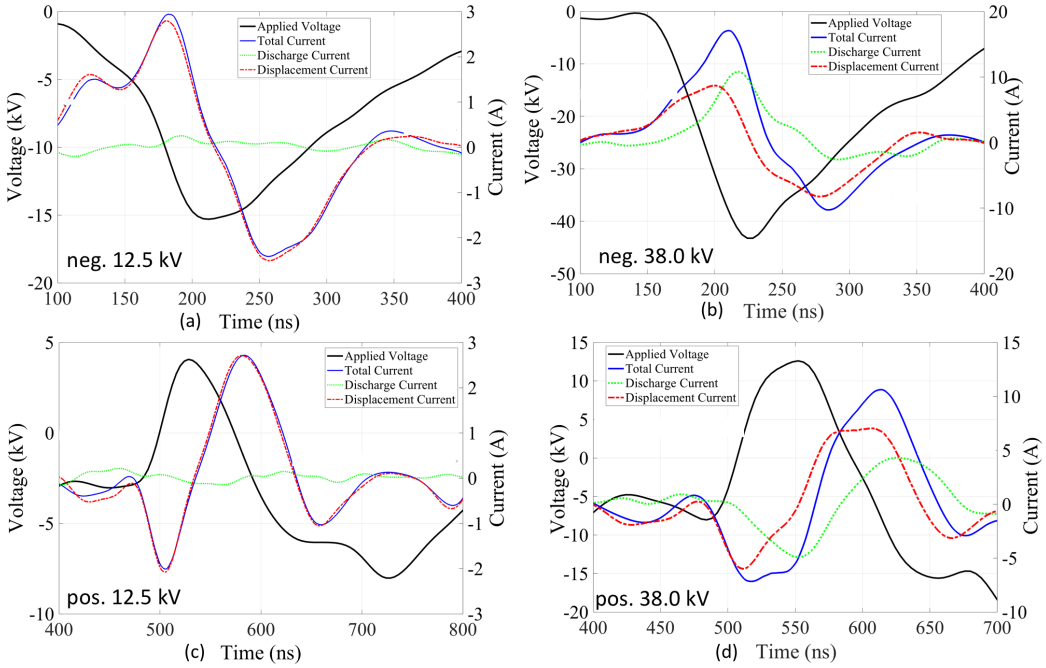

Figure 6.2: The voltage and current waveforms at charge voltages of (a,c) 12.5 kV and (b,d) 38 kV. All waveforms are taken at 101.3 kPa. The solid black lines are the measured voltage across the electrodes, and the solid blue lines are the total measured current on the grounded electrode. The red dash lines are the displacement current calculated from the systems electrical transfer function $C(\omega)$, with no discharge, and the time derivative of the applied voltage. The dotted green lines are the discharge current which is calculated from the total measured current and the displacement current. Each waveform is determined from the average of 30 independent test trials. A positive current corresponds to electron flow to the ground electrode.

current is determined predominantly by the displacement current. A non-zero discharge current is registered in the negative cycle as the displacement current deviates from the total measured current [see Fig. 6.2(a)]. The voltage at which the displacement current begins to deviate from the total measured current is defined as the corona onset voltage for the negative polarity. If the voltage does not exceed this level the corona will never transition to a streamer. The corona onset voltage is determined to be -10 kV for a pressure of 101.3 kPa (Fig. 6.2(a)).

As the discharge voltage increases two discharges are possible: a streamer or a corona with conductivity greater than the base case at 200 kPa. A streamer will form once the corona has sufficient space charge to shield the applied field. For voltages below this condition, known as Meek's criterion, a corona will be observed. Therefore, to determine the type of discharge instantaneous broadband images must be correlated with the V-I characteristics.

The comparison between Figs. 6.2(a) and 6.4(B) (averaged) shows that a low-luminosity corona discharge is observed, but the single transient image Fig. 6.4(A) shows that a faint streamer discharge is observed. The averaging of the images spatially integrates the discharge, and when low luminosity streamers are present only the corona region at the electrode tip is imaged. This is caused by the stochastic nature of the streamer discharge. Therefore, at voltages near breakdown, the single frame images provide a better determination of the discharge state (Corona or Streamer).

In the negative cycle of the discharge Figs. 6.2(a) and 6.4(B), the

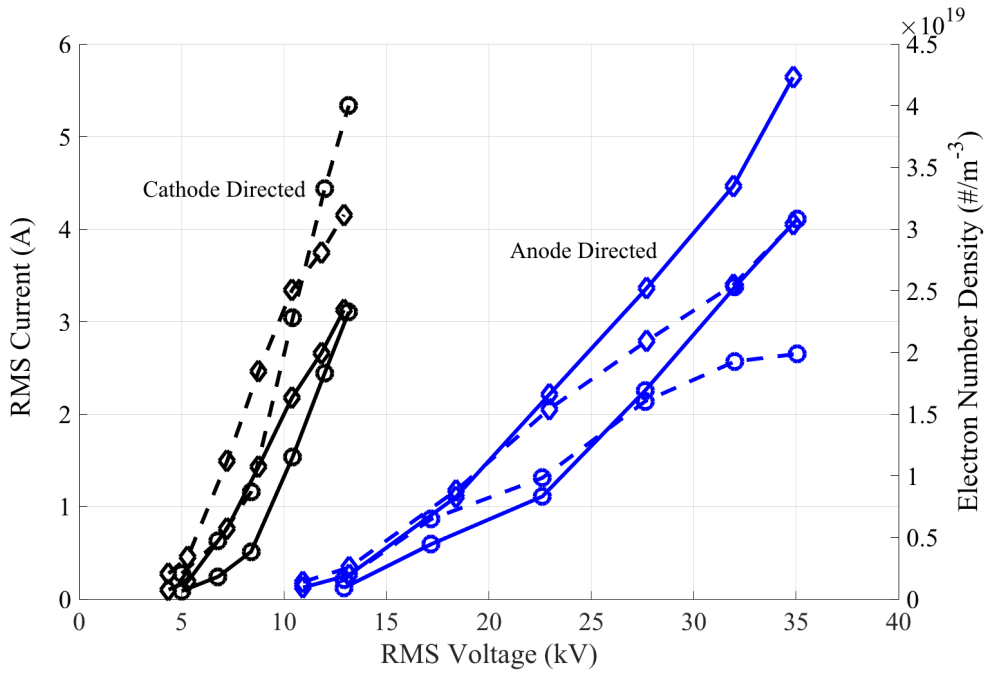

Figure 6.3: The root-mean-square (RMS) current (left) and electron number density (right) as a function of the RMS voltage. Solid lines indicate RMS current while dashed lines indicate electron density. Black lines are for the cathode-directed streamers, and blue lines are for the anode-directed streamers. Circle markers indicate two atmosphere tests while the diamonds are for one atmosphere tests.

filamentary structures observed in Fig. 6.4(A) will not form as these are characteristic of cathode-directed streamers. Therefore the registered current in Fig. 6.2(a) is attributed to the coronal glow at the electrode which has a greater conductivity than the 200 kPa base case.

Figure 6.2(c) shows the first positive V-I characteristics for the voltage of 12.5 kV [after the initial negative cycle shown Fig. 6.2(a)]. The current waveforms indicate that there is no discharge formed during the cathode-directed phase which implies that the voltage is below the cathode directed-

streamer breakdown voltage. However, in Figure 6.4(a,1), a filamentary streamer discharge is observed. These filamentary structures are associated with the cathode-directed streamers, while a diffuse discharge occurs during the anode-directed phase. Therefore, at these low voltages, the sensitivity and dynamic range of the current measurements are not able to distinguish between the displacement current and the current due to the cathode-directed streamer. The shot averaged images seen in Fig. 6.4(b,1) show that the observed radiation is in a small region near the electrode tip, typically characterized by a coronal discharge.

The V-I characteristics at a discharge voltage of 38 kV are shown in Figs. 6.2(b) and (d) for the anode- and cathode-directed phases, respectively. A significant deviation between the displacement and total measured currents is observed for both polarities. Furthermore, the discharge currents are an order of magnitude greater than in the case of corona [Figs. 6.2(a) and (b) from $\sim$1 to 10 A). Figure 6.4(a,7) shows a instantaneous broadband image integrated over the entire pulse (1500 ns) at the same conditions shown in Figs. 6.2(b) and (d). The radiation is more intense than that at the lower discharge voltage which corresponds to the increase in the discharge current. Additionally, cathode-directed streamers are observed during the positive cycle (filament structures).

The dissipated energy for each pulse is calculated by multiplying the discharge current by the voltage and integrating over the entire pulse duration. The deposited energy for the anode-directed streamers is found to vary signif-

icantly for the two pressures investigated. At 101.3 kPa the energy is ∼17.8 mJ, while at 202.6 kPa only ∼ 12.9 mJ is coupled into the discharge. For the cathode-directed streamers, the discharge energy is found to be independent of the pressure, with the energy being ∼4.0 mJ for both cases. Additionally, as the voltage is decreased the coupled energy into the discharge is reduced for the anode-directed streamers from ∼ 17.8 to 1 mJ. The deposited energy for the cathode-directed streamers showed minimal variation with voltage between ∼1.0-4.0 mJ.

6.2 Estimating Streamer Velocity From V-I Characteristics

The streamer velocity is estimated from the deviation of the discharge current and the streamer current. The discharge current is divided into three parts: (1) the streamer phase, (2) the current conduction and surface charging, and (3) the quench phase. To determine the streamer current, an expression is derived below for the alteration of the circuit impedance as the streamer transits the inter-electrode gap. After the streamer has bridged the gap forming a conduction pathway, the current increases and the dielectric surface is charged. As the dielectric is charged the effective electric field within the gap is reduced. This reduction in the electric field causes the discharge to quench. In this section an estimate for form of the streamer current is derived, and the velocity estimated.

As the streamer transits across the cathode-anode gap, it alters the

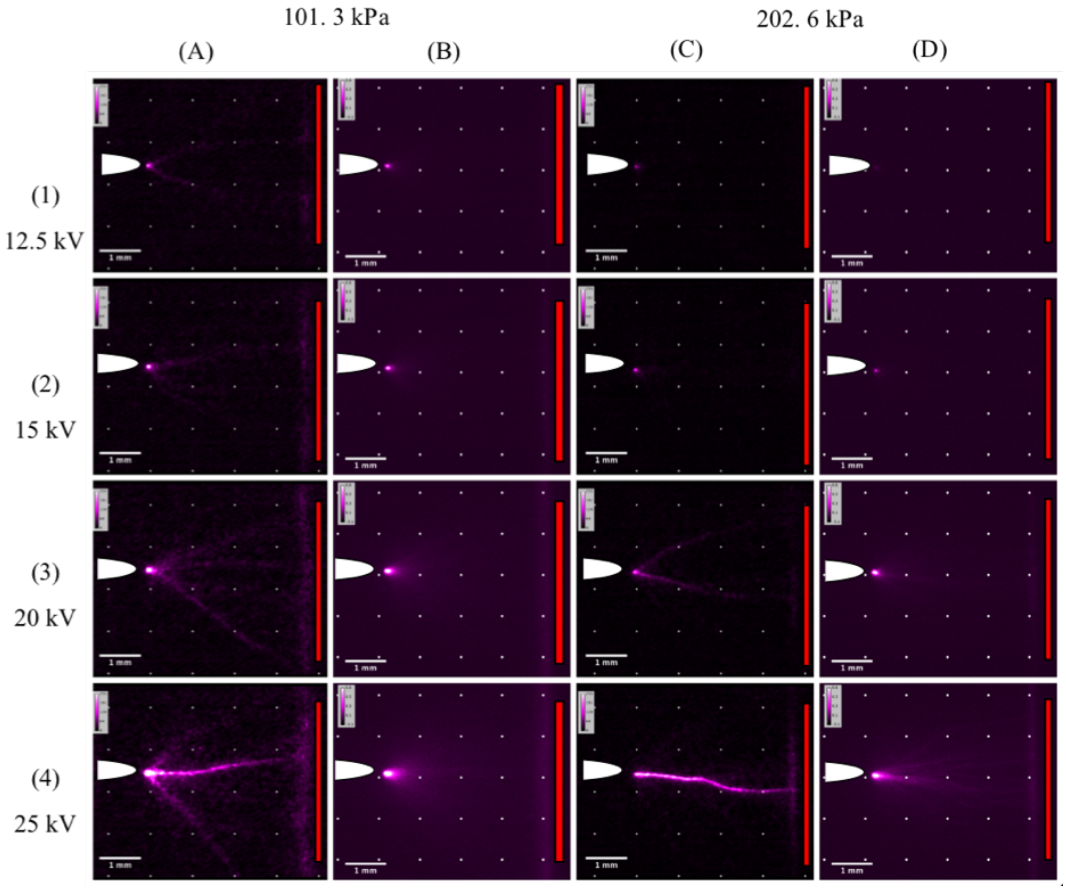

Figure 6.4: The effects of pressure and voltage on the discharge spatial evolution. Each image was taken with a camera gate time of 1500 ns for a inter-electrode spacing of 3.81 mm. The red rectangle indicates the location of the dielectric surface and the white point shows the location of the high-voltage electrode. The grid spacing is 1 mm. Columns A and B correspond to atmospheric pressure. Column A images are a single frame while column B are an average of 30 frames. Columns C and D are for a pressure of 202.6 kPa. Where column C is a single frame and column D consist of 30 frames averaged. Each row is for a different charge voltage as follows: 1-12.5 kV, 2-15 kV, 3-20 kV, 4-25 kV, 5-30 kV, 6-35 kV, 7-38 kV. The gain was held fixed for each frame for all test conditions, and the same image post-processing algorithms were used for each image. The dynamic range, brightness, and contrast were optimized for each image. The spectral range of the ICCD covers from 250 nm 900 nm with a peak quantum efficiency at 520 nm.

capacitance of the chamber. The time variation of the capacitance is estimated as:

$$C(t) = \frac{\epsilon_0 \epsilon_r A}{l} \frac{1}{1 - \frac{Vt}{l}} \tag{6.4}$$

Here, the streamer is assumed to act as parallel plate capacitor with a plate spacing that is a function of the streamer velocity (V), and the gap spacing (l). Additionally, A is the effective area, and ϵ_r is the relative permitivitty of the dielectric.

From the equations for the streamer capacitance and displacement current, an expression for the variation of the streamer current is found as a function of time. During the streamer transit time the voltage is assumed to be linear. The streamer current is then given as:

$$i_{streamer} = \frac{\epsilon_o \epsilon_r A}{l} \frac{dv}{dt} \frac{1}{1 - \frac{Vt}{l}} \tag{6.5}$$

Where, V is the velocity and it is assumed constant in the derivation, t is time, and $\frac{dv}{dt}$ is the time rate of change of the voltage assumed constant. The Taylor series expansion of Eq. 6.5 about zero gives:

$$i_{streamer} \approx A_o \left\{ 1 + \frac{V}{l} t + \left(\frac{V}{l} \right)^2 t^2 + ... \right\} \tag{6.6}$$

In the initial streamer phase, the current is assumed to follow the form of Eq. 6.6 with all the parameters in Eq. 6.5 are lumped into a single scaling constant A_o.

The streamer velocity is estimated assuming the streamer current follows a quadratic equation (Eq. 6.6). The streamer current is aligned with the discharge current and a least squares fit is done over the first 2 ns of the discharge. This time is selected based on the streamer velocities determined from simulations and the gap distance. The velocity is determined from the time it takes to bridge the inter-electrode gap and the inter-electrode distance. The time to bridge the inter-electrode gap is determined from the time of the initial current rise (t_1) and the time determined from the deviation of the discharge current and the streamer current (predicted by Eq. 6.6), t_2. With the known gap distance, l_1, the streamer velocity is estimated as $V = \frac{l_1}{t_2 - t_1}$ $\sim$580 $\pm$ 100 km/s at 2 atmospheres and discharge voltage of 38 kV.

6.3 Estimating Electron Density From V-I Characteristics

The electron density can be estimated from the streamer current and voltage characteristics. First the streamer current must be determined from the discharge current, and the breakdown field strength from the applied voltage. Once these are known, broadband images were used to determine the conduction area and streamer current density. The current density was then used as an estimate for the electron density. This procedure is outlined here and the results presented.

First, the root-mean-square (RMS) currents and voltages were calculated for each test condition. The RMS values represent averaged quantities

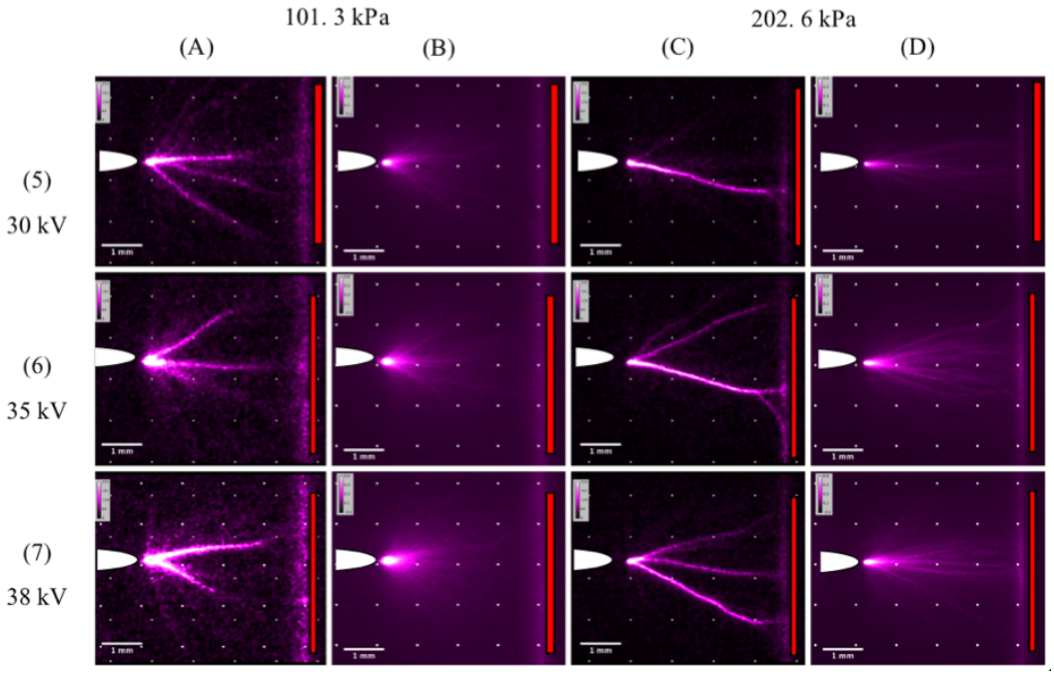

Figure 6.5: Fig. 6.4(Continued). Effects of pressure and voltage on discharge spatial evolution.

for each pulse and allow an average electron density to be estimated. The electron density is computed as:

$$j_{Dis} = \frac{i_{Dis}^{RMS}}{A_{eff}} = q_e n_e \mu_e E = q_e n_e V_d \tag{6.7}$$

Here, E is the electric field, and j_e is the current density given by the RMS discharge current i_{Dis}^{RMS} and the effective cross-sectional area A_{eff} of the discharge. The effective area is calculated based on the average streamer diameter determined from broadband images shown in Fig. 6.4. The diameter is assumed to be constant for both polarities but dependent on pressure.

The diameter at 101.3 kPa was determined to be 170 $\pm$ 32 μm while at 202.6 kPa it was 123 $\pm$ 28 μm. Section 6.5 describes the procedure for determining the streamer diameter. It could not be definitely concluded from the experiments that an increase in the gas pressure leads to a decrease in the streamer diameter due to the associated errors, but this result agrees with the numerical modeling results presented in the previous section. This effect is explained by the increasing breakdown electric field for increasing gas pressure. In order to obtain the higher electric fields for a given E, the streamer head radius must decrease for higher pressures.

The drift velocity,V_d, is tabulated as a function of the reduced electric field E/N [86–89]. The reduced electric field for each test condition is estimated based upon the RMS voltage (V_{RMS}) and electrode diameter (Ψ)as:

$$E \approx \frac{V_{RMS}}{\Psi} \tag{6.8}$$

The reduced electric field is calculated based on the above electric field and the background density. Figure 6.3 shows the RMS voltage and current, and the calculated electron number density.

As in the numerical modeling, the breakdown voltage (V_B) is defined as the voltage when a corona-to-streamer transition occurs. At voltages below V_B, a small current is registered due to the presence of the corona. Correlating instantaneous broadband images and the $V - I$ characteristics, the breakdown voltage is determined for both polarities. As shown in Fig. 6.3, the cathode-directed streamer has a lower breakdown voltage ($\sim$7.5 kV) compared to the anode-directed one ($\sim$17.5 kV) for both pressures. A similar trend was obtained in the fluid modeling (see previous section, Fig. 5.4) and in Ref. [34].

Figure 6.3 shows that for a given RMS voltage, the cathodic streamer electron density is greater than that of the anodic streamer which agrees with the results of our fluid simulations. The electron density is in the range $0.5 - 4.0 \times 10^{19}$ m^{-3}. At low voltages, the plasma density of both streamers for both pressures tends to the same value. This lower limit corresponds to a corona discharge, which remains localized around the high-voltage electrode.

For anodic streamers, the electron densities for all two atmosphere cases are always below that of the one atmosphere cases. Furthermore, the deviation between the densities for these two pressures increases with increasing voltages.

For both pressure cases, the anode-directed streamer RMS current and electron density tend to increase at decreasing rates as the RMS voltage is increased.

Cathodic streamers on the other hand, show an inversion of the electron density pressure dependencies at voltages above ∼10 kV. That is, at low voltages and high pressures (2 atm), cathodic streamers electron densities are lower compared to low pressure tests (1 atm). As the voltage increases, the deviations in electron densities decreases for the two pressures, until the two curves intersect (at ∼10 kV). After this point, the high pressure (2 atm) tests electron density is greater than the low pressure (1 atm) cases. The cathode directed streamers RMS current and electron density increase exponentially with the RMS voltage for high pressures. The low pressure tests show that at higher voltages the electron density begins to increase at decreasing rates.

6.4 Streamer Diameter and Branching as a Function of Gas Pressure, Voltage, and Polarity

Figure 6.4 shows a set of instantaneous broadband images taken for various voltages and pressures. Each image was taken with a 1500 ns gate time, with an inter-electrode spacing of 3.81 mm. At 1500 ns integration times, several positive and negative polarity voltage cycles are observed (Fig. 6.1). In each of the images, the red line indicates the location of the dielectric surface. The white object is used to show the approximate location of the high-voltage electrode. The columns correspond to the two pressures investigated: (a) and (b) for 101.3 kPa and (c) and (d) for 202.6 kPa. The first columns for

each pressure are a single image [(a) and (c)], while the second columns are a set of 30 median averaged images. Each row designates the corresponding discharge voltage at which each image was taken: 12.5, 15, 20, 25, 30, 35, and 38 kV.

The system electrical properties, $C(\omega)$ were determined at the pressure of 202.6 kPa and a discharge voltage of 12.5 kV. For these conditions, there is a low emission observed near the high-voltage electrode which corresponds to a corona discharge [Fig. 6.4(c,1)]. In the averaged set of images [Fig. 6.4(d,1)], no discharge is observed. This condition has been defined as the no discharge case. Even though there is a small discharge observed in Fig 6.4(c,1), the current and electron density associated with this discharge are assumed negligible.

At atmospheric pressure and 12.5 kV, the discharge is registered in both the single and integrated images [Fig. 6.4(a,1) and (b,1)]. In the single frame, a low-luminosity constricted cathode-directed streamer which bridges the inter-electrode gap is observed. The current measurements presented in Fig. 6.2(c) did not register a current during this phase of the discharge. This indicates that the anode-directed streamer at these low voltages did not have sufficient current to be registered with the instrumentation and calibration used. Furthermore, the average set of images shows only a localized corona discharge at the high-voltage electrode and no discharge on the dielectric surface.

As the voltage is increased for both pressures investigated, more fila-

mentary streamers are observed. Additionally, with the increase in voltage the emission of each discharge is increased as well as the measured current. For a constant background pressure and increased voltage more streamers are able to be formed during a given pulse. At any given voltage, the higher-pressure case has less numerous streamer discharges, with each being more emissive and constricted than the lower pressure case. From this set of images the streamer diameter, and branching angles are determined.

The streamer diameter is determined for each pressure and voltage condition. A single frame with 1500 ns gate time is used to estimate the streamer diameter for each set of conditions. When multiple streamer filaments are present, all diameters are estimated and an average for that pressure-voltage condition is used. The diameter is determined from the FWHM of the measured intensity profile for each streamer element. Then for each pressure all of the measured diameters for every voltage condition are averaged giving two effective diameters for each pressure condition. The diameters for the pressures 101.3 and 202.6 kPa are 170 μm $\pm$ 32 and 120 μm $\pm$ 28, respectively. At higher pressures the streamers diameter is reduced which agrees with the results of our fluid modeling.

The number of branching streamers for a given voltage condition is lower at higher pressures. Anodic streamers for these voltage-pressure conditions tend to remain in a diffuse mode and do not exhibit branching. This indicates that the reduced electric field is not high enough to support the branching of anode-directed streamers. Conversely, the cathode-directed streamers are

observed to show significant branching with multiple filamentary structures.

The branching angle is defined as the half angle between the two outer most streamers. The branching angle is estimated for each pressure-voltage condition. In Fig. 6.4 and 6.5 as the voltage is increased for both pressures the branching angle increases. Furthermore, after a critical voltage is reached, the branching angle tends to a constant value. At 38 kV and 101.3 kPa the branching angle is determined to be $\sim 45°$, while at 202.6 kPa the branching angle is $\sim 25°$. For a constant voltage, the high-pressure case is always observed to have a lower branching angle than the low-pressure case. Plasma fluid models can not predict branching, and particle in cell simulations are needed.

6.5 Streamer Dynamics as a Function of Polarity: Anode-Versus Cathode-Directed Streamers

Figure 6.6 shows the temporal evolution of the discharge through a sequence of broadband images. These images show the radiation of excited states emitting in the range of the CCD detector, 200-900 nm. Each image is an average of 32 independent frames taken with a gate time of 100 ns. The delay time, or location of each frame relative to the initiation of the voltage pulse, was varied. This produces a pseudo sequence of images in time which are used to analyze the evolution of the discharge with respect to the applied voltage. Figure 6.7 shows the location of each camera integration window with respect to the voltage pulse. All images were taken at the pressure of 202.6

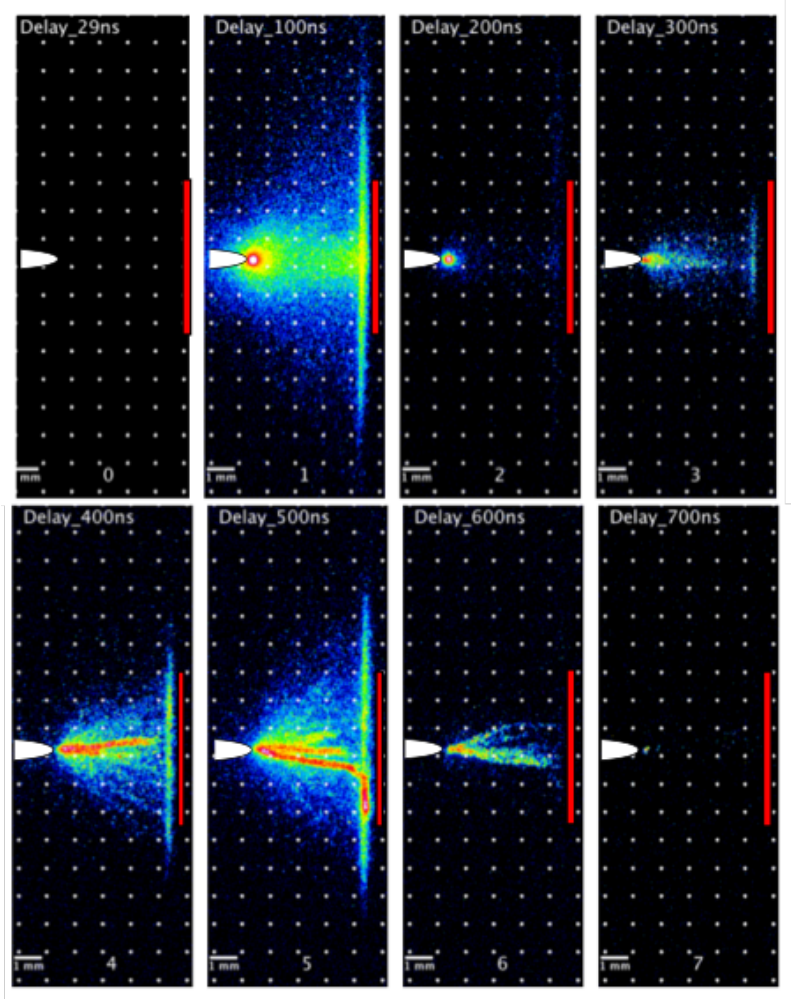

Figure 6.6: Instantaneous broadband images taken with a 100 ns gate time. 32 individual frames were averaged to produce each image. The pressure and discharge voltage are 202.6 kPa and 38 kV, respectively. The delay time indicates the position of the beginning of the 100 ns integration window. The point and red rectangle indicate the relative location of the high-voltage electrode and the dielectric surface, respectively. Frames 0-2 occur during a cathode-directed phase, and frames 4-6 occur during an anode phase. Figure 6.7 shows each camera window throughout the voltage pulse.

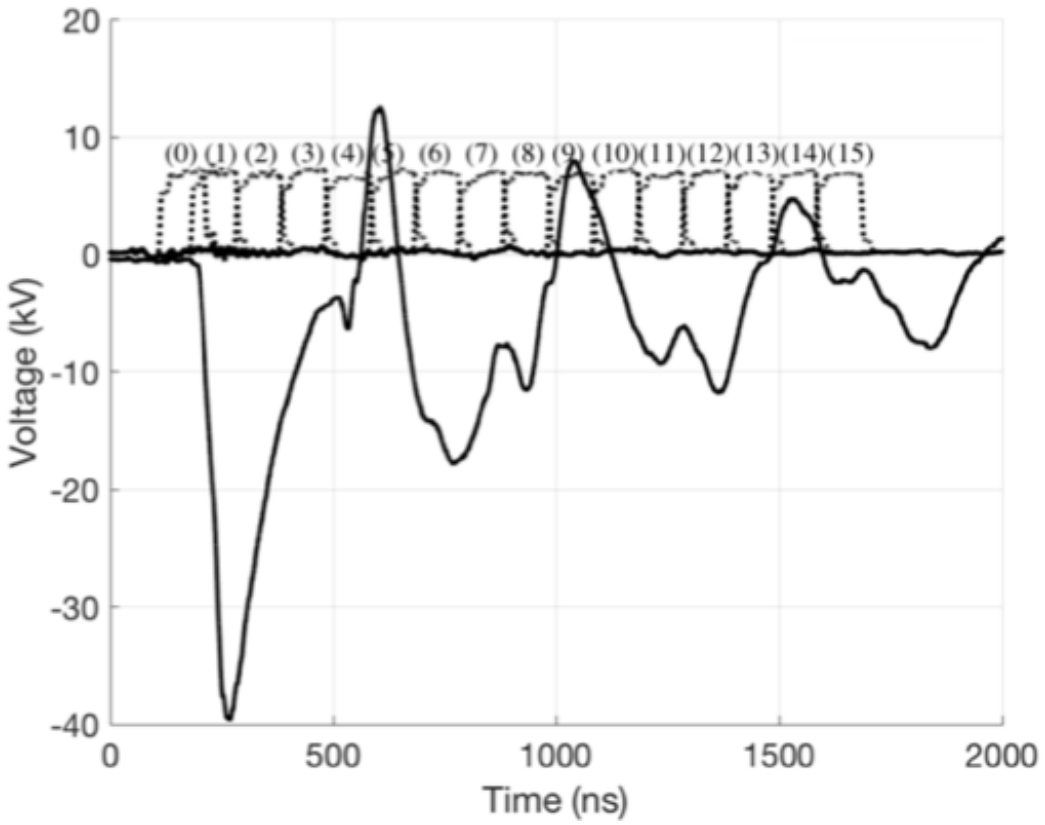

Figure 6.7: The position of the camera integration window, dotted black line, with respect to the applied voltage pulse, solid black line. The numbers correspond to the delay times associated with the instantaneous broadband images in Figure 6.6.

kPa and the discharge voltage of 38 kV.

In Fig. 6.6, frames 0-2 correspond to the anode-directed phase. Initially in frame 0, no discharge is observed until a critical breakdown voltage is reached. Then, the discharge bridges the inter-electrode gap (Fig. 6.6, frame 1) and a diffuse streamer discharge is observed. During this phase, a large current is conducted through the gap and the dielectric surface is charged. After the peak voltage is reached, the discharge quenches (Fig. 6.6, frame 2)

leaving a wake region of excited species and electrons.

The dominant electronically excited species are O^* and CO^* (see narrowband instantaneous imaging results results and Fig. 6.8). There are two main mechanisms for their quenching, namely, the spontaneous emission and the quenching due to collisions with the primary species, e.g. $CO^* + CO_2 \rightarrow CO + CO_2$. The typical value of the rate coefficient of the latter reaction is $\sim 10^{-16} - 10^{-18}$ m^3/s [90]. The Einstein coefficient of spontaneous emission of O^* is 10^7 s^{-1} [91], and at atmospheric-pressure conditions, the gas density is $\sim 10^{25}$ m^{-3}. Therefore, the time scale for spontaneous emission is ∼100 ns while the time scale for collisional quenching is ∼10-100 ns. Hence, both collisional and radiative processes must be considered in the quenching of excited species. Furthermore, it is concluded that any excited species produced during the first negative cycle are not quenched prior to the next voltage pulse ($\tau_{pulse} = 250$ ns).

Figure 6.6 (frame 3) shows the generation of a secondary anode-directed streamer. The primary streamer is quenched once the surface charge on the dielectric is sufficient to shield the applied field, and reduce the field strength within the gap to a level below the breakdown threshold. At this point, the excited species and electrons begin to recombine. A secondary streamer is initiated once the plasma density in the gap left after the previous streamer decreases to such value that the applied electric field starts penetrating inside the plasma. The generation of this streamer at lower voltage can be explained by the presence of electrons left after the previous streamer. These electrons

act as the seed background for the secondary streamer.

As the gap voltage becomes positive, a filamentary cathode-directed streamer bridges the inter-electrode gap (frame 4 in Fig. 6.6). The discharge emission intensity increases as the peak positive voltage is reached (frame 5). After the voltage drops below the positive breakdown voltage, the discharge begins to quench (frame 6).

From Fig. 6.6, it is concluded that the pulse is described by two main features: (1) a single primary anode-directed streamer is observed only at high negative voltages, while (2) multiple cathode-directed streamers form at low positive voltages with longer quench times. The anode-directed streamers have larger diameter ∼1-2 mm (frame 1, Fig. 6.6), while the cathode-directed ones have diameters ∼140 μm (frame 5). Furthermore, anodic streamers for these voltage-pressure conditions tend to remain in a diffuse mode without exhibiting branching. This indicates that the reduced electric field is not high enough to support the branching of anode-directed streamers as discussed in [34]. Though, for these conditions, the cathode-directed streamers are observed to show significant branching with multiple filamentary structures.

6.6 Instantaneous Narrowband Imaging: Excited Species Spatial and Temporal Evolution as Function of Polarity

In this section, the temporal evolution and the spatial distribution of the excited species densities are presented (see Fig. 6.8). Two bandpass filters

are used to investigate the evolution of excited species during the voltage pulse. The filters have a 10 nm FWHM and center wavelengths of 520 nm and 780 nm. Each of these wavelengths corresponds to a specific electronically excited species (either CO^* or O^*). The 520 nm filter corresponds to the rovibronic molecular transition of the CO Angstrom system:

$$CO(B^1\Sigma^+) \rightarrow CO(A^1\Pi^+) + h\nu \tag{6.9}$$

for $(\nu', \nu'') = (0, 2)$, where $'$ indicates upper vibrational state and $''$ lower vibrational state. The band head for these transitions is located at 518.217 nm. The wavelength of 780 nm corresponds to the transition:

$$O(^5P_J) \rightarrow O(^5S^0) + h\nu \tag{6.10}$$

for $J = 1$, 2, or 3. These lines are located at 777.194, 777.417, and 777.539 nm, respectively. Figure 6.8 shows the results for the two filters: (a) 520 nm CO Angstrom band, and (b) 780 nm O(^5P) triplet. The images are composed of 32 averaged frames with an integration time of 200 ns. The delay times for each image is shown in the top left corner. These times correspond to the same delay times used in Fig. 6.6 and shown in Fig. 6.7, but with an integration window of 200 ns rather than 100 ns as shown.

Comparing Fig. 6.8(a) and (b) it is evident that certain excited species are preferentially produced by different voltage polarities. The population density of these excited states (n_j) is directly proportional to the measured intensity of light (I_{ji}):

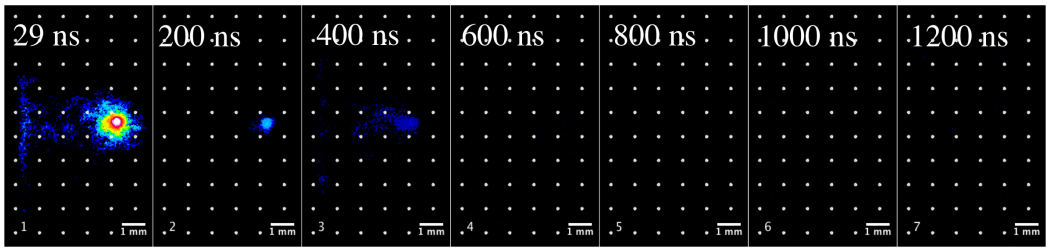

(A) 520 nm

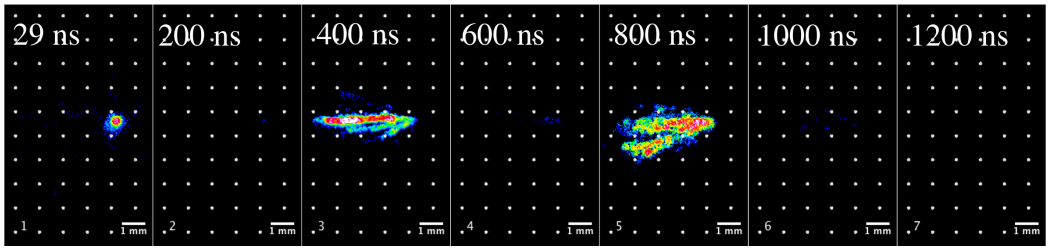

(B) 780 nm

Figure 6.8: Instantaneous narrowband imaging of the discharge evolution in time. Each image consists of 32 averaged frames each with a 200 ns integration time. (A) shows the narrowband imaging results for a bandpass filter with a 10 nm FWHM centered at 520 nm. This spectral range is associated with a band of the CO Angstrom system. (B) shows the narrowband imaging results for a bandpass filter with a 10 nm FWHM centered at 780 nm. This spectral range is associated with electronically excited Oxygen (^5P).

$$I_{ji} \propto n_j \frac{hc}{\lambda_{ji}} A_{ji} \tag{6.11}$$

here A_{ji} is the spontaneous emission transition probability, or Einstein coefficient, and $\frac{hc}{\lambda_{ji}}$ is the energy of the emitted photon from the transition from upper state j to lower state i. Therefore, the filtered images in Fig. 6.8 indicate the relative density distribution of electronically excited states.

Figure 6.8(a) (29 ns) shows that CO^* is dominantly produced in the first 200 ns of the voltage pulse. This time corresponds to the anode-directed streamer. After this time, the CO^* density decreases, with peak densities observed in the cathode sheath at the high-voltage electrode [Fig. 6.8(a), 200 ns]. At longer times there is no generation of CO^*.

Figure 6.8(b) shows the distribution of O^* throughout the voltage pulse. During the stage of the anode-directed streamer, a small emission region is observed in the vicinity of the high-voltage cathode sheath only [Fig. 6.8(b), 29 ns]. These species rapidly quench as the voltage decreases [Fig. 6.8(b), 200 ns]. Once the voltage becomes positive, the cathode-directed streamer is formed and the high-density region of excited oxygen is observed [Fig. 6.8(b), 400 ns] that bridges the inter-electrode gap. This streamer unlike the anode-directed one generates O^* in the entire cathode-anode gap. The discharge again quenches during the negative voltage cycle [Fig. 6.8(b), 600 ns]. Emission is observed when a second cathode-directed streamer emerges during the positive voltage cycle [Fig. 6.8(b), 800 ns]. After this time, no further discharges are observed as the pulse decays.

The mechanism of Ref. [85] does not contain any detailed kinetics of CO^* and O^*. Therefore, only a qualitative explanation of the results shown in Fig. 6.8 are presented. Excited species CO^* and O^* can be produced by two mechanisms. Namely, they can be generated from CO_2 by direct electron impact dissociation, for example:

$$CO_2 + e \rightarrow CO^* + O + e \tag{6.12}$$

or they can be generated through the excitation of CO and O. The first mechanism 6.12 is efficient at the streamer head and in the vicinity of the cathode sheath where the electron temperature is high [energy threshold of reaction (6.12) is ∼21 eV]. The excitation of the ground states of CO and O can be efficient only in the streamer tail and in the vicinity of the cathode sheath. This is explained by the fact that the streamer head velocity is high and it propagates a distance which is equal to the streamer head thickness during $\sim 10^{-11}$s, i.e. the probability for electron to dissociate CO_2 and then excite one of the fragments is very low.

It is concluded from Fig. 6.8 that during the anode-directed streamer stage, both CO^* and O^* are generated mainly in the vicinity of the cathode sheath edge. The time of flight of ions through the sheath is estimated as ∼10 ns which is much shorter than the delay time of each frame in Fig. 6.8. When ions reach the cathode they induce the secondary electron emission. Secondary emitted electrons gain high energy in the sheath and excite CO

and O generated by the streamer and through reaction (6.12). The more efficient generation of CO^* in the rest of the cathode-anode gap is explained by $\sim$2 times larger excitation cross section of CO than O.

Efficient generation of O* and inefficient generation of CO* by the cathode-directed streamer seen in Fig. 6.8 at 400 ns can be explained as follows. The streamer head generates only ground state CO and O because T_e is insufficient for reactions such as (6.12). Therefore, CO* and O* are generated in the streamer tail by the excitation of CO and O. However, as follows from Fig. 5.3 and Table 5.1, the electron temperature in the tail is $<$ 1eV. Such conditions are favorable for the excitation of the vibrational levels of CO rather than electronic states. At the same time, O is an atomic gas, and therefore there are no vibrational levels of these species. Hence, O is either converted to O* or it participates in chemical reactions.

The absence of radiation in the frame corresponding to 600 ns (Fig. 6.8), i.e. anode-directed streamer, can be explained by the lower voltage along the gap obtained at this time interval (see Fig. 6.1). At the same time, Fig. 6.1 shows comparable voltages at both intervals 400 ns and 800 ns at which we obtained the cathode-directed streamer.

6.7 Optical Emission Spectroscopy (OES)

Optical emission spectroscopy (OES) of the streamer discharge was conducted. A half meter spectrometer was used with a 100 μm slit. Two gratings were used: 300 g/mm and 1800 g/mm. The 300 g/mm was used to

analyze the entire spectral region (250-900 nm) while the 1800 g/mm was used to resolve line broadening for electron density, and rotational line structure for estimating the gas temperature.

Each emission spectrum was temporally integrated over the entire voltage pulse, 6 μs. During this duration multiple streamer discharges of both positive and negative polarity occur. The plasma properties therefore correspond to average values taken with a pulse frequency of 4 MHz. To accumulate sufficient signal, 500 on ICCD accumulations were required for each data frame. A minimum of 5 data frames were taken and median averaged for each spectral range.

Each voltage pulse had a repetition frequency was 4-7 Hz, with each voltage pulse containing multiple streamers. The pulse frequency and flow rate were set such that the chamber residence time was less than the pulsing period. Therefore, each voltage pulse occurs in pure CO_2. The plasma spectroscopy setup was discussed in Chapter 3.

Figure 6.9 shows the emission spectrum of the plasma discharge in pure CO_2 in the range 350-850 nm. In this region the light is characterized by ro-vibronic emission bands of diatomic molecules and atomic emission spectra. From analysis of the ro-vibronic bands and atomic emission lines the plasma properties are determined: gas temperature, vibrational temperature, electron temperature and density, and species concentrations.

The molecular and atomic spectra were identified using Pearse and Gay-

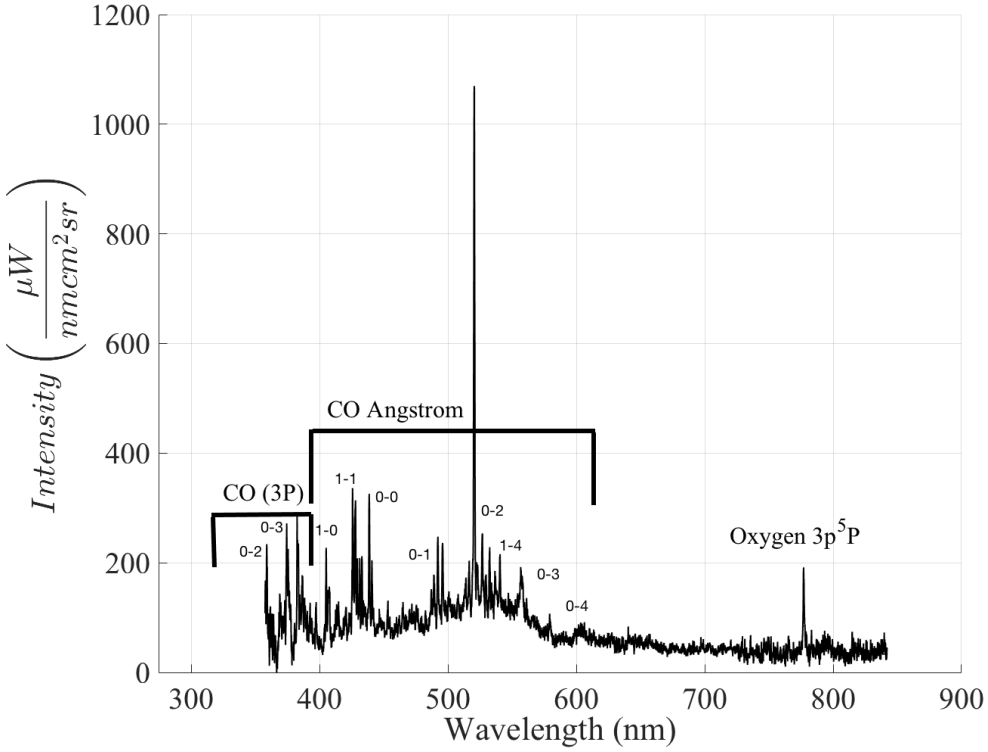

Figure 6.9: Spectrum in pure CO_2. The dominant lines include CO Angstrom and CO 3P band systems. In the NIR the atomic oxygen triplet ($O(3p^3P)$) is observed at 777 nm. The spectrum was captured with a 0.5 meter spectrometer using a 100 μm slit and a 300 g/mm grating.

don [92], and Silva et al [93]. In the pure CO_2 spectrum (Fig. 6.9) the emission is mainly attributed to the CO Angstrom band system ($B^1\Sigma^+ \rightarrow A^1\Pi$) which appears as a result of dissociation of CO_2 in the optical wavelength range of 400-700 nm. In the NUV region (λ <400 nm) the third positive system of CO_2 ($b^3\Sigma^+ \rightarrow a^3\Pi$) is observed. Other CO bands in the optical interval consider such as the triplet, Herman, and Asundi band systems [92, 93] were not observed. In the NIR region a single atomic oxygen line was observed at 777 nm corresponding to the $3p^5P - 3s^5S$ transition. In addition to line radiation a continuum is observed which is attributed to the chemiluminescence recombination of CO and O ($CO(X) + O(^3P) \rightarrow CO_2(X^1\Sigma_g^+) + h\nu$) [94].

The following sections will discuss the process for determining the plasma properties: electron density and temperature, vibrational temperature, gas temperature, and CO concentration. The effects of argon on the discharge will be discussed as well as the vibrational distribution function for CO_2.

6.8 Electron Density

The plasma electron density is determined from the broadening of the hydrogen Balmer β transition at 486.1 nm. This requires the addition of a small amount of hydrogen to the plasma. Here 4% of hydrogen by mass is premixed with CO_2. This ensures that the hydrogen H_β line is distinguishable from the background emission, and is not significant enough to greatly influence the plasma kinetic processes.

Broadening of a spectroscopic line consist of two main mechanisms: pressure broadening and thermal broadening. Pressure broadening mechanisms arise due to various collisional effects including: Stark, Van der Waals, and resonance broadening. Thermal broadening is caused by the Doppler effect, which is directly proportional to the temperature of the radiator. Griem's classic text on plasma spectroscopy provides a good review of line broadening mechanism which will be summarized here [16]. In addition to the above broadening mechanisms, natural broadening and instrumental broadening should be considered.

1. **Natural Broadening:** Natural line broadening is a consequence of the Heisenberg uncertainty principle associated with the finite lifetime of the state connected by the transition. The lineshape due to natural broadening is expressed by a Lorentzian profile with a Half-Width-Half-Maximum (HWHM) given in Eq. 6.13, where A_{ij} are the Einstein transition probabilities, λ_{ul} is the transition wavelength, and c is the speed of light. Natural broadening is three orders of magnitude lower than other broadening mechanisms, and is neglected in determining the broadening of the H_β line.

$$\Delta\lambda_{Natural} = \frac{\lambda_{ul}}{4\pi c}\left(\sum_{n<u} A_{un} + \sum_{n<l} A_{ln}\right) \tag{6.13}$$

2. **Instrumental Broadening:** The instrumental broadening is estimated from two light sources: a HeNe laser at 632 nm, and a low pressure

hydrogen discharge tube. The instrumental broadening is a function of the wavelength of the spectrometer. A HeNe laser was used to estimate the instrumental profile, and provide a means for determining if the low pressure gas discharge lamps, are at a sufficiently low density that the instrumental broadening profile dominates and all other line broadening mechanisms are negligible. Analyzing the HeNe source showed that the instrumental profile was well approximated as a Gaussian profile. Comparing the HeNe and hydrogen gas discharge tube showed that line broadening of the hydrogen lines in the gas discharge tube can be neglected. The instrumental profile was then estimated from fitting a Gaussian profile to the H_β emission line of the low pressure gas discharge tube shown in Fig. 6.10. The instrumental profile Full-Width-Half-Maximum (FWHM) is $\Delta\lambda_{Instrumental} = 0.106$ nm.

3. **Resonance Broadening:** Resonance broadening occurs due to collisions of the radiator with like particles, in this case the collision between two hydrogen atoms. The perturber's initial state is connected to the upper and lower state of the transition by a radiatively allowed transition to either the upper or lower state of the radiator [95]. The resonance broadening HWHM is calculate by Eq. 6.14. Where u, l and g are the upper, lower, and ground states, respectively. g_i are the degeneracies, and f_i are the oscillator strengths. All constants can be found from NIST atomic database [96]. From Eq. 6.14 the resonance broadening HWHM is determined to be 0.021 nm.

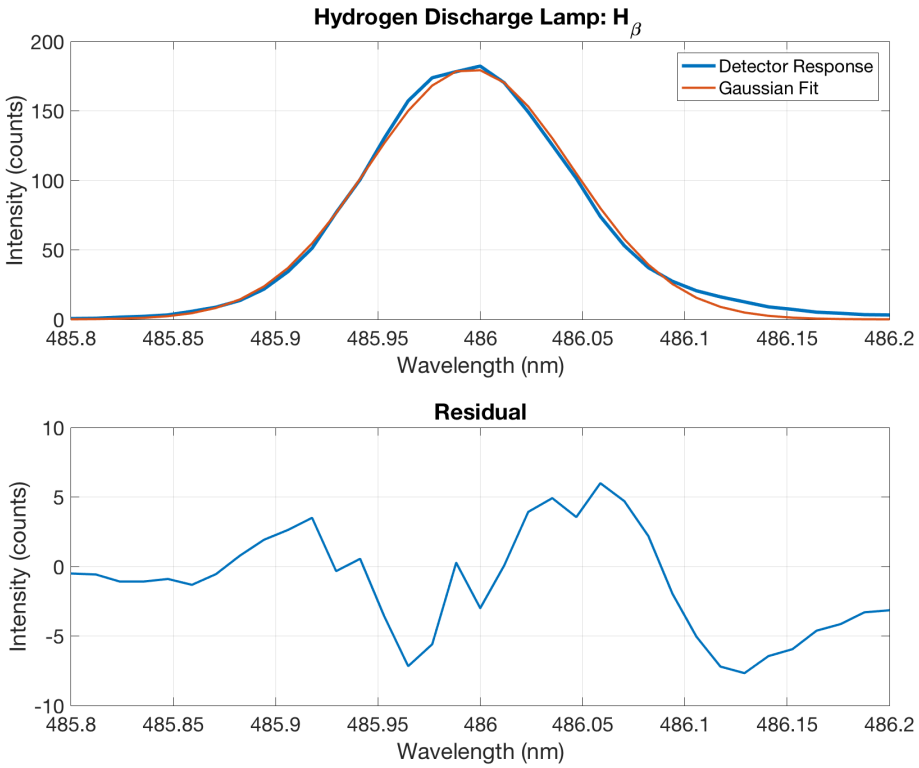

Figure 6.10: Gaussian fit to the hydrogen gas discharge lamp, and the resulting residuals from comparing the Gaussian fit to the raw data.

$$\Delta\lambda_{Resonance} = \frac{3e^2}{16\pi^2\epsilon_0 m_e c^2}\lambda_{ul}^2 \left[\lambda_{lg} f_{lg}\sqrt{\frac{g_g}{g_l}}n_g + \lambda_{ug} f_{gu}\sqrt{\frac{g_g}{g_u}}n_g + \lambda_{ul} f_{lu}\sqrt{\frac{g_l}{g_u}}n_1\right] \tag{6.14}$$

4. **van der Waals Broadening:** van der Waals broadening is a type of collisional broadening which accounts for the radiators interactions with non resonant, or neutral perturbers. The interaction potential can be described by a Van der Waals potential ($V(R) = \hbar C_6/R^6$), with a Lorentzian lineshape. Where C_6 is the Van der Waals interaction constant for the collision partners [97]. The line HWHM is given by Eq. 6.15, with λ in nm, T in K, the reduced mass (μ) in atomic mass units, and the background number density (n_b) in m^{-3}.

$$\Delta\lambda_{Van\ der\ Waals} = 8.5\times10^{-17}\lambda_{pq}^2 \times C_6^{\frac{2}{5}}\left(\frac{T}{\mu}\right)^{3/10} n_b \tag{6.15}$$

The van der Waals constant, C_6, has units of m^{6}s^{-1}, and is usually tabulated or can be estimated by Eq. 6.16. α_d is the dipole polarizability of the perturbers, and $< R_i^2 >$ is the mean-square radius of the i^{th} level [97]. The van der Waals HWHM is then determined to be 0.0297 nm from evaluation of Eq. 6.15.

$$C_6 = \frac{e^2}{4\pi\epsilon_0\hbar}\alpha_d| < R_p^2 - R_p^2 > | \tag{6.16}$$

5. **Doppler Broadening:** Doppler or thermal broadening is due to the relative velocities of the radiators with respect to the observer. Radiators moving towards the observer will generate a blue shift (or increase in frequency), while those moving away from the observer lead to a red shift. These blue and red shifts are relative to the emission line and result in a Gaussian broadening profile that is dependent upon the thermal velocity of the radiator. Assuming a Maxwellian velocity distribution of the radiating atom at a characteristic temperature T, the Doppler HWHM is given by Eq. 6.17. T is estimated as the gas temperature which is estimated from the rotational temperature as discussed in section 6.11. The Doppler HWHM is determined to be 0.004 nm at a gas temperature of 678 K.

$$\Delta\lambda_{Doppler} = \frac{1}{2}\lambda u, l\sqrt{\frac{8k_b T \ln 2}{m_h c^2}} \tag{6.17}$$

6. **Stark Broadening:** Stark broadening is caused by the radiating atoms Coulomb interaction with the ion field of the plasma. Both the electron and ion fields contribute to the Stark effect, but it is the electrons that are dominant due to their higher velocities and hence higher collision frequencies [95]. The lineshape for Stark broadening is well approximated by a Lorentzian function except at the line center. Near the center of the line electrostatic interactions with the ion field cause a dip in the line profile. Calculations of the line profile have been tabulated by Gigosos and Cardenoso for non-equilibrium plasma discharges as a function of

the electron density [98, 99] and reduced mass. A fit of this data gives the Stark Broadening FWHM (Eq. 6.18) for a non-equilibrium plasmas in CO_2, which is solely a function of the electron density in m^{-3}.

$$\Delta\lambda_{Stark} = 4.8\left(N_e/10^{23}\right)^{0.68116} \tag{6.18}$$

To determine the electron density a high resolution spectrum of the Balmer H_β line was taken in a $CO_2 + H_2(5\%)$ discharge. The Balmer H_β line is a multiplet of seven lines resulting from the fine structure spin-orbit splitting of the upper and lower levels [95]. The H_β line can be approximated by a Voigt profile if the HWHM for each line is greater than 0.005 nm [95]. This condition is fulfilled for the conditions of the streamer discharge investigated here, and the H_β line is well approximated by a Voigt profile, Eq. 6.19.

$$V(\lambda;\sigma,\gamma) = D(\lambda,\sigma) * L(\lambda,\gamma) = \int_{-\infty}^{\infty}\left[\frac{e^{\frac{-y^2}{2\sigma}}}{\sigma\sqrt{2\pi}}\right]\times\left[\frac{\gamma}{\pi(\gamma^2+(\lambda-y)^2)}\right]dy \tag{6.19}$$

A Voigt distribution is a convolution of two distributions: a Gaussian and a Lorentzian. The first term on the right hand side of Eq. 6.19 is the Gaussian distribution, and the second term is the Lorentzian distribution. Where σ^2 is the variance of the Gaussian distribution, γ is the HWHM for the Lorenz distribution. The FWHM for a Gaussian is a function of the variance given as: $FWHM = 2\sqrt{2\ln 2}\sigma$.

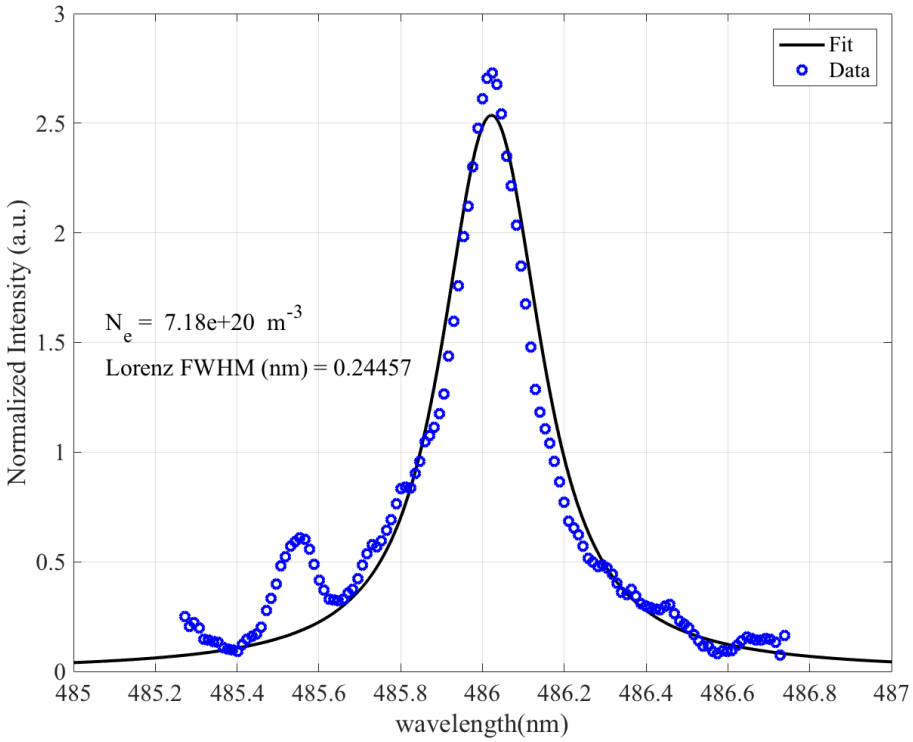

Figure 6.11: Electron density estimated from broadening of the H_β line. The discharge was seeded with 4% hydrogen by mass. The Gaussian contribution is held fixed and determined by the gas temperature and instrumentation function.

A Voigt distribution has been fitted to the Balmer H_β line for determining the electron density. The line profile and fit for the H_β transition are shown in Fig. 6.11. The fitted Voigt distribution is determined from a least-squares minimization of the Voigt distribution, and the experimental data. For fast evaluation of the convolution integral in Eq. 6.19, the Voigt distribution is represented by the Faddevva function. Prior to solving the minimization problem, the Gaussian contribution in Eq. 6.19 is determined. Therefore, the minimization problem takes place in the 1D space defined by the Lorenz HWHM γ. The resulting Lorentz HWHM (γ_{Min}) is then used to determine the electron density.

To determine the Gaussian contribution, the convolution of each Gaussian broadening mechanism (Doppler and Instrumental) must be determined. The convolution of any two Gaussian distribution produces a third Gaussian distribution with a squared FWHM equal to the sum of the original FWHM's squared ($FWHM^2_{Convultion} = FWHM^2_{Doppler} + FWHM^2_{Instrumental}$). Similarly, the Lorentzian contributions (Stark effect, van der Waals, Resonance, and Natural) must be convoluted together. The convolution of multiple Lorentz distributions results in a Lorentz distribution with $\gamma = \sum_i \gamma_i$. The electron density is then determined from the subtraction of the calculated values of the Van der Waals, resonance, and natural broadening mechanisms from the Lorenz HWHM determined the minimization problem. This subtraction gives the HWHM due to Stark broadening, $\Delta\lambda_{Stark}$. With the Stark HWHM and Eq. 6.18 the electron density is determined to be: 7.18×10^{20} m^{-3}.

6.9 Electron Temperature

To determine the electron temperature 5% argon is seeded into the plasma discharge. The mean electron energy is determined from a Boltzmann plot using the Argon atomic line emission. Figure 6.12 shows a spectrum of the plasma discharge with argon. The spectrum is dominated by the CO Angstrom band system, and the transition array from the excited 4p argon states. Additionally, two atomic oxygen lines are observed at 777 nm ($O(3p^5P)$) and 844 nm ($3p^3P$). For a detailed review of the Boltzmann plot technique see Appendix A and Chapter 8.

The thermal limit for validity of the Boltzmann plot, is specified by a principal quantum number (n_{th}), which is a function of the electron density and temperature [97]. For an electron density of 10^{22} m^{-3} and a temperature of $\sim$1 eV, only states with the principal quantum number $>$4 are in LTE. These estimates indicate that for the primary radiative transitions of the streamer discharge, arising from the $3p^54p \rightarrow 3p^54s$ transitions, LTE and PLTE assumptions are not completely valid for all transitions. Additionally, since streamers are not spatially uniform nor steady, the thermal limit will be further increased. Therefore, the excitation temperature defined determined from the Boltzmann plot technique should be viewed suspect and will not be equal to the electron temperature for all 4p transitions. This deviation from the thermal limit is seen in Fig. 6.12 by the deviation between the line and continuum radiation. This indicates that both collisional and radiative processes are important for the argon 4p transitions. To better determine the

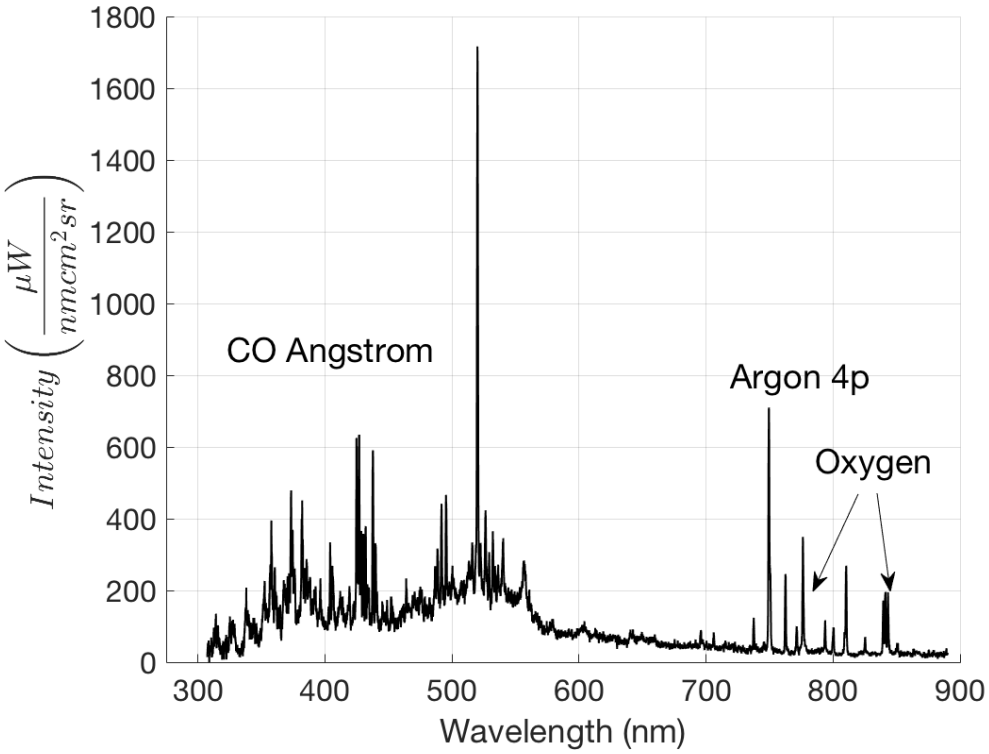

Figure 6.12: Spectrum of a plasma streamer discharge in CO_2 + 5% Ar. argon is used to determine the electron temperature from the 4p transition array.

electron temperature argon lines which are closest to the continuum are used to determine the electron temperature.

Figure 6.13 shows the Boltzmann plot of 7 argon 4p lines which are nearest to the continuum radiation field. The slope of the Boltzmann plot determined from plotting the $ln\left(\frac{\epsilon\lambda}{gA}\right)$ to the excitation energy gives the characteristic excitation temperature, where ϵ is the observed emission intensity, g is the degeneracy of the transition, and A is the transition probability (Einstein coefficient). The excitation temperature is defined as the temperature which would produce the given distribution of states assuming a Boltzmann distribution. For the argon 4p transitions, it is assumed that this temperature is related to the electron temperature, which assumes that the electrons are primarily responsible for producing the observed populations of the argon 4p states. From the Boltzmann plot the excitation temperature is determined to be $T_{EXT} = 0.46 \pm .18$ eV.

The electron temperature is then determined from the line to continuum intensity ratio and the excitation temperature determined from the Boltzmann plot technique as outlined in Sola et al. [100]. This method increases the accuracy in determining the electron temperature for non-LTE systems, due to the sensitivity in the ratio of line to continuum radiation to the electron and excitation temperatures. The electron temperature is calculated for each line-continuum ratio as given by Eq. 6.20 which is a function of only the electron temperature. In Eq. 6.20 λ is in nm, G is the free-free Gaunt factor, ζ is the free-bound continuum correction factor, E_2 is the energy of the upper level,

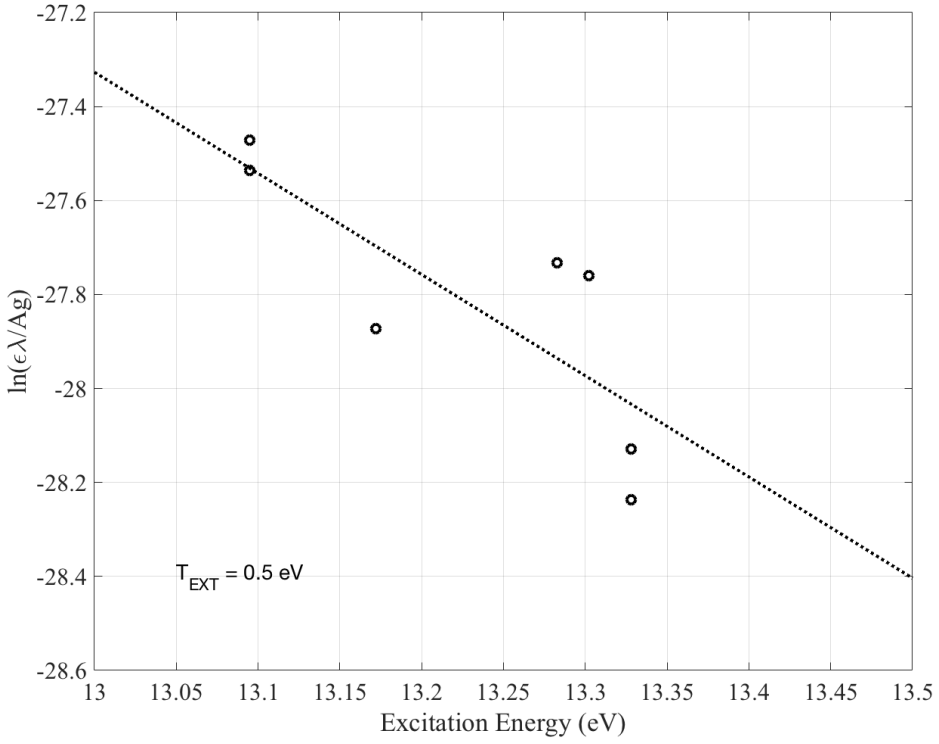

Figure 6.13: A Boltzmann plot of the argon 4p lines. The slope of the line determines the excitation temperature.

E_i is the ionization energy, ΔE_i is the lowering of the ionization potential, T_e is the electron temperature, U_i is the partition function of the ion, ϵ is the measured emission intensity of the continuum, and I is the integrated line emission intensity. All the spectroscopic constants for argon are taken from Sola et al. [100].

$$\frac{I(\lambda)}{\epsilon} = 2.0052 * 10^{-5} \frac{A_{21} g_2}{U_i} \frac{\lambda}{T_e} e^{\frac{E_i - \Delta E_i}{k_B T_{EXT}}} \frac{e^{-\frac{E_2}{k_B T_e}}}{\zeta \left(1 - e^{\frac{-hc}{\lambda k_B T_e}}\right) + G e^{\frac{-hc}{\lambda k_B T_e}}} \tag{6.20}$$

From Eq. 6.20, and the excitation temperature $T_{EXT} = 0.46 \pm .18$ eV, the average electron temperature is determined to be T_e =0.598 $\pm$ 0.018 eV.

6.10 Vibrational Temperature

To determine the vibrational temperature the plasma discharge was seeded with a mixture of CO_2 and 5% N_2. The vibrational temperature for CO_2 was then determined from the vibrational distribution of the excited $N_2(C)$ state, or second positive system (SPS) of nitrogen. Figure 6.14 shows the spectrum of the plasma discharge seeded with 5% nitrogen. The discharge is dominated by the nitrogen second positive system corresponding to the $C^3\Pi_u \rightarrow B^3\Pi_g$ ($\Delta\nu = \nu^{'} - \nu^{''} = -1, 0, 1$)

A Boltzmann plot of the N_2 vibrational bands is shown in Fig. 6.15, $ln(\epsilon\lambda/A)$ vs $ExcitationEnergy$. The Einstein coefficient (A) for a ro-vibronic transition is given by Eq. 6.21. For vibrational transitions the rotational inten-

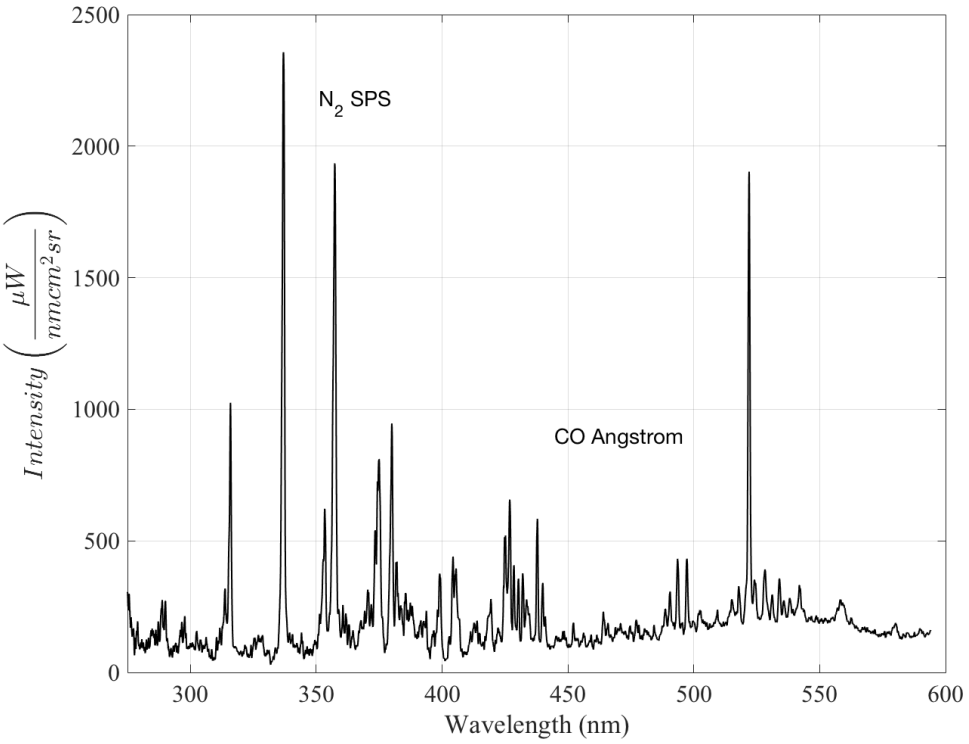

Figure 6.14: A spectrum of a CO_2 + 5% N_2 discharge. The vibrational temperature is determined from the $N_2(C)$ state of the second positive system.

sity strength (Honl-London factor) $S_{J'J''}$ is summed over all rotational transitions, and equals to one. $q_{v'v''}$ is the Franck-Condon factor, and $|R_e(\bar{r}_{v'v''})|^2$ is the squared electronic-vibrational transition matrix elements. The spectroscopic constants for the nitrogen system can be found in [101]. The vibrational temperature for $N_2(C^3\Pi_u)$) was determined to be 4260 K.

$$A^{n''v''J''}_{n'v'J'} = \frac{64\pi^4}{3h\lambda^3 d} \left|R_e(\bar{r}_{v'v''})\right|^2 q_{v'v''} S_{J'J''} \tag{6.21}$$

To estimate the vibrational temperature of the asymmetric stretch mode of CO_2, the vibrational resonance between the $N_2(X, \nu = 1)$ and $CO_2(001)$ is exploited. It is known that if the vibrational frequencies of two oscillators are in near resonance the VV' relaxation process between different molecules is a dominant energy exchange process [93]. Since the vibrational energy spacing level of $CO_2(v_3)$ and $N_2(X, \nu = 1)$ are close relative their respective ground states, it is assumed that the vibrational states are in thermal equilibrium, due to the energy exchange reaction: $CO_2(000) + N_2(X, \nu = 1) \rightarrow CO_2(v_3) + N_2(X, \nu = 0)$. To estimate the CO_2 vibrational temperature the vibrational temperature of the ground electronic state $N_2(X)$ must be determined.

In a streamer discharge there are always some electrons with energies exceeding 11.18 eV which directly excite the nitrogen ground state $N_2(X)$ to the electronically excited $N_2(C)$ state. The electronically excited vibrational bands are assumed stationary on the time scales of the streamer discharge (few

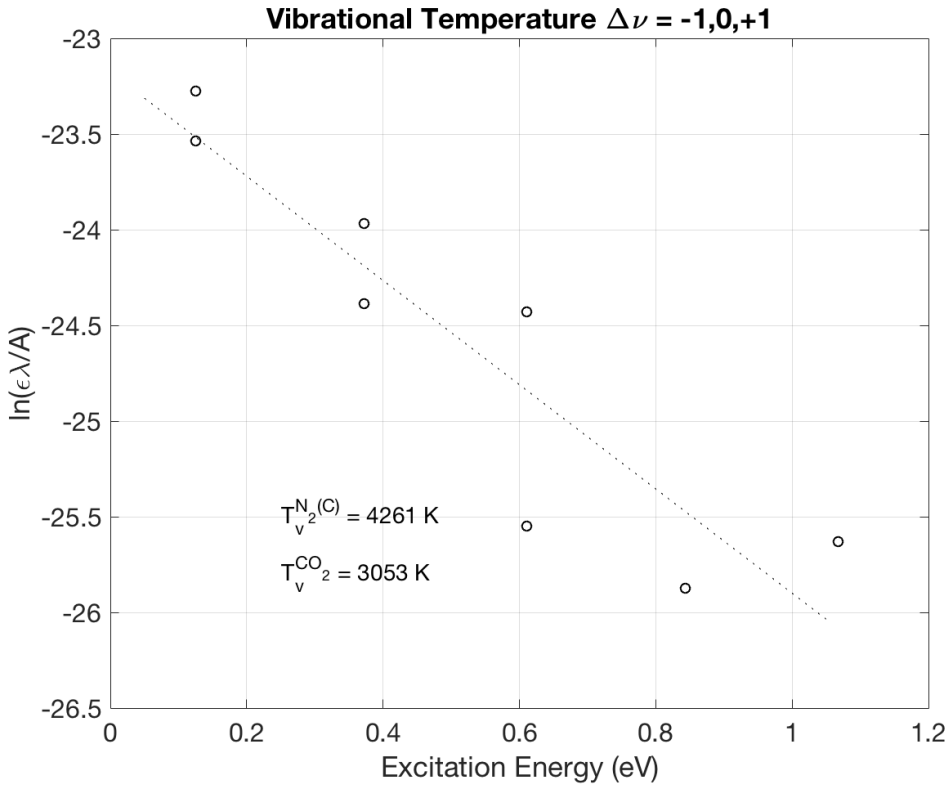

Figure 6.15: A Boltzmann plot of the second positive system of N_2. The slope of the line gives an estimate of the vibrational temperature of Nitrogen.

ns) then the electronically excited and ground state vibrational distributions are linked by the Franck-Condon matrix $q_{v'v''}$, $[N_2(C)] \propto q_{v'v''}[N_2X]$ [100]. Inversion of the $q_{v'v''}$ matrix multiplying by the population of $[N_2(C)]$ an expression for the vibrational temperature of the ground state was determined by [102], given by Eq. 6.22. Eq. 6.22 is valid for 3000 K $< T_{v'}(N_2(C^3\Pi_u))$ $<$ 8000 K. Evaluation of this expression with the vibrational temperature for $N_2(C^3\Pi_u)$ results in a vibrational temperature for $N_2(X^1\Sigma_g^+)$ and $CO_2(v_3)$ of $T_v\,[CO_2(v_3)] = 3053$ K.

$$T_v(N_2(X^1\Sigma_g^+)) = 1775 + 175e^{\frac{T_{v'}\left(N_2(C^3\Pi_u)\right)}{2143}} \tag{6.22}$$

6.11 Rotational and Gas Temperature

The gas temperature is a measure of the heavy species energy distribution. In optical emission spectroscopy only excited species are observed. Hence, to determine the gas temperature, the rotational temperature is measured and assumed to be equivalent to the gas temperature. This assumption is valid so long as the relaxation time is less than the time of the pulsed discharge. As discussed previously, the total pulse duration associated with OES integrated measurements is 6 μs. The relaxation time for sufficient number of collisions for translational rotational equilibration can be estimated by Z_{rot} and the collision frequency for the discharge conditions. Z_{rot} is the number of collisions necessary for rotation-translational (RT) equilibrium, and is estimated to be $\sim$ 7 for CO [93]. This Z_{rot} corresponds to a $\tau^{RT}_{relaxation} \sim 2$

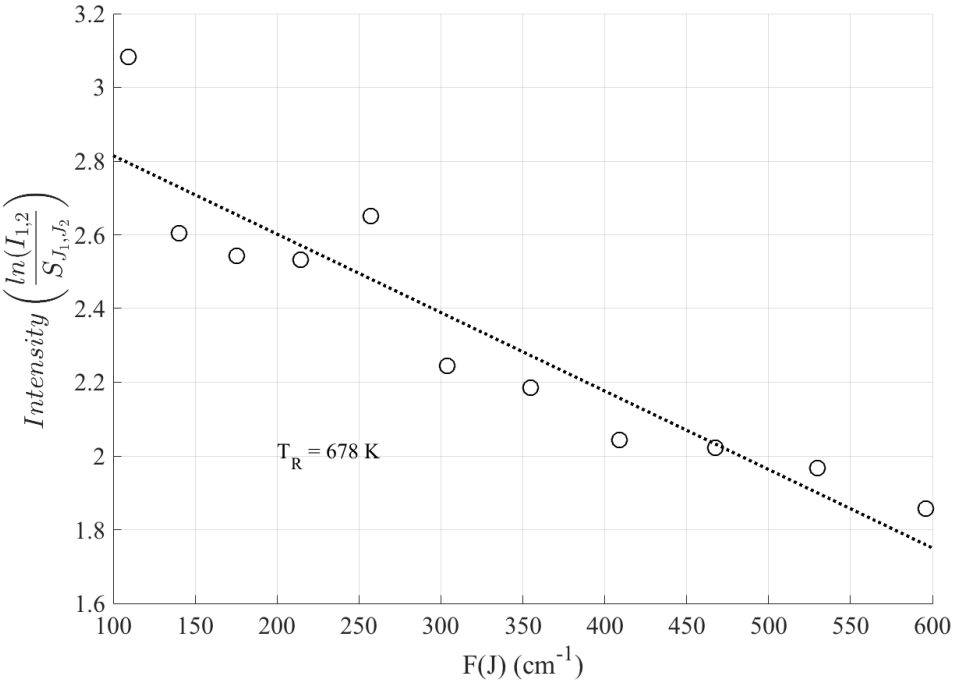

Figure 6.16: Boltzmann plot of the rotational temperature of the rotational sub-band $CO(B)(v' = 0) \rightarrow CO(A)(v' = 1)$.

ns. Therefore, the translational and rotational temperature for CO can be considered in thermal equilibrium for the discharge conditions.

The emission intensity of a line is expressed by Eq. 6.23, with $A^{n''v''J''}_{n'v'J'}$ given by Eq. 6.21.

$$I_{em} = N\frac{hc}{\lambda}A^{n''v''J''}_{n'v'J'} \tag{6.23}$$

Assuming that the rotational level populations follow a Boltzmann distribution the emission intensity in a rotational band is given by Eq. 6.24.

$$I_{em} = \frac{C}{Q_R}\frac{1}{\lambda^4}S_{J'J''}e^{-\frac{F(J')hc}{k_B T_{rot}}} \tag{6.24}$$

Here, C is a constant resulting from combining all fundamental constants and non-dependent terms on J, Q_R is the rotational statistic sum, and $F(J')$ is the rotational energy term. A plot of the $ln\left(I_{em}/S_{J'J''}\right)$ vs F(J') will result in a straight line (if the populations follow a Boltzmann distribution) with the slope determined the rotational temperature. Figure 6.16 shows the Boltzmann plot for the rotational sub-band $CO(B)(v'=0) \rightarrow CO(A)(v'=1)$. The rotational temperature is estimated to be 678 $\pm$ 17 K.

It should be noted that even with the spectral resolution of the spectrometer, the rotational structure tends to be blurred due to the convolution of the Gaussian slit function. A better estimate of the rotational temperature is achieved if a simulated spectrum is calculated for the rotational bands, and convolved with the instrumental function. Bruggeman et al. provided a nice review of gas temperature determination from rotational lines in non-equilibrium plasmas [73]. In addition to OES, the rotational or gas temperature can be determined from line profiles (Doppler Broadening), or active diagnostics such as absorption techniques (cavity ring down spectroscopy (CRS), laser induced fluorescence (LIF)), or scattering (Raleigh, Raman).

To verify the temperature estimate from the Boltzmann plot technique, the method proposed by Silva et al. is used, as discussed in [103]. In this work, several rotational spectra of the CO Angstrom system were simulated for various gas temperatures. These simulated spectra were used to derive a formula (given by Eq. 6.25) which related the intensity ratio (R) of two rotational transitions (481.61, and 482.48 nm) to the gas temperature. The

method is valid for temperature less than 3000 K. From Eq. 6.25, the gas temperature is estimated at 630 ± 30 K. This agrees well with the Boltzmann technique.

$$T_{gas} = 343\,(0.36 + log(R))^{-1} \tag{6.25}$$

6.12 Actinometry: CO Concentration

The CO concentration is determined from the actinometry method [93]. The actinometry method uses an actinometer of known concentration to determine the unknown concentration of the desired species. This is done by taking the ratio of two emission lines, one from the actinometer and the second from the species under investigation. Here, N_2 is used as an actinometer to determine the CO ground state concentration, and conversion efficiency of the streamer discharge. N_2 is chosen because the electronic excitation energy of $N_2(C) = 11.05$ eV is close to that of $CO(B) = 10.78$ eV. It is assumed that due to the proximity of these energies the two states population distributions will correlate as a result of having the same excitation energy [93].

In OES only the excited states are measured. Therefore, a model must be used to correlated the observed electronically excited state populations to the ground state populations. Usually a collisional-radiative model is used. Collisional-radiative models account for electron excitations, collisional losses, and radiative transfer to determine the observed state populations. Comparing the observed spectrum to a simulated spectrum allows the plasma properties

and species ground state densities to be determined. A simple approximation to full CR modeling is the corona model which results in an analytical expression relating the observed intensity to the ground state population.

The corona model assumes that the dominant excitation process is through electron collisions. These electronically excited states then decay only through radiative transitions. Hence, the corona model assumes that the collisional depopulation of excited states is negligible. With these assumptions a rate balance equation is formed from the balance of electronic excitation rates to upper level p and the sum of all radiative transitions from the excited state as given by Eq. 6.26. [104]

$$n_1 n_e k_e^{exc}(T_e) = n(p) \sum_k A_{pk} \tag{6.26}$$

Where n_1 is the density of the ground state, n_e is the electron density, k_e^{exc} is the excitation rate coefficient due to electron collisions, and $n(p)$ is the population of the upper state. Combining expression 6.26 with the Eq. 6.23 for the intensity of a spectral line the emission intensity under the corona approximation is given by Eq. 6.27.

$$I_{em}^{X^*} = \frac{h\nu_{ij} A_{ji} k_e^{exc} n_e}{\sum_{j<i} A_{ji}} n_1 \tag{6.27}$$

The dependence on the electron density is eliminated by taking the ratio of two lines with similar excitation energies. Dividing the $CO(B)(v' = 0) \rightarrow CO(A)(v'' = 1)$ emission intensity given by Eq. 6.27 by that of the

actinometer $N_2(C)(v' = 0) \rightarrow N_2(B)(v'' = 2)$, the CO ground state density can be estimated from Eq. 6.28 [93].

$$\frac{I_{CO}}{I_{N_2}} = \frac{A_{ji}^{CO} k_e^{CO} \sum A_{ji}^{N_2} n_{CO}}{A_{ji}^{N_2} k_e^{N_2} \sum A_{ji}^{CO} n_{N_2}} \tag{6.28}$$

From Eq. 6.28 the CO density was determined to be: 2×10^{23} m^{-3}. This corresponds to a CO_2 conversion of 0.83 %.

6.13 Effect of argon addition

Figure 6.17 shows the electronically excited atomic oxygen ($O(3p^5P)$) for both pure CO_2 and with the addition of 5% argon. Comparison of the absolute integrated intensity between the pure and 5% argon shows that the addition of argon increases the absolute radiance of $O(3p^5P)$ by a factor of $\sim$ 1.5. Assuming a coronal model, the increase in radiance is directly proportional to the ground state density, the electron density, and the excitation rate coefficient, Eq. 6.27. The rate coefficient is a function of the electron energy, and if it is assumed that the addition of argon does not greatly alter the electron energy distribution function, then the intensity ratio for the two $O(3p^5P)$ lines is related to the density of the ground state and electron density.

The increase in the upper state population could be attributed to either an increase in the electron density or ground state oxygen. To determine which effect lead to the observed population increase of the $O(3p^5P)$ excited state, the density of the $CO(B)(v' = 0) \rightarrow CO(A)(v'' = 1)$ transition is also analyzed.

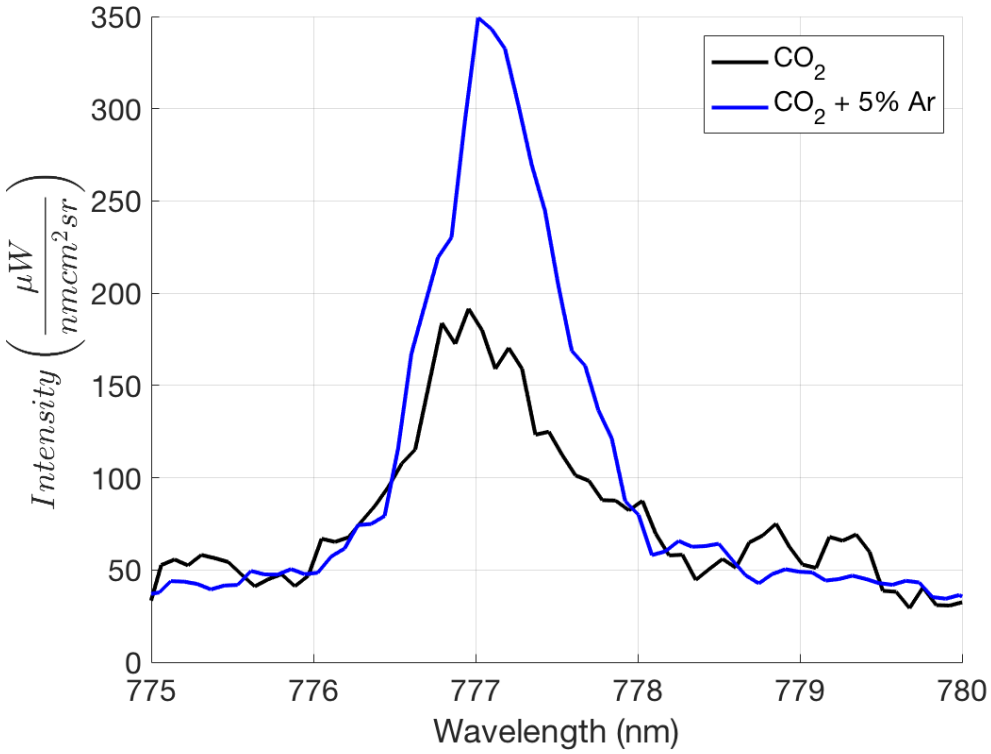

Figure 6.17: Comparison of a plasma discharge in pure CO_2 (Black) and CO_2 + 5% Ar (Blue), showing that the presence of argon increase the $O(3p^5P)$ density.

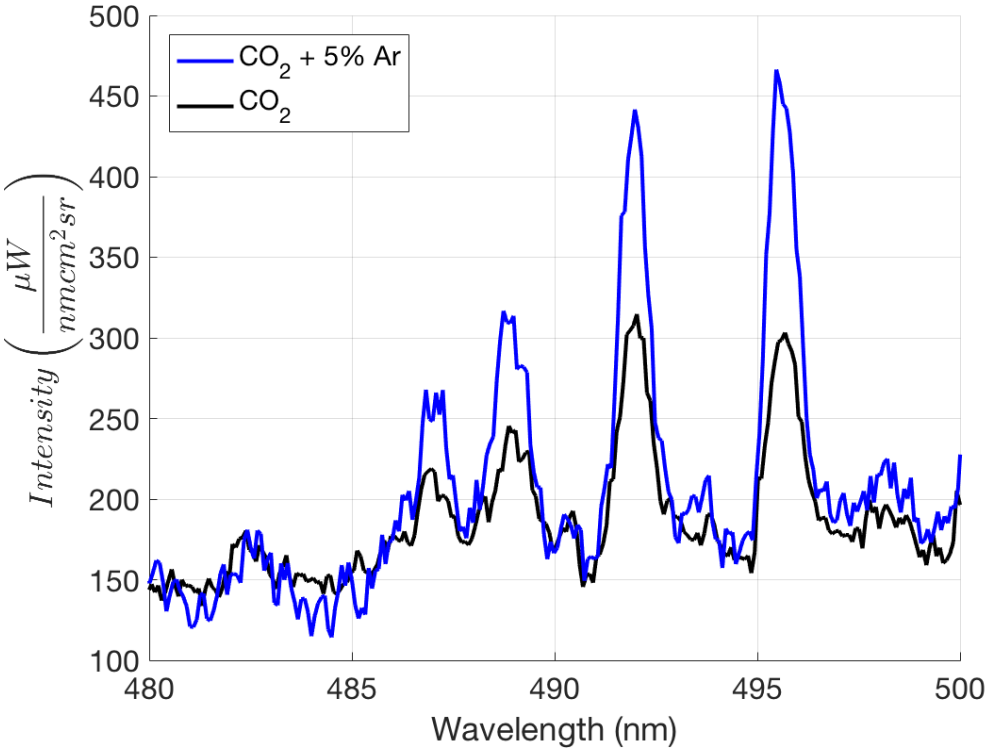

Figure 6.18: Comparison of a plasma discharge in CO_2 (black), and CO_2 + 5% Ar (Blue), showing that the presence of argon alters the CO density.

Figure 6.18 shows the spectra for CO_2 (Black) and CO_2 + 5% Ar (Blue) for the transition $CO(B)(v' = 0) \rightarrow CO(A)(v'' = 1)$ which corresponds to the transition used for determining the CO ground state population. Comparing the peak line emission height of the two plasma discharges, it is evident that the excited state population for the CO_2 is 1.5 times smaller than with 5% Ar, as observed with the $O(3p^5P)$.

CO and O are produced through dissociation of CO_2 in the streamer head. It is expected that the O ground state populations will be directly

proportional to the CO concentration for the time scales of the streamer (that is recombination can be neglected), and equal for both discharges, CO_2 and 5% argon. The CO and O concentrations will be similar for both discharges if the production rates are similar, and the production rates will be of similar order given that T_e, n_e, and n_{CO_2} are similar.

To estimate the production rates the ionization energy and cross-sections need to be compared. Since the ionization threshold for both CO_2 and Ar are close, 13.6 and 15.76, the streamer head temperature will be similar for both discharges. Furthermore, the electron density production in the streamer head for $T_e \sim 10eV$ will be nearly identical, as seen by the ionization cross-sections for CO_2 and Ar given in Fig. 6.19. Therefore, in the streamer head, which is responsible for the production of CO and O ground states (see sec. 5, the electron dynamics and are not significantly altered by the presence of argon, and the CO and O concentrations should be similar for both discharges. Therefore, it is in the streamer tail where the production of electrons will be altered by the addition of argon. The low energy electrons in the streamer tail will go into vibrational excitation of CO_2, and ionization of argon.

The observed increase in the $O(3p^5P)$ density with the addition of argon is attributed to an increase in the electron density in the streamer tail. Since argon is an atomic species, all the electron energy goes directly into electronic excitation or ionization rather than vibrational (rotational) excitation. Hence, with the addition of argon fewer low energy electrons ($T_e = 0.6eV$) lose their energy to excitation of vibrational levels, and result in more ionization

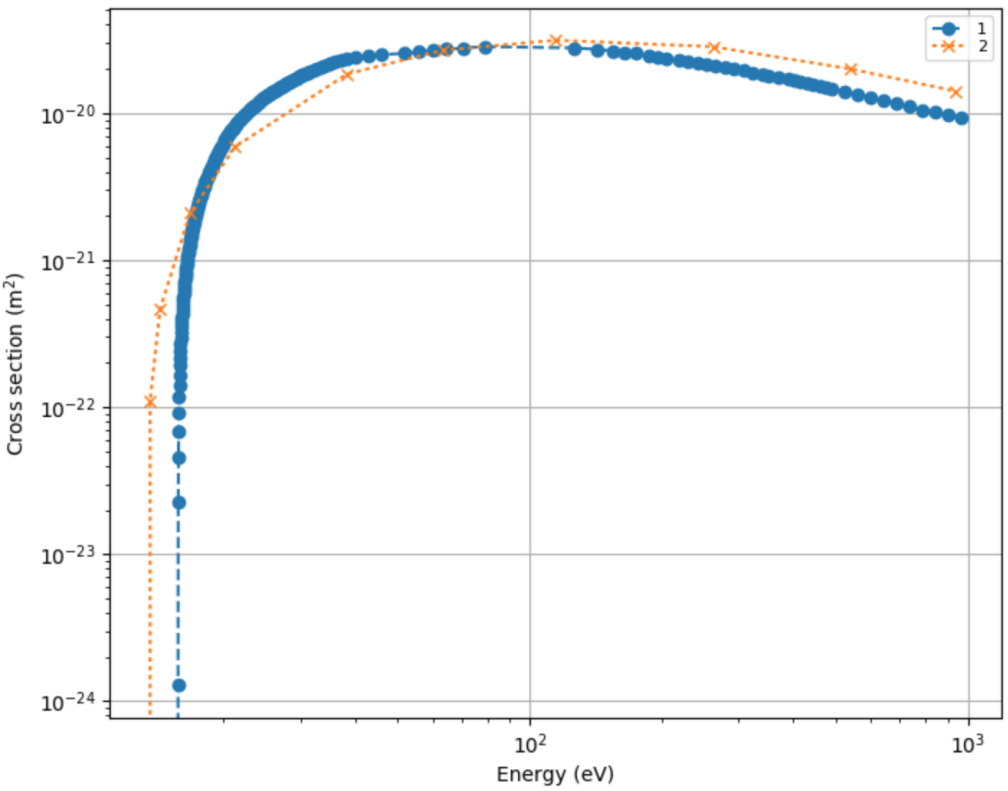

Figure 6.19: Ionization cross-sections for argon (1) and carbon dioxide (2). [1, 2, 10]

reactions. This results in an increase in the electron density. Future work should look at the effects of argon on the conversion efficiency, and vibrational dynamics.

6.14 Vibrational Distribution

The vibrational distribution function for the asymmetric vibrational stretch mode of CO_2 is calculated assuming a Boltzmann distribution given by Eq. 6.29 or the Treanor distribution given by Eq. 6.31. The Boltzmann distribution assumes thermal equilibrium of the vibrational degrees of freedom which produces a distribution of states given by Eq. 6.29. In non-thermal plasmas where $T_v > T_o$, the rate of vibrational excitation of higher lying vibrational states is faster than vibrational-translational losses, that occur primarily from $v = 1$. This thermal non-equilibrium produces a vibrational distribution that deviates from the Boltzmann equilibrium distribution, and leads to population of high lying vibrational states several orders of magnitude higher than predicted by the Boltzmann distribution. Figure 6.20 shows a Boltzmann and Treanor vibrational distribution. A vibrational temperature (T_{10}) of 3058 K and gas temperature (T_o) of 678 K are used, as determined previously from spectroscopic measurements. The vibrational temperature is used to determine the Boltzmann distribution given by Eq. 6.29, where N_1 and N_o are the first vibrational and ground state densities.

$$\frac{N_1}{N_o} = e^{\frac{-E_1}{T_{10}}} \tag{6.29}$$

In Eq. 6.29 the vibrational energy (E_1) for the asymmetric mode is given by Eq. 6.30.

$$\frac{E_{CO_2}}{hc} = \sum_i \omega_i(v_i + d_i/2) + \sum_{j \geq i} x_{ij}(v_i + d_i/2)(v_j + d_j/2) + x_{l_2 l_2} l_2^2 \qquad (6.30)$$

Where ω_i, x_{ij}, and $x_{l_2 l_2}$ are spectroscopic constants determined by experiment and $d_i = (1, 2, 1)$ is the degeneracy of the vibrational modes [85]. The Boltzmann distribution (Eq. 6.29) produces a linear relationship with respect to vibrational energy on a semi-log plot as seen in Fig. 6.20. The Treanor distribution, Eq. 6.31 [4], has a quadratic term in the exponential relationship with vibrational energy, Fig. 6.20.

$$f(\nu, T_{10}, T_o) = B \times exp\left(-\frac{\hbar\omega\nu}{T_{10}} + \frac{x_e \hbar\omega\nu^2}{T_o}\right) \qquad (6.31)$$

In Eq. 6.31, ν is the vibrational quantum number, $\hbar$ is reduced Planck's constant, ω is frequency of the vibrational level, B is a scaling factor, and x_e is an anharmonic correction. $\hbar\omega\nu$ is the vibrational energy of a harmonic oscillator with frequency $\hbar\omega$.

Figure 6.20 shows the vibrational distribution of the asymmetric vibrational mode for both a Boltzmann and Treanor distribution. At the vibrational temperature of 3053 K, only the low lying vibrational levels are populated for a Boltzmann distribution. Analyzing the Treanor distribution for the experimental gas and vibrational temperatures, it is observed that the

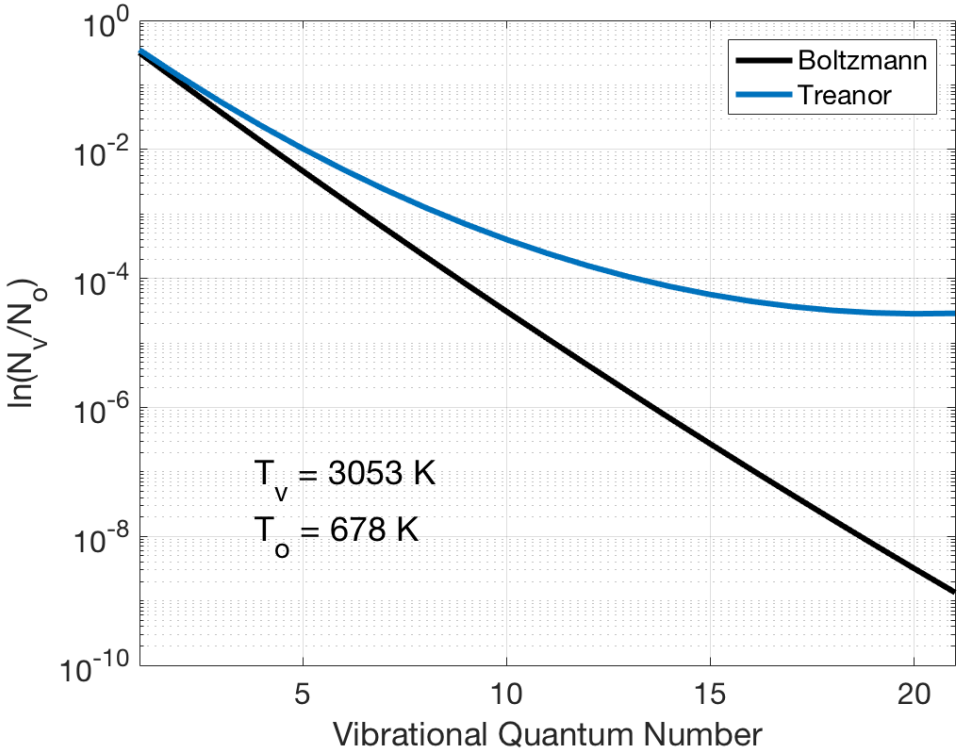

Figure 6.20: The vibrational distribution function of the asymmetric vibrational mode of CO_2 assuming a Boltzmann and Treanor Distributions

non-equilibrium nature of the discharge leads to over-population of higher lying vibrational levels. Additionally, the Treanor and Boltzmann distributions for low lying vibrational states ($\nu_3 < 4$) have similar vibrational populations.

The Treanor distribution does not account for vibrational-translation losses nor dissociation, and therefore is only an approximation to the actual VDF. In Fig. 6.20 the actual vibrational distribution will deviate from the Treanor distribution due to dissociation which results in depopulation of high lying vibrational states. Furthermore, in a single streamer discharge there

is not sufficient time (ns) for vibrational-vibrational relaxation which takes place over several hundred nanoseconds to a few microseconds, as discussed in section 7.2. Therefore, for a single streamer discharge only the first low lying vibrational levels are populated, while for pulsed discharges a Treanor "like" distribution will be observed (see section 7.2).

Based on the pulsed nature of the experiment (pulsed 4 MHz for 6 μs) vibrational pumping is expected leading to the population of high lying vibrational levels, and an increase in dissociation. This is confirmed by the comparison of the dissociation estimated from experiments $n_{co} = 2 \times 10^{23}$ m^{-3} and simulations $n_{co} = 10^{23}$ m^{-3}, section 7.2.

It is concluded that: (1) for single streamers only the low lying vibrational levels will be populated by electron impact reactions, (2) the Treanor distribution can be used to approximate multi-streamer discharges VDF's such as with these experiments, and (3) the vibrational temperature can be determined from a Boltzmann plot of the low lying vibrational levels ($\nu_3 < 4$) and used to predict the vibrational distribution assuming a Treanor distribution. Additionally, the higher lying vibrational levels reduced the energy barrier for dissociation of CO_2, and hence these levels tend to dissociate more easily which will increase the CO_2 conversion.

Chapter 7

Parametric Investigations and Optimization Strategies for CO_2 Reforming

The streamer discharge was determined to have a conversion percentage of $\frac{N_{CO}}{N_{CO_2}} = 0.01$ %. This low conversion percentage is due to the mechanism of conversion in streamer discharges. In streamers the dominant dissociation mechanism is through direct electron impact dissociation. The rate of this reaction is directly proportional to the electron density, and at atmospheric pressures non-equilibrium discharges (such as the streamer) are characterized by low electron densities $n_e < 10^{23}$ m^{-3} with ionization fractions less than a percent. These low densities, and the fact that streamers are constricted transient discharges, limits their conversion efficiency. Therefore, to optimize streamer discharges for dissociation, the population of low lying vibrational levels must be optimized such that the vibrational ladder climbing mechanism becomes efficient. In this section the effects of gas pressure and temperature, pulse frequency, and multiple streamers are analyzed.

7.1 Parametric Investigation: Pressure and Temperature

To determine the optimum streamer discharge conditions for excitation of low lying vibrational levels a parametric investigation was conducted. The study considered four pressures ranging from 1×10^3 to 2×10^5 Pa. The first asymmetric stretch vibrational level of CO_2 is analyzed to determine the optimal operating conditions. As discussed previously, the asymmetric stretch mode has slower VT relaxation than the symmetric and bending mode, and faster VV relaxation [4]. Therefore, population of the asymmetric stretch mode will lead to a non-equilibrium Treanor "like" distribution of the vibrational states resulting in dissociation, so long as $T_o < T_v$ [4].

Figure 7.1 shows the ratio of the first asymmetric vibrational level density to the background CO_2 density as a function of the background pressure. Four pressures are investigated: (A) 1, (B) 10, (C) 100, and (D) 200 kPa. For these simulations the gas temperature is held constant at 300 K. At low pressures (A) a diffuse glow discharge is observed. As the pressure is increased the discharge transitions from the glow state into a streamer (B-D). The glow discharge is characterized by a lower fractional population of $CO_2(v_3 = 1)$ when compared to higher pressures (D). Therefore, to achieve the highest population of vibrationally active states for streamer discharges, high pressures are desired. This is in direct contrast to microwave discharges which have their highest conversion efficiencies at sub atmospheric pressure [4, 57]. Experiments showed a similar trend with an increase in pressure resulting in higher electron

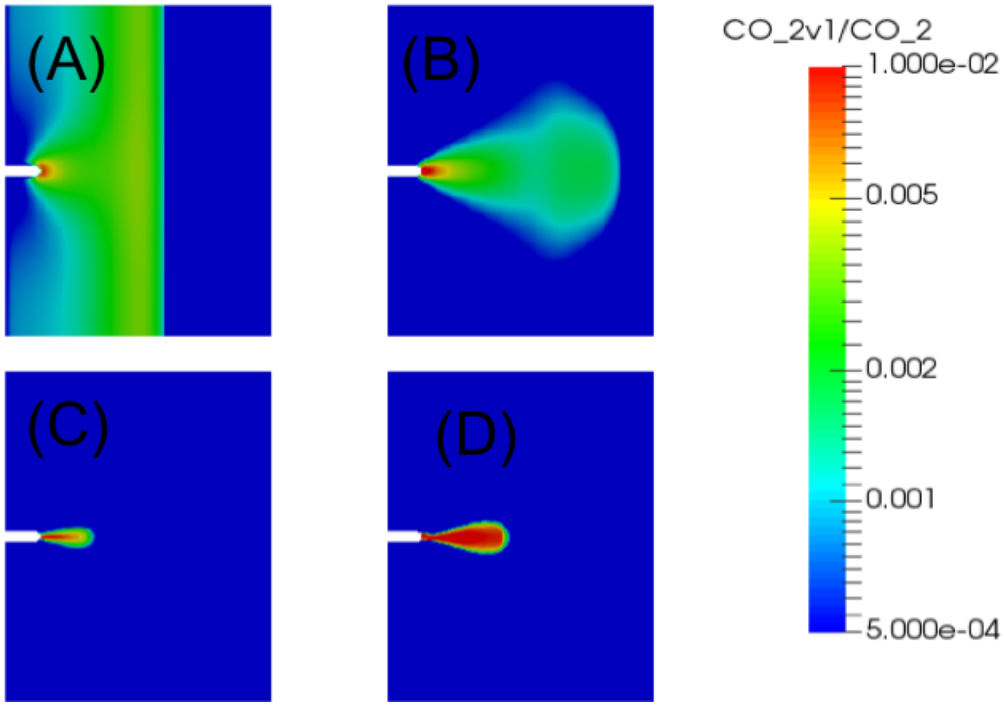

Figure 7.1: The ratio of the asymmetric vibrational density to the background CO_2 as a function of the background pressure: (A) $1 * 10^3$, (B) $1 * 10^4$, (C) $1 * 10^5$, and (D) $2 * 10^5$

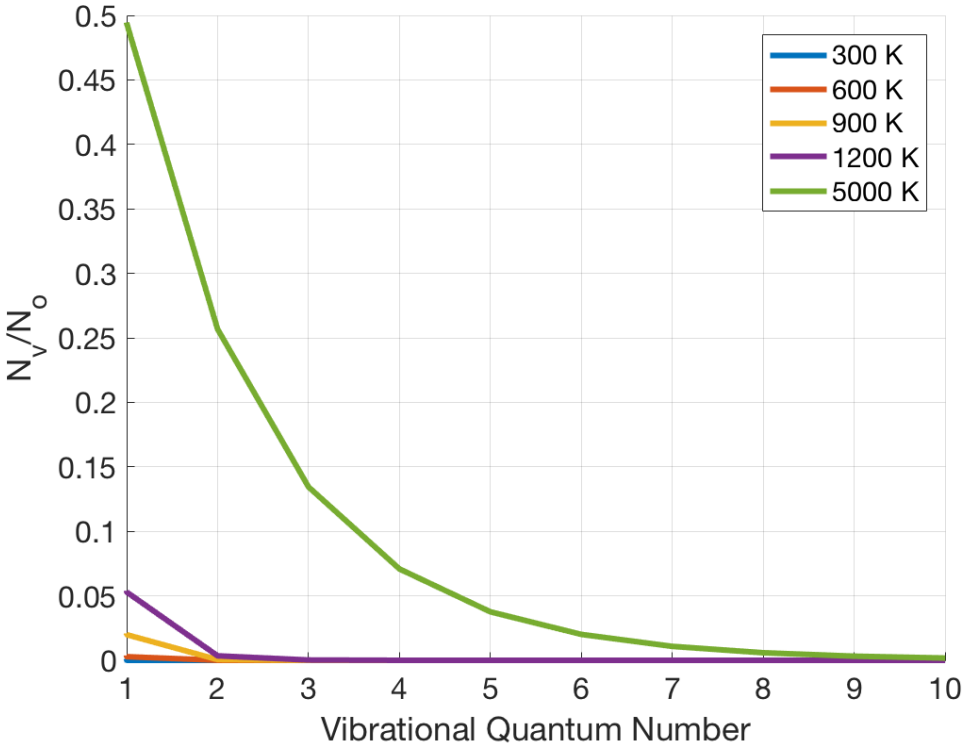

Figure 7.2: Vibrational equilibrium distribution as a function of temperature.

density, if the reduced electric field exceeds the breakdown threshold by ~ 1.5 times, as shown in Fig. 6.3.

An investigation on the effects of temperature was also conducted from 300-1200 K. The plasma fluid model results showed little dependence of gas temperature on the population of the first excited state of the asymmetric vibrational mode. This is explained by analyzing the equilibrium vibrational distribution function. Figure 7.2 shows the equilibrium vibrational distribution function for 300, 600, 900, 1200, and 5000 K. For those temperatures

investigated with the plasma fluid model (300-1200 K), the vibrational population of the first asymmetric level ($v_3 = 1$) varied by only 5%. This variation of 5% did not influence the streamer dynamics, nor population of the upper vibrational levels. It was not until the temperature exceeded 5000 K that significant populations with $v_3 > 1$ were observed.

To show the effects of vibrational relaxation as a function of the gas temperature, a 0D model with the same chemical mechanism was used to simulate the after-glow of the streamer discharges. To simulate the streamer pulse the electron Joule heating of a streamer discharge was determined from the 2D simulations, and was used as an external power source term for the 0D simulations. Figure 7.3 shows the relaxation of the first asymmetric level of CO_2 in the after-glow of a streamer discharge. It is evident from Fig 7.3 that for high gas temperatures the asymmetric vibrational mode relaxes quickly due to VT exchange. Therefore, a low gas temperature is desired to maximize the lifetime of excited vibrational levels in the streamer pulse. Then with subsequent pulsing the population of these levels can be increased leading to VV exchange (as discussed in section 7.2).

Though the vibrational population distribution established by the streamer discharge showed minimal response to gas heating, in the after-glow stage it is observed that the vibrational population distribution is reduced due to increased VT relaxation at elevated temperatures. For example, Eq. 7.1 [4]

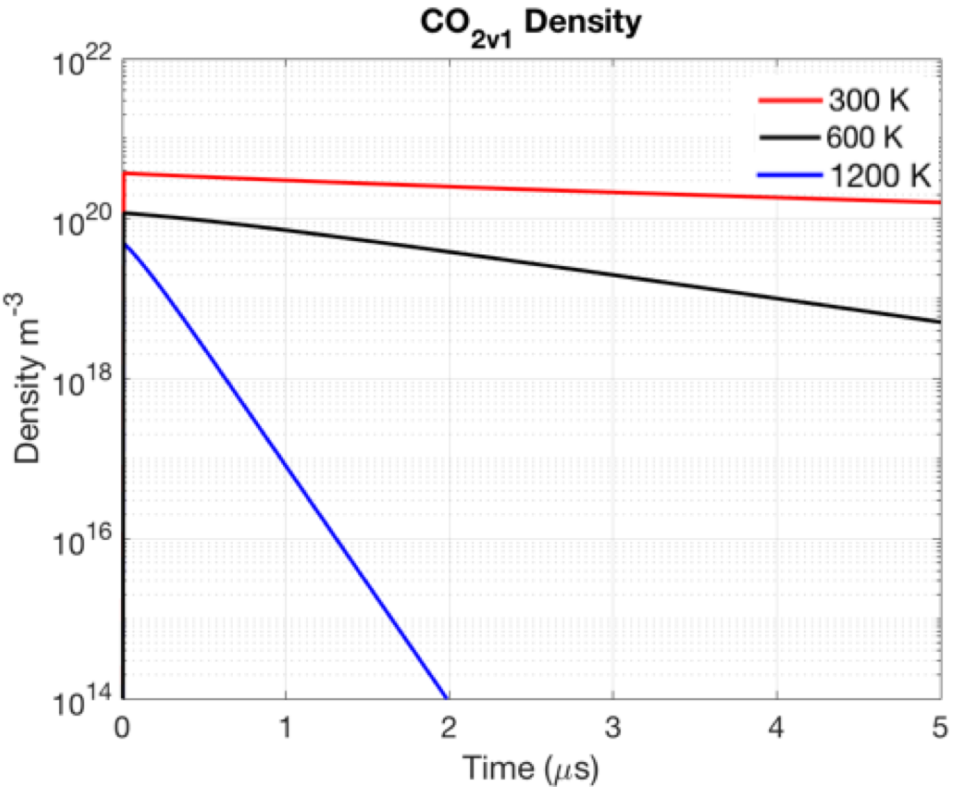

Figure 7.3: 0D simulation of the after glow of a streamer discharge showing the relaxation of the first asymmetric vibrational level ($v_3 = 1$) of CO_2 for three temperatures: 300 (red), 600(black), and 1200 (blue).

gives the rate coefficient for VT relaxation as a function of T_o.

$$k_{VT} \approx 10^{-10} exp\left(\frac{-72}{T_o^{\frac{1}{3}}}\right)\left[\frac{cm^3}{s}\right] \tag{7.1}$$

Evaluating Eq. 7.1 at the lower (300 K) and upper bounds (1200 K) of the temperature range investigated gives a factor of 50 increase in the VT relaxation rate. These estimates compared with simulations (Fig. 7.3) confirmed the fast relaxation at elevated gas temperatures.

To conclude, low temperatures and high pressures are desired to optimize streamer discharges. These conditions will minimize VT losses which increase exponentially with gas temperature. Additionally, maintaining the thermal non-equilibrium of the vibrational and translational degrees of freedom results in more efficient VV relaxation. This leads to an over population of highly excited vibrational levels, known as the Treanor distribution. These highly excited vibrational states ultimately result in dissociation through a non-adiabatic transfer between $CO_2(^1\Sigma^+)$ ground state and the electronically excited state $CO_2(^1B_2)$. The non-adiabatic transfer results in the most efficient dissociation mechanism requiring only the bond dissociation energy for CO_2, 5.5 eV, and acts as a secondary mechanism for dissociation in streamer discharges.

7.2 Effects of Pulsing

A multitude of streamers are present in a dielectric barrier discharge (DBD) reactor. In these DBD reactors several streamers process the gas stream

prior to exiting the chamber. Figure 7.4 shows a cylindrical DBD reactor (A). The gas enters the reactor from the right (1) and is processed as it transits through the chamber volume (3). The exit plane of the DBD reactor (2) is shown in (B) with the plasma ignited. The distinct glow discharge is observed in (B) and constricted structures may be observed. When looking closely, the plasma discharge observed in Fig. 7.4 (B) is a temporal integration of a multitude of single streamer elements. It has been shown experimentally in [78] that DBD reactors have a conversion efficiency of nearly 8%, which is three orders of magnitude greater then a single streamer (0.01%). To analyze the effects of multiple streamers in the conversion of CO_2 as well as the population of low lying vibrational levels, a 0D reaction kinetics model is used.

The 0D model is formed by neglecting the spatial terms in the plasma fluid model equations. To model the streamer a 2D axisymmetric model is used to determine the Joule heating profile for a single streamer element. The Joule heating profile is modeled as a square wave power source term in the governing equations. The Joule heating pulse is characterized by a width of 0.1 ns and a peak power of 5×10^{12} Wm^{-3}. Two pulse frequencies are investigated: 50 and 100 MHz. Figure 7.5 shows a Joule heating profile used for a pulse frequency of 100 MHz. The Joule heating profile is given by a 100 MHz square wave pulse with a on time of 0.1 ns.

In the timescales of the streamer discharge, the Joule heating is primarily deposited into the mobile electrons. These electrons then redistribute their energy through electron impact reactions with the background species

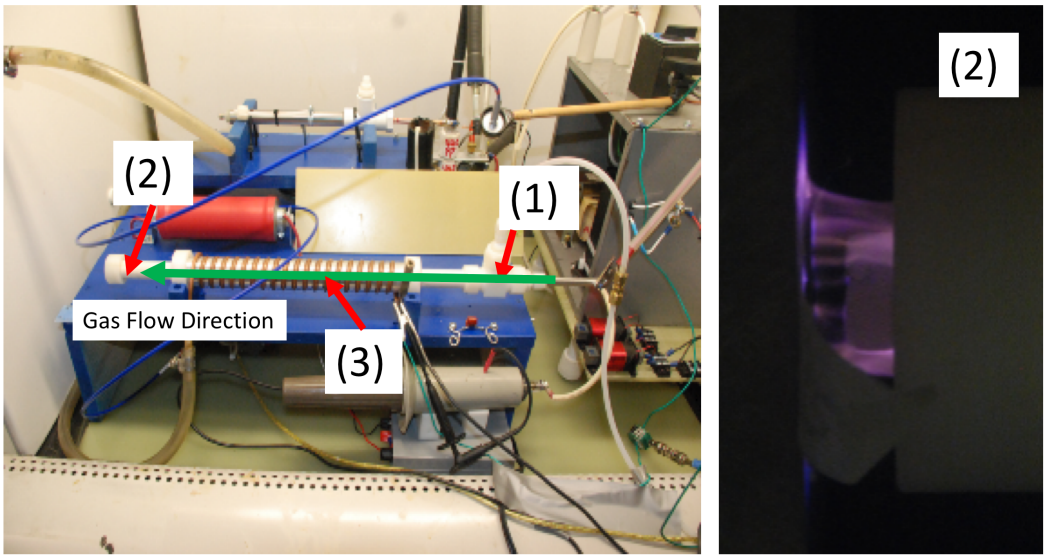

Figure 7.4: A DBD reactor (A) with the flow from right to left. The gas inlet (1) has two gas streams which are premixed prior to entering the discharge chamber (3). The plasma discharge (B) is shown at the reactor exit plane (2).

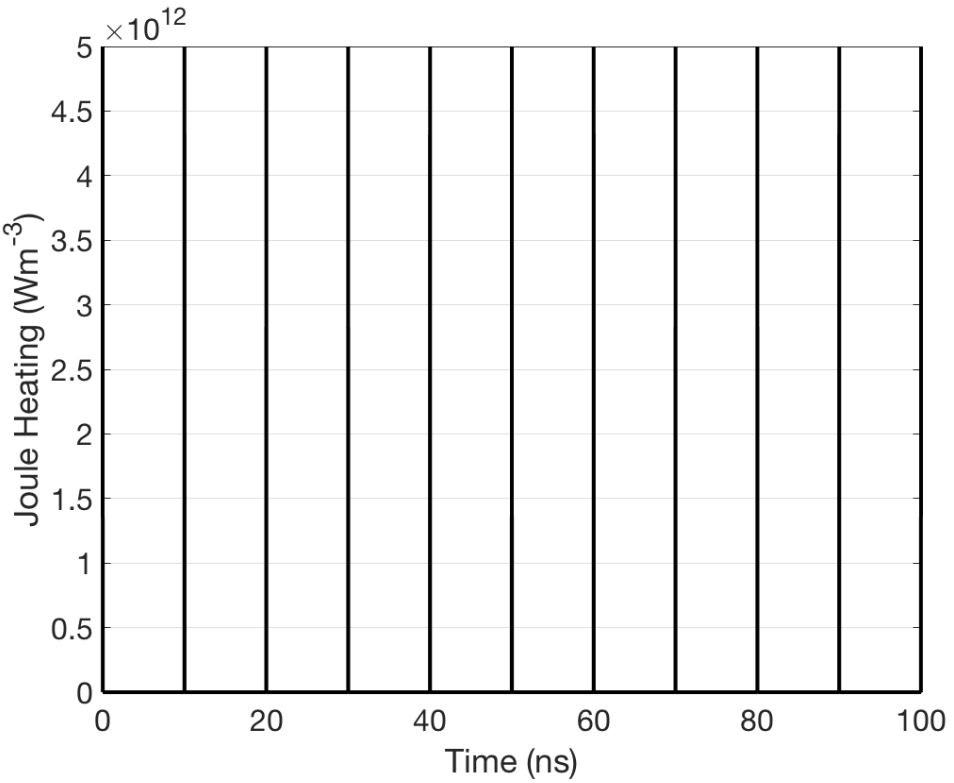

Figure 7.5: The Joule heating square pulse waveforms at 100 MHz and an on time of 0.1 ns.

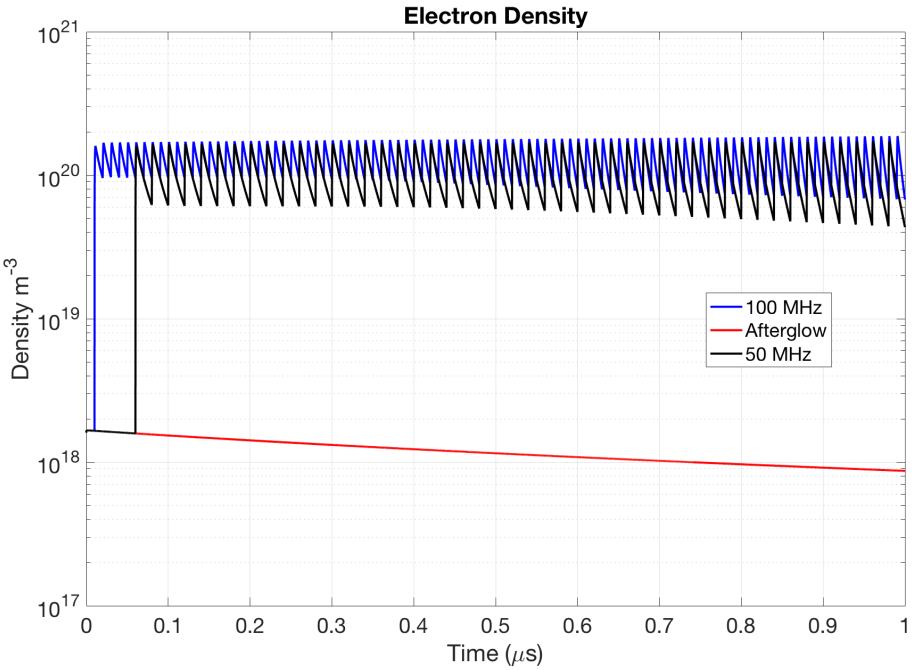

Figure 7.6: The effects of pulsing on the electron density. The 50 MHz case has been shifted temporally by 0.04 μs to stagger the plots for clarity. The afterglow is also shown in red, which has no pulsing.

resulting in population of excited species. But within 3 ns after the streamer discharge the electron temperature relaxes to the background temperature which results in a decrease in the rate coefficients for electron impact excitation reactions. Hence, the chemical kinetics after the pulse are governed by reactions with excited species and the background. To increase the conversion of CO_2 through the vibrational ladder climbing mechanism, a high density of these excited species are necessary. Therefore, in order to increase the population of these excited levels, particularly the low lying vibrational levels, a high density of electrons is required.

To increase the electron density, pulsing is used. Figure 7.6 shows the evolution of the electron density for two pulse frequencies: 50 and 100 MHz as well as the afterglow state. In the afterglow (red) a monotonic decaying electron density is observed. When the pulse frequency is increased to 50 and 100 MHz the electron density increases by approximately two orders of magnitude. The increase in the electron density as a function of frequency is related to the quenching rate for electrons which is dependent on the collision frequency, and therefore the pressure and temperature. The quenching rate for electrons for the conditions of this study was found to be: $8 * 10^{21}$ $(m^{-3}/\mu s)$. Considering the typical electron densities observed in streamer discharges, $10^{18} - 10^{21}$ m^{-3}, the electrons will be fully consumed within 1 μs. Therefore, the pulsing frequency must be greater than 1 MHz to prevent complete electron quenching.

In Fig. 7.6, at higher pulse frequencies one sees a gain in electrons from the initial streamer density (afterglow). Comparing the 50 and 100 MHz cases shows that the electron production is a non-linear function of the pulse frequency, with a clear upper limit dictated by electron energy loss reactions (consider a DC discharge where production and consumption are balanced).

Figure 7.7 shows the CO density as a function of the pulse frequency. In the afterglow (red) the CO density slowly decays while pulsing increases the CO density with higher pulse frequencies showing an increase in the CO density (50 vs 100 MHz). The CO concentration in the afterglow slowly decays (for the timescales considered) for two reasons: (1) the electron density is monotonically decreasing as seen in Fig. 7.6, and (2) the insufficient popu-

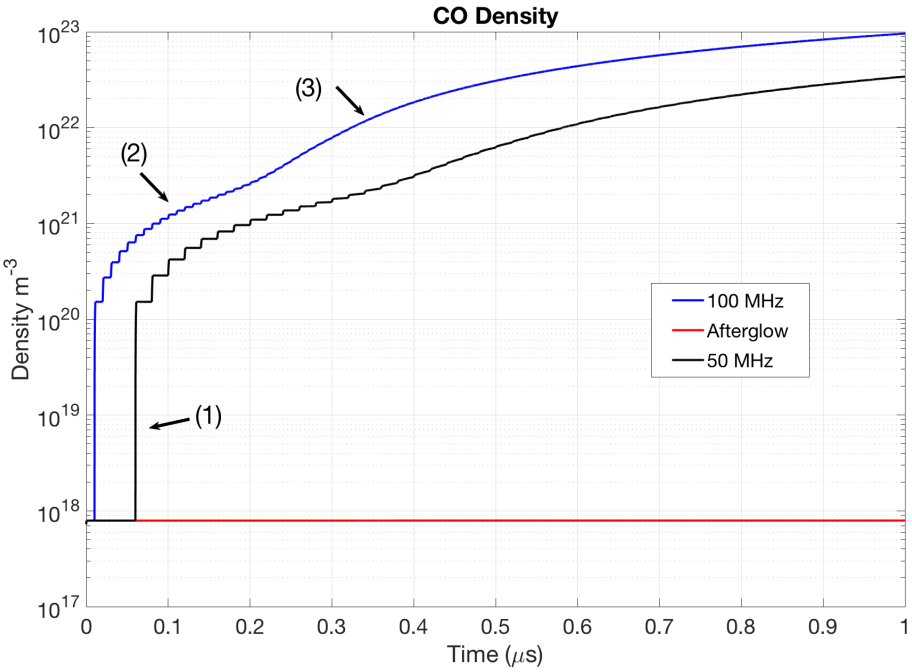

Figure 7.7: CO density as a function of the pulse frequency. The 50 MHz case has been shifted temporally by 0.04 μ s to stagger the plots for clarity. (1) corresponds to the increase in electron density due to the second Joule heating pulse, (2) corresponds to subsequent Joule heating pulses, and (3) shows the effects of vibrational ladder climbing. The red line indicates the non-pulsed afterglow state.

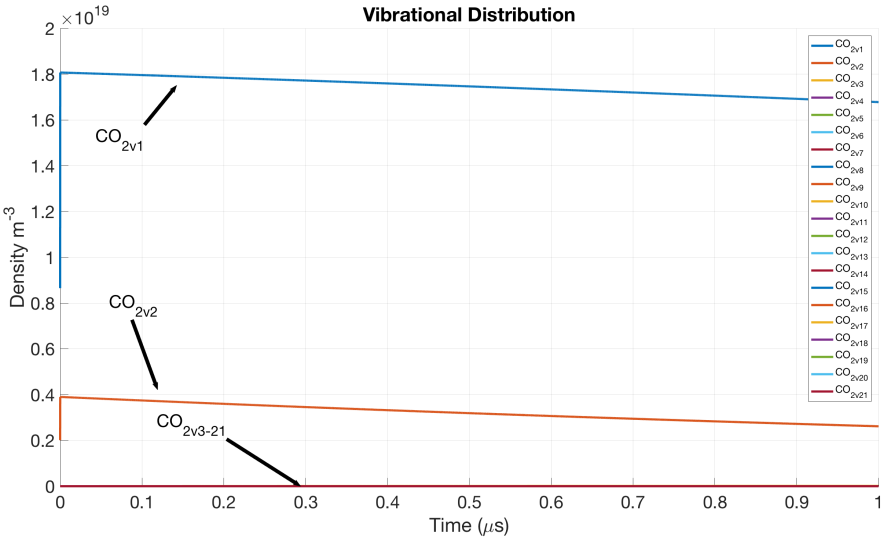

Figure 7.8: Vibrational distribution in the afterglow. Only the first two vibrational levels are populated.

lation of the first vibrational levels which are necessary for vibrational ladder climbing.

Figure 7.8 shows the asymmetric vibrational distribution for all 21 levels (v_3) considered in this model for the afterglow. At the electron densities observed (Fig. 7.6), only the first two vibrational levels are populated (Fig. 7.8). This indicates that the dominant mechanism for CO dissociation is through electron impact dissociation, and that there exist a minimum population of the first asymmetric vibrational level before the ladder climbing mechanism becomes significant.

For pulse frequencies of 50 and 100 MHz, three distinct features are observed in the CO density (Fig 7.7): (1) a sharp discontinuity where the

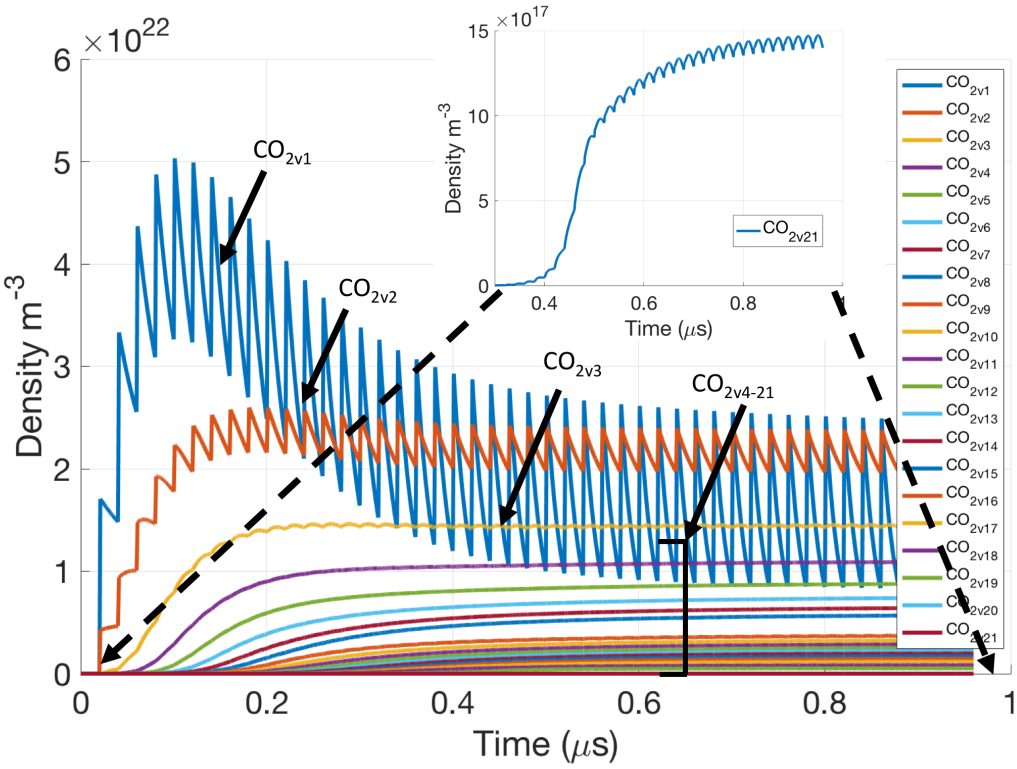

Figure 7.9: Vibrational distribution at 50 MHz. Vibrational ladder climbing can be seen by the population of high vibrational levels. The plot is time shifted by $0.04\mu s$ *to maintain the same location as the previous plots.*

CO density increases by two orders of magnitude due to the second Joule heating pulse, (2) subsequent increases due to additional Joule heating pulses, and (3) increase due to the effects of vibrational ladder climbing. The initial Joule heating pulse increases the electron density (Fig. 7.6) by two orders of magnitude. With the increase in the electron density the inelastic collisional losses also increase by two orders of magnitude while the Joule heating pulse remains constant. Therefore, in subsequent pulses the electron density is limited to $1 - 2 \times 10^{20}$ m^{-3} for these conditions. The CO density initially follows the same trends as the electron density (1 and 2 in Fig. 7.7). This is because the dominant reaction mechanism for CO production at these times is through direct electron impact dissociation. For times greater than 0.2μs for the 100 MHz case and 0.3μs for the 50 MHz case, a secondary mechanism for CO production is observed. This secondary mechanism is attributed to the vibrational ladder climbing mechanism, since the electron density remains fixed (Fig. 7.6).

Figure 7.9 shows the vibrational distribution of the 21 asymmetric vibrational levels considered in the model for a pulse frequency of 50 MHz. Several key features are observed in this plot:

1. The first three vibrational levels respond to the Joule heating pulse each with a reduced magnitude. This is due to the scaling of the electron impact cross-sections for vibrationally excited states, given by the Fridman approximation, Eq. 4.18. The Fridman approximation shifts and scales the cross-sections for vibrationally excited levels.

2. For the critical electron density of $\sim 10^{21}$ m^{-3} achieved by high pulse frequencies (50 and 100 MHz), CO_{2v1} becomes sufficiently populated that vibrational ladder climbing occurs. This results in significant population of the high vibrational levels, including CO_{2v21} which shows an increase of over four orders of magnitude (see the insert in Fig. 7.9).

3. Each vibrational level is shifted in time. This is a consequence of the collision frequency of the excited species and the finite time required for vibrational ladder climbing mechanism to occur.

Therefore, from the above observations, the increase in CO density observed in Fig. 7.7 (3) must be attributed to the dissociation of CO_2 via the ladder climbing mechanism.

Figure 7.10 shows the vibrational distribution function determined for the 50 MHz pulsed streamer discharge at 0.8 μs, (red). A quasi-equilibrium is observed in the streamer vibrational distribution function (VDF) within the first microsecond of pulsing. The streamer vibrational distribution function is compared with Boltzmann distributions at two different temperatures: the gas temperature 300 K (solid black), and a vibrational temperature of 2000 K (dotted black). The Treanor distribution for the above defined gas and vibrational temperatures is also plotted (blue).

In Fig. 7.10 the vibrational distribution for the pulsed streamer discharge shows population of the high vibrational levels, and deviation from both the Boltzmann and Treanor vibration distribution functions (VDF's).

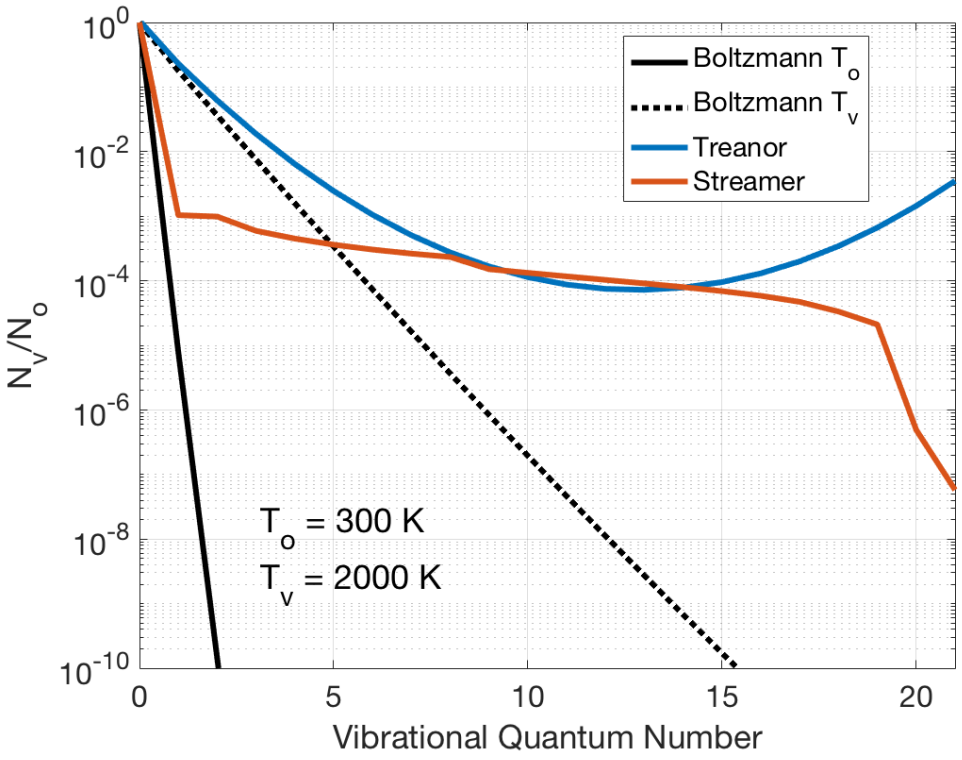

Figure 7.10: Streamer vibrational distribution at 50 MHz (red) compared with a Boltzmann distribution at 300 K (solid black) and 2000 K (dotted black), and a Treanor Distribution (blue) with a gas 300 K, and vibrational temperature of 2000 K.

The deviation from Boltzmann is expected due to the non-thermal nature of the discharge. In the case studied a high power density and low gas temperature are used, but if the gas temperature (vibrational-translational relaxation) is increased, and the power density lowered (vibrational excitation), then both the Treanor distribution and the observed vibrational streamer distribution will tend to the equilibrium Boltzmann distribution ($T_v \rightarrow T_o$).

The observed vibrational distribution also deviates from the Treanor distribution. This is because the Treanor distribution is derived for the anharmonic oscillator without dissociation nor vibrational-translational losses [4, 64]. Dissociation leads to depopulation of the highly excited vibrational levels. This is attributed to the decrease in the activation energy for dissociation reactions of highly excited vibrational levels. The decrease in activation energy of these levels increases the dissociation rate coefficients which leads to depopulation of the high lying vibrational levels. Vibrational-translation relaxation is responsible for vibrational energy losses, and without it the vibrational temperature and VDF are over predicted.

7.3 Multi-Streamer Interactions

In the design of a DBD reactor the pulsing frequency (discussed previously) as well as the relative spatial spacing of the streamers must be considered. Here, the effects of multiple streamers distributed spatially in a linear array is analyzed to determine the optimal electrode spacing for a DBD reactor. To study these effects, a reduced chemical mechanism consisting of a

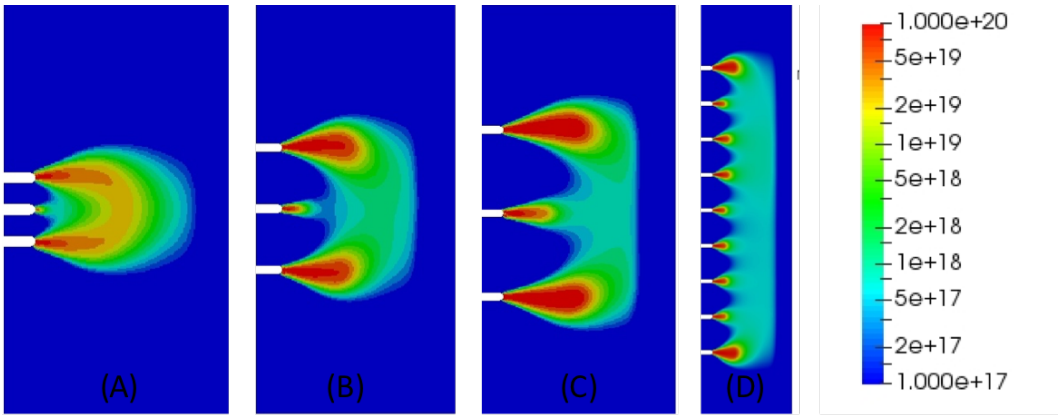

Figure 7.11: Electron density contours (m^{-3}) for a three component plasma. A three electrode linear array was investigated for electrode configurations with L/D's of: 2 (A), 6 (B), 9 (C). A 9 element linear array was used with L/D of 7 (D).

three component plasma is used. The species used in the model are: CO_2, CO_2^+, and electrons. The model does not seek to understand the chemical kinetics of multiple streamer discharges which is anticipated to be the same as that discussed in the previous sections, but rather it seeks to understand the dynamics of interacting streamers. Additionally, by only considering a three species plasma, the computational time is significantly reduced which allows multiple 2D axisymmetric fluid models to be investigated.

Figure 7.11 shows the results of four simulations of a three component CO_2 plasma. The ratio of the electrode diameter to the inter-electrode spacing, L/D, where L is the inter-electrode spacing and D is the electrode diameter, was varied between $L/D = 2$ (A), 6 (B), 9 (C), and 7 (D). Additionally, in A-C a linear array of three electrodes was investigated, while D consisted of 9 uniformly spaced electrodes.

When L/D is small (A), the outer streamers suppress the inner streamer preventing its growth. The suppression is caused by the electrostatic repulsion between the streamers, and is a function of L/D. At these narrow spacings of order $L/D = 2$, the streamers merge forming a leader channel. A leader channel is a highly conductive region. In this conductive region the current increases which results in significant Joule heating, and an increase in the gas temperature [105, 106]. The increase in gas heating is not desirable for CO_2 dissociation, since VT relaxation increases with gas temperature.

To prevent the streamers from merging, L/D is increased. As the distance between the streamer discharges is increased, the electrostatic repulsion decreases, Fig. 7.11 (B-C). It is seen in Fig. 7.11 that at these applied field and for $L/D > 6$ (B), the streamer suppression is insignificant. As seen in Fig. 7.11 (C), the inner streamer is shielded slightly by the outer streamers, but the densities remain similar to the outer dominant streamers. Furthermore, the streamers produce a relatively uniform high electron density region in the volume of the domain with the outer dominant streamers propagating faster than the electrostatically shielded inner streamers.

An L/D condition for non-interacting streamers was determined to be $L/D > 6$ based on Fig. 7.11. The L/D ratio can be used to define a packing factor for the streamer discharge. The packing factor, P, is defined as the ratio of the streamer volume to the volume of the discharge region as given by Eq. 7.2 [105].

$$P = \frac{l \times D}{l \times D + l \times L} = \frac{1}{1 + \frac{L}{D}} \tag{7.2}$$

The packing factor determines the maximum density of non-interacting streamer discharges possible for a DBD reactor. Figure 7.11 (C) shows an array of 9 streamer discharges with a $L/D = 7$. This L/D corresponds to a packing factor of $P = 0.125$, or 12.5 % of the discharge volume is occupied by streamers. Therefore, to have non-interacting streamers a large portion of the discharge volume remains unused. To increase the packing density the electric field must be minimized.

Chapter 8

Surface Streamers for Thermal Plasma Ignition

[1] A non-equilibrium atmospheric streamer discharge was investigated as a means to seed a large gap arc breakdown as discussed in Appendix A. The previous work focused on thermal plasma-material interactions. Many of the applications for thermal discharges (and non-equilibrium) require relatively large volumes to enhance process throughputs. The large volume also means that the inter-electrode distances are large, with the concomitant problem of unrealistically high gas breakdown voltages, resulting from the Paschen breakdown condition. For example, in atmospheric air the breakdown electric field is ∼30 kV/cm, hence several 100 kV would be necessary for large scale reactors. With the surface streamer ignition source described herein, arc breakdown for a 10 cm inter-electrode gap at atmospheric pressure in argon was demonstrated at voltages as low as 1.6 kV. For these gap distances, the Paschen breakdown voltage was $\sim$ 100 kV.

[1]This work has already been published in: M. V. Pachuilo, F. Stefani, R. D. Bengtson, Dipti, R. Srivastava and L. L. Raja, "Dynamics of Surface Streamer Plasmas at Atmospheric Pressure: Mixtures of Argon and Methane," in IEEE Transactions on Plasma Science, vol. 45, no. 7, pp. 1776-1787, July 2017. doi: 10.1109/TPS.2017.2711604. The author is the main contributor of this work. Srivastava and Dipti conducted the CR modeling.

In other pulsed thermal discharges of similar scale, a thin metal fuse wire was used to short the electrodes. When the discharge was initiated, large currents passed through the wire causing it to vaporize. The metal vapor plasma then generated a conduction pathway at voltages below the Paschen breakdown threshold [22, 107]. The approach described here, eliminates the need for a fuse wire, and the associated problems of mechanically mounting the wire for each breakdown event and the resulting metal contamination. Importantly, the surface streamer approach generates a seed plasma in the same gas medium as the arc, and allows for repetitive operation at high frequencies for pulsed arc applications.

A systematic study of the mechanisms of a surface streamer discharge, for ignition of a large-gap, low-voltage, pulsed arc discharge in argon-methane mixtures is presented. An inert argon background gas has been chosen in order to isolate the effects of methane on the development of the surface streamer. Several applications involving streamer discharges in methane, e.g. dry reforming of methane for hydrogen production, provides the backdrop that motivate the studies presented in this work.

The streamer was analyzed with instantaneous broadband imaging, photodiode light intensity, and current-voltage measurements. The temporal evolution of the discharge included a localized surface corona and a positive surface streamer. The addition of small concentrations of methane suppressed ionization. This inhibited surface streamer propagation and ultimately prevent arc transition.

The results of this work are summarized here:

1. The electron temperature was determined from time and spatially averaged spectra and a collisional-radiative model. The electron temperature in argon was measured to be 1.25 eV for an electron density range of $10^{19} - 10^{21}\ m^{-3}$.

2. Partial local thermodynamic equilibrium calculations showed that the Ar II 4p states followed a Boltzmann distribution with an excitation temperature of 0.7 eV.

3. The gas temperature was estimated at 815 K from a black-body distribution.

4. The velocity of the surface streamer in argon was estimated at 100 km/s with a diameter of 500 μm.

A full description of the work is found in [108].

8.1 Experimental Apparatus

Figure 8.1 shows an overview of the experimental setup. For these studies which involve only the streamer phase, arc formation is prevented by using a 500 pF capacitor in series with a large resistance of 100 MΩ in the main electrode power supply. The large resistance was used to current-limit the discharge, and prevent arc formation. The capacitor allowed the system to be charged to typical arc operating voltages while limiting the available

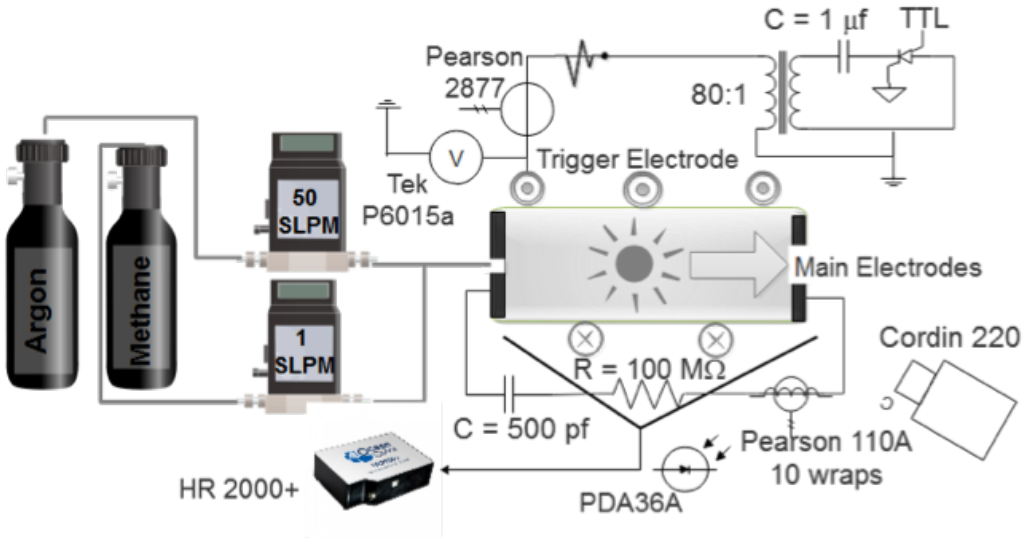

Figure 8.1: Schematic of the experimental setup. High purity gas cylinders provide feed gas for the plasma discharge. Each gas stream was monitored with a flow meter prior to mixing and entering the chamber. The main electrodes were not charged during the application of a negative high voltage pulse to the trigger electrode. The discharge diagnostics included: voltage, current, light intensity, instantaneous broadband imaging, and spectral irradiance measurements.

energy into the discharge. The high voltage trigger pulse was generated when a 1 μF capacitor charged to 500 V was discharged into an 80:1 automotive step-up transformer. An applied voltage across the main electrodes of 1-5 kV (characteristic arc charge voltages) had no significant effect on the surface streamer discharge dynamics. Hence, in the work presented here, discussion will be limited to test cases where the main electrodes were grounded and only the trigger electrode was pulsed.

8.2 Streamer Discharge Characteristics in Argon

As the applied voltage pulse increases, no current nor light emission is observed until a critical breakdown voltage (V_B) is reached. At this voltage, a sharp increase in light and current is registered. After this critical breakdown voltage, a sharp decrease in the applied voltage (voltage unloading) occurs. This initial event is defined as the primary discharge pulse. During a single pulse transient, multiple current pulses and voltage unloading events are observed. Each of these events are labeled as primary, secondary and tertiary pulses. The secondary and tertiary pulses have significantly less light emission and current. Therefore, the main focus will be on the primary pulse, as it is most likely to lead to arc formation.

The primary pulse occurs at the lowest applied voltage which is defined as the breakdown threshold, V_B. The plasma breakdown potential,V_p, is directly proportional to the applied breakdown voltage (V_B) owing to the presence of the quartz dielectric. Figure 8.2 shows the typical characteristics for a primary discharge pulse in argon. It is important to note that the photodiode response time is $\sim$160 ns for the required gain setting to acquire sufficient signal to register the discharge. Therefore, the slow rise and decay of the photodiode signal is related to this characteristic response time.

Initially, there is no current registered until the plasma breakdown voltage (V_p) is reached. The photodiode signal precedes the current by about 150 ns; this is caused by the slow response time of the photodiode and manually shifting the signal. At the applied breakdown voltage (V_B) of 17.4 kV, a sharp

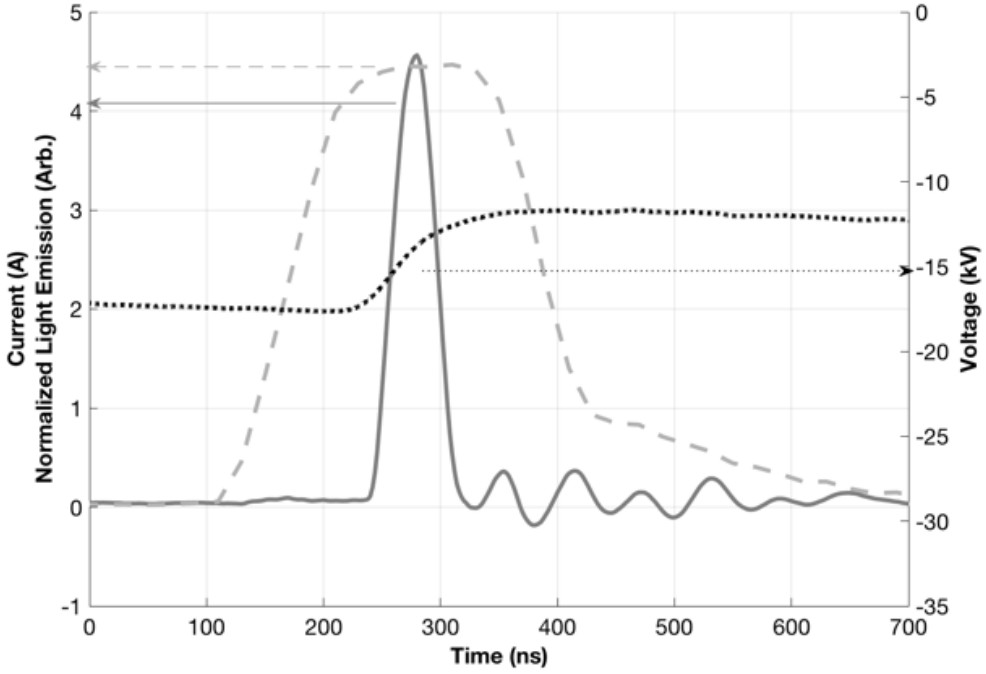

Figure 8.2: Typical argon voltage-current characteristics on the trigger electrode and the photodiode signal measured for a primary streamer pulse. The dotted black line indicates the voltage (P6015a), and the dark gray solid line specifies the current waveform (Pearson 2877). The dashed light gray line indicates the scaled photodiode signal with 20 dB gain and 1 MHz bandpass (∼160 ns response time).

increase in the current is observed with a peak current 4.6 A (i_p). The primary current pulse has a FWHM of 43 ns, while the voltage unloading lasts 120 ns. The peak of the light intensity corresponds with the peak in the current pulse. The location of the peak light emission is also confirmed by instantaneous broadband images taken throughout the duration of the pulse.

After the current pulse, light emission is still observed. The slow decaying tail of the photodiode signal indicates that residual excited species (typically associated with the Ar I $3p^5 4s$ metastable state) remain, even after the power deposition phase of the discharge. The power deposition phase is defined as the time when the current is non-zero and the voltage trace exhibits an unloading. This phase lasts 100 ns, while a luminous phase exists for 600 ns. The peak power and energy is calculated for the primary streamer pulse and found to be: 81 kW and 8.1 mJ respectively. After the power deposition phase, ringing persists in the current trace. This ringing is likely the result of the inductance of the experimental apparatus.

8.3 Estimation of electron density from VI characteristics

The electron number density is estimated from the conduction current density of the primary pulse, as defined by:

$$j_c = e n_e \mu_e E \tag{8.1}$$

Here j_c is the conduction current density, n_e is the number density of electrons, e is the elementary charge, μ_e is the mobility of electrons, and E is the electric field. In Eqn. 8.1, it is assumed that the electrons are the main current carrying species during the 100 ns pulse. To estimate the electron number density, the conduction current density must be determined as well as the electric field. First, an estimate of the current density through the discharge is made by estimating the conduction current as well as conduction area. The total measured current consist of three components: the probe current, the discharge current (conduction current), and displacement current. The probe current is determined from the resistance of the probe and voltage, and is negligibly small (order of 1 mA). The displacement current is determined by estimating the system capacitance without a discharge, C_{eff}, and the time rate of change of the voltage ($\frac{dV}{dt}$) signal, given by:

$$j_d = C_{eff}\frac{dV}{dt} \tag{8.2}$$

The current density also requires estimation of the conduction area. To estimate the conduction area an instantaneous broadband image of the discharge was used. The effective conduction area is estimated from Fig. 8.3 which shows a long exposure (300 μs) image of a typical discharge in argon. The gas inlet which also serves as the anode of the chamber was located at the right in the figure.

A constricted filamentary discharge forms at the right main electrode and branches out into multiple filaments, which follow along the helically

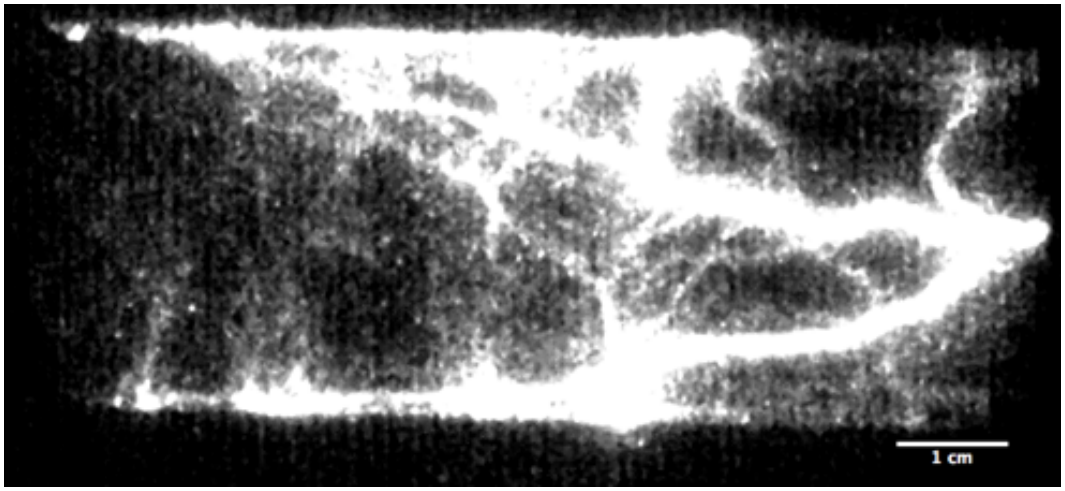

Figure 8.3: Long exposure image of the entire trigger electrode pulse (300 μs) in argon. The main electrodes were grounded as the trigger electrode was pulsed negatively. Gas flow is from the gas inlet at the right to the gas exit on the left. A constricted streamer filament emerges from the gas inlet and propagates in the regions of the helically wound trigger electrode until completely bridging the main inter-electrode gap.

wound trigger electrode. The peak light intensities are observed around the embedded trigger wire, with more intense illumination at the top and bottom of the chamber. These regions of peak intensity are due to the three-dimensionality of the chamber and line of sight integration (2D) of the ICCD. A less luminous, diffuse discharge exists along the dielectric surface between the wraps of the trigger electrode.

In the vicinity of the right main electrode (gas inlet), the conduction area of the constricted filament is estimated by assuming a uniform cylindrical streamer with a 500 μm diameter. The diameter is estimated from averaging a series of instantaneous broadband images taken during multiple primary discharges. In the region where the streamer made contact with the left main electrode (gas exit), the conduction area is estimated as an annulus, assuming the same streamer diameter as above. Taking the circumference of the main electrode and multiplying by the streamer diameter gives an estimate of the second conduction area.

The electron number density is calculated using the current density, and an estimate of the mobility and electric field. Previous experiments showed that the mobility in argon was equal to 0.03 $\frac{m^2}{Vs}$ [109, 110], and a simple electrostatic simulation gave an estimate of 66 Td for the reduced electric field. With these parameters and Eqn. 8.1, the electron number density is estimated to be $1.7 \times 10^{19}\ m^{-3}$, which is in agreement with spectral measurements presented in section 8.5. It is important to note that the electron density is sensitive to the conduction area, and varied by orders of magnitude depending on the

geometry assumed. For example, if we assume two streamers of equal diameter (500 μm) at the inlet and exit, we get a density of order $10^{21}m^{-3}$. Therefore, the bound for the electron density estimates from the current density varies between $10^{19} - 10^{21}m^{-3}$.

To check the validity of these electron density measurements, we assume that the plasma was in local thermodynamic equilibrium (LTE). In LTE, the upper state populations follow a Boltzmann distribution, and the Saha equation (Eqn. 8.3) is used to estimate the upper limit of the electron density. The electron temperature is assumed to be 1.25 eV, which is taken from the collisional-radiative model presented later.

$$\frac{n_e n_i}{n_o} = \frac{2g_i}{g_o a_o^3}\left(\frac{k_B T_e}{4\pi E_H}\right)^{3/2} exp\left(-\frac{E_{0i}}{k_B T_e}\right) \tag{8.3}$$

In Eqn. 8.3 n_e, and n_i are the number density of electrons and ions respectively. The ion and electron number densities are assumed equal for a quasi-neutral, singly ionized, argon plasma. n_o is the neutral number density. g_i and g_o are the degeneracy of singly ionized argon state and the neutral state, while a_o is Bohrs radius. E_H is the ionization energy of hydrogen (13.6 eV), T_e is the electron temperature, and k_B is Boltzmanns constant. E_{0i} is the ionization energy for argon (15.76 eV). Using the necessary fundamental constants, degeneracy of states, and ionization energies, the upper limit of the electron density (assuming LTE) is found to be: $n_e^{LTE} = 2.23 \times 10^{23}\, m^{-3}$. The density estimates are below the LTE limit, and are in good agreement with other authors for non-equilibrium atmospheric discharges in argon [109].

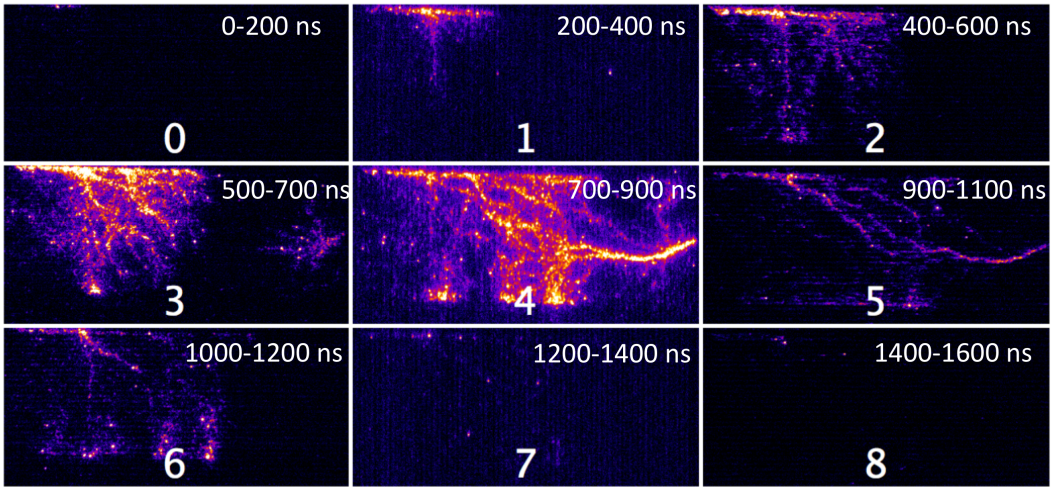

Figure 8.4: Time evolution of a surface streamer during the primary unloading pulse. Each frame had a gate time of 200 ns. Each row of images corresponded to an independent primary pulse. Frames 0-2 started prior to the unloading pulse. Frame 2 and 3 were overlapped by 100 ns. Frames 3-5 cover before and after the primary unloading. Frame 4 captured the peak of current pulse. Frames 6-8 were taken after the primary pulse with frame 5 and 6 overlapping by 100 ns. The time labels are for reference and do not correspond to times of Fig. 8.2.

8.4 Instantaneous Broadband Imaging of Surface Streamer

Instantaneous broadband intensified image sequences were taken throughout the voltage pulse prior to and after the primary discharge. Fig. 8.4 shows the discharge dynamics throughout the primary voltage pulse. Each row of image sequences (0-2, 3-5, and 6-9) were taken from three independent tests. Within each image sequence group, three exposures were acquired for a single test case. All of the image sequences were taken with a 200 ns gate time and aligned throughout the voltage pulse. Overlapping of camera integration periods occurred for the independent tests due to jitter associated with the triggering of the discharge.

Initially, there is no light emission observed. At 400 ns prior to the voltage unloading, a corona forms around the left trigger electrode (Fig. 8.4 image sequence 0). The photodiode does not have the sensitivity to resolve the coronal discharge, and only registers emission during the streamer discharge, and in the afterglow (Fig. 8.2). As the voltage increases towards the breakdown threshold, a streamer channel forms (Fig. 8.4 image sequence 1). The streamer channel initiates at the main electrode (anode) and propagates along the quartz dielectric (cathode) towards the initial localized coronal region. The streamer follows the helically wrapped trigger electrode, and deposits charge along the surface as it progresses (Fig. 8.4 sequence 2). Once the voltage unloading is reached, a sharp increase in luminosity is observed (Fig. 8.4 sequence 3), and a secondary cathode directed streamer forms near the gas inlet (right side). After the primary voltage unloading occurs, the two cathode-directed streamers merge, bridging the main electrode gap (Fig. 8.4 sequence 4). Shortly after the main power deposition phase, the discharge quickly dissipates (200 ns) leaving an afterglow of the primary streamer and surface discharge regions (Fig. 8.4 sequence 5). At 400 ns after the main pulse, a coronal discharge remains localized around the high voltage trigger electrode (Fig. 8.4 sequence 6), and slowly decays until no light emission is observed (Fig. 8.4 sequence 6-8).

An estimate of the streamer velocity and diameter were determined from an average of several independent instantaneous broadband images. Each image consisted of three image sequences, each separated by 200 ns. An aver-

age of four independent tests were used to estimate the propagation velocity. An estimate of the length of the surface discharge for each image sequence was calculated from the number of pixels and a scale factor. Hence, knowing the length and the time between each image sequence (200 ns), the velocity for each test could be determined. When the streamer branched as it tracked along the surface, the ionization front was used to estimate the propagation velocity (V_p). Using this method, the velocity in argon is: $94 \pm 44\ km/s$. The large error associated with this measurement is due to the low spatial resolution of the imaging setup.

The diameter of the streamer was estimated from a single instantaneous broadband image integrated over the entire pulse duration. Since the streamer tracks along the surface, the diameter was estimated from the volume streamer formed at the gas inlet. The diameter was calculated from the number of pixels across this filament and a scale factor. Using a scale factor of 290 μm per pixel, the diameter (ψ, is estimated at $500 \pm 290\ \mu m$. The large error in estimating the diameter (and velocity) is due to the low spatial resolution of the imaging setup, as evident in the scale factor.

The instantaneous broadband image sequences show that cathode directed streamers emerge from both the main electrodes. The left streamer preferentially tracks along the dielectric surface following the embedded trigger wire, while the right streamer initializes in the low-density gas inlet region. This streamer at the gas inlet will be defined as the main filament. In the interior of the chamber, smaller streamer filaments branch out from the main

filament. These smaller streamers then propagate towards the localized surface discharge regions. Once the ionization pathway forms between the main electrodes, an arc breakdown can be ignited.

8.5 Argon Spectroscopy

The thermodynamic properties of the streamer were estimated from spatially and temporally averaged spectral measurements. The light emission was integrated over 1000 pulses to accumulate sufficient light because of the low emission of the discharge and resolution of the instrument. Hence, each streamer pulse was assumed to be independent with similar structure and emission characteristics. From the integrated light emission, estimates of the average electron temperature and density were made. In determining the thermodynamic properties, the light emission from the streamer was assumed to dominate and coronal emissions neglected. This assumption can be justified since streamer electron number densities are $\sim$1000 times greater than coronal discharges. Fig. 8.5 shows the spectrum for an atmospheric argon streamer in spectral irradiance vs wavelength. The relative spectral irradiance was determined from a calibrated tungsten filament source which was NIST certified.

The spectrum consisted of both line and continuum radiation. The line radiation consisted of neutral argon and three singly ionized argon lines denoted as argon I and argon II, respectively. Continuum radiation was observed in the NIR/IR region and in the NUV. The continuum radiation consisted of

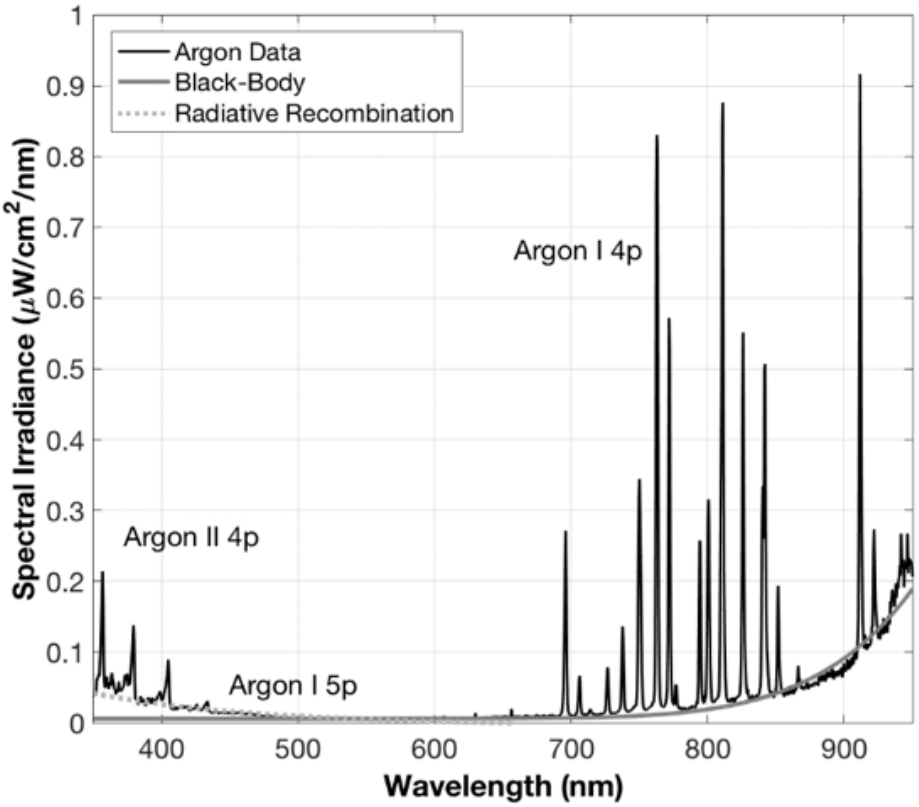

Figure 8.5: A time and spatially integrated argon spectra. Line radiation dominates the spectrum with neutral (Ar I) 4p and 5p argon lines and argon singly ionized lines (Ar II). The solid black line indicates the experimental spectrum. The solid gray line is a black-body fit with a temperature of 815 K, and the dotted gray line is a radiative recombination fit with a temperature of 0.7 eV and density of $2 \times 10^{20}\, m^{-3}$

Bremsstrah-lung, and radiative recombination. Radiative recombination must be considered for the region below 500 nm, while Bremsstrah-lung/absorption radiation should be considered above 500 nm. The effects of Bremsstrahlung radiation have been neglected for the spectral region where radiative recombination dominates (<500 nm) [111].

The argon spectrum was then analyzed via two methods: equilibrium thermodynamic considerations, and a more robust collisional-radiative (CR) model coupled with the spectral measurements. Though streamer discharges are highly transient and not in thermal equilibrium, an LTE approximation still provides insight into the plasma parameters. In addition, the LTE assumption can provide bounded estimates for the electron temperature and density. LTE presumes that the plasma processes are collisionally dominated and radiative transfer processes are negligible in determining the population densities. Comparatively, a CR model solves the coupled rate and radiative transition equations. The next sections will provide the details and results of each method.

8.5.1 Local Thermodynamic Equilibrium Considerations

In order for complete thermodynamic equilibrium (TE) to exist, several assumptions for the plasma must be made. First, the radiation field should emit as a black-body following Planck's radiation law. The energy/velocity distribution for each species should follow a Maxwellian distribution, and the population densities from upper state p to lower state q should be expressed by

the Boltzmann distribution A.2. In normal laboratory plasmas, TE does not exist due to radiation not being fully absorbed by the plasma. This radiation leaking leads to a non-Planckian radiation field.

A more relaxed equilibrium condition known as LTE can then be formed where the radiation field is allowed to deviate from a black-body distribution but the population of states still follows from Boltzmann distribution Eqn. A.2. Additionally, the ionization stages should be given by Saha's equation 8.3. For these conditions to be valid, the plasma must be sufficiently dense that collisions dominant over radiative transfer. If these conditions are met, and using the principle of detailed balance, the state of the system can to be completely specified by a single temperature. This temperature is typically defined as the electron temperature, since electron impact reactions are the dominant process for dense laboratory plasmas. Though the state of the system can be defined by a single electron temperature, this does not require that two kinetic temperatures of electrons and ions be the same [16]. Even in plasmas where LTE is not fully realized, the upper levels near the ionization threshold may still follow a Boltzmann distribution. This is because as the principal quantum number increases, the collisional cross-sections increase while radiative decay rates decrease. In such a case, the equilibrium conditions can be applied to the upper levels, and a single electron temperature can be used to characterize the state of the system, even though the lower lying states are not thermalized. This is defined as Partial-LTE (PLTE), and is characterized by a thermal limit for which states above a given principal quantum threshold are

considered thermalized and states below non-thermal. Re-absorption of radiation within the plasma can shift the thermal limit lower for LTE/PLTE, while spatial inhomogeneity and transients can cause deviations from Maxwellian velocity distributions, which increase the thermal limit [112].

In order to estimate the limits of LTE and PLTE, we assume that the streamer has an average electron temperature of 1-2 eV and densities of $10^{19} - 10^{22}\ m^{-3}$ in the quasi-neutral streamer tail. For these conditions, radiative recombination dominates, and the thermal limit for LTE is $10^{23} m^{-3}$from [97]:

$$n_e[m^{-3}] \leq 10^{20} \left(\frac{E_z(\infty) - E_z(g)}{eV} \right)^{5/2} \left(\frac{k_B T_e}{eV} \right)^3 \tag{8.4}$$

In Eqn. 8.4, E_z corresponds to the ionization energy (∞) and ground state energy (g) for an atom of ionization state z. The less limiting PLTE thermal limit down to the $3p^5 4s$ excited states, requires an electron density of 10^{22} m^{-3} [112]. The thermal limit can also be specified by a principal quantum number (n_{th}), which is a function of the electron density and temperature [97]. For an electron density of 10^{22} m^{-3} and a temperature of 1.25 eV, the principal thermal quantum number is 4. These estimates indicate that for the primary radiative transitions of the streamer discharge, arising from the $3p^5 4p \rightarrow 3p^5 4s$ transitions, LTE and PLTE are not completely valid for all transitions. Additionally, since streamers are not spatially uniform nor steady, the thermal limit will be further increased. Therefore, the excitation temperature defined in Eqn. A.2, should be viewed as suspect and will not be equal to the electron temperature for all 4p transitions. The excitation temperature should

be viewed as the temperature of an equivalent Boltzmann distribution which would lead to the level populations in Fig. 8.5. Although the 4p transitions will deviate from PLTE/LTE, we should expect the upper lying 5p states to be thermalized.

The excitation temperatures of the various excited states were determined using the Boltzmann plot technique. The accuracy in determining the excitation temperature is increased when the population energy between excited states is large, under the assumption that all populated states are in equilibrium. The excitation temperature for transitions arising from both the Ar I 4p and 5p excited states is 84 eV. Even though the separation between the 4p and 5p population energies is relatively large, this excitation temperature did not accurately represent the average electron temperature because the 4p states are not thermalized. The deviation of the 4p transitions from PLTE is explained by the fact that these transitions have a large photoionization cross-section which is directly proportional to the radiative recombination cross-section (as expressed by the Milne relation) [97, 113]. This indicates that the plasma region associated with the underpopulated 4p states, with respect to LTE condition, is a recombination zone [100].

The deviation from PLTE for the 4p states is also observed in Fig. 8.5, as there is a large deviation between the line and continuum radiation indicating that both collisional and radiative processes must be considered [112]. The Ar I 4p LTE temperature estimates had a large scatter which further indicates that the LTE approach is not valid. Though, some of the 4p states may

be thermalized, these transitions near the thermal limit, where radiation and electron impact rates are of similar magnitudes, require a collision-radiative model to predict the electron temperature and density. When considering only the 5p transitions, the excitation temperature is 0.5 eV. These 5p transitions are considered thermalized ($n > n_{th}$), from both the line-continuum ratio (Fig. 8.5) and the thermal limit calculation. Therefore, the average electron temperature for the discharge is estimated from the excitation temperature of the 5p transitions. It should be noted, that there are only two 5p transitions, and a better estimate of the electron temperature is found when analyzing the 4p ion lines. The five 4p ions produce a linear plot, with a R^2 value of 0.98. This indicates a good-fit, and that the 4p ions are in PLTE. Hence, the average electron temperature is better approximated by the ion excitation temperature: $Te \approx T_{EXT} = 0.7eV$. Since the ions may be considered in PLTE, coupling the Saha-Eggert equation with the corona equation for ionization equilibrium, an estimate of the electron number density is possible. Solving the equations for multiple ion neutral line ratios the electron density is estimated to be $2 \times 10^{20} m^{-3}$.

Analysis of the continuum radiation field provides an estimate of the gas temperature, and electron density from radiative recombination. In the NUV to UV regions radiative recombination dominated, where the emission coefficient is given by:

$$\epsilon_{\lambda}^{fb}(\lambda) = \left(\frac{32\sqrt{\pi}c\left(\alpha a_o\right)^3 E_R}{3\sqrt{3}} \right) n_z(g)\, n_e\, z^2 \left(\frac{E_R}{k_B T_e} \right)^{1/2} \frac{1}{\lambda^2} exp\left(1 - \frac{hc}{\lambda k_B T_e} \right) \xi^{fb} \tag{8.5}$$

Here E_R and α are the Rydberg energy and fine structure constant. For wavelengths less than 500 nm, the absorption coefficient is negligible, and the plasma is assumed to be optically thin. The electron density is determined from minimization of the error between the radiative recombination fit (Eqn. 8.5) and the spectral curve for <500 nm. First, the emission coefficient ($\epsilon_{\lambda}^{fb}(\lambda)$) is converted to spectral irradiance by multiplying by the plasma diameter, and then it is plotted against the spectral irradiance in Fig. 8.5. The emission coefficient is calculated assuming that the electron temperature is 0.7 eV (from PLTE), with a constant Biberman coefficient (ξ^{fb}) of 1.8. With these values, and the necessary constants, the electron density which minimizes the error is: $2 \times 10^{20} m^{-3}$.

At wavelengths >500 nm, the absorption coefficient (inverse Bremsstrahlung) is no longer negligible. At these longer wavelengths, the plasma becomes increasingly optically thick, as the absorption coefficient scales as λ^3 [97]. At these longer wavelengths, the emitted photon will be reabsorbed and emitted several times prior to exiting the plasma. This causes the radiation field to have a continuum component, and at long wavelengths a blackbody distribution will be realized. Fitting this continuum spectrum with Plancks radiation law, gives an effective black-body temperature, $T_B \sim 815K$. This black-body

temperature provides an estimate of the temperature of the bulk species (T_g) in the discharge. The deviation from STP conditions (namely T_g,initial = 300 K), indicates that gas heating occurs in the streamer discharge. The bulk temperature differs from the electron temperature by an order of magnitude, this is to be expected for non-equilibrium discharges.

8.5.2 Collisional Radiative Model

A set of strong lines arising from $3p^5 4p \rightarrow 3p^5 4s$ transition array of neutral argon (Fig. 8.5) are used to determine the average electron temperature. As described above these 4p transitions deviated from the PLTE approximation. Therefore, in order to estimate the time averaged electron temperature, we compare the experimental neutral spectra with a collisional radiative model. In these low temperature plasmas, the dominant processes of population and depopulation of excited states occurs through two primary mechanisms: electron impact excitation, and de-excitation, and radiation from the excited states. To investigate the rate balance of the emitting $3p^5 4p$ states, $2p_i$ in Paschens notation, we use a collisional-radiative (CR) model. The model incorporates 42 energy levels of Ar and accounts for the dominant population and depopulation mechanisms of the $2p_i$ states. Atomic cross-sectional data is calculated using a relativistic distorted wave approximation and fed into the CR model. Details of the CR model can be found in the paper [114]. The CR model is then solved for a range of number densities and temperatures to calculate the population of fine-structure $2p_i$ levels, and consequently emis-

sion intensities are obtained as a function of n_e and T_e. The emission intensity of any line I_{ji} due to radiative transition from level j to i is expressed as a function of the population density and is directly proportional the emission coefficient, A.4. The population density, n_j, is calculated as a function of electron density, n_e, and electron temperature, T_e. After normalizing intensities (I) of the measured spectra, and the spectra calculated using the CR model, a deviation parameter is calculated as:

$$Dev = \sum_{x}^{all\ lines} \left(I_{x,expt}^{normalized} - I_{x,CR\,model}^{normalized}\right)^2 \tag{8.6}$$

The electron temperature for a given electron density is found from minimization of this deviation parameter. The density is varied over a range of 10^5, from $10^{18} - 10^{23}\ m^{-3}$. The time averaged electron temperatures for these densities, are in the range of $1.2eV < T_e < 3.5\ eV$. For a typical streamer discharge, with number densities ranging from $10^{19} - 10^{20}\ m^{-3}$, the electron temperature is 1.25 ± 0.3 eV when considering the 10 strongest argon neutral lines.

Fig. 8.6 shows the deviation parameter as a function of temperature for a number density of $6 \times 10^{19}\ m^{-3}$. The black solid line with diamonds considers 14 neutral line transitions in the CR model, while the gray dashed line with circles considers only the 10 dominant neutral lines for comparison. The minimum of the deviation parameter for the 10 dominant neutral lines gives an electron temperature of 1.25 eV. When considering the 14 transitions the temperature was found to have two minima at 1.25 eV and 2.5 eV,

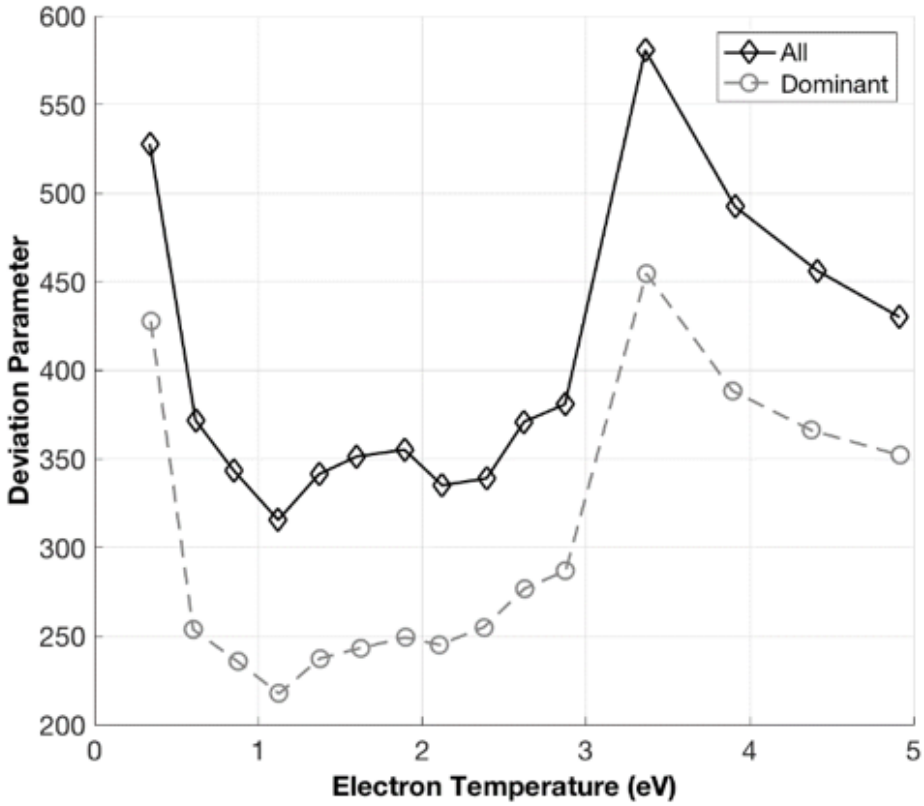

Figure 8.6: A plot of the deviation parameter, which compared the argon neutral spectra with the simulated Collision-Radiative spectra as a function of electron temperature at an electron number density of $6 \times 10^{19} m^{-3}$. *The black line with diamonds considered 14 argon neutral lines, and the red line with circles considered only the 10 dominant argon neutral lines. The deviation parameter was at a minimum at an electron temperature of 1.25 eV. The symbol markers denote data points.*

N_e $[m^{-3}]$	T_e(eV) Neutral Lines	T_e(eV) Dominant Lines
1×10^{19}	2.5	2.5
5×10^{19}	1.25	1.25
6×10^{19}	1.25	1.25
7×10^{19}	1.25	1.25
8×10^{19}	1.25	1.25
9×10^{19}	1.25	1.25
1×10^{20}	1.25	1.25
2×10^{20}	1.25	1.25
3×10^{20}	1.25	1.25
4×10^{20}	2.5	1.25
1×10^{21}	2.5	1.25

Table 8.1: Electron number density and temperature from the CR model and minimization of the deviation parameter. With all 14 neutral argon lines and 10 dominant lines.

with the lowest minima at 1.25 eV. Table 8.1 summarizes the electron temperature calculations which minimized the deviation parameter for number densities,$10^{19} - 10^{20} m^{-3}$. Minimizing the deviation parameter over the electron density space of the neutral spectra, gives an electron density of $6 \times 10^{19}\, m^{-3}$. These values of electron temperature and density are in good agreement with other authors for atmospheric argon streamer discharges [109].

8.6 Effects of Methane

The effect of methane addition to argon on the streamer dynamics is presented. It was observed previously that minor concentrations of methane prevented reliable triggering of an arc discharge. This inability to ignite an arc was attributed to the surface streamer seed electron source. In order to isolate

the effects of methane on the surface streamer dynamics the gas composition was varied from $\phi = 0 - 5\,\%$, where ϕ is the methane to argon mass flow ratio defined by the ratio of the measured volumetric flow rates and molar mass of methane and argon.

The voltage, current, and integrated light intensity were observed as a function of the methane concentration (ϕ), and correlated with instantaneous broadband image sequences. Fig. 8.7 shows a typical waveform for a methane concentration of 1.0%. With the addition of methane, the critical breakdown voltage (V_B), which was directly proportional to the plasma breakdown voltage (V_p), increases considerably from 18.9 to 25.4 kV. Additionally, the peak current and surface charge decrease from 4.6 to 0.76 A, and 238 to 144 nC, respectively. These trends indicate that energetic electrons lose energy to low lying vibrational levels of methane which reduce the conductivity of the plasma and increase the voltage breakdown threshold. Additionally, in Fig. 8.7, several minor voltage unloadings are observed with a negative current, indicating that electrons, or negative ions, are deposited on the surface. Finally, the secondary discharge is weaker than those observed in argon discharges, and both the primary and secondary discharges occur near the voltage limit of the source, indicating that a higher voltage source is required to ignite higher concentrations of methane.

Fig. 8.8 shows several instantaneous broadband image sequences integrated over the entire pulse duration for four different methane concentrations: 0.0, 0.1, 1.0, and 5.0 %, which are designated as 01, 02, 03, and 04 respectively.

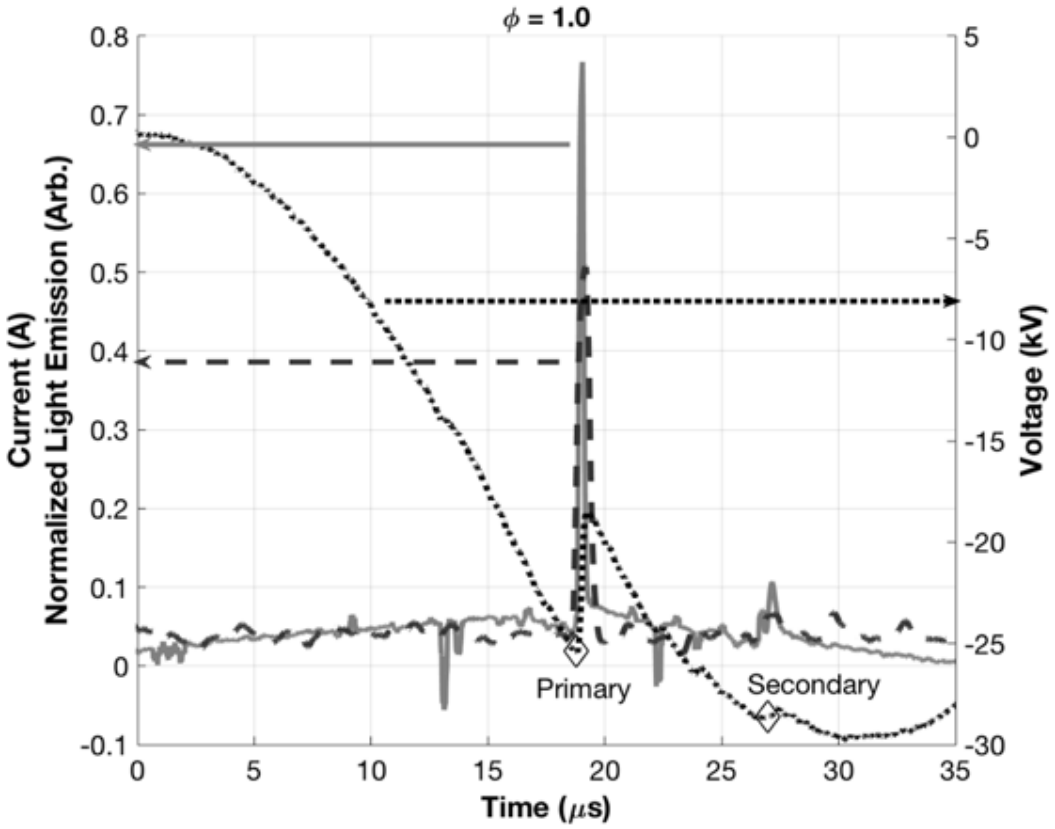

Figure 8.7: Discharge characteristics for a methane to argon ratio of 1%, measured on the trigger electrode for a single negative polarity pulse. The dotted black line indicates the applied voltage measured by the Tektronix P6015a 75 MHz probe. The dark gray dashed line indicates the scaled integrated light intensity measured with a PDA36A photodiode with a gain of 20 dB and a bandwidth of 1 MHz. The solid light gray line denotes the current measured by the Pearson 2877 current monitor. Diamonds specify regions of voltage unloading and current deposition.

In the pure argon case, a diffuse corona discharge is present along the helical trigger wire, and a constricted streamer forms that spans the entire gap. As the methane concentration is increased, to only 0.1 %, the diffuse corona is reduced, and the streamer becomes more constricted and filamentary. At this low concentration, the streamer is still capable of sufficiently bridging the gap. At 1% methane, two separate streamers are observed. Both streamers emerge from the main electrodes: the left discharge remains localized near the main electrode while the right forms a constricted filament that branches near the midpoint of the chamber towards the embedded trigger electrode. At 5% methane concentration, the discharge remains localized at the gas inlet. In general, as the methane concentration is increased, the discharge becomes more constricted and does not bridge the inter-electrode gap.

The instantaneous broadband images are correlated with the current-voltage characteristics as a function of methane concentration. In Fig. 8.9, the voltage and current for methane concentrations of 0.0, 1.0, 5.0, and 10.0% are plotted. The arrows in Fig. 8.9 indicate the direction of positive time on the VI plot for each pulse. Integration of the VI plot provides an estimate of the power deposition into the chamber. As the concentration of methane is increased the breakdown voltage increases, and the peak current decreases exponentially with respect to voltage. The power deposited into chamber decreases rapidly as the streamer channel quenches at higher concentrations. At a concentration of 10% methane, no discharge is observed, and no power is coupled into the chamber as indicated by the closed VI loop in Fig. 8.9. The

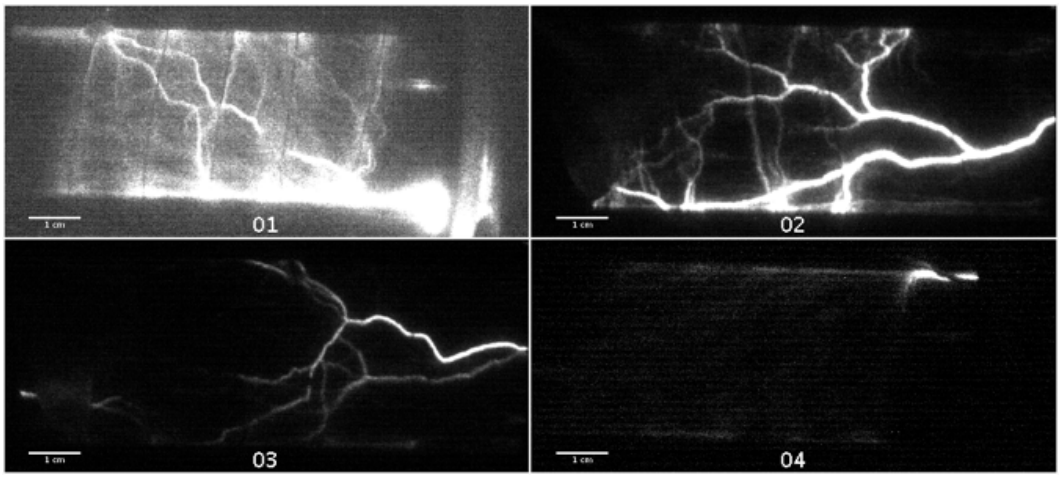

Figure 8.8: Long exposure images of the entire electrode pulse (300 s) in argon and methane mixtures. The main electrodes were grounded and the trigger electrode was pulsed negatively. Gas flow was from the right to the left. The images show the streamer dynamics for methane concentration ratios of 0.0, 0.1, 1.0, and 5.0 % which correspond to the labels 01, 02, 03 and 04 respectively.

VI plot also provides an indication of the electron density, and conductivity of the plasma. As seen by Eqn. 8.1, the number density is directly proportional to the current density. The lower conductivity plasma also contributes to a decrease in the surface charge deposition, and the reduced voltage rise needed for a secondary discharge to occur.

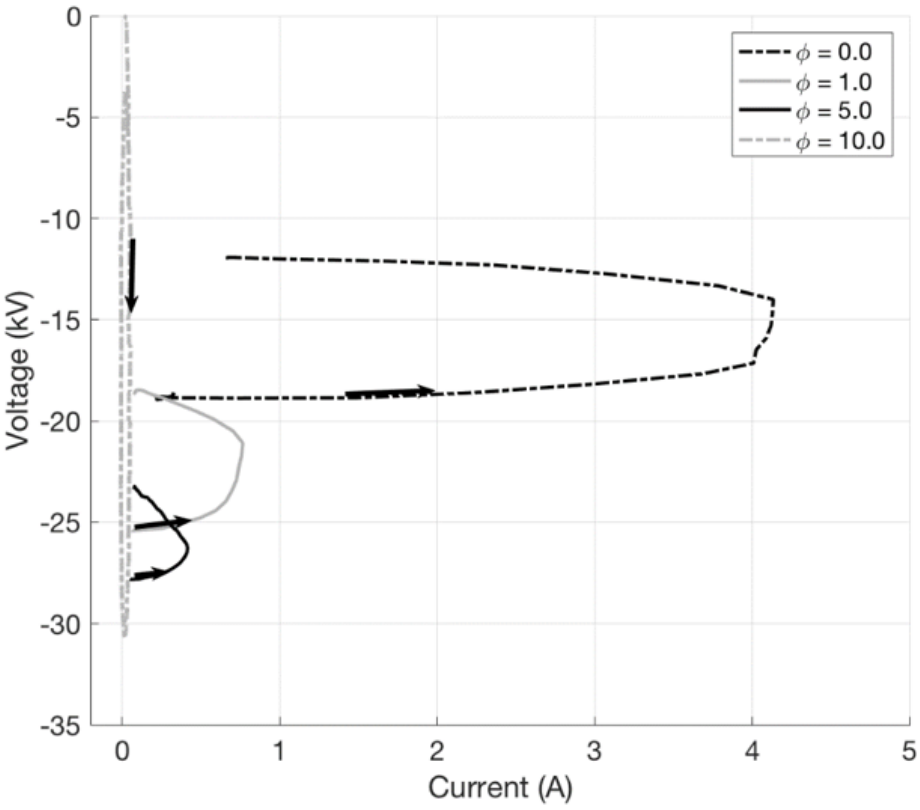

Figure 8.9: Voltage and Current traces as a function of methane concentration. The black arrows indicate the direction of positive time. The dashed black line was for pure argon, solid gray was for 1.0% methane, solid black was for 5.0% methane, and the dashed gray line for 10.0% methane. As the methane concentration was increased the power coupled into the discharge reduced, indicating quenching of the surface streamer discharge.

Chapter 9

Conclusions and Recommendations

Streamer discharges in molecular gases have been investigated for two applications: (1) CO_2 reforming, and (2) ignition of thermal discharge. It was found that the streamer's low energy tail primarily excites vibrational modes of molecular gases, while the streamer head is responsible for ionization and dissociation reactions. In (1) the excitation of the vibrational modes resulted in a secondary dissociation mechanism which was utilized to increase the conversion of CO_2. In this work pulsing of the streamer discharges populated the low lying vibrational levels which lead to vibrational exchange, and excitation of high vibrational levels. These high vibrational levels then dissociate increasing the conversion of CO_2. In (2) excitation of the vibrational modes prevented the surface streamer discharge from bridging the inter-electrode gap. The decrease in conductivity due to vibrational losses prevented the ignition of a thermal discharges in argon-methane mixtures.

9.1 Volume Streamer Conclusions for CO_2 Reforming

The objective of this work was to determine the dominant reaction kinetics of non-equilibrium streamer discharges in CO_2 and how to optimize

these discharges for reforming applications. Two mechanisms were found to be present in streamer discharges for CO_2 dissociation: direct electron impact dissociation, and vibrational ladder climbing.

The primary dissociation mechanism in streamer discharges was shown to be direct electron impact dissociation which leads to low conversion efficiencies of 0.01% for a single streamer discharge. The reactions occur primarily in the streamer head where the electron temperatures are order 10 eV and results in low energetic efficiency. It was determined that to optimize the streamer discharges for dissociation reactions, the low lying vibrational states must be populated to sufficiently high densities that vibrational ladder climbing is possible.

The low energy electrons in the streamer tail with energies of 1-2 eV were observed to populate the first three asymmetric stretch vibrational levels. In the afterglow of the streamer discharge these levels did not have sufficient populations for vibrational-vibrational (VV) relaxation. Pulsing was used to increase the density of these levels. It was found that the population of the vibrational levels was dependent upon the pulse frequency. At higher pulse frequencies an increase in the electron density resulted in higher populations of the first vibrational level which ultimately lead to VV exchange. The VV relaxation produced a high density of upper level vibrational states which increased the CO_2 conversion rate.

In addition to the simulations, experiments were conducted and the results compared. The experiments and simulations showed good agreement in

predicting the streamer trends including: streamer dynamics, properties, and conversion. The experiments showed an average CO density of 10^{23} m^{-3} at a pulse frequency of 4 MHz. At these frequencies simulations predicted a CO density of 10^{18} m^{-3}, but at higher pulse frequencies when VV exchange was present the CO density tended to a value of 10^{23} m^{-3}. Therefore, it is expected that VV exchange occurs in the pulsed streamer discharge. Simulations and experiments also showed that streamer properties such as the electron temperature and density are dependent upon the polarity of the streamer, with positive cathode-directed streamers producing the optimal conditions for population of CO_2 vibrational levels.

The optimization of a streamer discharge for dissociation can be summarized as follows:

1. High pressures are desired to produce a high initial density of vibrationally excited CO_2.

2. The gas temperature should be minimized so that VT relaxation is reduced, while maximizing VV exchange. This non-equilibrium between the gas temperature and vibrational temperatures leads to population of high lying vibrational levels. (Treanor Distribution)

3. High frequency pulsing results in an increase in the electron density and population of low lying vibrational states. Maintaining the population of these levels at sufficiently high density results in VV exchange and additional conversion of CO_2 via the ladder climbing mechanism.

4. Streamer spacing must be optimized such that the streamer interaction is minimized and merging is prevented with a packing factor determined from the reduced electric field.

9.1.1 Summary of key findings:

1. The computational model predicts velocities in the range of 100-1000 km/s while experiments determined the velocity to be 580 km/s. The velocity is dependent upon the polarity and voltage. As the voltage is increased the streamer velocity is increased for a given pressure. Additionally, the velocity of anode-directed streamers is greater than that of cathode-directed streamers. This occurs for two reasons: (1) the anodic streamers head radius is smaller which provides larger electric fields at the streamer head, and (2) the electron drift for anodic streamers is in the direction of the streamer propagation.

2. Numerical modeling and experiments showed that as the pressure is increased the streamer diameter decreases. This is due to an increase in the collision frequency and low energy inelastic collisional losses, such as vibrational excitation. Both simulations and experiments showed that the diameter of anode directed streamers is larger for all pressure conditions compared to the cathode-directed. This polarity dependence is again due to the streamer head. In anodic streamers a net negative space charge exists at the streamer head, accelerating electrons away from the head which leads to further ionization and increase in diameter.

3. Experiments showed that the breakdown voltage for anode directed streamers was higher than that of cathode directed, which was confirmed by simulations. Due to the higher breakdown thresholds, no filamentary branching was observed for negative streamers. In the cathode directed cases, several branched streamers were observed. As the voltage increased, or pressure decreased, the branching ratio (for cathodic streamers) increased, as well as the half angle. The plasma fluid model cannot show branching because a uniform background electron density is used to seed the domain.

4. Simulations showed the plasma is electro-positive, with a dominant positive ion density approximately an order of magnitude greater than that of the negative ions. The dominant positive ion $C_2O_4^+$ is efficiently generated from three-body collisions in the streamer tail. Whereas the dominant negative ion, O^- is generated in electron impact dissociative attachment.

5. The first asymmetric stretch vibrational level for CO_2, was found to be efficiently populated with densities of $10^{22} - 10^{23}$ m^{-3}. Cathode-directed streamers showed the most efficient population of the low lying vibrational states during the streamer phase due to lower electron temperatures ($\sim$ 1 eV) in the tail comparatively to anode-directed case ($\sim$ 3eV).

6. The streamer electron temperature and density were found to be functions of pressure, voltage, and polarity. Hence, streamers can be opti-

mized to produce an electron energy in the tail which efficiently couples energy into the low lying vibrational levels. Then, in the case of a DBD reactor, these low lying levels can transfer energy through VV reactions, leading to secondary splitting mechanism for molecular species.

7. Simulations showed that the electron density for anode-directed streamers are an order of magnitude lower than cathode-directed streamers, while the electron temperature in the tail for the anode-directed is 2-3 eV greater than the cathode-directed. These low electron temperatures are not efficient for ionization. Therefore, the streamer head, with temperatures for both polarity streamers of $\sim$10 eV, is responsible for the large ionization rates, electron density in the tail, and streamer self-propagation. The larger electron density in the cathode-directed streamer is therefore attributed to the streamer head dynamics. The main difference between the two streamers is the space charge polarity at the head. For cathodic streamers a positive space charge exists which consumes electrons and increases the electron density in the tail. Comparatively, anodic streamers have a negatively charged head, and push electrons in the direction of propagation. Experiments confirm that for a given RMS voltage, cathode-directed streamers have a higher electron density than the anode-directed ones. The higher electron densities in positive streamers will directly translate to an increase in the CO_2 vibrational levels, and high conversion efficiencies.

8. Experiments showed preferential excitation of electronically excited species,

CO* and O*, depending on whether the streamer was cathodic or anodic. For anode-directed streamers, the peak CO* and O* densities were localized in the sheath region, indicating that direct electron impact dissociative excitation is the dominant reaction mechanism since the energy threshold is $\sim$ 20 eV. Additionally, in the anodic streamer, CO* is seen to bridge the entire cathode-anode gap, while O* remains localized in the sheath region. In cathode-directed streamers, CO* is quenched while O* shows a density throughout the filamentary streamer structure. The lack of CO* is attributed to low electron energy vibrational losses.

9. Plasma spectroscopy of the discharge indicated that a highly non-equilibrium plasma is generated by streamer discharges. The average electron temperature and density were found to be T_e =0.6 eV, and n_e= 10^{20} m^{-3}, with a vibrational temperature for CO_2 of T_v= 3000 K, and a gas temperature T_g=680 K. The CO density was estimated from actinometry to be n_{CO} =10^{23} m^{-3}, which correlated well with the pulsed 0D simulations.

10. Simulations showed that single streamer elements populate the first three vibrational levels, and in the after glow the density of these states is not sufficient for VV ladder climbing. Therefore, pulsing is used to increase the CO_2 excited vibrational state population which leads to VV relaxation and an increase in CO dissociation.

11. Simulations showed that there is a packing factor associated with the minimum spacing between adjacent streamer discharges to prevent the

formation of a leader channel and thermalization. This packing factor results from the electrostatic repulsion of adjacent streamer discharges, and results in a large volume of the discharge region being unoccupied.

9.2 Surface Streamer Conclusions

Atmospheric streamer dynamics were investigated for argon and methane mixtures for ignition of a pulsed thermal arc device. All the streamer discharges show a filamentary structure originating from a single filament with roots localized at the main electrodes. The filaments exhibited splitting and branching from the main core into the interior volume. The branching structure preferentially propagated into the localized coronal regions along the dielectric surface which formed a surface tracking pathway in pure argon. At methane concentrations above 1% the streamer remained constricted and localized near the main electrodes. Additionally, the coronal discharges were quenched preventing further propagation of the streamer throughout the volume. The addition of methane reduced the ionization within the discharge domain and prevented a conductive channel from forming between the inter-electrode gaps which would lead to an arc breakdown. The reduced ionization and increased breakdown voltages observed with minor additions of methane can be explained by low energy inelastic vibrational levels, absorption, as well as attachment processes. These processes are summarized below as well as a summary of the argon discharge.

9.2.1 Argon Discharge Summary

A surface tracking streamer discharge in argon was analyzed to determine the mechanism for successful ignition of arc discharges in large gap severely under-voltage conditions. The discharge was characterized by two cathode-directed streamers that emerged from the anodic main electrodes and traversed along the dielectric surface. Within a few hundred nanoseconds these streamers merged, bridging the main electrode gap with a luminous conducting plasma. From the high-speed image sequences the propagation velocity and diameter of the discharge were estimated: $\sim$100 km/s and $\sim$500 μm. The electrical characteristics of the discharged provided estimates of the breakdown threshold, V_B, surface charge, and electron number density ($n_e\sim$ 10^{20} m^{-3}), which was in agreement with the spectroscopic results.

The time and spatially averaged electron density and temperature were estimated from a LTE/PLTE perspective and a collisional-radiative model. It was found that the ions exhibited PLTE with an excitation temperature, T_{EXT} $\sim$0.7 eV, while the argon neutrals, specifically the 4p transition array did not. The electron number density was estimated ($n_e\sim$ $10^{20}\,m^{-3}$) from Saha's equation coupled with coronal equilibrium. The bulk temperature was determined to be 815 K from fitting a black-body curve to the observed spectrum. The CR model provided better predictions of the electron temperature and density for the 4p transition array. It was determined that the average temperature of the streamer was $\sim$1.25 eV and a density of 6×10^{19} m^{-3}. The PLTE, current density, and CR methods all predicted the electron density to be $10^{19} - 10^{20}$

m^{-3}. While the PLTE ion excitation temperature under predicted the electron temperature.

9.2.2 Argon-Methane Mixtures Summary

The reduced ionization and increase in breakdown voltage for methane mixtures can be explained as follows. In pure argon there are no electron attachment processes, while in methane, a weakly electronegative gas for the low reduced applied electric fields considered here (66 Td), electron attachment is not negligible [115–117]. Additionally, the effective ionization coefficient is a function of both the methane concentration and the reduced electric field. Therefore, in order to maintain a constant effective ionization coefficient, for reduced electric fields below 120 Td, the voltage must be increased with the addition of methane, as observed in Fig. 8.8 and 8.9 [116, 117]. Furthermore, at these low reduced electric fields, and average electron temperatures ($\sim$1.25 eV), ionization occurs primarily through a two-step collisional process: initially electron impacts form metastable and excited species which then ionize by secondary collisions [118].

Methane also has four vibrational modes which have an activation threshold range of 0.18-0.35 eV [119]. The vibrational modes absorb the electron energy and reduce ionization for low reduced electric fields and electron energies. It is these low energy vibrational modes that were primarily responsible for reducing ionization and preventing the streamer from bridging the main electrode gap. Lastly, methane has a relatively large absorption cross-section

which suppresses the photoionization mechanism [115, 120]. The reduction of the photo-ionization coefficient decreases the region of ionizing radiation at the streamer head necessary for secondary electron avalanches which facilitate positive streamer propagation. In Fig. 8.8 we see that as methane was added, the localized coronal discharge within the interior of the domain was suppressed, and ionization was only observed near the main electrodes. Therefore, for an efficient ignition of an arc discharge in methane, one requires an increased reduced electric field to overcome electron energy loss mechanisms such as absorption, vibrational excitations, and attachment processes.

9.3 Recommendations for Future Work:

Streamer discharges have shown a wide array of applications from biomedical germicidal treatment, plasma assisted combustion, and flow control. This wide array of applications is due to the versatility of the atmospheric pressure streamer discharges. The main benefits of plasma streamers are their ability to operate outside vacuum conditions, plasma chemistry in particular production of radical species, low cost, and controllability. In this thesis presented, it is shown that two mechanisms for dissociation exist in pulsed streamer discharges. (1) the direct electron impact dissociation which is independent of pulsing, and (2) the low lying vibrational levels which are excited in the streamer tail. Under certain pulsing conditions low lying vibrational levels becomes sufficiently populated that vibration-vibration exchange becomes important. This VV exchange results in a secondary dissociation mechanism

due to vibrational ladder climbing.

9.3.1 Volume Streamers in CO_2 for reforming

Experimental Recommendations

1. Development of a collisional-radiative (CR) model for CO_2 to determine the plasma properties, specifically electron temperature and density.

2. Tomography of the plasma discharge to determine the three dimensionality and branching ratio.

3. Laser spectroscopy to determine CO_2 vibrational distribution to compare with modeling results.

4. Design and test a DBD reactor to validate optimization techniques, and investigate the effects of gas mixtures for CO_2 reforming.

Computational Recommendations

1. Develop a multi-dimensional simulation to replicate a DBD reactor with detailed chemistry.

2. Develop a chemical mechanism for CO_2 mixtures such as water and argon, and study the effects of mixtures on conversion

Appendices

Appendix A

Thermal Plasma Source and Plasma Material Interactions

[1] A brief description of the work done by the author prior to non-equilibrium streamers in carbon dioxide is presented. The author was apart of a project interested in thermal plasma material surface interactions for various applications including: space propulsion, rail-gun armatures, igniter for pulsed electro-thermal launchers, and plasma pyrolysis. In this work, a low purity, high power, thermal plasma source was designed and tested. The device relied on non-equilibrium surface streamer discharges to form the initial ionization source necessary for thermal arc breakdown. A description of the work will be presented. [11, 108]

[1]This work was previously published in: Pachuilo, Michael V., Francis Stefani, Laxminarayan L. Raja, Roger D. Bengtson, Graeme A. Henkelman, A. Cuneyt Tas, Waltraud M. Kriven, and Kumar Sinha Suraj. "Development of a Gas-Fed Plasma Source for Pulsed High-Density Plasma/Material Interaction Studies." IEEE Transactions on Plasma Science 42, no. 10 (2014): 3245-3252. The author was the primary contributer. Dr. Tas conducted the SEM and EDXS work.

A.1 Thermal Plasma Surface Interactions

A high purity gas-fed plasma source was developed to study plasma-surface interactions. The device produced large volume thermal arcs characterized by temperatures of $T_e = 1 - 2 \quad eV$ and electron densities of $n_e = 10^{23} \quad m^{-3}$. Typically, capillary arc devices expand the hot arc core which is at pressures of ∼10 MPa, to ambient atmospheric pressure. The plume of the arc is then allowed to interact with the sample substrate. During this expansion process the arc temperature drops significantly from ∼1 eV to nearly 0.1 eV [22, 121]. This rapid expansion causes the discharge to deviate from thermal equilibrium [122]. Furthermore, this drop in temperature causes several plasma species to condense out, and inevitably deposit on the target substrate. The device designed, produces large volume arcs which allowed samples to be inserted directly into the plasma chamber.

Previous capillary designs [22], and in the authors early work, relied upon an ablative liner and fuse ignition wire to generate the thermal plasma source. These sources prevented multiple firings, and introduced containments such as carbon soot and metal vapor which formed deposits on target sample surfaces. These thick soot layers obscured material diagnostics (Scanning Electron Microscopy SEM). The device designed herein, alleviated these issues by using a non-equilibrium plasma ignition source which was not directly coupled to the thermal arc power supply. The new ignition source allowed thermal arc breakdown at low voltages ($\sim 1 - 6 \quad kV$) at Pd products which would otherwise require $100's \quad kV$ (Paschen breakdown condition). Additionally, the

thermal arc source could be operated at "relatively" high firing rates, limited only by the charge time of thermal pulsed power system.

A full description of the work is found in:

- Pachuilo, Michael V., Francis Stefani, Laxminarayan L. Raja, Roger D. Bengtson, Graeme A. Henkelman, A. Cuneyt Tas, Waltraud M. Kriven, and Kumar Sinha Suraj. "Development of a Gas-Fed Plasma Source for Pulsed High-Density Plasma/Material Interaction Studies." IEEE Transactions on Plasma Science 42, no. 10 (2014): 3245-3252.

A.2 Experimental Design

Figure A.1 shows a schematic of the experimental thermal plasma system, and Fig. A.2 shows a detailed solid rendering of the plasma chamber. The chamber consist of two concentric cylinders with an embedded copper ignition wire. The cylinders are capped with two refractory electrodes from which the thermal arc is supported. The helically wound ignition wire is used to generate a non-equilibrium surface streamer discharge (explained in the following section). The surface streamer discharge acts as an fuse wire providing the necessary conductivity to ignite a thermal discharge in the volume. The thermal arc composition is controlled through the usage of high purity gas cylinders.

The pulsed thermal arc discharge power supply consisted of 185 μF electrolytic capacitors with a peak charge voltage of 3 kV. The system is

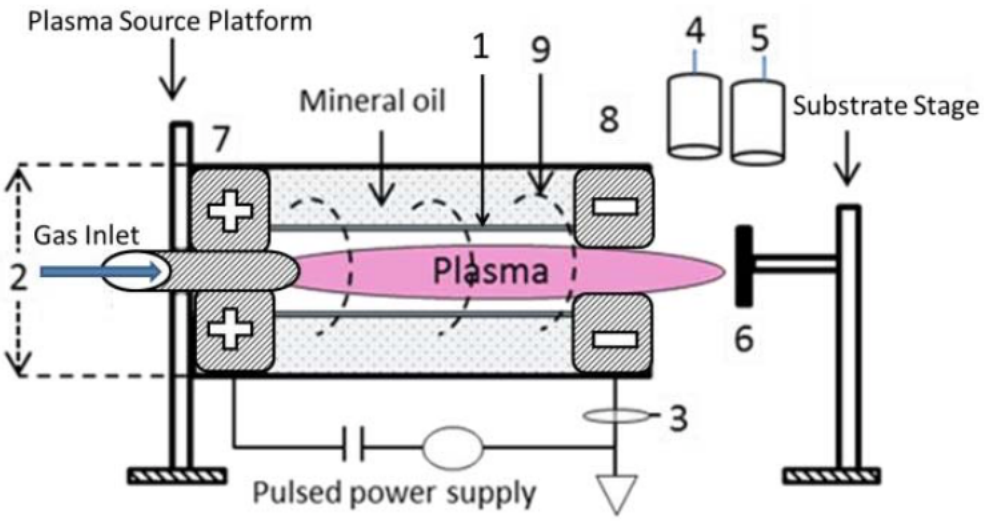

Figure A.1: Schematic of the experimental setup [11]. The chamber is composed of two concentric tubes (1) the inner, fused quartz tube, and (2) the outer polycarbonate tube. Two annular electrodes (7) and (8) cap the ends of the tubes. A copper ignition wire (9) is wrapped helically around the fused quartz tube. The volume between the two concentric tubes is filled with mineral oil to prevent undesired breakdown to surrounding from the ignition trigger electrode. The sample (6) can be placed in the expanded plume or inside the chamber. (3-5) indicate the Rogowski coil, optical emission spectroscopy, and photodiode diagnostics.

Operating Conditions	Low	Typical	High
Number of capacitors	2	4	8
Capacitance (μF)	89	178	356
Charge voltage (kV)	1.6	3.2	5.0
Peak current (kA)	6	25	76
Plasma energy (J)	85	670	3100
Peak power (MW)	5	40	150
Pulse duration (μs)	40	70	140
Peak pressure (kPa)	200±50	1500±500	>4000

Table A.1: Range of operating conditions in 99.5% argon.

operated in a series-parallel configuration to increase the peak charge voltage to 6 kV. A low inductance strip line (500 nH) was used to prevent ringing of the power supply, and damage of the capacitors. Various configurations were used, providing a range of operating conditions summarized in Table A.1.

The plasma temperature is "relatively" insensitive to the capacitor energy, with temperatures of 1-2 eV. Altering the operating conditions, mainly serves to change the RC time constant and the plasma material interaction times. The limits of operation of the device are based on mechanical failure of the quartz confining vessel at high powers. The lowest charge voltage is determined by the surface streamer ignition source, and the ability to generate a sufficiently conductive channel which bridges the inter-electrode gap.

A.3 Optical Emission Spectroscopy of Thermal Discharge

Optical emission spectroscopy of a thermal discharge in Ar + 2% H_2 was preformed, and the spectrum was time and spatially integrated. An Ocean

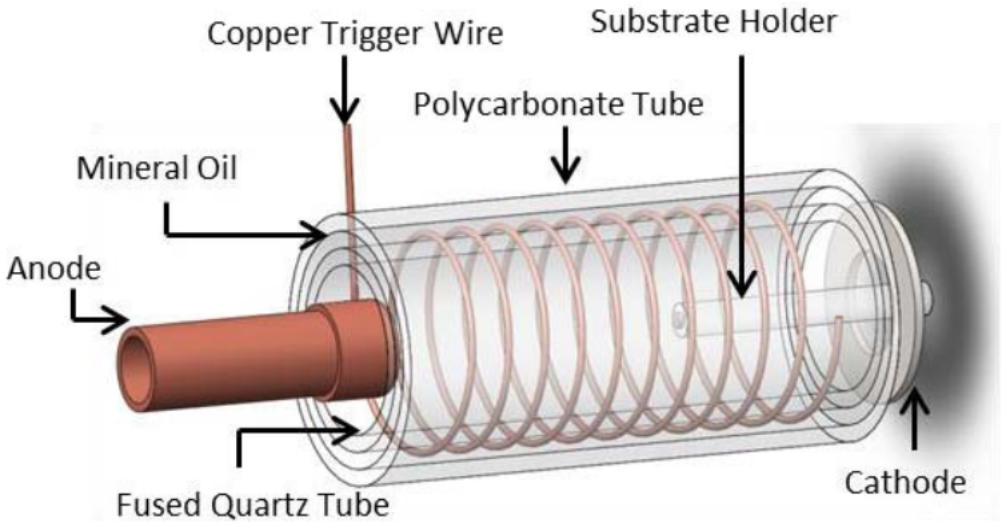

Figure A.2: Solid model of the reaction chamber [11]. The chamber is composed of two concentric tubes the inner fused quartz tube, and the outer polycarbonate tube. Two annular electrodes cap the ends of the tubes, and a copper ignition wire is wrapped helically around the fused quartz tube.

Optics HR2000+ spectrometer with a wavelength range of 200-1000 nm was used to record the spectrum. The light emission from the plasma source was dominated by lines of neutral argon (Ar I) and singly ionized argon (Ar II). In addition, the presence of doubly ionized argon (Ar III) was detected in the ultraviolet, singly ionized silicon (Si II), and hydrogen (H_α). Some discharges showed additional excited silicon neutral lines. The presence of silicon in the spectra indicated the ablation of the quartz chamber walls which was confirmed by surface analysis. A small amount of Hydrogen (2%) was added to the argon backing gas to estimate the electron density.

Figure A.3 shows the emission spectrum (A.3a) of the discharge, and a table of the dominant lines and their respective spectroscopic data (A.3b). The spectrum is dominated by line radiation. In the wavelength range of 700 to 1000 nm the spectrum is dominated by the Ar (4p-4s) transition array. In the wavelength range of 400-700 nm, argon transitions from the upper states 5d, 4d, 6s, and 7s decay to the 4p state. The plasma temperature was estimated from these two spectral regions of electronically excited Argon using the Boltzmann plot technique, as discussed below.

The Boltzmann plot technique is a relatively simple and widely used technique for determining the temperature of a plasma from optical emission spectroscopy. The technique requires that the plasma is in local thermodynamic equilibrium (LTE). For this to be true the radiative losses must be much less than the collisional excitations, that is the plasma must be collisional dominate. At high pressures, LTE is usually a valid assumption. A limit of LTE

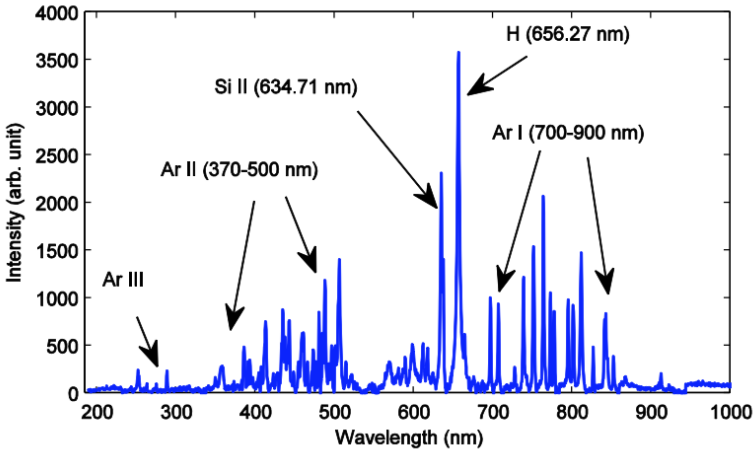

(a) Emission Spectrum

Species	Wavelength	Lower Energy Levels		Upper Energy levels	
		E_i (eV)	J_i	E_k (eV)	J_k
Ar III	250.89	23.14	3	28.08	3
	274.38	23.39	3	27.91	2
Ar II	384.54	16.64	5/2	19.86	3/2
	434.80	16.64	5/2	19.49	7/2
					5/2
	440.09	16.40	7/2	19.22	3/2
	472.68	17.14	3/2	19.76	5/2
	480.60	16.64	5/2	19.22	5/2
	487.98	17.14	3/2	19.68	5/2
					5/2
	501.71	18.65	3/2	21.12	5/2
Si II	634.71	8.121	1/2	10.07	3/2
H_α	656.52	10.19	3/2	12.08	5/2
Ar I	696.02	11.54	2	13.32	1
	706.72	11.54	2	13.30	2
	714.70	11.54	2	13.28	1
	727.29	11.62	1	13.32	1
	738.39	11.62	1	13.30	2
	750.38	11.82	1	13.47	0
	763.51	11.54	2	13.17	2
	772.37	11.54	2	13.15	1
	772.42	11.72	0	13.32	1
	794.81	11.72	0	13.28	1
	800.61	11.62	1	13.17	2
	810.36	11.62	1	13.15	1
	826.45	11.82	1	13.32	1
	840.82	11.82	1	13.30	2
	842.46	11.62	1	13.09	2
	852.14	11.81	1	11.62	2
	912.29	11.54	2	12.90	1

(b) Emission Lines

Figure A.3: Thermal arc emission spectrum in the wavelength range 200-1000 nm for Ar + 2%H_2 at charge voltage 4 kV. [11]

applicability can be determined by considering that radiative transition probability from the upper state j to the ground state, (A_j), occurs at much lower rate than collisional excitation from i to j (C_{ij}). Which gives the condition that: $A_j << C_{ij}$, where $C_{ij} = n_e < \sigma_e \nu >$. n_e is the electron density, σ_e is the collision cross-section for electronic excitation, and ν is the relative velocity. The average of the cross-section and velocity $< \sigma_e \nu >$ is defined as the rate coefficient. A plot can be constructed from the rate coefficient as a function of temperature (functional expression A.1 or Bolsig) and the radiative transition probability condition for LTE. From the plot the range of applicable temperatures and densities for LTE, and hence the Boltzmann plot, to be valid can be determined. Eqn. A.1 [97] shows an expression for the evaluation of the rate coefficient. The first term is a set of constants where: α is the fine structure constant, c is the speed of light, a_o is Bohr radius, and R_y is the Rydberg constant. f_{ij} is the oscillator strength, and $P\left(\frac{E_{ij}}{k_B T_e}\right)$ is the Gaunt factor.

$$< \sigma_e \nu >= \left(16\sqrt{\frac{\pi}{3}}\alpha c \pi a_o^2\right) f_{ij} \left(\frac{R_y}{E_{ij}}\right) \left(\frac{R_y}{k_B T_e}\right)^{\frac{1}{2}} exp\left(-\frac{E_{ij}}{k_B T_e}\right) P\left(\frac{E_{ij}}{k_B T_e}\right) \tag{A.1}$$

In [12], it was shown that in an Argon plasma comparing the Ar I 555.87 nm transition, that the LTE is valid for $n_e = 10^{23} - 10^{24}\ m^{-3}$ and $T_e = 7000 - 10000\ K$. Figure A.4 shows a plot of the valid LTE region. The electron temperature is given in 10,000 K increments. It is evident that at lower temperatures higher electron densities are required to maintain colli-

sional dominated plasmas. As the temperature increases the electron density restriction can be relaxed, since the collision frequency has increased.

Assuming that LTE is valid the Boltzmann plot method can be formulated. Consider two energy levels E_i and E_j, where i and j refer to the upper and lower energy states. For each energy level a state population or density is given by N_i, for the lower, and N_j for the upper. In thermal equilibrium the Boltzmann distribution can be used to establish a relation between the density of states (apart of the same ionization state ie $Z_i = Z_j$) and and the excitation temperature T_{EXT} as:

$$\frac{N_j}{N_i} = \frac{g_j}{g_i} exp\left(-\frac{E_j - E_i}{k_B T_{EXT}}\right) \tag{A.2}$$

Summing over all states (N_i) where the total population density is

$$N = N \sum_n \frac{N_n}{N}$$

, produces the Boltzmann distribution for a given atomic state (j) as:

$$\frac{N_j}{N} = \frac{g_j}{Z_a(T)} exp\left(-\frac{E_j}{k_B T_{EXT}}\right) \quad with \quad Z_a(T) = \sum_n g_n exp\left(-\frac{E_n}{k_B T_{EXT}}\right) \tag{A.3}$$

where g_j is the statistical weight or degeneracy of state j, and $Z_a(T)$ is the atomic or internal partition function [17]. When an excited atom in upper state j decays to lower energy state i, the emission coefficient ϵ_{ji} of the spectral line is then given as:

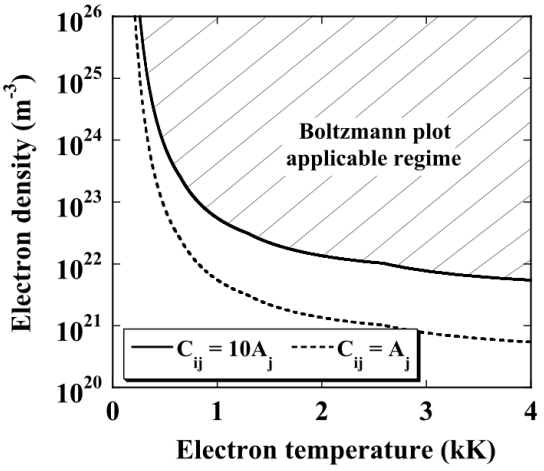

Figure A.4: Validity of the Boltzmann Plot Technique [12]

$$\epsilon_{ij} = \frac{hc}{4\pi\lambda_{ji}} A_{ji} N_j \tag{A.4}$$

Here, λ_{ji} is the transition wavelength of the spectral line from state j to i, and A_{ji} is transition probability or Einstein's spontaneous emission coefficient from a randomly orientated photon emission. Taking Eqn. A.3 and Eqn. A.4 rearranging and taking the natural logarithm of both sides produces:

$$log\left(\frac{\epsilon_{ij}\lambda_{ji}}{g_j A_{ji}}\right) = -\frac{E_j}{k_B T} + C_1 \tag{A.5}$$

C_1 is a constant. A plot of Eqn. A.5 will produce a straight line if LTE is valid, and from the slope of the line the temperature can be determined. If optical density or absorption is significant for any given line, it would appear as a significant deviation from the linear fit. In this work optical density

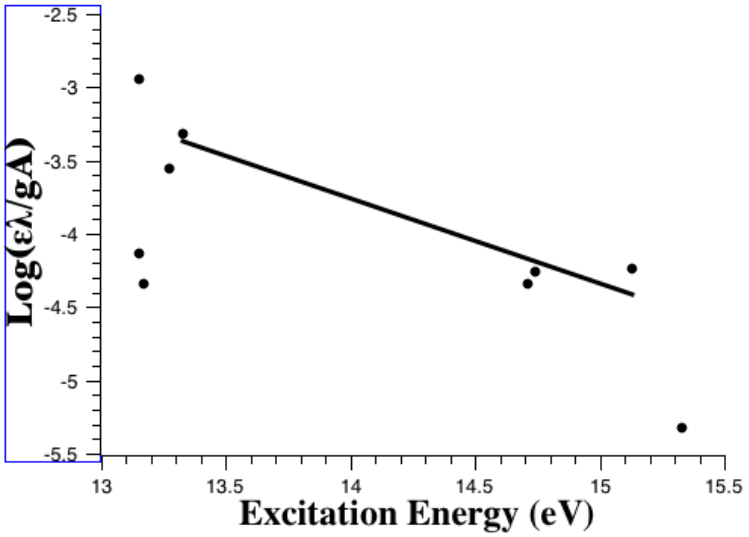

Figure A.5: Boltzmann plot for an argon + 2%H_2 plasma discharge. The temperature was determined to be 1.9 eV.

was not considered. Figure A.5 shows the Boltzmann plot for the dominant lines shown in Fig. A.3a. The temperature was determined to be 1.9 eV. It is important to note that the Boltzmann plot method is sensitive to the line selection, optical density, energy between atomic states ($E_j and E_i$), and atomic dataset accuracy. The value presented here is an estimate of the temperature in the plasma arc core and is within the typical range expected for thermal plasma discharges [24].

The electron density was estimated from Stark broadening of hydrogen, H_α line ($656.3\,nm$). Collisions between radiating atoms and surrounding particles leads to broadening of the spectral lines. Three collisional broadening mechanism are classified as: (1) Stark, (2) Van der Waals, and (2) resonance

broadening. Stark broadening or pressure broadening occurs due to the microfields between charged species and the radiating atom. In the presence of this external electric field, the electrons and nuclei will be pulled in opposite directions. The change in the electronic state causes the some electrons to be at lower or higher energies and therefore broadening of spectral lines. Furthermore, the Stark effect is responsible for splitting of degenerate states. Van der Waals (2) broadening occurs from dipole interactions between an excited state and the induced dipole of the ground state atom. Resonance broadening (3) or self broadening, occurs between two identical species and is limited to species in the lower or upper state with an electric dipole transition to the ground state (resonance). (2) and (3) are small compared to Stark broadening and have been neglected in the calculation of the electron density. The Stark broadening for hydrogen is given by where α is tabulated in [123]:

$$\Delta\lambda_{\frac{1}{2}}^{S} = \left(2.50 \times 10^{-9}\right) \alpha_{1/2} N_e^{1/2} \tag{A.6}$$

Additionally to Stark broadening or more generally pressure broadening of spectral lines, other broadening mechanism must be considered and deconvolved from the spectral line to determine the electron density. These additional broadening mechanisms are: (1) thermal or Doppler broadening, (2) natural line broadening, and (3)instrumentation broadening. Doppler broadening is caused by the thermal motion of the the emitting particles. The line profile is Gaussian given by:

$$\Delta\lambda_{\frac{1}{2}}^{D} = \left(7.16 \times 10^{-7}\right) \lambda \left(\frac{T}{M}\right)^{1/2} \tag{A.7}$$

Where T is the temperature of the emitters in Kelvin, and M is the atomic weight in a.m.u. For the H_α line this corresponds to a FWHM of 0.05 nm at an electron temperature of 1 eV. Natural broadening is caused by the uncertainty in the energy (Heisenberg) of the spontaneous emission and is given by:

$$\Delta\lambda_{\frac{1}{2}}^{N} = \frac{\lambda_{ji}^{2}}{2\pi c} A_{ji} \tag{A.8}$$

In the argon plasma consider natural broadening is negligibly small ($1\times10^{-5}nm$). The instrument broadening is determined from a line source such as low pressure gas discharge lamp (were one can assumes negligible broadening of lines) or a coherent radiation source, HeNe laser. The broadening for the HR2000+ is significant at 1.2 nm (determined from laser source). It should be noted that the instrumentation profile is a function of wavelength.

The spectral line profile consist of both Gaussian (instrumentation and Doppler broadening) and Lorentz (Stark) line profiles which can be expressed by Voigt function. Since the spectral line is a convolution of these broadening mechanism, to determine the Stark broadening the Gaussian contributions must be deconvolved from the line profile. The Voigt line profile is given:

$$f(\lambda) = \frac{\Delta\lambda_{Lorenz}}{\pi^{3/2}\Delta\lambda_{Guass}} \int_0^{\infty} \frac{1}{(x-\lambda_{line})^2 + \Delta\lambda_{Lorenz}^2} \times exp\left(-\frac{(x-\lambda_{line})^2}{\Delta\lambda_{Guass}}\right) dx$$

$$with$$

$$\Delta\lambda_{Guass} = \left(\Delta\lambda_{Doppler}^2 + \Delta\lambda_{Instrument}^2\right)^{1/2} \tag{A.9}$$

Upon deconvolving the Gaussian component of the spectral line, the Stark width can be determined and the number density of electrons calculated from Eqn. A.6. The electron density was estimated to be $\sim 10^{23}\ m^{-3}$. The temperature and density measurements are within the expected bounds for thermal plasma discharges. Additionally, comparing the values with Fig. A.4, the LTE approximation is valid.

A.4 Thermal Discharge Temporal Evolution

High-speed imaging shows the thermal plasma evolution. The findings are summarized: 1) the plasma discharge is constricted and does not occupy the available chamber volume for large diameters and 2) multiple arcs can form in large volumes, with a high degree of randomness to their shape. Consequently, there is significant shot-to-shot variation in how the core of the plasma interacts with samples in the reaction chamber. Reduction of the chamber volume produces more uniform arcs.

Fig. A.6 shows high-speed image sequences for two separate shots of the arc discharge. Fig. A.6 (a) shows a time evolution of the plasma arc

discharge. The arc initially exhibits multiple branched filaments from the anode (left) at 10 μs. The arc filaments attach and track along the surface of the alumina sample-holder to the cathode. At 35 μs the arc filaments have coalesced into a single diffuse arc discharge. Fig. A.6 (b) shows the time evolution of another constricted arc filament bridging the inter-electrode gap at 10 and 20 μs. There is minimal interaction with the sample holder. Initially, the arc occupies a small localized volume. As the current and temperature rises, the arc volume grows while retaining the initial geometric configuration. These image sequences show that a large thermal arc discharge is formed within the volume, but reduction of the chamber diameter is necessary to form a wall stabilized arc which will inevitability cause increased surface erosion of the quartz confining chamber. The randomness of the volume arc prevents direct sample interaction, but for dielectric surfaces such as the alumina rod the arc strongly interacts preferring to track along the surface.

The images show the high degree of randomness in the initial formation and development of the arc filament. Once an arc is formed, the diameter increases until the arc occupies approximately a quarter of the chamber volume. Reduction of the chamber volume produces a more uniform discharge, as the capillary wall stabilizes the arc [22, 24].

A.5 Thermal Plasma Material Interactions

The device has been used to study the interaction of thermal plasmas with three test targets: silicon, alumina, and sapphire targets. The samples

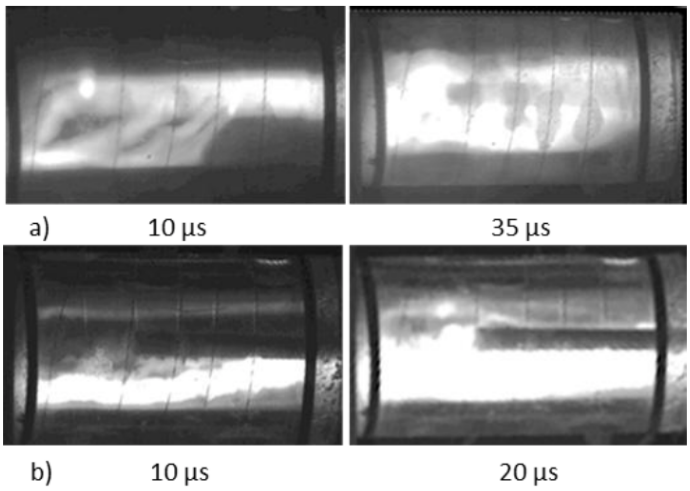

Figure A.6: High-speed imaging of the thermal arc discharge in argon. (a) Time evolution of filamentary branching and surface tracking along the sample holder at 10 μs, and growth of the filamentary arc at 35 μs. (b) Time evolution of the constricted plasma arc filament that does not interact with the sample holder at 10 and 20 μs. [11]

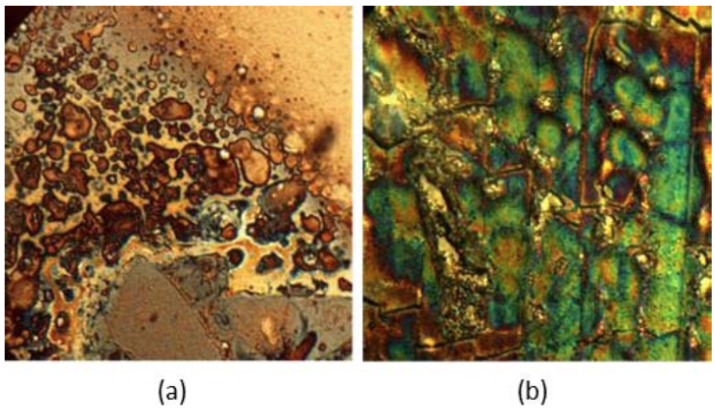

Figure A.7: Photomicrograph of silicon (a) and (b) sapphire showing deposits of copper from early tests using brass electrodes. Similar samples tested with Elkonite electrodes show no evidence of copper. [11]

were orientated orthogonal to the flow. Initial studies used a brass anode and a steel cathode. In these studies, the samples became coated with copper from the anode, as shown in Fig. A.7 . The deposition of copper on the surface was undesirable for material analysis.

To decrease electrode material deposition on test samples, new electrodes were fabricated from Elkonite 50W3, an infiltrated 10% copper and 90% tungsten contact material. The high-melting temperature of tungsten prevents evaporation of electrode material when the arc is in contact with the surface. Copper's high thermal and electrical conductivity allow large currents to easily flow and reduce local thermal loadings, while the tungsten provides a support matrix preventing electrode erosion. The electrodes must be conditioned prior to material testing to evaporate copper present in the surface where arc roots traverse. About 50 shots were required to evaporate the cop-

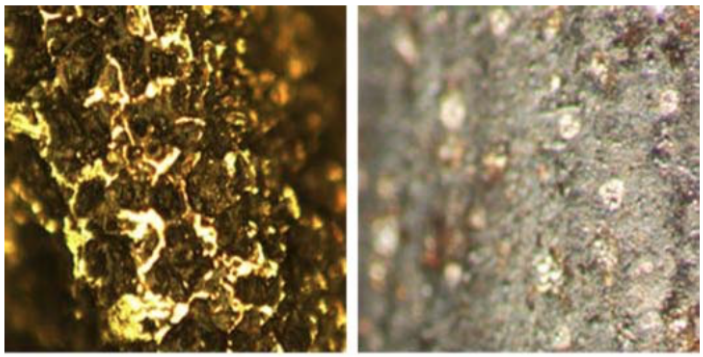

Figure A.8: Photomicrographs of (a) brass and (b) Elkonite electrodes after several hundred tests. The brass shows gross removal of molten material while the Elkonite surface is smooth with stochastic arc root spots. [11]

per from the surface leaving only the tungsten. Fig. A.8 compares the surface of the brass and Elkonite anodes. The brass shows evidence of gross melting from the arc roots, whereas the Elkonite shows only small spots that are presumably arc attachment spots on the Elkonite surface. After the electrode conditioning, samples did not show any metallic depositions.

A second source of contamination was observed from the evaporation and deposition of silicon on test target substrates. The test samples were investigated with Hitachi S-4700 high- resolution SEM equipped with an Oxford Instruments EDXS microanalysis system. Fig. A.9 shows an SEM photograph of a single-crystal sapphire sample after 15 exposures to the plasma. The sample was coated with a fine dusting of silicon particles with an average particle size of 3040 nm. At the center of the photograph is an area where the silicon deposits were mechanically removed, revealing the sapphire substrate. Com-

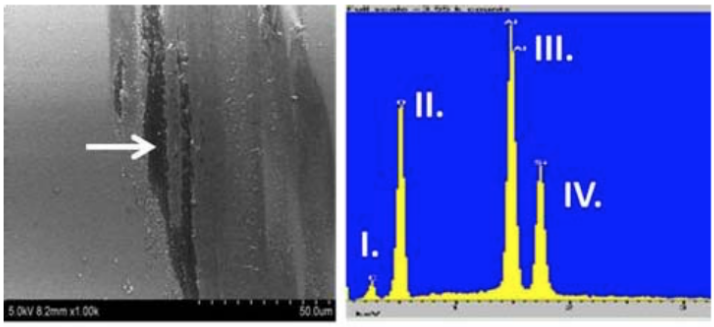

Figure A.9: Surface of sapphire (single crystal) with silicon deposited onto the sample. The arrow indicates where scratching of the surface exposed the sapphire substrate. (b) EDXS analysis of the sample confirming the presence of (I) carbon, (II) oxygen, (III) aluminum, and (IV) silicon. [11]

parison of the exposed sapphire sample substrate with an unexposed sample showed no changes. EDXS analysis of the sample, Fig. A.9, confirmed the presence of a significant amount of silicon. Trace amounts of of carbon were also detected. These set of images indicate that the pulsed thermal plasma discharge has little effect on plasma facing components, for 15 exposures.

Fig. A.10 shows a section of the quartz plasma chamber. The sample was removed after 300 exposures to an argon plasma with a charge voltage of 3.2 kV. The interior of the chamber closest to the gas inlet, anode, was discolored and opaque. (left portion of quartz chamber Fig. A.10). Comparatively, no damage was observed at the gas outlet, cathode (right portion quartz chamber Fig. A.10). SEM analysis of the damaged region showed the surface to contain a number of spheroidal pores on the order of 1 μm in diam-

eter, A.10. Taking a cleaved cross-section perpendicular to the plasma facing surface allowed the depth of plasma interaction to be investigated. Analysis of the cleaved cross-section, Fig. A.10, showed three distinct zones: (1) the boundary between the unaffected quartz and the reacted zone above, (2) a vitrification zone, and (3) a highly porous zone.

From the SEM analysis it was determined that the damaged zone extended 3.23.4 μm into the inner surface of the quartz chamber. Whereas cross-sections of the cathode side of the chamber did not show any damage. Energy dispersive x-ray spectroscopy (EDXS) analysis of the quartz anode region showed a significant silicon deficiency with respect to an unexposed control. EDXS also confirmed the presence of minor concentrations of carbon contamination. This carbon soot corresponds to the discoloration observed in A.10. The presence of carbon is due to the o-rings present in the chamber assembly. In order to prevent silicon deposition on target materials, the plasma chamber must be replaced after 100 exposures. Additionally, analysis of the chamber indicated that even after hundreds of exposures minimal surface damage is observed for plasma facing materials. The anode region was most damaged, because the arc initiated at the anode and was stabilized by the quartz wall as evident in A.6. (This is likely due to the protrusion of the gas inlet electrode and electric field enhancement.) The arc then separates from the surface either tracking along the specimen holder, or forms a volume arc terminating at the cathode with minimal interaction with the quartz surface.

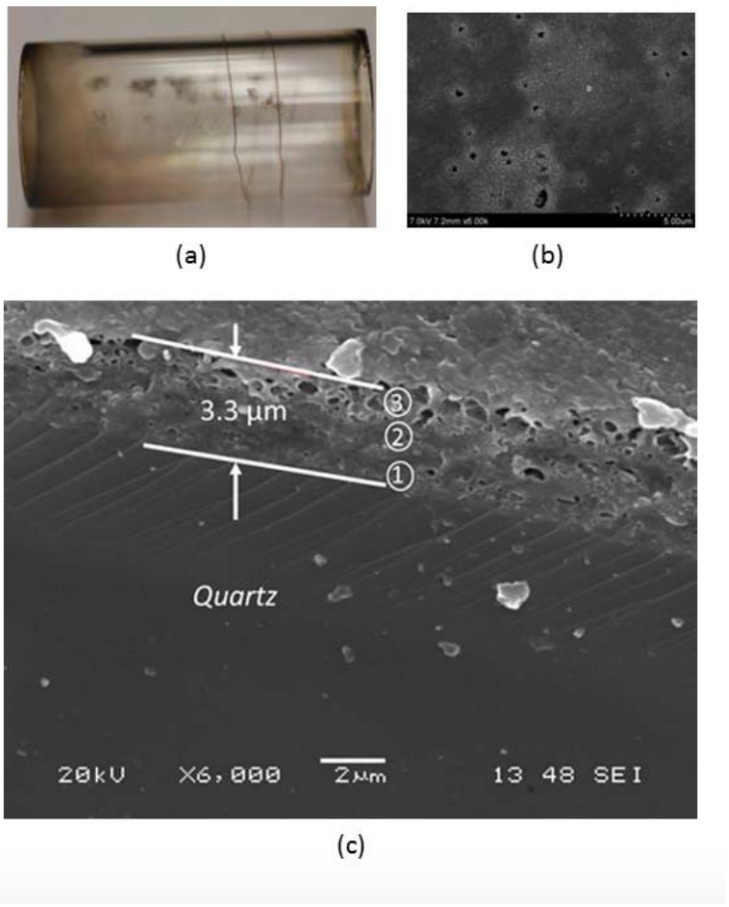

Figure A.10: (a) Plasma quartz chamber after 300 exposures. Left: the damaged portion of the fused quartz was at the anode, and the cathode end of the tube showed no damage (a small ring of discoloration on the cathode side is on the exterior of the tube, caused by the decomposition of an O-ring). (b) SEM analyses of the surface near the anode showed an abundance of spheroidal holes. (c) SEM analysis of a chipped edge at the anode, showed that the depth of the affected zone is about 3.3 µm. [11]

A.5.1 Molecular Dynamics

Molecular dynamic simulations of thermal argon plasmas on various materials were investigated. The results indicated that the low energy atoms mostly constitute surface reorganization and minimal surface ablation, characterized only by the high energy tail. The results of this work are provided in [13] and correlate well with experimental findings. In Fig. A.11 shows the ablation yield versus plasma temperature. At low temperatures, characteristic of thermal plasmas, the ablation yield is low. It isn't until the kinetic energy of the argon atom is 3-4 times the surface bond energy that an atom is ejected.

- Sharia, Onise, Jeffrey Holzgrafe, Nayoung Park, and Graeme Henkelman. "Rare event molecular dynamics simulations of plasma induced surface ablation." The Journal of chemical physics 141, no. 7 (2014): 074706. [13]

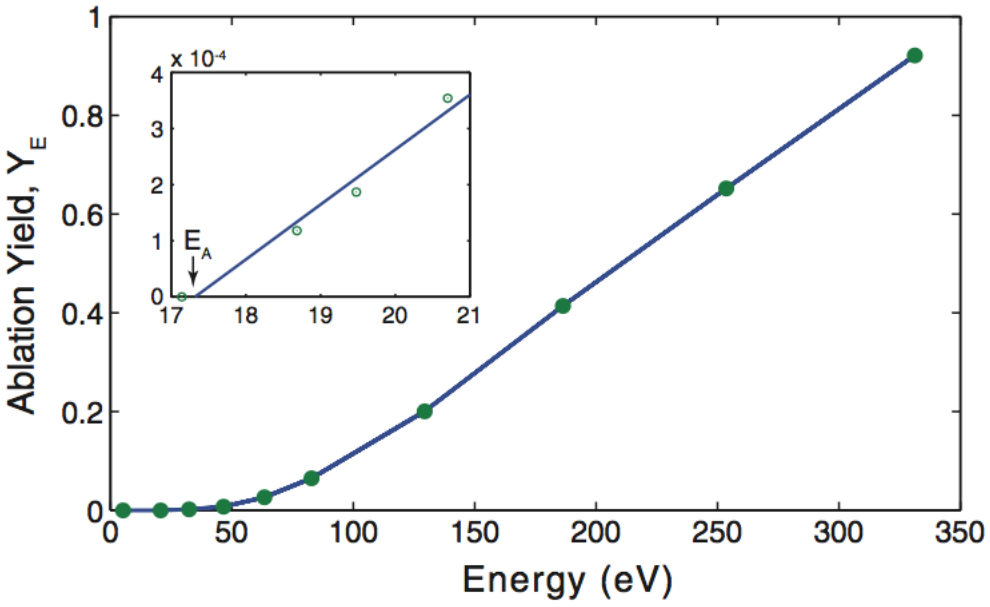

Figure A.11: Molecular dynamic simulations of argon plasma. The ablation yield γ as function of argon kinetic energy [13].

Bibliography

[1] G. Hagelaar and L. Pitchford, "Solving the boltzmann equation to obtain electron transport coefficients and rate coefficients for fluid models," *Plasma Sources Science and Technology*, vol. 14, no. 4, p. 722, 2005.

[2] R. Hake Jr and A. Phelps, "Momentum-transfer and inelastic-collision cross sections for electrons in o 2, co, and c o 2," *Physical Review*, vol. 158, no. 1, p. 70, 1967.

[3] M. I. Boulos, P. Fauchais, and E. Pfender, *Thermal plasmas: fundamentals and applications*. Springer Science & Business Media, 2013.

[4] A. Fridman, *Plasma chemistry*. Cambridge university press, 2008.

[5] U. Ebert, C. Montijn, T. Briels, W. Hundsdorfer, B. Meulenbroek, A. Rocco, and E. Van Veldhuizen, "The multiscale nature of streamers," *Plasma Sources Science and Technology*, vol. 15, no. 2, p. S118, 2006.

[6] Y. P. Raizer and J. E. Allen, *Gas discharge physics*. Springer Berlin, 1997, vol. 2.

[7] M. Aresta, A. Dibenedetto, and E. Quaranta, "The carbon dioxide molecule," in *Reaction Mechanisms in Carbon Dioxide Conversion*. Springer, 2016, pp. 1–34.

[8] P. Instruments. (2017, August) Princeton instruments pi-max 4: 1024i. [Online]. Available: http://www.princetoninstruments.com/userfiles/files/assetLibrary/Datasheets/Princeton_Instruments_PI-MAX4_1024i_P1-5-10-16.pdf

[9] (2017, August) Newport modular integrating sphere. [Online]. Available: https://www.newport.com/f/integrating-spheres

[10] Y. Itikawa, "Cross sections for electron collisions with carbon dioxide," *Journal of Physical and Chemical Reference Data*, vol. 31, no. 3, pp. 749–767, 2002.

[11] M. V. Pachuilo, F. Stefani, L. L. Raja, R. D. Bengtson, G. A. Henkelman, A. C. Tas, W. M. Kriven, and K. S. Suraj, "Development of a gas-fed plasma source for pulsed high-density plasma/material interaction studies," *IEEE Transactions on Plasma Science*, vol. 42, no. 10, pp. 3245–3252, 2014.

[12] N. Ohno, M. A. Razzak, H. Ukai, S. Takamura, and Y. Uesugi, "Validity of electron temperature measurement by using boltzmann plot method in radio frequency inductive discharge in the atmospheric pressure range," *Plasma and fusion research*, vol. 1, pp. 028–028, 2006.

[13] O. Sharia, J. Holzgrafe, N. Park, and G. Henkelman, "Rare event molecular dynamics simulations of plasma induced surface ablation," *The Journal of chemical physics*, vol. 141, no. 7, p. 074706, 2014.

[14] P. Raizer Yu, "Gas discharge physics," 1991.

[15] V. I. Parvulescu, M. Magureanu, and P. Lukes, *Plasma chemistry and catalysis in gases and liquids*. John Wiley & Sons, 2012.

[16] H. Griem, *Plasma Spectroscopy*. McGraw-Hill, 1964.

[17] H. R. Griem, *Principles of plasma spectroscopy*. Cambridge University Press, 2005, vol. 2.

[18] L. Bromberg, D. Cohn, A. Rabinovich, and N. Alexeev, "Plasma catalytic reforming of methane," *International Journal of Hydrogen Energy*, vol. 24, no. 12, pp. 1131–1137, 1999.

[19] E. Stuhlinger, "Electric space propulsion systems," *Space Science Reviews*, vol. 7, no. 5-6, pp. 795–847, 1967.

[20] P. J. Wilbur, R. G. Jahn, and F. C. Curran, "Space electric propulsion plasmas," *IEEE Transactions on Plasma Science*, vol. 19, no. 6, pp. 1167–1179, 1991.

[21] M. Zhukov, "Electric arc generators of thermal plasma (review)," *Plasma Devices and Operations*, vol. 5, no. 1, pp. 1–36, 1996.

[22] J. D. Powell and A. E. Zielinski, "Capillary discharge in the electrothermal gun," *IEEE transactions on magnetics*, vol. 29, no. 1, pp. 591–596, 1993.

[23] E. Gomez, D. A. Rani, C. Cheeseman, D. Deegan, M. Wise, and A. Boccaccini, "Thermal plasma technology for the treatment of wastes: a critical review," *Journal of Hazardous Materials*, vol. 161, no. 2, pp. 614–626, 2009.

[24] E. Pfender, "Thermal plasma technology: where do we stand and where are we going?" *Plasma chemistry and plasma processing*, vol. 19, no. 1, pp. 1–31, 1999.

[25] M. I. Boulos, "Thermal plasma processing," *IEEE transactions on Plasma Science*, vol. 19, no. 6, pp. 1078–1089, 1991.

[26] C. H. Flurscheim, *Power circuit breaker theory and design*. Iet, 1982, vol. 1.

[27] P. Muller, S. Tenbohlen, R. Maier, and M. Anheuser, "Characteristics of series and parallel low current arc faults in the time and frequency domain," in *2010 Proceedings of the 56th IEEE Holm Conference on Electrical Contacts*. IEEE, 2010, pp. 1–7.

[28] M. A. Lieberman and A. J. Lichtenberg, *Principles of plasma discharges and materials processing*. John Wiley & Sons, 2005.

[29] J.-S. Chang, P. A. Lawless, and T. Yamamoto, "Corona discharge processes," *IEEE Transactions on plasma science*, vol. 19, no. 6, pp. 1152–1166, 1991.

[30] U. Kogelschatz, "Filamentary, patterned, and diffuse barrier discharges," *IEEE Transactions on plasma science*, vol. 30, no. 4, pp. 1400–1408, 2002.

[31] U. Ebert, S. Nijdam, C. Li, A. Luque, T. Briels, and E. van Veldhuizen, "Review of recent results on streamer discharges and discussion of their relevance for sprites and lightning," *Journal of Geophysical Research: Space Physics*, vol. 115, no. A7, 2010.

[32] A. Schutze, J. Y. Jeong, S. E. Babayan, J. Park, G. S. Selwyn, and R. F. Hicks, "The atmospheric-pressure plasma jet: a review and comparison to other plasma sources," *IEEE transactions on plasma science*, vol. 26, no. 6, pp. 1685–1694, 1998.

[33] D. Breden, L. L. Raja, C. A. Idicheria, P. M. Najt, and S. Mahadevan, "A numerical study of high-pressure non-equilibrium streamers for combustion ignition application," *Journal of Applied Physics*, vol. 114, no. 8, p. 083302, 2013.

[34] T. Briels, J. Kos, G. Winands, E. Van Veldhuizen, and U. Ebert, "Positive and negative streamers in ambient air: measuring diameter, velocity and dissipated energy," *Journal of Physics D: Applied Physics*, vol. 41, no. 23, p. 234004, 2008.

[35] U. Kogelschatz, "Dielectric-barrier discharges: their history, discharge physics, and industrial applications," *Plasma chemistry and plasma processing*, vol. 23, no. 1, pp. 1–46, 2003.

[36] P. Stritzke, I. Sander, and H. Raether, "Spatial and temporal spectroscopy of a streamer discharge in nitrogen," *Journal of Physics D: Applied Physics*, vol. 10, no. 16, p. 2285, 1977.

[37] Z. Machala, M. Janda, K. Hensel, I. Jedlovskỳ, L. Leštinská, V. Foltin, V. Martišovitš, and M. Morvova, "Emission spectroscopy of atmospheric pressure plasmas for bio-medical and environmental applications," *Journal of Molecular Spectroscopy*, vol. 243, no. 2, pp. 194–201, 2007.

[38] J. F. Kolb, A.-A. H. Mohamed, R. Price, R. Swanson, A. Bowman, R. Chiavarini, M. Stacey, and K. Schoenbach, "Cold atmospheric pressure air plasma jet for medical applications," *Applied Physics Letters*, vol. 92, no. 24, p. 241501, 2008.

[39] D. Breden, K. Miki, and L. Raja, "Self-consistent two-dimensional modeling of cold atmospheric-pressure plasma jets/bullets," *Plasma Sources Science and Technology*, vol. 21, no. 3, p. 034011, 2012.

[40] C. Enloe, T. E. McLaughlin, R. D. Van Dyken, K. Kachner, E. J. Jumper, and T. C. Corke, "Mechanisms and responses of a single dielectric barrier plasma actuator: plasma morphology," *AIAA journal*, vol. 42, no. 3, pp. 589–594, 2004.

[41] T. C. Corke, C. L. Enloe, and S. P. Wilkinson, "Dielectric barrier discharge plasma actuators for flow control," *Annual review of fluid mechanics*, vol. 42, pp. 505–529, 2010.

[42] K. Urashima and J.-S. Chang, "Removal of volatile organic compounds from air streams and industrial flue gases by non-thermal plasma technology," *IEEE Transactions on Dielectrics and Electrical Insulation*, vol. 7, no. 5, pp. 602–614, 2000.

[43] A. Y. Starikovskii, N. B. Anikin, I. N. Kosarev, E. I. Mintoussov, M. M. Nudnova, A. E. Rakitin, D. V. Roupassov, S. M. Starikovskaia, and V. P. Zhukov, "Nanosecond-pulsed discharges for plasma-assisted combustion and aerodynamics," *Journal of Propulsion and Power*, vol. 24, no. 6, pp. 1182–1197, 2008.

[44] R. Snoeckx, R. Aerts, X. Tu, and A. Bogaerts, "Plasma-based dry reforming: a computational study ranging from the nanoseconds to seconds time scale," *The Journal of Physical Chemistry C*, vol. 117, no. 10, pp. 4957–4970, 2013.

[45] X. Tu and J. Whitehead, "Plasma-catalytic dry reforming of methane in an atmospheric dielectric barrier discharge: Understanding the synergistic effect at low temperature," *Applied Catalysis B: Environmental*, vol. 125, pp. 439–448, 2012.

[46] X. Tu, H. J. Gallon, M. V. Twigg, P. A. Gorry, and J. C. Whitehead, "Dry reforming of methane over a ni/al2o3 catalyst in a coaxial dielectric barrier discharge reactor," *Journal of Physics D: Applied Physics*, vol. 44, no. 27, p. 274007, 2011.

[47] R. Aerts, W. Somers, and A. Bogaerts, "Carbon dioxide splitting in a dielectric barrier discharge plasma: a combined experimental and computational study," *ChemSusChem*, vol. 8, no. 4, pp. 702–716, 2015.

[48] M. Noeske, J. Degenhardt, S. Strudthoff, and U. Lommatzsch, "Plasma jet treatment of five polymers at atmospheric pressure: surface modifications and the relevance for adhesion," *International journal of adhesion and adhesives*, vol. 24, no. 2, pp. 171–177, 2004.

[49] J. Loureiro and J. Amorim, "Kinetics and spectroscopy of low temperature plasmas," *Kinetics and Spectroscopy of Low Temperature Plasmas. Series: Graduate Texts in Physics, ISBN: 978-3-319-09252-2. Springer International Publishing (Cham), Edited by Jorge Loureiro and Jayr Amorim*, 2016.

[50] E. E. Kunhardt and L. H. Luessen, *Electrical Breakdown and Discharges in Gases: Part A Fundamental Processes and Breakdown.* Springer Science & Business Media, 2013, vol. 89.

[51] L. B. Loeb and J. Meek, "The mechanism of spark discharge in air at atmospheric pressure. ii," *Journal of Applied Physics*, vol. 11, no. 7, pp. 459–474, 1940.

[52] H. Raether, "The development of electron avalanche in a spark channel (from observations in a cloud chamber)," *Zeitschrift fur Physik*, vol. 112, p. 464, 1939.

[53] J. Meek, "A theory of spark discharge," *Physical review*, vol. 57, no. 8, p. 722, 1940.

[54] L. B. Loeb and J. M. Meek, *The mechanism of the electric spark*. Stanford University Press, 1941.

[55] L. B. Loeb, "The threshold for spark development by streamer mechanism in uniform fields," *Physical Review*, vol. 74, no. 2, p. 210, 1948.

[56] L. B. Loeb and A. F. Kip, "Electrical discharges in air at atmospheric pressure the nature of the positive and negative point-to-plane coronas and the mechanism of spark propagation," *Journal of Applied Physics*, vol. 10, no. 3, pp. 142–160, 1939.

[57] V. D. Rusanov and A. A. Fridman, "The physics of a chemically active plasma," *Moscow Izdatel Nauka*, 1984.

[58] M. Boness and G. Schulz, "Vibrational excitation in c o 2 via the 3.8-ev resonance," *Physical Review A*, vol. 9, no. 5, p. 1969, 1974.

[59] T. Nozaki, S. Abe, S. Moriyama, S. Kameshima, K. Okazaki, V. Goujard, and A. Ağıral, "One step methane conversion to syngas by dielectric barrier discharge," *Japanese Journal of Applied Physics*, vol. 54, no. 1S, p. 01AG01, 2014.

[60] G. Petitpas, J.-D. Rollier, A. Darmon, J. Gonzalez-Aguilar, R. Metkemeijer, and L. Fulcheri, "A comparative study of non-thermal plasma

assisted reforming technologies," *International Journal of Hydrogen Energy*, vol. 32, no. 14, pp. 2848–2867, 2007.

[61] M. S. Bak, S.-K. Im, and M. Cappelli, "Nanosecond-pulsed discharge plasma splitting of carbon dioxide," *IEEE Transactions on Plasma Science*, vol. 43, no. 4, pp. 1002–1007, 2015.

[62] N. Ramdani, A. Lousdad, A. Tilmatine, and S. Nemmich, "Dielectric barrier discharge-based investigation and analysis of wastewater treatment and pollutant removal," *Water Science and Technology*, vol. 73, no. 12, pp. 2858–2867, 2016.

[63] A. Bogaerts, T. Kozák, K. van Laer, and R. Snoeckx, "Plasma-based conversion of co 2: current status and future challenges," *Faraday discussions*, vol. 183, pp. 217–232, 2015.

[64] T. Kozák and A. Bogaerts, "Evaluation of the energy efficiency of co2 conversion in microwave discharges using a reaction kinetics model," *Plasma Sources Science and Technology*, vol. 24, no. 1, p. 015024, 2014.

[65] R. Snoeckx, S. Heijkers, K. Van Wesenbeeck, S. Lenaerts, and A. Bogaerts, "Co 2 conversion in a dielectric barrier discharge plasma: N 2 in the mix as a helping hand or problematic impurity?" *Energy & Environmental Science*, vol. 9, no. 3, pp. 999–1011, 2016.

[66] M. Ramakers, I. Michielsen, R. Aerts, V. Meynen, and A. Bogaerts, "Effect of argon or helium on the co2 conversion in a dielectric barrier

discharge," *Plasma processes and polymers*, vol. 12, no. 8, pp. 755–763, 2015.

[67] I. Omae, "Aspects of carbon dioxide utilization," *Catalysis Today*, vol. 115, no. 1, pp. 33–52, 2006.

[68] C. Song, "Global challenges and strategies for control, conversion and utilization of co 2 for sustainable development involving energy, catalysis, adsorption and chemical processing," *Catalysis Today*, vol. 115, no. 1, pp. 2–32, 2006.

[69] X. Qiu, I. Chalmers, and P. Coventry, "A study of alternative insulating gases to sf6," *Journal of Physics D: Applied Physics*, vol. 32, no. 22, p. 2918, 1999.

[70] T. Uchii, Y. Hoshina, T. Mori, H. Kawano, T. Nakamoto, and H. Mizoguchi, "Investigations on sf6-free gas circuit breaker adopting co2 gas as an alternative arc-quenching and insulating medium," in *Gaseous Dielectrics X*. Springer, 2004, pp. 205–210.

[71] L. Polak, D. Slovetsky, and Y. P. Butylkin, "Carbon dioxide dissociation in electric discharges: arc discharge," 1977.

[72] Y. P. Butylkin, A. Grinenko, A. Levitskii, L. Polak, N. Rytova, and D. Slovetskii, "Mathematical-modeling of the kinetics of the thermal-decomposition of carbon-dioxide in an electric-arc discharge and quench-

ing of the products," *HIGH ENERGY CHEMISTRY*, vol. 13, no. 6, pp. 456–461, 1979.

[73] P. Bruggeman, N. Sadeghi, D. Schram, and V. Linss, "Gas temperature determination from rotational lines in non-equilibrium plasmas: a review," *Plasma Sources Science and Technology*, vol. 23, no. 2, p. 023001, 2014.

[74] L. Yu, L. Pierrot, C. O. Laux, and C. H. Kruger, "Effects of vibrational nonequilibrium on the chemistry of two-temperature nitrogen plasmas," *Plasma Chemistry and Plasma Processing*, vol. 21, no. 4, pp. 483–503, 2001.

[75] A. Goede, W. Bongers, M. Graswinckel, M. van de Sanden, M. Leins, J. Kopecki, A. Schulz, and M. Walker, "Epj web of conferences, 3rd eur," in *Energy Conference*, 2013.

[76] M. A. Malik, A. Ghaffar, and S. A. Malik, "Water purification by electrical discharges," *Plasma Sources Science and Technology*, vol. 10, no. 1, p. 82, 2001.

[77] H. L. Chen, H. M. Lee, S. H. Chen, and M. B. Chang, "Review of packed-bed plasma reactor for ozone generation and air pollution control," *Industrial & Engineering Chemistry Research*, vol. 47, no. 7, pp. 2122–2130, 2008.

[78] K. Van Laer and A. Bogaerts, "Improving the conversion and energy efficiency of carbon dioxide splitting in a zirconia-packed dielectric barrier discharge reactor," *Energy Technology*, vol. 3, no. 10, pp. 1038–1044, 2015.

[79] D. Mei, X. Zhu, Y.-L. He, J. D. Yan, and X. Tu, "Plasma-assisted conversion of co2 in a dielectric barrier discharge reactor: understanding the effect of packing materials," *Plasma Sources Science and Technology*, vol. 24, no. 1, p. 015011, 2014.

[80] V. Rusanov, A. Fridman, and G. Sholin, "The physics of a chemically active plasma with nonequilibrium vibrational excitation of molecules," *Physics-Uspekhi*, vol. 24, no. 6, pp. 447–474, 1981.

[81] M. Seeger, P. Stoller, and A. Garyfallos, "Breakdown fields in synthetic air, co 2, a co 2/o 2 mixture, and cf 4 in the pressure range 0.5–10 mpa," *IEEE Transactions on Dielectrics and Electrical Insulation*, vol. 24, no. 3, pp. 1582–1591, 2017.

[82] A. K. Gaigalas, L. Wang, H.-J. He, and P. DeRose, "Procedures for wavelength calibration and spectral response correction of ccd array spectrometers," *Journal of research of the National Institute of Standards and Technology*, vol. 114, no. 4, p. 215, 2009.

[83] S. Mahadevan and L. L. Raja, "Simulation of direct-current surface plasma discharges in air for supersonic flow control," *AIAA journal*, vol. 50, no. 2, pp. 325–337, 2012.

[84] T. Deconinck, S. Mahadevan, and L. L. Raja, "Computational simulation of coupled nonequilibrium discharge and compressible flow phenomena in a microplasma thruster," *Journal of Applied Physics*, vol. 106, no. 6, p. 063305, 2009.

[85] T. Kozák and A. Bogaerts, "Splitting of co2 by vibrational excitation in non-equilibrium plasmas: a reaction kinetics model," *Plasma Sources Science and Technology*, vol. 23, no. 4, p. 045004, 2014.

[86] H. Hasegawa, H. Date, M. Shimozuma, K. Yoshida, and H. Tagashira, "The drift velocity and longitudinal diffusion coefficient of electrons in nitrogen and carbon dioxide from 20 to 1000 td," *Journal of Physics D: Applied Physics*, vol. 29, no. 10, p. 2664, 1996.

[87] Y. Nakamura, "Drift velocity and longitudinal diffusion coefficient of electrons in nitrogen and carbon monoxide," *Journal of Physics D: Applied Physics*, vol. 20, no. 7, p. 933, 1987.

[88] W. Roznerski and K. Leja, "Electron drift velocity in hydrogen, nitrogen, oxygen, carbon monoxide, carbon dioxide and air at moderate e/n," *Journal of Physics D: Applied Physics*, vol. 17, no. 2, p. 279, 1984.

[89] J. Pack, R. Voshall, and A. Phelps, "Drift velocities of slow electrons in krypton, xenon, deuterium, carbon monoxide, carbon dioxide, water vapor, nitrous oxide, and ammonia," *Physical Review*, vol. 127, no. 6, p. 2084, 1962.

[90] D. Slovetsky, "Chemical reaction mechanisms in nonequilibrium plasmas," *Moscow Nauka*, p. 310, 1980.

[91] P. H. Krupenie, "The band spectrum of carbon monoxide," DTIC Document, Tech. Rep., 1966.

[92] R. W. B. Pearse and A. G. Gaydon, *Identification of molecular spectra*. Chapman and Hall, 1976.

[93] T. Silva, N. Britun, T. Godfroid, and R. Snyders, "Optical characterization of a microwave pulsed discharge used for dissociation of co2," *Plasma Sources Science and Technology*, vol. 23, no. 2, p. 025009, 2014.

[94] C. Rond, A. Bultel, P. Boubert, and B. Chéron, "Spectroscopic measurements of nonequilibrium co 2 plasma in rf torch," *Chemical Physics*, vol. 354, no. 1, pp. 16–26, 2008.

[95] C. Laux, T. Spence, C. Kruger, and R. Zare, "Optical diagnostics of atmospheric pressure air plasmas," *Plasma Sources Science and Technology*, vol. 12, no. 2, p. 125, 2003.

[96] W. L. Wiese, M. W. Smith, and B. Glennon, "Atomic transition probabilities. volume 1. hydrogen through neon," NATIONAL BUREAU OF STANDARDS WASHINGTON DC INST FOR BASIC STANDARDS, Tech. Rep., 1966.

[97] H.-J. Kunze, *Introduction to plasma spectroscopy*. Springer Science & Business Media, 2009, vol. 56.

[98] M. A. Gigosos, M. Á. González, and V. Cardeñoso, "Computer simulated balmer-alpha,-beta and-gamma stark line profiles for non-equilibrium plasmas diagnostics," *Spectrochimica Acta Part B: Atomic Spectroscopy*, vol. 58, no. 8, pp. 1489–1504, 2003.

[99] M. A. Gigosos and V. Cardeñoso, "New plasma diagnosis tables of hydrogen stark broadening including ion dynamics," *Journal of Physics B: Atomic, Molecular and Optical Physics*, vol. 29, no. 20, p. 4795, 1996.

[100] A. Sola, M. Calzada, and A. Gamero, "On the use of the line-to-continuum intensity ratio for determining the electron temperature in a high-pressure argon surface-microwave discharge," *Journal of Physics D: Applied Physics*, vol. 28, no. 6, p. 1099, 1995.

[101] F. R. Gilmore, R. R. Laher, and P. J. Espy, "Franck–condon factors, r-centroids, electronic transition moments, and einstein coefficients for many nitrogen and oxygen band systems," *Journal of physical and chemical reference data*, vol. 21, no. 5, pp. 1005–1107, 1992.

[102] J. Levaton, J. Amorim, V. Monna, J. Nagai, and A. Ricard, "A detailed discussion of the n 2 (c 3 π u) and n 2 (x 1 σ g+) vibrational temperatures in n 2 glow discharges," *The European Physical Journal-Applied Physics*, vol. 26, no. 1, pp. 59–64, 2004.

[103] T. Silva, N. Britun, T. Godfroid, and R. Snyders, "Simple method for gas temperature determination in co 2-containing discharges," *Optics letters*, vol. 39, no. 21, pp. 6146–6149, 2014.

[104] U. Fantz, "Basics of plasma spectroscopy," *Plasma sources science and technology*, vol. 15, no. 4, p. S137, 2006.

[105] G. Milikh, A. Likhanskii, M. Shneider, A. Raina, and A. George, "2-d model of the streamer zone of a leader," *Journal of Plasma Physics*, vol. 82, no. 1, 2016.

[106] U. Ebert and D. D. Sentman, "Streamers, sprites, leaders, lightning: from micro-to macroscales," *Journal of Physics D: Applied Physics*, vol. 41, no. 23, p. 230301, 2008.

[107] L. L. Raja, P. L. Varghese, and D. E. Wilson, "Modeling of the electrothermal ignitor metal vapor plasma for electrothermal-chemical guns," *IEEE Transactions on Magnetics*, vol. 33, no. 1, pp. 316–321, 1997.

[108] M. V. Pachuilo, F. Stefani, R. D. Bengtson, R. Srivastava, L. L. Raja *et al.*, "Dynamics of surface streamer plasmas at atmospheric pressure: Mixtures of argon and methane," *IEEE Transactions on Plasma Science*, 2017.

[109] A. Sarani, A. Y. Nikiforov, and C. Leys, "Atmospheric pressure plasma jet in ar and ar/h 2 o mixtures: Optical emission spectroscopy and temperature measurements," *Physics of Plasmas*, vol. 17, no. 6, p. 063504, 2010.

[110] Z. Kucerovsky, "Electron mobility in argon and carbon dioxide," *IEEE transactions on industry applications*, vol. 42, no. 4, pp. 900–908, 2006.

[111] A. Batal, J. Jarosz, and J. Mermet, "A spectrometric study of a 40 mhz inductively coupled plasma—vi: Argon continuum in the visible region of the spectrum," *Spectrochimica Acta Part B: Atomic Spectroscopy*, vol. 36, no. 10, pp. 983–992, 1981.

[112] A. Gomes, "Criteria for partial lte in an argon thermal discharge at atmospheric pressure; validity of the spectroscopically measured electronic temperature," *Journal of Physics D: Applied Physics*, vol. 16, no. 3, p. 357, 1983.

[113] H. Hyman, "Photoionization cross sections for excited states of argon and krypton," *Applied Physics Letters*, vol. 31, no. 1, pp. 14–15, 1977.

[114] R. Gangwar, L. Sharma, R. Srivastava, and A. Stauffer, "Argon plasma modeling with detailed fine-structure cross sections," *Journal of Applied Physics*, vol. 111, no. 5, p. 053307, 2012.

[115] G. Naidis, "Modelling of transient plasma discharges in atmospheric-pressure methane–air mixtures," *Journal of Physics D: Applied Physics*, vol. 40, no. 15, p. 4525, 2007.

[116] J. De Urquijo, C. Arriaga, C. Cisneros, and I. Alvarez, "A time-resolved study of ionization, electron attachment and positive-ion drift in methane," *Journal of Physics D: Applied Physics*, vol. 32, no. 1, p. 41, 1999.

[117] J. De Urquijo, I. Alvarez, E. Basurto, and C. Cisneros, "Measurement of ionization and electron transport in methane-argon mixtures," *Journal*

of Physics D: Applied Physics, vol. 32, no. 14, p. 1646, 1999.

[118] S. Nijdam, F. Van De Wetering, R. Blanc, E. Van Veldhuizen, and U. Ebert, "Probing photo-ionization: experiments on positive streamers in pure gases and mixtures," *Journal of Physics D: Applied Physics*, vol. 43, no. 14, p. 145204, 2010.

[119] R. Čurík, P. Čársky, and M. Allan, "Vibrational excitation of methane by slow electrons revisited: theoretical and experimental study," *Journal of Physics B: Atomic, Molecular and Optical Physics*, vol. 41, no. 11, p. 115203, 2008.

[120] E.-E. Koch and d. M. Skibowski, "Optical absorption of gaseous methane, ethane, propane and butane and reflection of solid methane and ethane in the vacuum ultraviolet," *Chemical Physics Letters*, vol. 9, no. 5, pp. 429–432, 1971.

[121] D. E. Wilson, K. Kim, and L. L. Raja, "Theoretical analysis of an external pulsed plasma jet," *IEEE transactions on magnetics*, vol. 35, no. 1, pp. 228–233, 1999.

[122] E. Pfender, J. Fincke, and R. Spores, "Entrainment of cold gas into thermal plasma jets," *Plasma Chemistry and Plasma Processing*, vol. 11, no. 4, pp. 529–543, 1991.

[123] A. N. Cox, *Allen's astrophysical quantities*. Springer, 2015.

Vita

Michael Vincent Pachuilo was born in Euless, Texas, the son of Keith and Tammy Pachuilo. He received the Bachelor of Science degree in Aerospace Engineering from The University of Texas at Austin in May 2010, and the Masters of Science degree in Engineering from The University of Texas at Austin in May 2013. He began his PhD work in August 2012.

Permanent address: mvpachuilo@utexas.edu

This dissertation was typeset with LaTeX[†] by Michael Vincent Pachuilo.

[†]LaTeX is a document preparation system developed by Leslie Lamport as a special version of Donald Knuth's TeX Program.